Micro-geochemistry of the mantle and its volcanic rocks

MALARKEY, JACQUELINE

Micro-Geochemistry of the Mantle and its Volcanic Rocks

Jacqueline Malarkey

A thesis submitted in partial fulfilment of the requirements for the degree of Doctor of Philosophy at Durham University.

Department of Earth Sciences
Durham University

November 2009

ABSTRACT

This thesis comprises three studies which utilise detailed micro-sampling techniques to understand the effects of melt infiltration in the continental lithosphere and the relationship of deeply derived kimberlite melts to lithospheric processes. To be able to make these links it is necessary to better constrain the geochemical composition of the primary kimberlite melt.

- The first study investigates inter-grain trace element and Sr isotope variation in clinopyroxene (cpx), amphibole and melt from two spinel lherzolite xenoliths from the Middle Atlas Mountains, Morocco. These results support a multi-stage metasomatic process in which cpx and amphibole are recent additions to the lithospheric mantle, most recently equilibrated with a carbonatite melt. The limited Sr isotope variation in the cpx from this study is typical of global off-craton cpx implying that the majority of cpx in off-craton settings may have a recent, metasomatic origin.

- The second micro-sampling study examines inter-grain trace element and Sr isotope variation in garnet and cpx in garnet lherzolite xenoliths within cratonic peridotites from Bultfontein, South Africa, and Pyramidfels, Greenland. The Sr isotope and trace element variation, combined with a lack of trace element equilibrium between cpx and garnet, imply that the majority of cpx is a recent addition, associated with the host kimberlite-type magma, whereas the garnet is added by an older event, probably by a melt related to either Group II kimberlite or lamproite. A global database of Sr and Nd isotope data for cpx and garnet indicates that these conclusions can be applied more widely. The metasomatic addition of cpx and garnet is limited to vein-wallrock reactions and therefore the majority of lithospheric mantle is concluded to be depleted harzburgite or dunite.

- The third micro-sampling study focuses on constraining the primary geochemical characteristics of kimberlite magma by analysing the constituent phases (perovskite, olivine, apatite, phlogopite, calcite) for trace element and Sr isotope ratios from a sample of hypabyssal kimberlite from Jos, Somerset Island, Canada. An analogue study was carried out on an olivine melilitite from Saltpetre Kop, South Africa with a similar mineral suite (with the addition of melilite). These results show that phenocrystal olivine and apatite provide the best record of the source Sr isotope composition whereas perovskite, typically analysed by laser ablation, is more variable and influenced by crustal interaction, albeit to a limited extent. The results indicate that previously recorded differences between the Sr isotope compositions of whole rock kimberlites and the low-Cr megacryst suite, used to rule out a genetic relationship between the two, can be ascribed to later stage crustal interaction with the kimberlite. As a result, the link between kimberlites and the formation of the low-Cr megacryst suite is strengthened.

DECLARATION

I declare that this thesis, which I submit for the degree of Doctor of Philosophy at Durham University, is mu own work and not substantially the same as any which has previously been submitted at this or any other university.

Jacqueline Malarkey

Durham University

November 2009

ACKNOWLEDGEMENTS

First and foremost I would like to thank both of my supervisors, Graham Pearson and Jon Davidson, as this thesis would not have been possible without the time and effort that they both invested into this project. Graham is thanked in particular for his attention to detail throughout the project as well as for always making time in his busy schedule be it to discuss new data, answer my many questions or to go through the various manuscript/thesis drafts that landed on his desk with increasing frequency towards the end. I would like to thank Jon for always listening to my various problems and offering advice and support despite the ever changing project description which eventually led me to focus solely on mantle samples. Jon is also credited with asking probing questions that challenged my understanding of some of the key issues addressed in this thesis as well as providing useful feedback on both figures and manuscript drafts.

The analytical aspect of this project, in particular with the kimberlite study, presented many challenges. Geoff Nowell is thanked for giving up many hours of his valuable time to work through these issues in order to obtain the best possible data through sampling, chemistry and mass spectrometry. Ofra Klein BenDavid, Laura Font and especially Vikki Martin are thanked for patiently introducing me to the temperamental MicroMill, micro-Sr chemistry and the dubious joys of spending days on the Triton. Nadine Wittig is thanked for helping and encouraging me with analytical aspects of the project as well as always being available for discussion or new ideas, often accompanied with chocolate. Chris Ottley is thanked for his assistance with the trace element analyses and for having the patience to explain analytical details more than once! The many members of the lab are thanked for making me feel welcome in the lab as well as making the long lab days pass more quickly. Chris Hayward is thanked for his assistance with the probe analyses of the mantle xenolith samples at the University of Cambridge. Jason Day and Sally Gibson are thanked for proving access and assistance with the LA trace element analyses at the University of Cambridge. Jane Stammer and Karin Hoal are

acknowledged for producing the QEMSCAN images at the Colorado School of Mines. Louis Carbi is thanked for processing the Jos kimberlite sample in order to retrieve the apatite and GSC are thanked for carrying out the probe work on both Jos and SPK at Carleton University.

Bruce Kjarsgaard, Nadine Wittig and Graham Pearson are thanked for providing the samples that have been analysed in this project. Graham is especially acknowledged for patiently searching for the 'perfect' the mantle xenoliths with large and fresh cpx, not as easy a task as it may seem.

NERC are gratefully acknowledged as the main source of funding for this PhD project and for providing payments with reassuring regularity. The Harkness Prize Fund and the 9IKC student bursaries are also thanked for covering my travel expenses to a number of conferences. Graham and NCIET are thanked for generously funding the majority of the lab work.

It would not be possible to name all the people who have provided useful, insightful and encouraging comments throughout the course of this project. However I would especially like to thank Larry Heaman for his knowledge and encouragement to persist with the kimberlite dissection when others were encouraging the LA route. Roger Mitchell is also thanked for sharing his expert knowledge of kimberlite petrography and for taking the time to discuss the data that has arisen from this project.

Last but not least I would like to thank all those who I have worked with, and especially 'The Bay', for providing a good ear (especially with various lab frustrations), cake and gossip throughout the past 3 years. A special thank you goes to those I have lived with (Vikki Martin, Kay Achenbach and Gareth Lloyd) for patiently listening to my various rants and always providing chocolate and reassurance that it would all work out in the end!

TABLE OF CONTENTS

Chapter 3: Mineralogical evolution of cratonic lithospheric mantle

Chapter 5: Discussion and Conclusions

Chapter 1:

INTRODUCTION

1.1 RATIONALE AND THESIS OUTLINE

Continental lithospheric mantle in both on- and off-craton settings can be directly sampled by mantle xenoliths bought to the surface by volcanic activity, typically in kimberlites and alkali basalts. Traditionally these xenoliths were thought to be a representative sample of the lithospheric mantle (e.g. Nixon 1987). Moreover, it was thought that within the peridotite fraction of the lithosphere the main modal mineralogical changes involved introduction of hydrous minerals such as phlogopite and/or amphibole (e.g. Menzies and Hawkesworth 1987, and references therein). However, more recent experimental work has implied that the abundance of clinopyroxene (cpx), and in cratonic settings garnet, is incompatible with melt depletion estimates from proxies such as olivine Mg number (Walter 1998; Pearson and Nowell 2002). This and other evidence led to the suggestion that modal metasomatism, the addition of new mineral phases by a melt, is responsible for the addition of cpx, garnet and, in some cases, orthopyroxene (opx; van Achterbergh et al. 2001; Pearson and Nowell 2002; Gregoire et al. 2003; Simon et al. 2003; Simon et al. 2008; Wittig et al. 2008).

Garnet and cpx are both important hosts for incompatible elements such as the REE and Sr and therefore the timing of any potential metasomatic addition has implications for the geochemical evolution of the lithospheric mantle: if these phases are relatively recent additions to the lithosphere then this challenges the assumption that the lithospheric mantle has been a geochemically enriched source through time. The addition of cpx and garnet would also influence

geophysical parameters such as density which in turn control the gravitational stability of the lithospheric mantle (Poudjom Djomani et al. 2001; Schutt and Lesher 2006).

Modal metasomatism is thought to predominantly occur via melt-wallrock interactions (e.g. Erlank et al. 1987; Foley 1992). Therefore this process is likely to be more prevalent in areas with a greater throughput of melt, such as regions of intraplate volcanic activity, where mantle xenoliths are typically bought to the surface. The xenoliths may not therefore be typical of prevalent mantle lithosphere away from areas of volcanic activity.

This study aims to investigate this by addressing the following questions:

- To what extent can garnet and cpx be considered as metasomatic phases in on- and off-craton peridotitic lithosphere?
- When were these phases added?
- What is the identity of the parental magma/magmas?
- What is the extent of the metasomatism? Is it limited to veins does it affect the whole lithospheric mantle?
- What are the implications of these conclusions for the geochemical and geophysical evolution of the lithospheric mantle?

In order to address these issues I have undertaken three case studies using detailed micro-sampling isotopic and trace element methods that have not previously been applied to mantle xenoliths. A range of methods were

employed (the details of which are summarised in each chapter) but a common thread of micro-sampling of mineral phases both by micro-drilling and by hand picking were employed (Charlier et al. 2006). The majority of this thesis therefore examines Sr isotope (analysed by TIMS) and trace element (analysed by ICP-MS) variation among cpx and garnet crystals within single xenolith samples. The advantage of this method is that inter-grain variations, which are typically averaged in a bulk analysis, can be determined providing detailed information on grain-scale processes that have influenced the evolution of these rocks. Two previous studies have used LA-ICP-MS to assess Sr isotope variation among cpx crystals (Schmidberger et al. 2003; Neumann et al. 2004) but this technique requires a complex array of corrections due to isobaric interferences which are removed by column chemistry in the method used here (Davidson et al. 2001; Charlier et al. 2006). It is also limited to high Sr, low Rb phases and hence solely to cpx in peridotites. LA-ICP-MS also cannot be used to analyse Sr isotope ratios on phases with higher Rb/Sr ratios such as garnet and the resolution of LA studies is significantly less than that achieved using micro-sampling and Sr isotope analysis by TIMS (Davidson et al. 2001).

The micro-geochemical approach was combined with a detailed petrographic study to examine the mineral relationships. A wealth of information can be derived from trace element data in terms of the parental melt composition and magmatic processes, such as crystallisation, that can fractionate different trace element ratios. Isotope ratios are not fractionated by these magmatic processes and therefore potentially preserve information about the source region of the magma. However both trace element patterns and isotopic ratios are susceptible

to overprinting by more recent events and therefore it is not always possible to obtain a complete metasomatic history using these processes.

The first case study (**Chapter 2**) investigates the origin of cpx in off-craton lithospheric mantle using a xenolith suite from the Middle Atlas Mountains in Morocco. Two spinel lherzolite xenoliths were chosen that have been well characterised in terms of their bulk rock chemistry (Wittig et al. 2005; Wittig et al. in revision-a; Wittig et al. in revision-b) and meet the requirements of the method (relatively fresh and large cpx). The metasomatic addition of cpx in on-craton settings has recently been demonstrated in some locations by a number of authors (van Achterbergh et al. 2001; Gregoire et al. 2003; Simon et al. 2003) but off-craton settings have received less attention. This is partly because it is more difficult to constrain the degree of melting that off-craton settings have experienced (Wittig et al. in revision-a). The Middle Atlas samples are no exception to this and Wittig et al. (in revision-a; in revision-b) have used numerous methods to constrain the melt depletion experienced by these xenoliths but the results are not conclusive due to many of the traditional methods, such as whole rock Al-Fe-Mg relations, being overprinted by metasomatic processes (Wittig et al. 2008). The available melt depletion estimates range from 10% to 20% (Raffone et al. 2009; Wittig et al. in revision-a), are below the 15-23% melt extraction required for complete cpx exhaustion (dependant on starting composition; Walter 1998). These estimates of melt depletion are incompatible with the high modal abundance of cpx (up to 14%), implying that the cpx must have been added later, probably as a result of metasomatism. This conclusion is further strengthened by the trace element and

isotope data presented here. The variation in trace element concentrations, including Sr, can modelled using diffusion constraints to establish the addition of cpx as recent, probably between 0.5Myr and 65Myr of emplacement. The cpx Sr isotope data from this study are compared with a global database of initial Sr and Nd isotope ratios from off-craton cpx mineral separates. This illustrates that the conclusions drawn from this study can be applied in a more global context.

The second case study (**Chapter 3**) focuses on two garnet lherzolites, one from the North Atlantic Craton (NAC) and the other from the Kaapvaal craton. These two cratons have lithospheric mantle that can be viewed as being at opposite ends of the spectrum in terms on Si re-enrichment after melt depletion (Bernstein et al. 2007; Pearson and Wittig 2008). The Kaapvaal craton, where most of the pioneering work on xenoliths was carried out, is known to have experienced significant Si-enrichment, manifested as high modal opx contents (Kesson and Ringwood 1989; Rudnick et al. 1991; Kelemen et al. 1998; Simon et al. 2008). Peridotites from the NAC, on the other hand, have very low modal opx abundances, and are more typical residues expected following a large melt depletion event (Bernstein et al. 2007; Pearson and Wittig 2008). The aim of this case study is therefore to contrast the origin of cpx and garnet from these two locations. A metasomatic origin for cpx has been suggested by previous authors for a number of sample sets (e.g. van Achterbergh et al. 2001; Gregoire et al. 2003; Simon et al. 2003; Simon et al. 2008) and this is the explanation preferred here for both cratonic locations. An alternative explanation that has been suggested is that the cpx and garnet exsolved from high temperature opx

(Cox et al. 1987; Canil 1992; Saltzer et al. 2001). This hypothesis, based on a close spatial relationship between opx, cpx and garnet, is shown not to be a significant process in these xenoliths. The lack of trace element and isotopic equilibrium between the cpx and garnet in both xenoliths indicates that one phase, cpx, is a recent addition to the lithospheric mantle while garnet was added earlier from a different melt.

The cpx is concluded, on the basis of trace element data, to have been added by the host rock prior to eruption probably from a melt genetically related to the kimberlite. These data are combined with a global database of Sr and Nd isotope values for cpx from bulk mineral separates. There is a close agreement between the Nd isotope ratios of global cpx and basaltic kimberlites. However there is a mismatch between the kimberlite and cpx data in terms of Sr isotope values with the kimberlites characterised by more radiogenic values. This difference can be resolved if the crustal contribution to the kimberlite magma can be deconvolved and this is the focus of **Chapter 4**.

Chapter 4 is an attempt to track back the mantle source component of kimberlite magma by 'dissecting' a kimberlite and analysing the constituent minerals in order to constrain the primary kimberlite Sr isotope signature. The primary Sr isotope ratio of the kimberlite magma is masked by a range of processes (Fig. 1.1). The most significant of these are the assimilation of crust and late stage interaction with groundwater. The primary aims of this part of the thesis are:

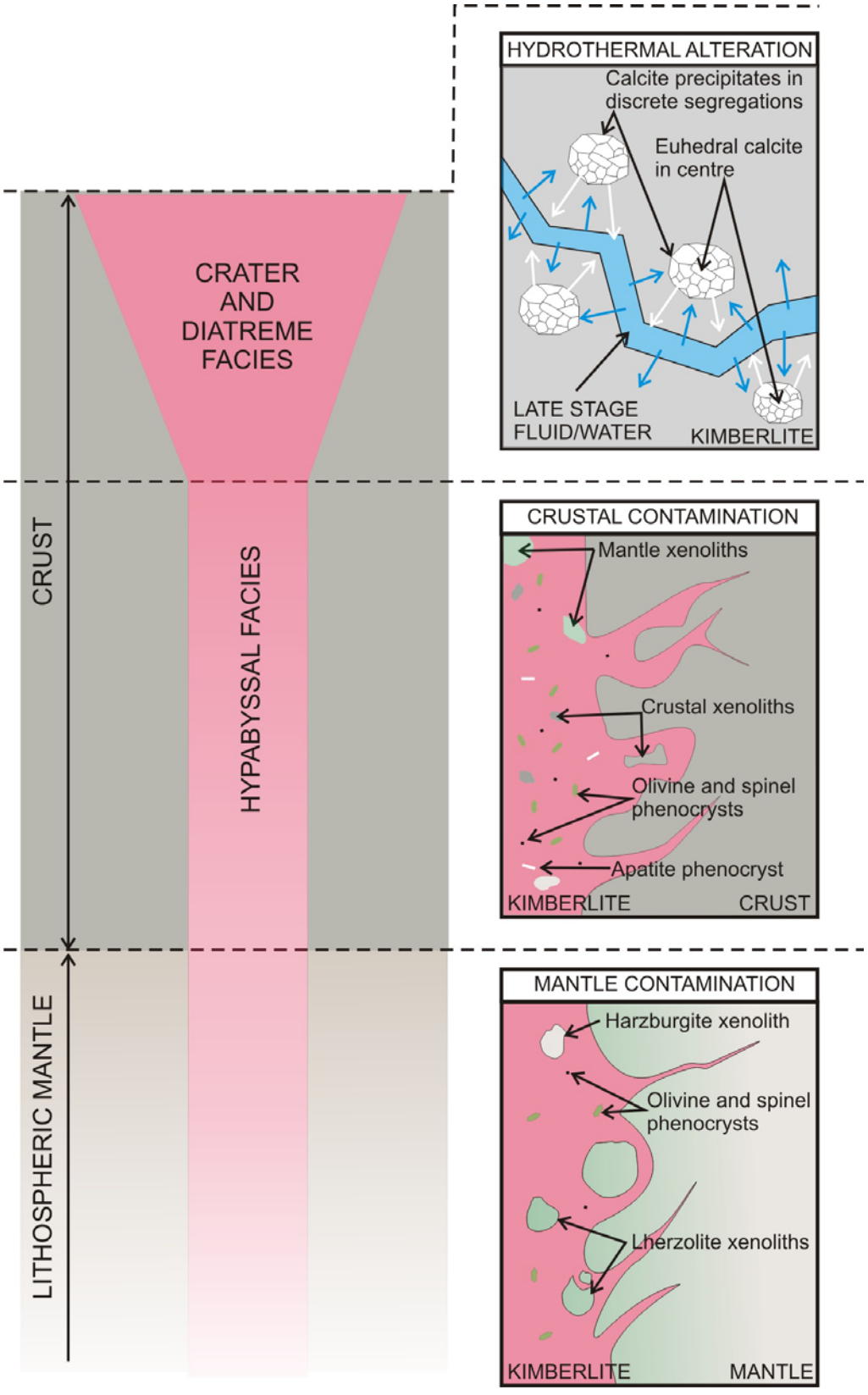

Figure 1.1.

Schematic illustration of the processes that affect the Sr isotope ratio of the kimberlite magma as it migrates through the lithosphere. The incorporation of lithospheric mantle has a limited effect on the Sr isotope composition of the magma, due to low Sr concentrations, but the latter two processes, entrainment of crust and hydrothermal alteration, introduce radiogenic Sr and therefore increase the $^{87}Sr/^{86}Sr$ ratio of the magma.

- What is the primary initial Sr isotope ratio of kimberlite magmas?
- Which mineral phase provides the best characterisation of the kimberlite source region?
- Is the primary kimberlite magma responsible for cpx addition to the lithospheric mantle prior to eruption?
- Is there a genetic link between kimberlites and the megacrysts found within them?
- Is it possible to trace the amount of crustal contamination of the kimberlite magma that has occurred by analysing the trace elements and Sr isotope ratios of the constituent minerals?
- Can micro-geochemistry be used to constrain the mineral crystallisation order in the kimberlite?

A number of LA-ICP-MS studies have addressed some of these questions by analysing groundmass perovskite (e.g. Paton et al. 2007a; Paton et al. 2007b; Kamenetsky et al. 2009; Woodhead et al. 2009). This is partly because perovskite has high Sr and low Rb concentrations and is relatively robust to alteration (Paton et al. 2007b). However the exact pressure and temperature conditions under which the various kimberlite minerals crystallise is poorly constrained and therefore significant crustal contamination may have occurred before the perovskite crystallises (Mitchell 1986). Therefore a more detailed multiphase approach was used to address the above questions. Before 'dissecting' the kimberlite, an olivine melilitite, from Saltpetre Kop, South Africa, was first picked apart. This sample has a similar suite of minerals to kimberlites but has undergone less contamination and alteration and is therefore

a simpler analogue with which to test the method. The results from the study of the olivine melilitite were promising revealing that the spread in Sr isotope values was larger in the later crystallising phases. This indicates that it is possible to investigate the effects of crustal contamination in this way, and that the source composition is best approximated by the earlier phases. The kimberlite sample, from the Jos kimberlite, Somerset Island, Canada, was more complex but the results lead to some interesting conclusions. The minerals which crystallise later (on the basis of petrography), including apatite and calcite, show a wide range in Sr isotopes with the earlier phases, such as olivine and perovskite, revealing a smaller range to less radiogenic values. The large range of initial Sr isotope ratios in the apatite argues for a large span in crystallisation time with some crystallising early and others late. This method therefore allows the Sr budget of the kimberlite to be calculated and a better approximation of the primary Sr isotope composition to be determined. These new data confirm that the primary kimberlite magma has much less radiogenic $^{87}Sr/^{86}Sr_i$ than the whole rock analysis. The Sr isotope composition estimated from the early apatite is similar to the lithospheric mantle values, represented by cpx, confirming that kimberlite magma is a potential candidate for the recent metasomatism.

The last section, **Chapter 5**, summarises the conclusions that have been reached in each chapter and answers the questions proposed in this introduction. This chapter also draws together the different themes to give a cohesive picture of metasomatism in the lithospheric mantle and how, in on-craton settings, this is closely related to kimberlites activity.

1.2. AUTHOR CONTRIBUTIONS

1.2.1. CHAPTER 2

This paper has been submitted to *Contributions to Mineralogy and Petrology* and is currently under review.

Jacqueline Malarkey: I carried out all the analytic work on these samples, with the exception of the probe work for the amphibole. This included the petrography, microsampling, chemistry and analysis of major elements, trace elements and Sr isotope ratios. I processed and modelled the data in order to draw the conclusions based on my interpretations which were aided by discussions with both my supervisors and other members of the geochemistry group. I wrote the manuscript in its entirety which was then passed onto the other authors for feedback. Although this feedback improved the flow and organisation of the manuscript it did not change the interpretation or the conclusions that were drawn.

Nadine Wittig: Nadine provided the two xenoliths, which were part of a larger sample set that she had previously characterised in order to investigate a number of processes. She also provided the major element data for the amphibole from her PhD thesis. Nadine assisted by providing useful discussion and comments on the final draft of the manuscript.

Graham Pearson: Graham, as my primary supervisor, conceived the project as well as providing guidance as to which direction the project should take. He assisted greatly with discussion of the results and also provided useful feedback on the initial drafting of the manuscript.

Jon Davidson: Jon, as my second supervisor, provided guidance and advice with both the interpretation of results as well as providing feedback on the manuscript especially with how to best convey the arguments to a wider audience.

1.2.2. CHAPTER 3

This paper will be submitted to *Journal of Petrology*.

Jacqueline Malarkey: I carried out all the analytical work on these samples including the probe and LA work (at the University of Cambridge). I then processed and modelled the data in order to reach the conclusions that have been reached in this paper. I wrote the manuscript in its entirety and then passed it onto fellow authors for feedback.

Graham Pearson: As my primary supervisor Graham conceived the project and provided useful assistance and direction throughout. He greatly assisted with the discussion of the results and also provided useful feedback on the manuscript. The samples were provided by Graham.

Jon Davidson: Jon provided useful discussion throughout this project and helped me to address some of the larger issues in a clearer manner. He also provided feedback on the manuscript which allowed the arguments to be clarified for a wider audience.

Geoff Nowell: Geoff provided invaluable assistance in the lab by sharing his expertise and discussing any chemistry or mass spectrometry issues that arose.

1.2.3. CHAPTER 4

This is an extended version of a paper that will be submitted to *Earth and Planetary Science Letters.*

Jacqueline Malarkey: I carried out the majority of the analytical work including the minerals picking (after concentration at GSC in the case of the apatite), chemistry and mass spectrometry. The probe work for the Jos sample was carried out at GSC. The data was processed and interpreted by myself with the aid of discussions with my supervisors and other members of the group as well as some useful feedback from conferences. I wrote the manuscript which was passed onto the other authors for comment and feedback which improved the flow but did not significantly change the conclusions drawn.

Graham Pearson: Graham provided the sample of olivine melilitite from Saltpetre Kop and together with Jon devised the project. Graham also provided useful feedback and discussion which helped to clarify the arguments presented.

Jon Davidson: Jon provided useful discussion and a broader outlook on the paper that helped make it more accessible to a larger audience.

Bruce Kjarsgaard: Bruce provided the sample of the Jos kimberlite and had the sample processed at Geological Society of Canada (GSC) in order to concentrate the apatite. He also arranged for the probe work to be carried out at GSC as no probe is available in Durham.

Geoff Nowell: Geoff provided technical assistance and was available for the many discussions required to separate the mineral fractions. Geoff also provided useful feedback on the finer details of the method and ensured all the data were valid.

Chris Ottley: Chris taught me how to run trace element analyses on the Element II ICP-MS and was available for discussing how to set process the data offline to ensure data quality.

Karin Hoal: Karin provided the QEMSCAN images and quantitative modal abundance estimates which were produced at the Colorado School of Mines by her technician Jane Stammer.

1.3. REFERENCES

Bernstein, S., Kelemen, P. B. and HanghÃ¸j, K. (2007). "Consistent olivine Mg# in cratonic mantle reflects Archean mantle melting to the exhaustion of orthopyroxene." Geology 35(5): 459-462.

Canil, D. (1992). "Orthopyroxene stability along the peridotite along the peridotite solidus and the origin of cratonic lithosphere beneath Southern Africa." Earth and Planetary Science Letters 111(1): 83-95.

Charlier, B. L. A., Ginibre, C., Morgan, D., Nowell, G. M., Pearson, D. G., Davidson, J. P. and Ottley, C. J. (2006). "Methods for the microsampling and high-precision analysis of strontium and rubidium isotopes at single crystal scale for petrological and geochronological applications." Chemical Geology 232(3-4): 114-133.

Cox, K. G., Smith, M. R. and Beswtherick, S. (1987). Textural studies of garnet lherzolites: evidence of exsolution origin from high-temperature harzburgites. Mantle Xenoliths. P. H. Nixon, John Wiley and Sons Ltd.**:** 537-550.

Davidson, J., Tepley Iii, F., Palacz, Z. and Meffan-Main, S. (2001). "Magma recharge, contamination and residence times revealed by in situ laser ablation isotopic analysis of feldspar in volcanic rocks." Earth and Planetary Science Letters 184(2): 427-442.

Erlank, A. J., Waters, F. G., Hawkesworth, C. J., Haggerty, S. E., Allsopp, H. L. and Menzies, M. A. (1987). Evidence for mantle metasomatism in peridotite nodules from the Kimberley Pipes, South Africa. Mantle Metasomatism. M. A. Menzies and C. Hawkesworth, Academic Press**:** 221-312.

Foley, S. (1992). "Vein-plus-wall-rock melting mechanisms in the lithosphere and the origin of potassic alkaline magmas." Lithos 28(3-6): 435-453.

Gregoire, M., Bell, D. R. and Le Rouex, A. P. (2003). "Garnet lherzolites from the Kaapvaal craton (South Africa): Trace element evidence for a metasomatic history." Journal of Petrology 44(4): 629-657.

Kamenetsky, V. S., Maas, R., Kamenetsky, M. B., Paton, C., Phillips, D., Golovin, A. V. and Gornova, M. A. (2009). "Chlorine from the mantle: Magmatic halides in the Udachnaya-East kimberlite, Siberia." Earth and Planetary Science Letters 285(1-2): 96-104.

Kelemen, P. B., Hart, S. R. and Bernstein, S. (1998). "Silica enrichment in the continental upper mantle via melt/rock reaction." Earth and Planetary Science Letters 164(1-2): 387-406.

Kesson, S. E. and Ringwood, A. E. (1989). "Slab mantle interactions 2: The formation of diamonds." Chemical Geology 78(2): 97-118.

Menzies, M. A. and Hawkesworth, C. J. (1987). Mantle metasomatism. London ; Orlando, Academic Press.

Mitchell, R. H. (1986). Kimberlites: Mineralogy, Geochemistry, and Petrology, Plenum Press.

Neumann, E. R., Griffin, W. L., Pearson, N. J. and O'Reilly, S. Y. (2004). "The evolution of the upper mantle beneath the Canary Islands: Information from trace elements and Sr isotope ratios in minerals in mantle xenoliths." Journal of Petrology 45(12): 2573-2612.

Nixon, P. H., Ed. (1987). Mantle Xenoliths, John Wiley and Sons.

Paton, C., Hergt, J. M., Phillips, D., Woodhead, J. D. and Shee, S. R. (2007a). "New insights into the genesis of Indian kimberlites from the Dharwar Craton via in situ Sr isotope analysis of groundmass perovskite." Geology 35(11): 1011-1014.

Paton, C., Woodhead, J. D., Hergt, J. M., Phillips, D. and Shee, S. (2007b). "Strontium isotope analysis of kimberlitic groundmass perovskite via LA-MC-ICP-MS." Geostandards and Geoanalytical Research 31(4): 321-330.

Pearson, D. G. and Nowell, G. M. (2002). "The Continental Lithospheric Mantle: Characteristics and Significance as a Mantle Reservoir." Philosophical Transactions: Mathematical, Physical and Engineering Sciences 360(1800): 2383-2410.

Pearson, D. G. and Wittig, N. (2008). "Formation of Archaean continental lithosphere and its diamonds: the root of the problem." Journal of the Geological Society 165: 895-914.

Poudjom Djomani, Y. H., O'Reilly, S. Y., Griffin, W. L. and Morgan, P. (2001). "The density structure of subcontinental lithosphere through time." Earth and Planetary Science Letters 184(3-4): 605-621.

Raffone, N., Chazot, G., Pin, C., Vannucci, R. and Zanetti, A. (2009). "Metasomatism in the Lithospheric Mantle beneath Middle Atlas (Morocco) and the Origin of Fe- and Mg-rich Wehrlites." Journal of Petrology 50(2): 197-249.

Rudnick, R., Mcdonough, W. F. and Orpin, A. (1991). Northern Tanzanian peridotite xenoliths: A comparison with Kaapvaal peridotites and inferences on metasomatic interactions. Proceedings of the Fifth International Kimberlite Conference. H. O. A. Meyer and O. h. Leonardos. Brazil. Kimberlites, related rocks and mantle xenoliths.

Saltzer, R. L., Chatterjee, N. and Grove, T. L. (2001). "The Spatial Distribution of Garnets and Pyroxenes in Mantle Peridotites: Pressure-Temperature History of Peridotites from the Kaapvaal Craton." J. Petrology 42(12): 2215-2229.

Schmidberger, S. S., Simonetti, A. and Francis, D. (2003). "Small-scale Sr isotope investigation of clinopyroxenes from peridotite xenoliths by laser ablation MC-ICP-MS - implications for mantle metasomatism." Chemical Geology 199(3-4): 317-329.

Schutt, D. L. and Lesher, C. E. (2006). "Effects of melt depletion on the density and seismic velocity of garnet and spinel lherzolite." Journal of Geophysical Research-Solid Earth 111(B5): -.

Simon, N. S. C., Irvine, G. J., Davies, G. R., Pearson, D. G. and Carlson, R. W. (2003). "The origin of garnet and clinopyroxene in "depleted" Kaapvaal peridotites." Lithos 71(2-4): 289-322.

Simon, N. S. C., Carlson, R. W., Pearson, D. G. and Davies, G. R. (2008). "The origin and evolution of the Kaapvaal cratonic lithospheric mantle." Journal of Petrology.

van Achterbergh, E., Griffin, W. L. and Stiefenhofer, J. (2001). "Metasomatism in mantle xenoliths from the Letlhakane kimberlites: estimation of element fluxes." Contributions to Mineralogy and Petrology 141(4): 397-414.

Walter, M. J. (1998). "Melting of garnet peridotite and the origin of komatiite and depleted lithosphere." Journal of Petrology 39(1): 29-60.

Wittig, N., Duggen, S., Baker, J. A., Kluegel, A. and Hoernle, K. (2005). "HIMU lithospheric mantle beneath Northwest Africa." Geochimica et Cosmochimica Acta 69(10): A288-A288.

Wittig, N., Pearson, D. G., Webb, M., Ottley, C. J., Irvine, G. J., Kopylova, M., Jensen, S. M. and Nowell, G. M. (2008). "Origin of cratonic lithospheric mantle roots: A geochemical study of peridotites from the North Atlantic Craton, West Greenland." Earth and Planetary Science Letters 274(1-2): 24-33.

Wittig, N., Pearson, D. G., Baker, J., Duggen, S. and Hoernle, K. (in revision-a). "Tracing the metasomatic and magmatic evolution of continental mantle roots with Rb-Sr, SM-Nd, Lu-Hf and U-Pb and Th-Pb isotopes: a case study of Middle Atlas (Morocco) peridotite xenoliths." Geochimica et Cosmochimica Acta.

Wittig, N., Pearson, D. G., Baker, J., Duggen, S. and Hoernle, K. (in revision-b). "A major element, PGE and Os isotope study of Middle Atlas (Morocco) peridotite xenoliths: Evidence for coupled introduction of metasomatic sulphides and clinopyroxenes." Lithos.

Woodhead, J. D., Hergt, J., Phillips, D. and Paton, C. (2009). "African kimberlites revisited: In situ Sr isotope analysis of groundmass perovskite." Lithos.

Chapter 2:

CHARACTERISING MODAL METASOMATIC PROCESSES IN YOUNG CONTINENTAL LITHOSPHERIC MANTLE – A MICRO-SAMPLING ISOTOPIC AND TRACE ELEMENT STUDY ON XENOLITHS FROM THE MIDDLE ATLAS MOUNTAINS, MOROCCO

2.1. INTRODUCTION

Modal metasomatism, or the addition of new mineral phases by a melt or fluid, has long been the accepted origin for the more exotic phases, such as amphibole and apatite, found in mantle peridotite xenoliths from both on- and off-craton settings (Menzies and Hawkesworth 1987). The more modally abundant mantle minerals (olivine (ol), orthopyroxene (opx), clinopyroxene (cpx) and spinel or garnet) were thought to be generally of primary origin, remaining after the initial melt extraction that occurred during lithosphere formation. Recent studies have suggested that the majority of cpx found in mantle xenoliths from on-craton settings may have a metasomatic origin (van Achterbergh et al. 2001; Pearson and Nowell 2002; Gregoire et al. 2003; Pearson et al. 2003; Simon et al. 2003; Simon et al. 2008). The addition of cpx and other metasomatic phases has generally been linked to kimberlite or proto-kimberlite activity and is therefore considered to predominantly affect on-craton lithospheric mantle. However cpx is also found, often in abundance, in a wide range of mantle xenoliths from off-craton continental settings and the majority of this cpx is enriched in LREE, which is inconsistent with melt depletion. This study examines the origin of cpx in an example of off-craton mantle lithosphere and questions whether it too has a metasomatic origin.

Cpx is an important mineral phase in the lithospheric mantle as it is the major host for incompatible elements, such as Sr and REE, in the mantle and therefore controls the long-term distribution of lithophile isotopes such as Pb, Sr and Nd.

The timing of cpx addition has significant implications for how long the sub-continental lithospheric mantle (SCLM) has been a relatively fertile source in terms of its geochemical composition. Recent metasomatic addition of cpx would mean that the SCLM is not necessarily a potential long term source for incompatible element enriched magmas (Pearson and Nowell 2002). Furthermore, fertility estimates, which are based on modal cpx abundances, could not be broadly extrapolated through geological history. Melting experiments also use fertile spinel lherzolites to represent the lithospheric mantle. However if the cpx is a recent metasomatic addition then these xenoliths may not be a representative starting material for mantle lithosphere.

The approach used in this study is to assess the origin of cpx in the lithospheric mantle by investigating potential variations in Sr isotope ratios and trace element systematics among coexisting crystals. This method has been applied to peridotite xenolith suites before. Schmidberger et al. (2003) investigated *in-situ* Sr isotope variation from mantle xenoliths included in the Somerset Island kimberlite and Neumann et al. (2004) studied spinel lherzolites within basalts from the Canary Islands. These studies both found considerable isotopic variation among cpx crystals that warrant further investigation. However a major difference between the current study and those from Somerset Island and the Canary Islands is that we use micromilling and high precision TIMS (Thermal Ionisation Mass Spectrometry) rather than online LA-ICP-MS (Laser Ablation ICP Mass Spectrometry) to analyse Sr isotope composition. The advantage of the micro-sampling technique is that for one drilled spot it is possible to retrieve trace element and isotope data. In addition, sample

preparation and analysis via TIMS minimises isobaric interferences and provides a larger Sr ion signal, allowing smaller differences in Sr isotope composition to be resolved than via LA-ICP-MS (Davidson et al. 2001). This study therefore presents the first micro-drilling study of cpx from mantle xenoliths. The data generated are compared to a worldwide database of off-craton cpx to evaluate the implications for metasomatism processes on a broader scale.

2.2. SAMPLES

2.2.1. GEOLOGICAL BACKGROUND

A suite of peridotite xenoliths were collected from a single Maar in the Azrou Volcanic Field, Middle Atlas Mountains, Morocco. They were erupted approximately 2Myr ago in a basaltic host that forms part of the intraplate volcanism in the Middle Atlas Mountains (Duggen et al. 2003; Wittig et al. 2008). The Middle Atlas Mountains represent a failed, inverted rift system which, since 45Ma, has been affected by the Africa-Europe collision (Duggen et al. 2003). As a result of this collision it has been suggested that there has been delamination of the SCLM beneath the Atlas Moutains as indicated by the high heat flow, gravity and geoid anomalies (Teixell et al. 2005; Missenard et al. 2006; Urchulutegui et al. 2006). The western part of this mountain chain is thought to have significantly thinner lithosphere (60-80km) than typical NW

African lithosphere (130 to 160km; Teixell et al. 2005; Missenard et al. 2006; Urchulutegui et al. 2006; Duggen et al. 2009).

There are two phases of magmatism observed in the Middle Atlas. The first stage is subduction-related, as a result of the collision, but between 6.2 and 4.8Ma there was a shift to the more recent intraplate dominated volcanism (Teixell et al. 2005; Duggen et al. 2009). The xenoliths studied here are from this latter, intraplate group.

2.2.2. PETROGRAPHY

The peridotite xenoliths collected from the Middle Atlas, Morocco, are coarse-grained, equi-granular spinel lherzolites and harzburgites (see Fig. B1; Wittig 2006; Wittig et al. in revision-b; Wittig et al. in revision-a). Two spinel lherzolites, 3U and 3V, were chosen for this study as they contained relatively abundant (7% and 14% respectively; Wittig et al. in revision-b), large (2-5mm), fresh cpx which is ideal for micro-drilling. The major minerals in these samples are olivine (Mg# 89), opx, cpx and spinel; although the xenoliths also contain minor amounts of amphibole. The peridotites show a high degree of textural equilibration with no apparent fabric or alignment among the minerals. The mineral phases are subhedral, with rounded edges on some of the cpx crystals, and although there are cracks within some crystals, there is only limited evidence of secondary alteration along some of the larger cracks.

Both of the xenoliths selected for this study contain quenched melt in 1-5mm 'pockets' as well as narrow veins along some grain boundaries. The melt pockets appear to represent preferential incongruent melting of amphibole, as indicated by rounded and resorbed residual amphibole within the centre of a melt pocket. In some cases spinel is observed in the centre of the melt pockets. Some melting of cpx is also evident from resorbtion of grain edges but there is no textural evidence of opx and ol contributing to the melt. A small number of primary cpx crystals, especially those close to melt pockets, have discrete 'spongy' rims that are packed with melt inclusions. The high density of these melts inclusions together with the previously mentioned resorbtion of cpx, suggest that the rim textures represent the effects of partial melting. A second generation of cpx and spinel microlites has also crystallised from the melt pockets. This late cpx was too small to be sampled during this study and will not be discussed further. The petrographic evidence indicates that melting is occurring *in-situ* in response to decompression, as there is no evidence of any new minerals, such as feldspar crystallising, that would be expected if the host basalt had invaded at crustal pressures.

2.2.3. CPX AND MELT COMPOSITIONS

The major element data for all the phases in these peridotites can be found in Table B.1. The cpx from the peridotites is diopside with a Mg# (Mg# = (Mg/(Fe+Mg))*100) of 89 and a Cr# (Cr# = (Cr/(Cr+Al))*100) of 9 in 3U and 8 in 3V. These compositions are typical of relatively young continental

lithospheric mantle (Pearson et al. 2003). There is remarkably little variation in major element composition among the cpx crystals in either sample. Despite the textural difference between cores and rims of cpx, there is no consistent major element zoning or discrete compositional differences.

Amphibole is present as inclusions in both 3V and 3U and as a relict crystal in a melt pocket in 3U. The amphibole data is taken from Wittig et al. (2006). The inclusion in 3V has an average Mg number of 86.7 whereas in 3U it is 88.4. The relict amphibole in 3U, on the other hand, has a Mg number of 86.7. There is some zoning observed in the amphibole inclusion in 3U with the rims showing lower Cr and Al contents and higher Ti.

2.3. METHOD

The cpx, olivine and opx were all analysed for major and minor elements by wavelength dispersion using a Cameca SX100 Electronprobe microanalyser at the Department of Earth Sciences, University of Cambridge, UK. A beam voltage of 15kv and a current of 10nA for the major elements and 100nA for the minor elements with a beam size of 1um (further details can be found in Table A.10.). The amphibole was analysed for major and minor elements by wavelength dispersion using a JEOL 733 SuperProbe microprobe at the analytical facility of the School of Geography, Environment and Earth Sciences at Victoria University of Wellington, New Zealand with a spot beam of ~ 1μm at 15kv and 20nA.

The cpx crystals were sampled using two methods: *in-situ* micro-drilling and, for comparison, individual fragments of cpx bounded by fracture planes were picked from a crushed hand sample. In sample 3V nine cpx fragments ranging from 70µg to 28µg were hand-picked from a clean cpx fraction. These samples were leached in 18mΩ MilliQ water (MQ) in a sonic bath for 10mins repeatedly, changing the MQ each time, until the MQ was devoid of particles. The cpx chips were then leached in 6N UpA HCl at in a warm ultrasonic bath for 30mins before a final MQ rinse.

The *in-situ* micro-drilling was carried out on 100µm thick sections of the bulk xenolith following the procedure outlined in Charlier et al. (2006), using a New Wave MicroMill at NCIET, Durham University, UK. Over 20 cpx crystals were sampled from one thick section of 3V (Fig. 2.1) and 9 crystals from a thick section of 3U. Only the cores of the crystals were drilled, avoiding any potential contamination along cracks or grain boundaries. The drilled powder was collected in MQ, dried down and weighed to allow accurate determination of trace element concentrations. The drilled weights varied from 5µg to 218µg.

Both the drilled powders and picked fragments were processed using micro-Sr dissolution and purification chemistry (Charlier et al. 2006). A 10% aliquot, by mass, was taken for trace element analysis and the remaining 90% was put through micro-Sr columns using cleaned Sr-spec resin. Romil triple distilled "UpA" grade acids were used throughout.

Sr isotope ratios were measured using a ThermoElectron Triton TIMS at the NCIET, Durham University, UK. The samples were loaded onto Re filaments using a TaF_5 activator. The analysis consisted of 180 ratios with an integration time of 4 seconds per ratio. The reproducibility of 25 3ng loads of the NBS987 standard (yielding beam sizes that are typical of the smaller samples sizes analysed here), over the period of this study, was 0.710237 (±16 2sd; see Table A.1. and Table A.2. for further details of the standards run). Sample values were normalized to a standard value of 0.710240 (Thirlwall 1991). All samples were corrected for blank contribution (see Table A.7 for details of Sr blanks). The mass of Sr analysed varied from 6ng to 30ng in the drilled samples and up to 100ng in the picked chips. The average total procedural Sr blank was 11pg (±14 2sd, n=8) which is considerably less than 1% of the analysed Sr. The blank correction, therefore, was less than the internal run uncertainties.

The trace element aliquot was dissolved into 480µl of UpA 3%HNO_3 and analysed for 21 trace elements using a ThermoElectron Element II ICPMS at Durham University, UK. The parameters used were similar to those used in Font et al. (2007) and the standards run are summarized in Table A.8.). Accuracy and repeatability of the trace element concentrations using the aliquotting technique are 10% or better and are given in Harlou et al. (2009).

2.4. RESULTS

2.4.1. TRACE ELEMENTS

2.4.1.1. Clinopyroxene

In-situ analysis allows detailed studies of intergrain and intragrain variation to be examined for trace elements as well as Sr isotopes (see Table B.2. for data table). In both samples a considerable range in trace element concentrations is observed among individual crystals, including adjacent grains. Sr concentrations range from 134 to over 300ppm in 3V (Fig. 2.1) and from 218 to over 300ppm in 3U. However, despite this large intergrain variation, the within-grain variation was much less and trace element concentrations from the same crystal are within 10% of each other. There is also a range in Rb concentrations from less than 0.01 to 0.7. This is comparable to ranges found in bulk cpx separates from other off-craton suites (Downes 1987). The large range in cpx trace element concentrations does not correlate with any textural or spatial parameters such as crystal size, location or proximity to other phases (including melt). However it should be noted that it is not possible to fully constrain the three-dimensional setting of the grains using a single two dimensional thin section. Similar trace element variation among cpx crystals in individual peridotite xenoliths has been observed using LA-ICP-MS (e.g. Ionov et al. 2002a; Schmidberger et al. 2003).

REE patterns for the Middle Atlas cpx (Fig. 2.2) from the two xenoliths are very similar with $[Ce/Yb]_N$ ratios ranging from 5 to 10.4 for 3V (n=33) and from 6.1 to 11.4 for 3U (n=7). The larger range for 3V can be attributed to a larger sample set. There are differences in $[La/Ce]_N$ ratios between the two xenoliths which has been reported before (Wittig et al. 2008; Wittig et al. in revision-b). In 3V the average $[La/Ce]_N$ ratio is 0.7 compared to 1.2 in 3U (Fig. 2.2.b). The variation in trace element concentrations between the picked fragments and the drilled cpx crystals is similar; although due to the larger sample size the range in the picked sample is smaller.

Complete multi-element patterns are, like the REE patterns, relatively similar (Fig. 2.2.a). However there are distinct differences in the most incompatible end of the spectrum, especially for Th and U concentrations which are distinctly higher in the cpx from 3U (average Th concentration in 3V is 0.56 compared to 4.2 in 3U). Rb concentrations are also higher in 3U which results in higher Rb/Sr ratios for 3U compared to 3V.

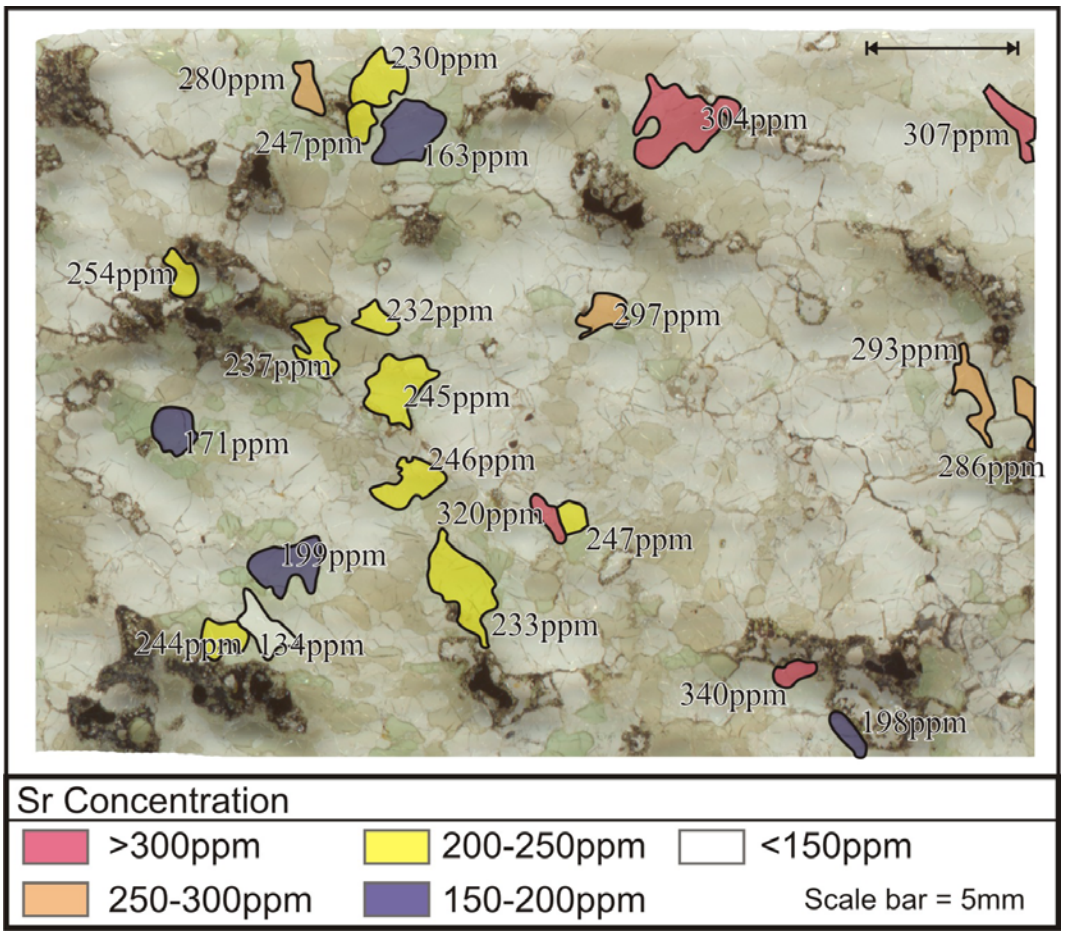

Figure 2.1.

A scanned image of the 100μm thick section of xenolith 3V used in the drilling campaign. The coloured crystals represent cpx crystals that were drilled and the shading represents the Sr concentration with the lowest values in purple and the highest in red. The absolute values are labelled adjacent to the cpx crystals. The extensive melt pockets are dark brown in colour. There are adjacent crystals which show a difference in Sr concentration of over 100ppm. The distance between the cores of these crystals is, in some case, less than 0.5cm.

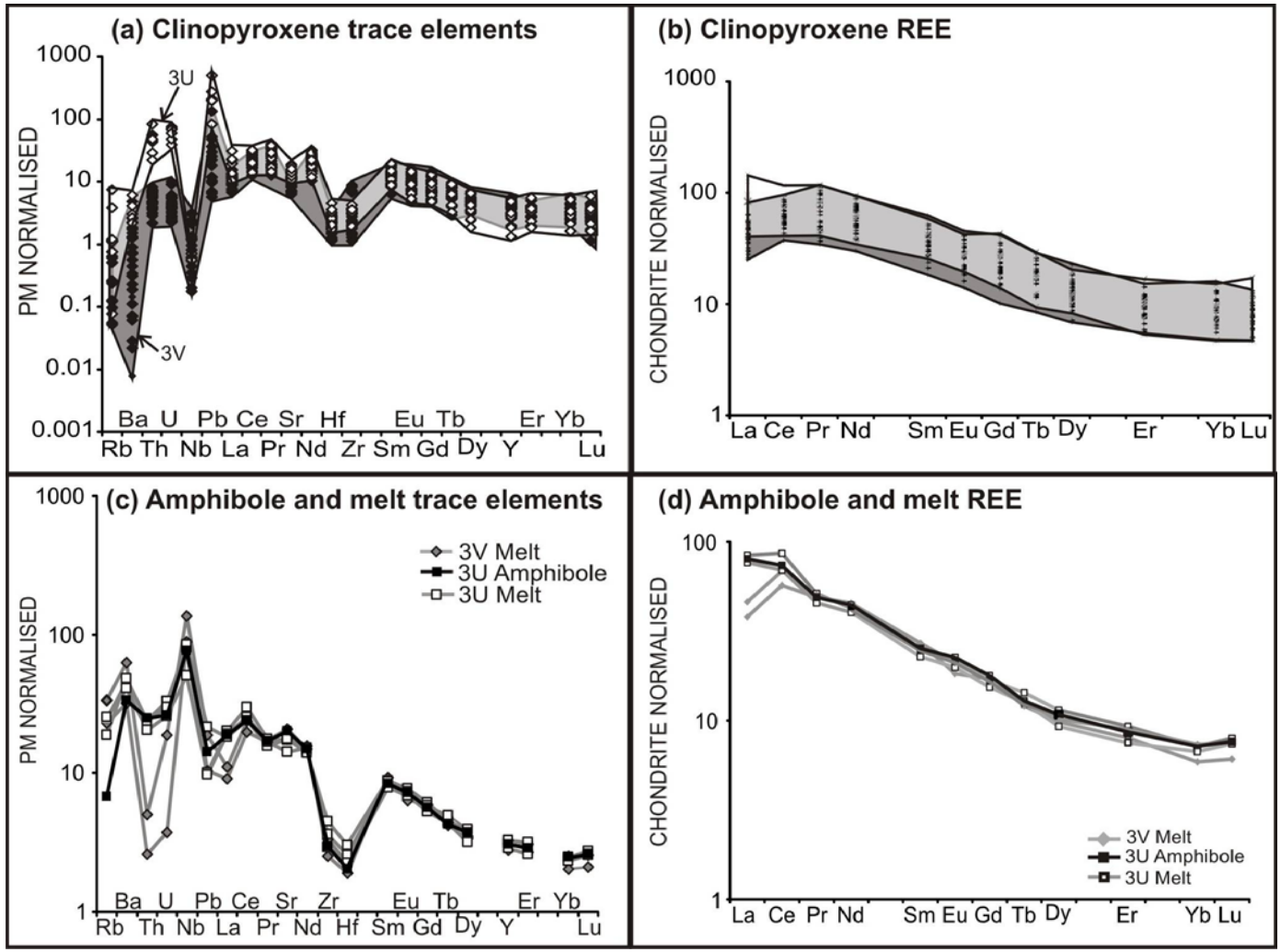

Figure 2.2.
(a) *Primitive mantle normalised (Sun and McDonough 1989) trace elements patterns for the drilled and picked cpx samples from xenoliths 3U (paler shading) and 3V (darker shading).*
(b) *Chondrite normalised (Sun and McDonough 1989) REE patterns for the cpx from 3U (paler shading) and 3V (darker shading).*
(c) *Primitive mantle normalised (Sun and McDonough 1989) trace element patterns for the one amphibole crystal from 3U (black) and melt drilled from both 3U (black, open squares) and 3V (grey diamonds).*
(d) *Chondrite normalised (Sun and McDonough 1989) REE patterns for one amphibole crystal from 3U (black) and melt drilled from the both 3U (black, open squares) and 3V (grey diamonds).*

2.4.1.2. Amphibole and melt

A rounded amphibole crystal from the centre of a melt pocket in xenolith 3U was drilled and analysed for trace elements and Sr isotopes along with the surrounding melt (see Table B.2. for data table). A number of other melt pockets from xenoliths, 3V and 3U, were also analysed. In 3U the trace element patterns of the melt and the amphibole essentially overlap (Fig. 2.2.c). The REE patterns in both the melt ($[La/Yb]_N$ = 10.8) and the amphibole ($[La/Yb]_N$ = 10.9) show a similar pattern to those observed in the cpx ($[La/Yb]_N$ mean = 9.5 for 3U, Fig. 2.2.d). The most prominent deviation from the cpx pattern is a positive Nb anomaly in the trace element patterns from both the melt and the amphibole. This is reflected in the $[U/Nb]_N$ ratio which, for 3U, is 0.31 and 0.32 in the amphibole and melt respectively compared to a mean of 91 for the cpx. The amphibole and melt also have higher Rb concentrations than the cpx, as expected from relative partition coefficients (Ionov et al. 2002a).

The melt analysed from 3V, where there was no amphibole remaining for comparison, shows a similar trace element pattern to the amphibole and melt from 3U (Fig. 2.2.c). There is evidence that there was amphibole present in 3V before melting took place as the melt has a positive Nb anomaly. The melt in 3V shows the same characteristically lower $[La/Ce]_N$ ratios and lower Th and U concentrations that are seen in the cpx in 3V compared to 3U.

2.4.2. Sr ISOTOPE VARIATION

2.4.2.1. Clinopyroxene

The cpx from the Atlas xenoliths show a range in $^{87}Rb/^{86}Sr$ from <0.001 to 0.018, which is typical of mantle diopside (e.g. Pearson et al. 2003). Downes et al. (1987), for example, observed a range in $^{87}Rb/^{86}Sr$ for bulk cpx separates from peridotite xenoliths of the Massif-Centrale region of <0.001 to 0.047. The range in $^{87}Rb/^{86}Sr$ observed in the cpx from the Atlas samples does not show any correlation with other trace element concentrations or ratios. This range in predominantly driven by variation in Sr concentrations but there is minor Rb variation.

The Atlas peridotite cpx analysed here show much more limited initial Sr isotope ($^{87}Sr/^{86}Sr_i$) variation (Fig. 2.3 and Table B.3.) than cpx from oceanic and cratonic lithospheric mantle xenoliths reported in LA-ICP-MS studies (Schmidberger et al. 2003; respectively; Neumann et al. 2004). The $^{87}Sr/^{86}Sr_i$ for the Atlas cpx, both picked and drilled, ranges from 0.703416 (±11 2SE) to 0.703681 (±12 2SE)). This range is considerably less than those observed from comparable microdrilling studies of cpx from on-craton peridotites (Fig. 2.4; Malarkey et al. 2008). Previous LA-ICP-MS studies, such as that by Schmidberger et al. (2003), observed a range in $^{87}Sr/^{86}Sr_i$ of 0.00079 from 0.70442 (±6 2SE) to 0.70521 (±10 2SE) in cpx from a single mantle xenolith (NK 2-3) from the on-craton Somerset Island kimberlite.

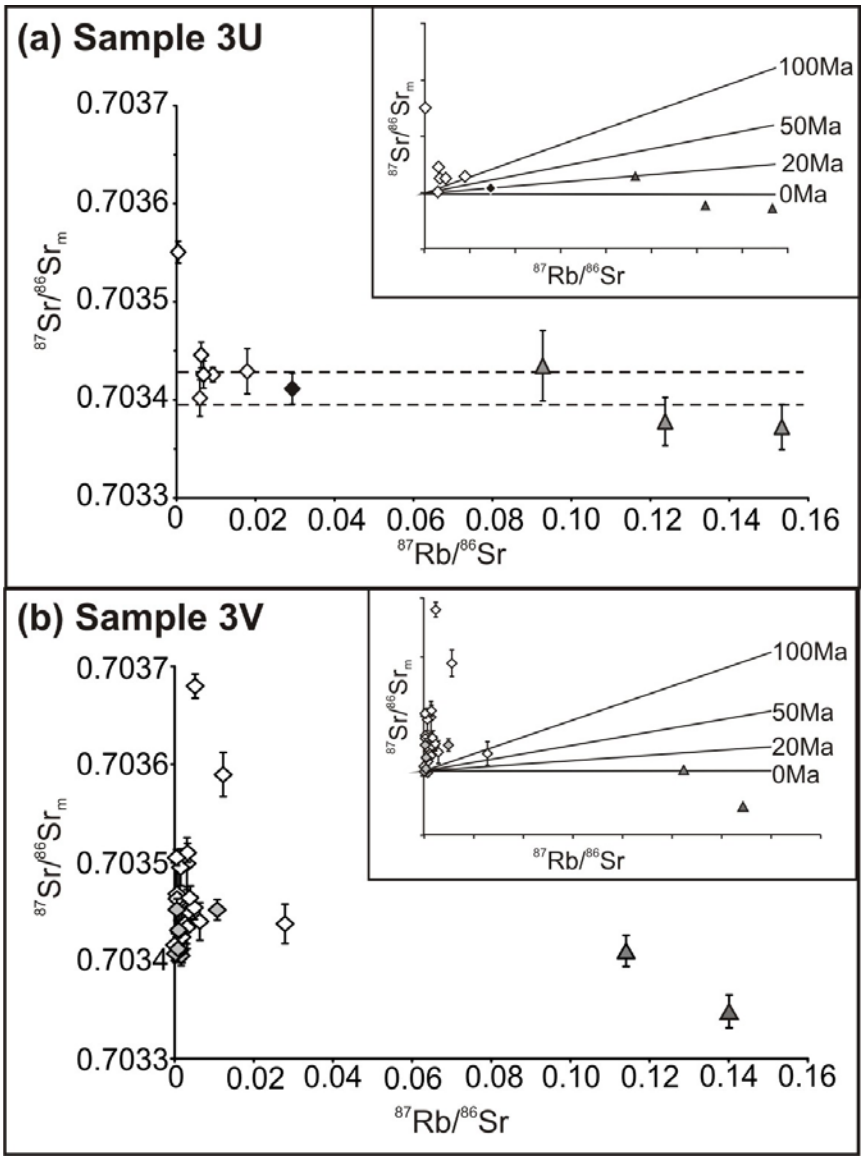

Figure 2.3.

(a) *An isochron plot of $^{87}Rb/^{86}Sr$ against $^{87}Sr/^{86}Sr_m$ for the drilled cpx (white diamonds), amphibole (black diamonds) and melt (grey triangles) from 3U. The error bars represent 2SE, where no error bars are seen the symbol is larger than the uncertainty. The inset illustrate reference isochrons plotted to illustrate the range in $^{87}Sr/^{86}Sr$ that can be generated through radiogenic in growth.*

(b) *An isochron plot of $^{87}Rb/^{86}Sr$ against $^{87}Sr/^{86}Sr_m$ for the drilled cpx (white diamonds), picked cpx (grey diamonds) and drilled melt (grey triangle). The error bars represent 2SE. The inset illustrate reference isochrons plotted to illustrate the range in $^{87}Sr/^{86}Sr$ that can be generated through radiogenic in growth.*

The drilled cpx show similar $^{87}Sr/^{86}Sr$ systematics to the picked chips although the picked crystals show a smaller range in isotopic composition, possibly due to fewer cpx crystals being sampled (9 picked chips compared to 19 drilled cpx crystals). In sample 3V two cpx grains were drilled twice to look for any heterogeneity within grains but the results are within uncertainty of each other. This is consistent with the lack of major and trace element zoning in the cpx. There are no correlations between the limited Sr isotope variability in the Atlas cpx and other trace element concentrations or ratios, including $[La/Ce]_N$ (which varies between the two xenoliths).

In order to assess how secondary alteration may affect the Sr isotope value of a cpx crystal this was sampled by drilling along the cracks lined with alteration and compared to a crack-free region of the same crystal. The drilled cracks were found to have a much more radiogenic $^{87}Sr/^{86}Sr_i$ value of 0.705644 (± 19 2SE) compared to 0.703416 (±11 2SE) for the fresh cpx. Therefore the range in $^{87}Sr/^{86}Sr_i$ observed in the Atlas cpx could, in principle, be explained by addition of about 4% 'crack alteration' to the least radiogenic cpx crystal. However this is unlikely to be the explanation for the following reasons. The leaching procedure applied to the handpicked cpx, efficiently removes such contamination and these samples yield Sr isotope systmeatics identical to the micro-drilled cpx. In addition great care was taken to avoid such cracks and alteration along the cracks is relatively uncommon.

The micro-sampled Atlas cpx can be compared to analyses of bulk cpx separates from peridotite xenoliths from similar off-craton intraplate settings. Such mineral separates give an average value for the whole xenolith but given the lack of previous in-situ studies on these types of samples these are the only data that can be used for comparison. A global database of $^{87}Sr/^{86}Sr_i$ values from off-craton cpx (see Fig. 2.4 for references), which is dominated by samples from Central Europe, and a database for on-craton cpx $^{87}Sr/^{86}Sr_i$ (see Fig. 2.4 for references) has been compiled in order to place the Atlas results in a more global context. Cpx from off-craton peridotites shows a much more restricted range than that observed from cratonic samples (Fig. 2.4). The mode $^{87}Sr/^{86}Sr_i$ value for off-craton cpx is 0.7035, similar to the Middle Atlas cpx.

2.4.2.2. Amphibole and melt

The only available amphibole crystal from 3U yielded an initial $^{87}Sr/^{86}Sr$ ratio of 0.703413 (±16 2SE; Table B.3.). This value plots towards the lower end of the range in Sr isotopes observed in the cpx from 3U but is within error of four out of the six cpx crystals analysed (Fig. 2.3.a). The amphibole $^{87}Sr/^{86}Sr_i$ value also overlaps with the value obtained for the melt surrounding the amphibole crystal (0.703431 ±36 2SE). The three samples of melt analysed from 3U are, as a group, slightly less radiogenic in terms of $^{87}Sr/^{86}Sr_i$ than the cpx but do overlap the least radiogenic cpx. This is the same in the two melt samples analysed from 3V. There was no corresponding amphibole remaining in 3V but a cpx within a melt pocket gave an $^{87}Sr/^{86}Sr_i$ of 0.703544 (±20 2SE) whereas the surrounding melt was significantly less radiogenic ($^{87}Sr/^{86}Sr_i$ = 0.703348 ±17

2SE). The melt from both Atlas xenoliths shows a range in $^{87}Sr/^{86}Sr_i$ from 0.703348 (±17 2SE) to 0.703431 (±36 2SE); significantly less radiogenic than the majority of the cpx from the two samples.

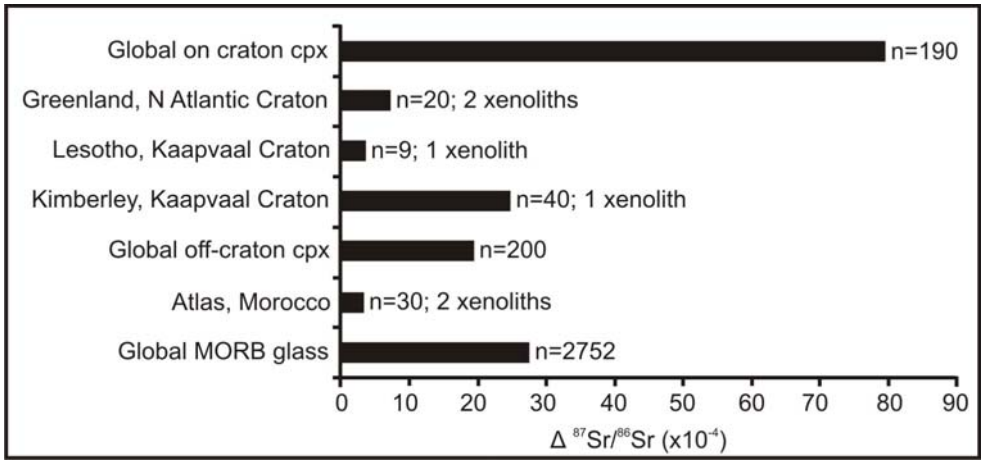

Figure 2.4.

The range in $^{87}Sr/^{86}Sr$ ($\Delta^{87}Sr/^{86}Sr$) observed in a range of cpx databases. The global on- and off-craton databases use bulk cpx mineral separate data whereas the cpx from Greenland, Lesotho, Kimberley and the Atlas Mts (this study) are from drilled cpx. The global MORB database is from GERM. On- and off-craton data sourced from Ionov et al. (2002a), Downes et al. (2003), Downes and Dupuy (1987), Stosch and Lugmair (1986), Witt-Eickschen et al. (2003), Menzies (1988), Porcelli et al. (1992), Roden et al. (1988), Deng and Macdougall (1992), Cohen et al. (1984), Xu et al. (2008), Choi et al. (2008), Tang and Chen (2008), Ionov et al. (2006), Pearson et al. (1995), Schmidberger et al. (2001; 2002; 2003), Carlson et al. (2004), Bedini et al. (2004), Macdougall and Haggerty (1999), Richardson et al. (1985), Erlank et al. (1987), Simon et al. (2003; 2008).

2.5. DISCUSSION

2.5.1. MELTING HISTORY

2.5.1.1. Melt depletion

In order to assess the origin of the cpx in the Middle Atlas peridotites it is important to first understand the melting history of the SCLM. In cratonic settings the lithospheric mantle is thought to have experienced 30 to 40% melt extraction (Boyd 1989; Pearson and Wittig 2008) which is well above the 23% melting required to exhaust cpx from the resitite (Walter 1998). However in off-craton settings the degree of melt extraction is much more difficult to constrain because extents of melting are smaller and the response of major elements more subtle (Ionov and Hofmann 2007). Wittig et al., (in revision-b; Wittig et al. in revision-a) have studied the melting history of the suite of peridotite xenoliths from the Middle Atlas, including the two samples studied here. The whole rock FeO and MgO contents, traditionally used to estimate the extent of melt removal; plot approximately along a 2GPa melting residue trend with melt extraction estimates ranging from 5 to 25%. However other parameters show a more complicated picture. The whole rock SiO_2 and Al_2O_3 compositions project away from the melting trend and towards amphibole and spinel-pyroxene indicating that there has been considerable modal metasomatic addition of these phases. This therefore brings into question the validity of

using whole rock major elements to quantify melt removal (see Wittig et al. in revision-b for an extended discussion of this issue).

Trace elements, especially the REE, can also be used to further constrain the melting history. REE in cpx show an increase in incompatibility from the HREE through to the LREE and are therefore sensitive tracers of melting and metasomatic processes. Although there are a number of factors that influence REE patterns a simplified view is that HREE in both the cpx and the whole rock predominantly reflect melting events whereas LREE are more strongly affected by metasomatism. If the lithospheric mantle beneath the Middle Atlas only experienced a melt depletion event, the residual cpx would therefore be relatively LREE depleted compared to the HREE. The effect of such partial melting on cpx in a peridotite host has been modelled (Hellebrand et al. 2002) to compare with the REE patterns from the Atlas samples. The trace element composition of a cpx from a fertile spinel lherzolite from the Vitim Basalt Field, Russia, (Ionov 2004) with a similar whole rock trace element composition to primitive mantle. Progressive fractional melting was modelled, starting at 3GPa (but within the spinel field) and the changing trace element composition of the cpx was calculated as the melt fraction increased (an example of a cpx remaining after 10% melt extraction is shown in Fig. 2.5). The results show that, as expected, the LREE become progressively depleted relative to the HREE resulting in REE patterns that are more reminiscent of cpx from Type 1A lherzolite xenoliths (Pearson et al. 2003). This is in contrast to the REE patterns from the Atlas cpx, which show relative LREE/HREE enrichment consistent with crystallisation from a metasomatic melt that postdates the melt

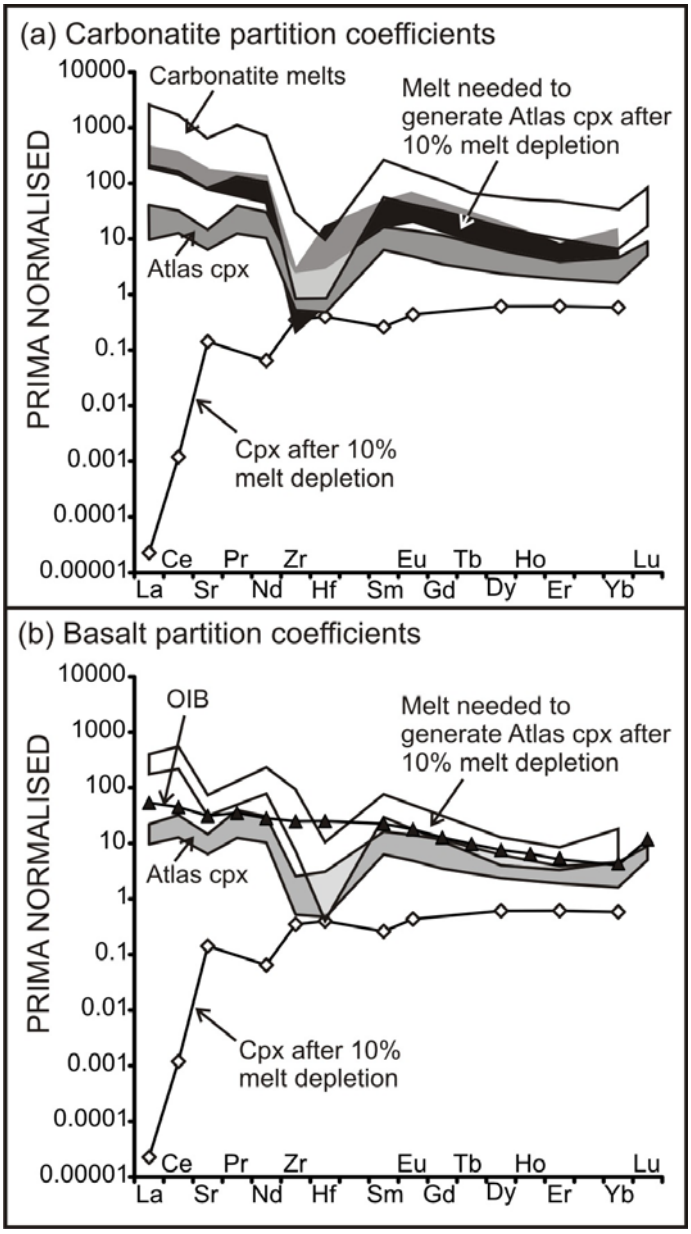

Figure 2.5.

PRIMA normalised (Sun and McDonough 1989) modelling of a cpx starting with 313-15 (Ionov et al. 2002a) and extracting 10% melt (see text for details; Hellebrand et al. 2002).

(a) *Metasomatic melt required to generate the Atlas cpx from the residual cpx is modelling using cpx-melt carbonatite partition coefficients (Blundy and Dalton 2000; Adam and Green 2001; Klemme et al. 2002). A range of carbonatite melts are also shown (Bizimis et al. 2003) for comparison.*

(b) *Metasomatic melt required to generate the Atlas cpx from the residual cpx is modelling using cpx-melt basalt partition coefficients (Hauri and Hart 1994; Blundy and Dalton 2000). Typical OIB is shown for comparison (Sun and McDonough 1989).*

depletion event that formed the lithosphere (Frey and Green 1974; Ionov et al. 2002a).

The HREE which are less affected by metasomatism may provide some information about the degree of melt extraction from the lithosphere. Canil et al. (2004), for example, used whole rock Yb to constrain melting history, arguing that it is robust to most metasomatic melts and it has been shown to be useful in cratonic peridotites. Wittig et al. (in revision-a) has shown that only one xenolith in the extended Atlas suite records shallow melting up to about 20% using Lu in cpx alone. This is supported by Raffone et al. (2009) used a correlation between decreasing Yb concentrations in cpx with increasing ol Mg number in a different suite of peridotite xenoliths from the Middle Atlas to assess the degree of melting. They concluded, using cpx Yb concentrations, combined with modal cpx contents that the lithosphere experienced about 20% melting. However there are other factors to consider; the decrease in modal cpx, for example, could be attributed to melt-peridotite reactions and Yb, although relatively robust to metasomatic effects, these effects cannot be ruled out (Raffone et al. 2009). The Atlas samples presented here show elevated Yb concentrations, compared to a depleted cpx, as seen from the trace element modelling (Fig. 2.5). In order to examine this further Yb concentrations have been plotted against Al_2O_3 in the cpx and compared to clear melting trends observed in abyssal peridotites (Fig 6; Hellebrand et al. 2002). The two Atlas samples show horizontal arrays plotting away from the melting trend, and although the low Yb cpx crystals from the Atlas peridotites overlap with the fertile end of the abyssal peridotite spectrum. Clearly, these data are not a

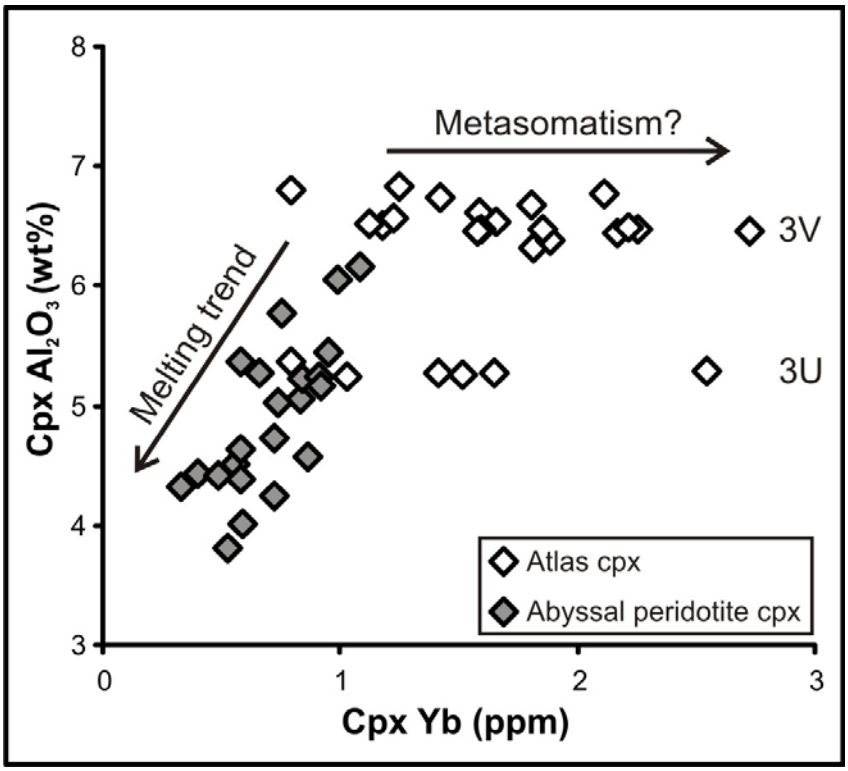

Figure 2.6.

Plot of cpx Al2O3 (wt%) against Yb concentration (ppm) showing abyssal peridotite data which shows a clear melting trend (Hellebrand et al. 2002) against data from the Atlas cpx. The cpx from the abyssal peridotites represents analyses from individual samples whereas the Atlas data are individual cpx analyses from two samples. The upper array of Atlas cpx are data from sample 3V and the lower array from sample 3U.

reliable tool to estimate melt depletion. In summary, it is difficult to constrain the degree of melt extraction for the Middle Atlas lithosphere as the effects of metasomatism have overprinted the geochemical proxies. Furthermore, it is unlikely that the currently observed 14% cpx would be remaining after the removal of up to 20% melt (Walter 1998).

2.5.1.2. Recent re-melting

The most recent event in the melting history of these peridotites is expressed petrographically as melt pockets containing quenched melt with secondary microlites of cpx and spinel. These melt pockets could be either the result of melt infiltration from the host basalt or they could represent in-situ decompressional melting related to emplacement. The latter is favoured here as the melt pockets do not contain any new minerals, such as plagioclase, that might be indicative of an infiltrating melt. This is further supported by the location of the melt pockets which are centred on the most fusible minerals, such as amphibole and cpx. The lack of plagioclase also implies that the melting is occurring at depth in the spinel facies. Only one amphibole crystal was observed (in 3U), found within a melt pocket. This crystal shows a resorbtion texture, with rounded edges and a high concentration of melt inclusions around the rim. These textures were also observed in the cpx crystals rimming the melt pockets. The petrography therefore suggests that the melt pockets represent *in-situ* melting of the peridotite during emplacement, as seen in some other off-craton peridotite xenoliths (Ionov et al. 1994).

The trace element patterns confirm that the melt pockets stem from *in-situ* melting. The melt analysed from both xenoliths shows a similar trace element pattern to the amphibole, with a characteristic positive Nb anomaly. Although the trace element signatures in the melt patches are also similar to the cpx, this positive Nb anomaly suggests that the majority of the melt has a significant amphibole component.

The Sr isotope data also supports *in-situ* melting where the melt is dominated by rapid batch melting of the amphibole. In 3U an amphibole crystal and the surrounding glass were both drilled and the resulting $^{87}Sr/^{86}Sr_i$ values are within uncertainty of each other. In 3V a cpx and the adjacent melt were drilled the Sr isotope ratios were significantly different at 0.703550 and 0.703358 respectively. This, with the trace element evidence puts forward a strong case for the melt pockets representing rapid, *in-situ* melting of amphibole where the amphibole and the melt have not equilibrated.

2.5.2. NATURE OF THE METASOMATISM

2.5.2.1. Controls on trace elements during metasomatism

A wide range of melt compositions have been implicated in the metasomatism of peridotite xenoliths in non-cratonic settings from carbonatite to alkali basalts (Frey and Green 1974; Downes 2001; Ionov et al. 2002a; Pearson et al. 2003).

These varying melt compositions have different trace element characteristics that can be used to characterise the melt that the cpx last equilibrated with. Blundy et al. (2000) determined partition coefficients between cpx and silicate or carbonatitic melts which makes it possible to use trace elements to distinguish between these two melts. The main differences between them are the partition coefficients for Hf and Zr. $D_{melt\text{-}cpx}$ for Zr, for example, varies from 0.15 to 1.4 for a carbonatitic melt but is an order of magnitude lower for silicate melts ranging from 0.028 to 0.06 (Blundy and Dalton 2000). Therefore cpx that crystallised from a metasomatic carbonatitic melt were found to have trace element patterns with negative Zr and Hf anomalies in their trace element patterns when compared to cpx crystallised form a silicate melt. Such elemental characteristics have been used to infer the action of carbonatitic melts in a number of peridotite xenoliths suites (Hauri et al. 1993; Ionov et al. 1993).

The processes involved in metasomatism have been well studied, especially in on-craton settings where there is more evidence for modal metasomatism with the presence of MARID-type suites and other micaceous lithologies (Menzies and Hawkesworth 1987; Gregoire et al. 2003; Burgess and Harte 2004). The most likely mechanism by which metasomatism occurs is percolative fractional crystallisation also known as reactive porous flow (e.g. Harte et al. 1993). In these models low degree metasomatic melts percolate through the mantle lithosphere crystallising mineral phases such as garnet and cpx either as rims on pre-existing minerals or as new crystals. The chromatographic effect creates an advancing metasomatic 'front' where the first minerals that interact with the melt are more enriched in incompatible elements such as LREE (Fig. 2.7). The

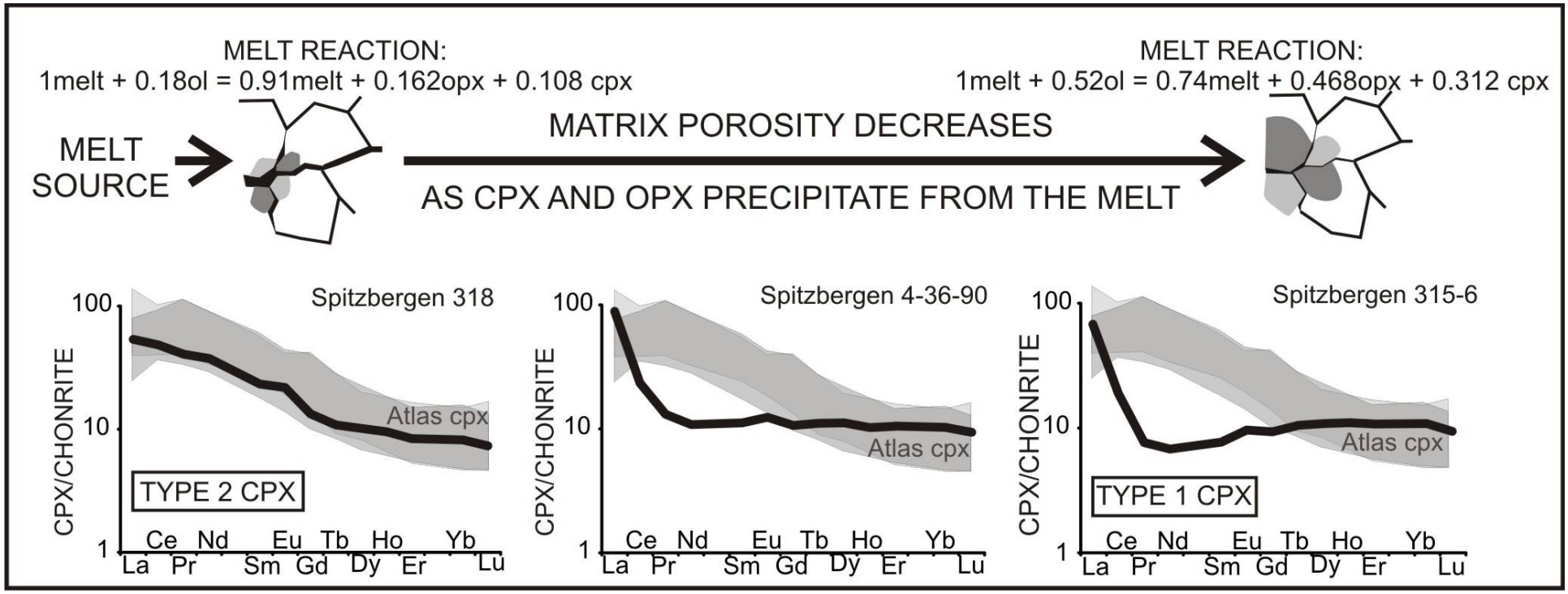

Figure 2.7.

A schematic diagram to illustrate Ionov's (2002) model for percolative fractional crystallisation where trace element concentration in cpx varies with distance from the melt source. The melt source is at the left of the diagram and as the melt moves away from the melt vein cpx and opx precipitate form the melt and the remaining melt evolves. This leads to the change in REE pattern observed on the left with the cpx crystallising closest to the melt at the bottom of the diagram. The black patterns are representative analyses from the Spitzbergen cpx samples that match the model predictions for each stage. The grey shaded area represents the cpx REE patterns analysed from the Atlas xenoliths.

minerals further from the melt source, or vein, therefore 'see' a melt that is more depleted in the most incompatible elements. If the metasomatism is more advanced then the effects of the metasomatic 'front' are obscured as the minerals approach equilibrium with the metasomatic melt (Ionov and Harmer 2002). This therefore means that a single evolving melt can be used to explain a range of trace element patterns rather than having to invoke a range of melts. This process is observed in exposed orogenic peridotites where metasomatism can be tracked from melt veins through a metasomatised lherzolite to a depleted harzburgite further away from the vein (McPherson et al. 1996; Bodinier et al. 2004).

The process of reactive porous flow has been modelled by Ionov et al. (2002a) to explain the elemental and isotope variations observed within a suite of off-craton spinel peridotites from Spitzbergen (Fig. 2.7). The cpx crystals in the xenoliths from Spitzbergen show a range of trace element patterns with a group of cpx (Type 2 cpx; Ionov and Harmer 2002) showing strong LREE enrichment relative to the HREE (e.g. $[La/Yb]_N$ of 6.5) and a negative Nb anomaly. The second group of Spitzbergen cpx crystals (Type 1 cpx; Ionov and Harmer 2002) show trace elements with flat HREE-MREE (e.g. $[Nd/Yb]_N$ of 0.6) with a steep La-Ce inflection (e.g. $[La/Ce]_N$ of 3.5). The amphibole present in the Spitzbergen samples has similar REE patterns to the corresponding cpx.

The numerical modelling is based on a 'plate model' (Vernieres et al. 1997) which numerically simulates porous melt flow. The matrix porosity is decreased from 1%, near the melt source, to approximately zero away from the source as the melt reacts with ol to crystallise cpx and opx thus decreasing the porosity. Basaltic and carbonatitic melts were modelled by Ionov et al. (2002a) used as the metasomatic agents but these differences did not show any differences in the REE and therefore only the silicate melt results are illustrated on Fig. 2.7. These models were run both with amphibole present and absent in the peridotite. This also had little effect on the REE but there were significant differences between the two scenarios in terms on Ta and Nb as amphibole has a high partition coefficient for these elements. The REE results of the model are summarised in Fig. 2.7, compared with representative cpx REE patterns from the Spitsbergen sample suite that match the model predictions (the Atlas samples are plotted in grey for comparison). The modelled cpx compositions show that a wide range of REE patterns from Type 2 to Type 1 can be generated as the distance from the melt source increases.

2.5.2.2. Metasomatism in the Middle Atlas

The trace element patterns recorded in the cpx from the Middle Atlas are LREE enriched, relative to the HREE, indicating a metasomatic origin. Trace element patterns and ratios can be used to characterise the metasomatic melt although care must be taken as reactive flow models have shown that trace element ratios can be fractionated by this process (Ionov et al. 2002a). The modelling of Ionov

et al. (2002a), however, does not fractionate Hf or Zr while generating the spectrum of REE patterns seen in the Atlas cpx. The negative anomaly for these elements observed in the multi-element plots is therefore indicative of cpx that has crystallised from, or re-equilibrated with, a carbonate melt (Blundy and Dalton 2000). The metasomatic melt that would be required to generate the trace element patterns observed in the Atlas cpx from a cpx that had been depleted by a cautious 10% melt extraction has been modelled (Fig 5; Hellebrand et al. 2002 used for melt depletion modelling). The predicted metasomatic melt needed to produce the trace element systematics observed in the Atlas cpx was generated using carbonatite-cpx partition coefficients (Fig. 2.5.a; Blundy and Dalton 2000; Adam and Green 2001; Klemme et al. 2002) and basalt-cpx partition coefficients (Fig. 2.5.b; Hauri and Hart 1994; Blundy and Dalton 2000). The results of this modelling show that the melt that generated the Atlas cpx had a negative Zr-Hf anomaly which is only observed in the carbonatite melts. Although the range of basaltic melts that would be required depends on partition coefficients the patterns are jagged and do not reflect basaltic melts. The addition of a carbonatite melt is therefore the most likely candidate for the most recent metasomatic event as the predicted melts approximately match a range of carbonatites (Bizimis et al. 2003). This is also supported by Wittig et al. (in revision-a). However this is not an exact match which could be attributed to a number of factors. For example, preexisting cpx may have experienced and recorded metasomatism with various reagents and equilibration of this cpx with a carbonatite may result in slightly atypical trace element systematics now observed. Similarly, it is likely that there is some discrepancy between erupted carbonatites and the carbonatite melt at depth

(Foley et al. 2009). In the case of the Atlas samples, which have been shown to have undergone a complex history, this carbonatite overprinting is recording the most recent metasomatic activity.

Wittig et al. (in revision-b) proposed significant metasomatic sulphide addition from whole rock PGE (platinum group element) systematics from the Middle Atlas peridotites. Although precipitation of sulphide during reactive flow is not well understood, silicate melts are thought to be more S-saturated than carbonatite-rich melts. Hence at least two metasomatic events may have affected these xenoliths. The first is probably a silicate event, required by the PGE and whole rock data, which added cpx, amphibole and sulphides to the depleted residue. This was followed, prior to eruption, by re-equilibration with a carbonatitic liquid that largely overprinted the highly incompatible elements and resulted in the current trace element characteristics. This would explain the range of trace element concentrations observed in the Atlas cpx, reflecting differing degrees of re-equilibration with the more recent carbonatitic melt superimposed on top of an earlier enrichment from a silicate melt. This re-equilibration is also responsible for the negative Zr-Hf anomalies observed in the cpx and amphibole from the Middle Atlas peridotites.

The trace elements in the Middle Atlas cpx are similar to those observed in the Spitzbergen Type 2 cpx that were modelled to be close to a melt vein (Fig. 2.7; Ionov et al. 2002a). This would suggest that either the cpx precipitated in the Middle Atlas xenoliths was close to a melt channel/source or that the

metasomatism was significantly advanced such that a wide zone had re-equilibrated with the melt that the majority of the range of trace element patterns were not be preserved. However there are differences in the $[La/Ce]_N$ rations between 3V (0.42 to 0.80) and 3U (0.98 to 1.4) which may record some evidence of reactive flow processes. In the Spitzbergen xenoliths there is considerable a range in $[La/Ce]_N$ from 0.92 to 3.59 as the melt becomes progressively fractionated away from the vein (Ionov et al. 2002a). These differences are largest for the $[La/Ce]_N$ ratio than any other ratio of adjacent REE and therefore these variations are the last to be equilibrated by continued metasomatism. This would therefore imply that 3U was maybe slightly further from the melt source and experienced a marginally more fractionated melt that 3V. This is consistent with the scenario proposed by Raffone et al. (2009) that these xenoliths had sampled the rejuvenated lithosphere close to the dunitic channels that represent relict metasomatic melt channels.

Sr isotopes are not fractionated by processes such as reactive flow unless the metasomatic agent has a significantly different Sr isotope ratio to the depleted host then mixed isotopic signatures may be observed in a zone at the metasomatic front (Ionov et al. 2002b). However in the Atlas samples the Sr isotopes show very limited variation and there is no observed correlation between $^{87}Sr/^{86}Sr$ and trace elements, such as Sr, which would indicate a mixing relationship. This implies that one of the metasomatic agents, most likely the carbonatite, has dominated the Sr isotope composition of the cpx.

2.5.3. TIMING OF METASOMATISM

2.5.3.1. Time constraints from Sr isotopes

The timing of this initial melt depletion event has been difficult to constrain using Re-Os isotopes due to the extensive metasomatic overprinting (Wittig et al. 2008). The lithophile budget in peridotites is dominated by any metasomatic effects and therefore it may be possible to date metasomatic events using Rb-Sr or Sm-Nd isotope systems (e.g. Erlank et al. 1987). In the Middle Atlas there are at least two events and therefore there must be a complete resetting of the system by each newer event in order that the most recent overprinting can be dated. There is a sufficient range in Rb/Sr in the Moroccan cpx to generate isotopic variation well outside the analytical error (Fig. 2.3). However the Rb-Sr data from the Middle Atlas cpx does not show an isochronous relationship (Fig. 2.3) and therefore it is not possible to accurately date the cpx addition using the Rb-Sr isochron technique. It is possible to plot reference isochrons through the cpx data but this does not yield any information (Fig. 2.3). The range in cpx Sr isotope ratios is therefore not generated by radiogenic ingrowth but probably the result of complex metasomatic interactions.

The trace and major elements imply that the amphibole and cpx were added at the same time by a silicic metasomatic melt. Therefore, had there been no further metasomatic overprinting then these two minerals should plot on an isochron that would yield the age of this event. Again this is not the case

probably because the Atlas samples have been overprinted by a more recent carbonatitic melt so any relationship between the amphibole and cpx has been obscured.

2.5.3.2. Time constraints from trace element distributions

It is possible to use other approaches to evaluate the timing of metasomatism. The Atlas samples show a considerable range in trace element concentrations between cpx crystals within the two xenoliths. In 3V, for example, there are two touching cpx crystals that differ in Sr content by about 80% (100ppm difference). These variations show that diffusive equilibrium has not been attained. The time over which diffusion would even out such differences between adjacent cpx crystals can be approximated using Fick's Law ($x = \sqrt{Dt}$ where x is the diffusion distance, t is the time and D is the diffusion coefficient) if the diffusion coefficients are known. Diffusion models have shown that Sr should equilibrate at the grain size scale in mantle peridotites over periods of 1 to 100Ma at lithospheric temperatures and pressures (Sneeringer et al. 1984). This timescale is strongly dependant on temperature and is further reduced by the presence of melt along grain boundaries. If a distance (x) of 0.5cm is taken between the cores of the adjacent crystals then with a diffusion coefficient (D) of $1.23 \times 10^{-16} cm^2 s^{-1}$ (calculated at 1000ºC; Sneeringer et al., 1984) then the time for complete equilibration for Sr would be 65Myr. However is this distance is reduced to 0.2cm, as is observed in the thin section then this time is reduced to 2.5Myr. It is unlikely therefore that the variation of 100ppm in Sr

concentrations, which represents significant disequilibrium, would persist for more than 2 or 3Myr before entrainment into the basalt. This timescale is supported by Wittig et al. (in revision-a) who argue, using Pb isotopes that the most recent metasomatism could not have occurred more than 20Ma. This constraint argues for a relatively recent enrichment event and may represent re-equilibration of the cpx with a carbonatitic melt as suggested by Wittig et al. (in revision-b). This, plus isotopic variation in metasomatic melts, may explain the lack of a clear isochronous relationship.

2.5.4. GLOBAL IMPLICATIONS

The Sr isotopic composition of the cpx from the Middle Atlas xenoliths is typical of cpx from similar off-craton settings. A probability density function (PDF) has been plotted for a global compilation of off-craton cpx data (n=205) from published mineral separates data with the Atlas cpx marked for comparison (Fig. 2.8). The $^{87}Sr/^{86}Sr$ mode for off-craton cpx is approximately 0.7035 which is similar to the average for the Atlas samples, 0.70346 and also within the range observed for OIBs (Sun and McDonough 1989). However this plot shows that the range in $^{87}Sr/^{86}Sr$ in most off-craton settings is limited and that therefore the metasomatic origin concludes for the cpx from the Middle Atlas may be common to many other off-craton peridotites. The narrow range and sharp peak observed in the Sr distribution would be incompatible with a range of ancient metasomatic melts and therefore indicates that the majority of off-craton cpx has been recently overprinted by the convecting mantle. This is

further confirmed by a PDF plot of off-craton cpx $^{143}Nd/^{144}Nd$ data, again form bulk cpx separate data. The PDF plot has a mode at 0.5126 which is close to present day bulk earth values (0.51264; Rollinson 1993). If these cpx crystals were residual, with Sm/Nd ratios higher than bulk earth, then the cpx would have considerably more radiogenic $^{143}Nd/^{144}Nd$ ratios than bulk earth. Alternatively if the cpx had formed from an ancient enriched metasomatic melt, with Sm/Nd ratios lower than bulk earth then the cpx would have considerably less radiogenic $^{143}Nd/^{144}Nd$. Therefore the coincidence of cpx Nd isotope ratios with present day bulk earth is inconsistent with long term enrichment or depletion in the lithosphere. However it should be stressed again that this may reflect a recent overprint and it is not possible to use Nd or Sr to 'see though' the most recent metasomatic event.

The global database therefore suggests that cpx may be a recent addition to much of the non-cratonic lithosphere. Cpx, in off-craton lithosphere, is an important host for incompatible elements and therefore the modal abundance and timing of cpx addition exercise a strong control on the relative fertility of the lithosphere. The recent addition of cpx to the lithosphere implies that the enriched nature of lithospheric mantle may only be a recent phenomenon as suggested by Pearson and Nowell (2002). However mantle xenoliths have long been known to provide a biased view of the mantle and therefore this apparent enrichment may not truly represent the bulk mantle (Menzies and Hawkesworth 1987). In peridotite massifs, where it is possible to sample away from metasomatic veins, LREE depleted REE patterns are more common and these may be more representative of the bulk depleted mantle. In this study the trace

element systematics suggest that the Moroccan xenoliths were located relatively close to melt veins during metasomatic activity and it likely therefore that it is the vein system being sampled (Menzies and Hawkesworth 1987; Bodinier et al. 1988). If this situation is common then it is likely that the incompatible element abundances in most lithospheric peridotites will consistently overestimate the incompatible abundances in the continental lithospheric mantle (Pearson and Nowell 2002).

The direct sampling of melt that has formed from low degree melting of the amphibole in the Atlas lithosphere, now present as melt pockets in the peridotite, did not generate melts with a wide range of Sr isotopic ratios despite predominantly melting an exotic phase such as amphibole. This would therefore imply that in off-craton settings, where the isotopic variation in the lithosphere is more restricted than in on-craton settings, it is not possible to generate lithospheric melts with very heterogeneous Sr isotopic variation. It then follows that the isotopic diversity observed in off-craton continental basalts – including many flood basalts – cannot reflect a lithospheric mantle source and must either be due to heterogeneity in the convecting mantle or/and crustal contamination.

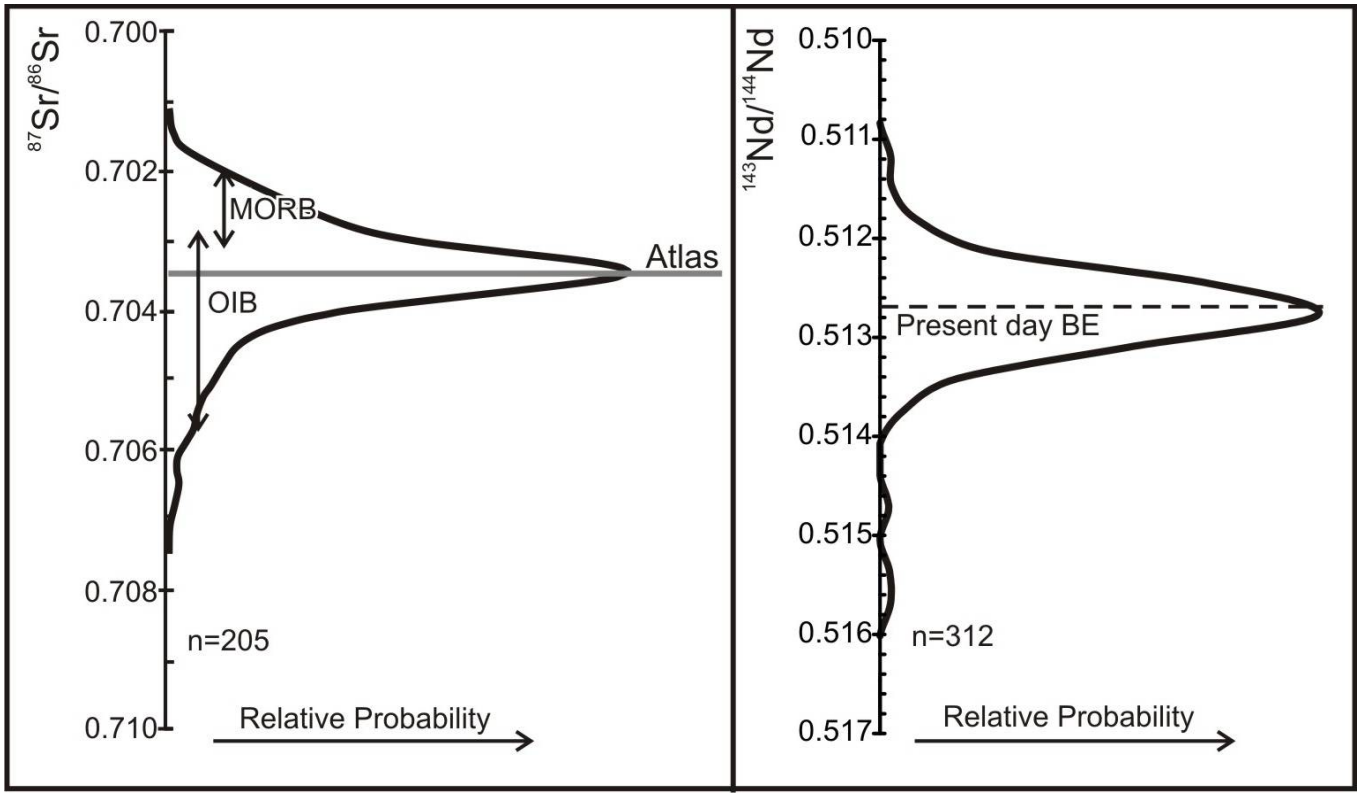

Figure 2.8.

PDF (Probability Density Function) plots of global off-craton cpx $^{87}Sr/^{86}Sr$ and $^{143}Nd/^{144}Nd$ data from mineral separates. The range of $^{87}Sr/^{86}Sr$ for MORB and OIB are shown as are the Atlas data (grey line). The present day bulk earth $^{143}Nd/^{144}Nd$ is also shown. Data taken from Ionov et al. (2002a), Downes et al. (2003), Downes and Dupuy (1987), Stosch and Lugmair (1986), Witt-Eickschen et al. (2003), Menzies (1988), Porcelli et al. (1992), Roden et al. (1988), Deng and Macdougall (1992), Cohen et al. (1984).

2.6. CONCLUSIONS AND IMPLICATIONS

1. The modal amount of cpx coupled with the trace element and major element concentrations in the cpx from these samples are consistent with a metasomatic, as opposed to a residual, origin.
2. The major element composition and mineral chemistry of constituent cpx suggest that cpx, amphibole and sulphides crystallised from a silicate metasomatic melt but the cpx and amphibole has been overprinted with a recent carbonatitic metasomatic event.
3. The $^{87}Sr/^{86}Sr$ values of cpx and amphibole in the Middle Atlas peridotites are inconsistent with long term enrichment or depletion and may be explained by recent crystallisation/re-equilibration with a melt originating in the convecting mantle.
4. PDF plots of a global off-craton database shows that the majority of off-craton cpx have a Sr isotope ratio of ~0.7035 consistent with the above process.
5. Spinel lherzolite xenoliths from off-craton settings, often used in melting experiments, are therefore unlikely to truly represent *primary* fertile mantle if the majority of the cpx is metasomatic.
6. The incompatible trace element budget of the bulk peridotite, in these spinel facies xenoliths, is dominated by the cpx. Therefore the recent addition of cpx to the SCLM implies that although the SCLM is relatively enriched now this may not always have been the case.

2.7. REFERENCES

Adam, J. and Green, T. (2001). "Experimentally determined partition coefficients for minor and trace elements in peridotite minerals and carbonatitic melt, and their relevance to natural carbonatites." European Journal of Mineralogy 13(5): 815-827.

Bedini, R. M., Blichert-Toft, J., Boyet, M. and Albarede, F. (2004). "Isotopic constraints on the cooling of the continental lithosphere." Earth and Planetary Science Letters 223(1-2): 99-111.

Bizimis, M., Salters, V. J. M. and Dawson, J. B. (2003). "The brevity of carbonatite sources in the mantle: evidence from Hf isotopes." Contributions to Mineralogy and Petrology 145(3): 281-300.

Blundy, J. and Dalton, J. (2000). "Experimental comparison of trace element partitioning between clinopyroxene and melt in carbonate and silicate systems, and implications for mantle metasomatism." Contributions to Mineralogy and Petrology 139(3): 356-371.

Bodinier, J. L., Dupuy, C. and Vernieres, J. (1988). "Behavior of Trace-Elements during Upper Mantle Metasomatism - Evidences from the Lherz Massif." Chemical Geology 70(1-2): 152-152.

Bodinier, J. L., Menzies, M. A., Shimizu, N., Frey, F. A. and McPherson, E. (2004). "Silicate, hydrous and carbonate metasomatism at Lherz, France: Contemporaneous derivatives of silicate melt-harzburgite reaction." Journal of Petrology 45(2): 299-320.

Boyd, F. R. (1989). "Compositional Distinction between Oceanic and Cratonic Lithosphere." Earth and Planetary Science Letters 96(1-2): 15-26.

Burgess, S. R. and Harte, B. (2004). "Tracing lithosphere evolution through the analysis of heterogeneous G9-G10 garnets in peridotite xenoliths, II: REE chemistry." Journal of Petrology 45(3): 609-634.

Canil, D. (2004). "Mildly incompatible elements in peridotites and the origins of mantle lithosphere." Lithos 77(1-4): 375-393.

Carlson, R. W., Irving, A. J., Schulze, D. J. and Hearn, B. C. (2004). "Timing of Precambrian melt depletion and Phanerozoic refertilization events in the

lithospheric mantle of the Wyoming Craton and adjacent Central Plains Orogen." Lithos 77(1-4): 453-472.

Charlier, B. L. A., Ginibre, C., Morgan, D., Nowell, G. M., Pearson, D. G., Davidson, J. P. and Ottley, C. J. (2006). "Methods for the microsampling and high-precision analysis of strontium and rubidium isotopes at single crystal scale for petrological and geochronological applications." Chemical Geology 232(3-4): 114-133.

Choi, S. H., Mukasa, S. B., Zhou, X. H., Xian, X. H. and Androniko, A. V. (2008). "Mantle dynamics beneath East Asia constrained by Sr, Nd, Pb and Hf isotopic systematics of ultramafic xenoliths and their host basalts from Hannuoba, North China." Chemical Geology 248(1-2): 40-61.

Cohen, R. S., Onions, R. K. and Dawson, J. B. (1984). "Isotope Geochemistry of Xenoliths from East-Africa - Implications for Development of Mantle Reservoirs and Their Interaction." Earth and Planetary Science Letters 68(2): 209-220.

Davidson, J., Tepley, F., Palacz, Z. and Meffan-Main, S. (2001). "Magma recharge, contamination and residence times revealed by in situ laser ablation isotopic analysis of feldspar in volcanic rocks." Earth and Planetary Science Letters 184(2): 427-442.

Deng, F. L. and Macdougall, J. D. (1992). "Proterozoic Depletion of the Lithosphere Recorded in Mantle Xenoliths from Inner-Mongolia." Nature 360(6402): 333-336.

Downes, H. (1987). "Tertiary and Quaternary volcanism in the Massif Centrale, France." Geological Society, Special Publications 30: 517-530.

Downes, H. and Dupuy, C. (1987). "Textural, Isotopic and Ree Variations in Spinel Peridotite Xenoliths, Massif-Central, France." Earth and Planetary Science Letters 82(1-2): 121-135.

Downes, H. (2001). "Formation and modification of the shallow sub-continental lithospheric mantle: a review of geochemical evidence from ultramafic xenolith suites and tectonically emplaced ultramafic massifs of western and central Europe." Journal of Petrology 42(1): 233-250.

Downes, H., Reichow, M. K., Mason, P. R. D., Beard, A. D. and Thirlwall, M. F. (2003). "Mantle domains in the lithosphere beneath the French Massif

Central: trace element and isotopic evidence from mantle clinopyroxenes." Chemical Geology 200(1-2): 71-87.

Duggen, S., Hoernle, K., van den Bogaard, P., Rupke, L. and Morgan, J. P. (2003). "Deep roots of the Messinian salinity crisis." Nature 422(6932): 602-606.

Duggen, S., Hoernle, K. A., Hauff, F., Klugel, A., Bouabdellah, M. and Thirlwall, M. F. (2009). "Flow of Canary mantle plume material through a subcontinental lithospheric corridor beneath Africa to the Mediterranean." Geology 37(3): 283-286.

Erlank, A. J., Waters, F. G., Hawkesworth, C. J., Haggerty, S. E., Allsopp, H. L. and Menzies, M. A. (1987). Evidence for mantle metasomatism in peridotite nodules from the Kimberley Pipes, South Africa. Mantle Metasomatism. Menzies, M. A. and Hawkesworth, C., Academic Press**:** 221-312.

Foley, S. F., Yaxley, G. M., Rosenthal, A., Buhre, S., Kiseeva, E. S., Rapp, R. P. and Jacob, D. E. (2009). "The composition of near-solidus melts of peridotite in the presence of CO2 and H2O between 40 and 60 kbar." Lithos 112(Supplement 1): 274-283.

Font, L., Nowell, G. M., Pearson, D. G., Ottley, C. J. and Willis, S. G. (2007). "Sr isotope analysis of bird feathers by TIMS: a tool to trace bird migration paths and breeding sites." Journal of Analytical Atomic Spectrometry 22(5): 513-522.

Frey, F. A. and Green, D. H. (1974). "Mineralogy, Geochemistry and Origin of Ilherzolite Inclusions in Victorian Basanites." Geochimica et Cosmochimica Acta 38(7): 1023-1059.

Gregoire, M., Bell, D. R. and Le Rouex, A. P. (2003). "Garnet lherzolites from the Kaapvaal craton (South Africa): Trace element evidence for a metasomatic history." Journal of Petrology 44(4): 629-657.

Harlou, R., Pearson, D. G., Nowell, G. M., Ottley, C. J. and Davidson, J. P. (2009). "Combined Sr isotope and trace element analysis of melt inclusions at sub-ng levels using micro-milling, TIMS and ICPMS." Chemical Geology 260(3-4): 254-268.

Harte, B., Hunter, R. H. and Kinny, P. D. (1993). "Melt Geometry, Movement and Crystallization, in Relation to Mantle Dykes, Veins and

Metasomatism." Philosophical Transactions of the Royal Society of London Series a-Mathematical Physical and Engineering Sciences 342(1663): 1-21.

Hauri, E. H., Shimizu, N., Dieu, J. J. and Hart, S. R. (1993). "Evidence for Hotspot-Related Carbonatite Metasomatism in the Oceanic Upper-Mantle." Nature 365(6443): 221-227.

Hauri, E. H. and Hart, S. R. (1994). "Constraints on Melt Migration from Mantle Plumes - a Trace-Element Study of Peridotite Xenoliths from Savaii, Western-Samoa." Journal of Geophysical Research-Solid Earth 99(B12): 24301-24321.

Hellebrand, E., Snow, J. E., Hoppe, P. and Hofmann, A. W. (2002). "Garnet-field melting and late-stage refertilization in 'residual' abyssal peridotites from the Central Indian Ridge." Journal of Petrology 43(12): 2305-2338.

Ionov, D. and Harmer, R. E. (2002). "Trace element distribution in calcite-dolomite carbonatites from Spitskop: inferences for differentiation of carbonatite magmas and the origin of carbonates in mantle xenoliths." Earth and Planetary Science Letters 198(3-4): 495-510.

Ionov, D. (2004). "Chemical variations in peridotite xenoliths from Vitim, Siberia: Inferences for REE and Hf behaviour in the garnet-facies upper mantle." Journal of Petrology 45(2): 343-367.

Ionov, D. A., Dupuy, C., Oreilly, S. Y., Kopylova, M. G. and Genshaft, Y. S. (1993). "Carbonated Peridotite Xenoliths from Spitsbergen - Implications for Trace-Element Signature of Mantle Carbonate Metasomatism." Earth and Planetary Science Letters 119(3): 283-297.

Ionov, D. A., Hofmann, A. W. and Shimizu, N. (1994). "Metasomatism-Induced Melting in Mantle Xenoliths from Mongolia." Journal of Petrology 35(3): 753-785.

Ionov, D. A., Bodinier, J. L., Mukasa, S. B. and Zanetti, A. (2002a). "Mechanisms and sources of mantle metasomatism: Major and trace element compositions of peridotite xenoliths from Spitsbergen in the context of numerical modelling." Journal of Petrology 43(12): 2219-2259.

Ionov, D. A., Mukasa, S. B. and Bodinier, J. L. (2002b). "Sr-Nd-Pb isotopic compositions of peridotite xenoliths from Spitsbergen: Numerical

modelling indicates Sr-Nd decoupling in the mantle by melt percolation metasomatism." Journal of Petrology 43(12): 2261-2278.

Ionov, D. A., Chazot, G., Chauvel, C., Merlet, C. and Bodinier, J. L. (2006). "Trace element distribution in peridotite xenoliths from Tok, SE Siberian craton: A record of pervasive, multi-stage metasomatism in shallow refractory mantle." Geochimica et Cosmochimica Acta 70(5): 1231-1260.

Ionov, D. A. and Hofmann, A. W. (2007). "Depth of formation of subcontinental off-craton peridotites." Earth and Planetary Science Letters 261(3-4): 620-634.

Klemme, S., Blundy, J. D. and Wood, B. J. (2002). "Experimental constraints on major and trace element partitioning during partial melting of eclogite." Geochimica et Cosmochimica Acta 66(17): 3109-3123.

Macdougall, J. D. and Haggerty, S. E. (1999). "Ultradeep xenoliths from African kimberlites: Sr and Nd isotopic compositions suggest complex history." Earth and Planetary Science Letters 170(1-2): 73-82.

Malarkey, J., Pearson, D. G., Davidson, J. P. and Wittig, N. (2008). "Origin of Cr-diopside in peridotite xenoliths: Recent metasomatic addition revealed by a micro-sampling, trace element and Sr isotopic study of on-craton and off-craton peridotites." 9th International Kimberlite Conference Extended Abstract Volume.

McPherson, E., Thirlwall, M. F., Parkinson, I. J., Menzies, M. A., Bodinier, J. L., Woodland, A. and Bussod, G. (1996). "Geochemistry of metasomatism adjacent to amphibole-bearing veins in the Lherz peridotite massif." Chemical Geology 134(1-3): 135-157.

Menzies, M. A. and Hawkesworth, C. J. (1987). Mantle metasomatism. London ; Orlando, Academic Press.

Menzies, M. A. (1988). "The Geometry of Archean and Proterozoic Lithospheric Mantle Domains beneath the Western USA." Chemical Geology 70(1-2): 54-54.

Missenard, Y., Zeyen, H., de Lamotte, D. F., Leturmy, P., Petit, C., Sebrier, M. and Saddiqi, O. (2006). "Crustal versus asthenospheric origin of relief of

the Atlas Mountains of Morocco." Journal of Geophysical Research-Solid Earth 111(B3): -.

Neumann, E. R., Griffin, W. L., Pearson, N. J. and O'Reilly, S. Y. (2004). "The evolution of the upper mantle beneath the Canary Islands: Information from trace elements and Sr isotope ratios in minerals in mantle xenoliths." Journal of Petrology 45(12): 2573-2612.

Pearson, D. G., Carlson, R. W., Shirey, S. B., Boyd, F. R. and Nixon, P. H. (1995). "Stabilization of Archean Lithospheric Mantle - a Re-Os Isotope Study of Peridotite Xenoliths from the Kaapvaal Craton." Earth and Planetary Science Letters 134(3-4): 341-357.

Pearson, D. G. and Nowell, G. M. (2002). "The continental lithospheric mantle: characteristics and significance as a mantle reservoir." Philosophical Transactions of the Royal Society of London Series a-Mathematical Physical and Engineering Sciences 360(1800): 2383-2410.

Pearson, D. G., Canil, D. and Shirey, S. B., Eds. (2003). Mantle sample included in volcanic rocks: xenoliths and diamonds. Treatise on Geochemistry: The Mantle and Core, Elsevier.

Pearson, D. G. and Wittig, N. (2008). "Formation of Archaean continental lithosphere and its diamonds: the root of the problem." Journal of the Geological Society 165: 895-914.

Porcelli, D. R., Onions, R. K., Galer, S. J. G., Cohen, A. S. and Mattey, D. P. (1992). "Isotopic Relationships of Volatile and Lithophile Trace-Elements in Continental Ultramafic Xenoliths." Contributions to Mineralogy and Petrology 110(4): 528-538.

Raffone, N., Chazot, G., Pin, C., Vannucci, R. and Zanetti, A. (2009). "Metasomatism in the Lithospheric Mantle beneath Middle Atlas (Morocco) and the Origin of Fe- and Mg-rich Wehrlites." Journal of Petrology 50(2): 197-249.

Richardson, S. H., Erlank, A. J. and Hart, S. R. (1985). "Kimberlite-Borne Garnet Peridotite Xenoliths from Old Enriched Subcontinental Lithosphere." Earth and Planetary Science Letters 75(2-3): 116-128.

Roden, M. F., Irving, A. J. and Murthy, V. R. (1988). "Isotopic and Trace-Element Composition of the Upper Mantle beneath a Young Continental

Rift - Results from Kilbourne-Hole, New-Mexico." Geochimica et Cosmochimica Acta 52(2): 461-473.

Rollinson, H. (1993). Using geochemical data: evaluation, presentation, interpretation, Pearson.

Schmidberger, S. S., Simonetti, A. and Francis, D. (2001). "Sr-Nd-Pb isotope systematics of mantle xenoliths from Somerset Island kimberlites: Evidence for lithosphere stratification beneath Arctic Canada." Geochimica et Cosmochimica Acta 65(22): 4243-4255.

Schmidberger, S. S., Simonetti, A., Francis, D. and Gariepy, C. (2002). "Probing Archean lithosphere using the Lu-Hf isotope systematics of peridotite xenoliths from Somerset Island kimberlites, Canada." Earth and Planetary Science Letters 197(3-4): 245-259.

Schmidberger, S. S., Simonetti, A. and Francis, D. (2003). "Small-scale Sr isotope investigation of clinopyroxenes from peridotite xenoliths by laser ablation MC-ICP-MS - implications for mantle metasomatism." Chemical Geology 199(3-4): 317-329.

Simon, N. S. C., Irvine, G. J., Davies, G. R., Pearson, D. G. and Carlson, R. W. (2003). "The origin of garnet and clinopyroxene in "depleted" Kaapvaal peridotites." Lithos 71(2-4): 289-322.

Simon, N. S. C., Carlson, R. W., Pearson, D. G. and Davies, G. R. (2008). "The origin and evolution of the Kaapvaal cratonic lithospheric mantle." Journal of Petrology 48: 589-625.

Sneeringer, M., Hart, S. R. and Shimizu, N. (1984). "Strontium and Samarium Diffusion in Diopside." Geochimica Et Cosmochimica Acta 48(8): 1589-1608.

Stosch, H. G. and Lugmair, G. W. (1986). "Trace-Element and Sr and Nd Isotope Geochemistry of Peridotite Xenoliths from the Eifel (West-Germany) and Their Bearing on the Evolution of the Subcontinental Lithosphere." Earth and Planetary Science Letters 80(3-4): 281-298.

Sun, S. S. and McDonough, W. F. (1989). "Chemical and isotopic systematics of oceanic basalts: implications for mantle composition and processes." Geological Society, London, Special Publications 42(1): 313-345.

Tang, Q. S. and Chen, L. (2008). "Structure of the crust and uppermost mantle of the Yanshan Belt and adjacent regions at the northeastern boundary of

the North China Craton from Rayleigh Wave Dispersion Analysis." Tectonophysics 455(1-4): 43-52.

Teixell, A., Ayarza, P., Zeyen, H., Fernandez, M. and Arboleya, M. L. (2005). "Effects of mantle upwelling in a compressional setting: the Atlas Mountains of Morocco." Terra Nova 17(5): 456-461.

Thirlwall, M. (1991). "Long term reproducibility of multicollector Sr and Nd ratio analyses." Chemical Geology (Isotope Science Section) 94: 85-104.

Urchulutegui, J. F., Fernandez, M. and Zeyen, H. (2006). "Lithospheric structure in the Atlantic-Mediterranean transition zone (southern Spain, northern Morocco): a simple approach from regional elevation and geoid data." Comptes Rendus Geoscience 338(1-2): 140-151.

van Achterbergh, E., Griffin, W. L. and Stiefenhofer, J. (2001). "Metasomatism in mantle xenoliths from the Letlhakane kimberlites: estimation of element fluxes." Contributions to Mineralogy and Petrology 141(4): 397-414.

Vernieres, J., Godard, M. and Bodinier, J. L. (1997). "A plate model for the simulation of trace element fractionation during partial melting and magma transport in the Earth's upper mantle." Journal of Geophysical Research-Solid Earth 102(B11): 24771-24784.

Walter, M. J. (1998). "Melting of garnet peridotite and the origin of komatiite and depleted lithosphere." Journal of Petrology 39(1): 29-60.

Witt-Eickschen, G., Seck, H. A., Mezger, K., Eggins, S. M. and Altherr, R. (2003). "Lithospheric mantle evolution beneath the Eifel (Germany): Constraints from Sr-Nd-Pb isotopes and trace element abundances in spinel peridotite and pyroxenite xenoliths." Journal of Petrology 44(6): 1077-1095.

Wittig, N. (2006). Application of novel U-Th-Pb and Lu-Hf techniques to tracing the melting and metsomatic history of mantle rocks. Danish Lithosphere Centre. Copenhagen, University of Copenhagen. PhD**:** 351.

Wittig, N., Pearson, D. G., Baker, J., Duggen, S. and Hoernle, K. (2008). "Evidence for young carbonatitic metasomatism in the continental mantle root beneath the Middle Atlas, Morocco." 9th International Kimberlite Conference Extended Abstract Volume.

Wittig, N., Pearson, D. G., Baker, J., Duggen, S. and Hoernle, K. (in revision-a). "Tracing the metasomatic and magmatic evolution of continental mantle roots with Rb-Sr, SM-Nd, Lu-Hf and U-Pb and Th-Pb isotopes: a case study of Middle Atlas (Morocco) peridotite xenoliths." Geochimica et Cosmochimica Acta.

Wittig, N., Pearson, D. G., Baker, J., Duggen, S. and Hoernle, K. (in revision-b). "A major element, PGE and Os isotope study of Middle Atlas (Morocco) peridotite xenoliths: Evidence for coupled introduction of metasomatic sulphides and clinopyroxenes." Lithos.

Xu, Y. G., Blusztajn, J., Ma, J. L., Suzuki, K., Liu, J. F. and Hart, S. R. (2008). "Late Archean to early proterozoic lithospheric mantle beneath the western North China craton: Sr-Nd-Os isotopes of peridotite xenoliths from Yangyuan and Fansi." Lithos 102(1-2): 25-42.

Chapter 3:

MINERALOGICAL EVOLUTION OF CRATONIC LITHOSPHERIC MANTLE

3.1. INTRODUCTION

Modal metasomatism, or the addition of new mineral phases by a melt, has long been recognised as an important process in adding exotic phases such as amphibole and mica to the lithospheric mantle (e.g. Dawson 1984; Erlank et al. 1987). More recently it has become apparent that peridotite mineral phases such as clinopyroxene (cpx) and garnet, traditionally regarded as residual mineral phases, may also have a metasomatic origin (van Achterbergh et al. 2001; Pearson and Nowell 2002; Gregoire et al. 2003; Simon et al. 2003). Support for this conclusion comes from the high modal abundance of cpx and garnet observed in peridotites that have experienced such high degrees of melt depletion that they should be depleted harzburgites or dunites (Pearson and Nowell 2002). If the cpx and garnet were purely residual in origin then these phases would be progressively depleted, as melt fraction increases, resulting in a negative correlation between the modal abundance of cpx+garnet and proxies of melting, such as olivine Mg number (Fig. 3.1.). However no such correlation is observed for datasets from either the Kaapvaal craton or the North Atlantic craton (NAC). In shallow melting experiments, where melting starts at approximately 3GPa (thought to be the most plausible scenario (Canil 2004; Wittig et al. 2008)) cpx and garnet are exhausted between 10 and 23% melt extraction even when very fertile starting composition are used (Walter 1998), which corresponds to an olivine Mg number of 90.3 to 91.2, well below the average for most cratons (92.6; Bernstein et al. 2006; Pearson and Wittig 2008). However there are clearly a large number of peridotite xenoliths with

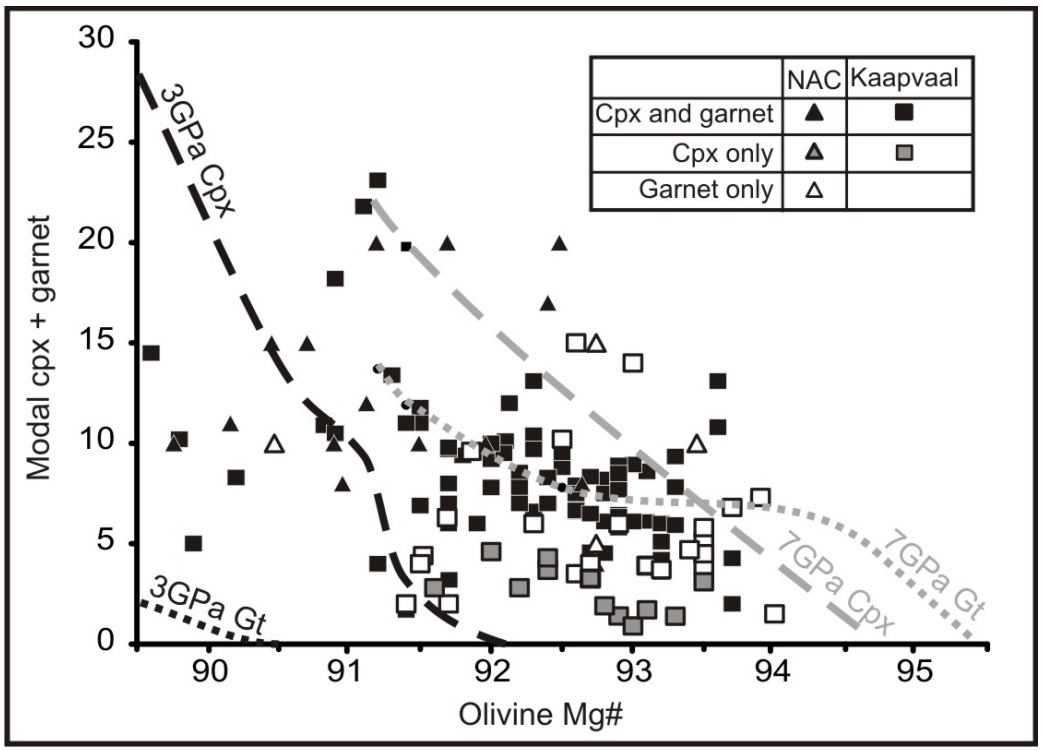

Figure 3.1.

Plot of modal cpx+garnet against olivine Mg# for xenoliths from the Kaapvaal craton and NAC (Boyd et al. 1999; Bizzarro and Stevenson 2003; Simon et al. 2003; Gibson et al. 2008; Simon et al. 2008; Wittig et al. 2008; Sand et al. 2009). The xenolith data are plotted according to modal mineralogy. The dashed and dotted lines represent the modal abundance of cpx and garnet in the residue (normalised to 100wt % solids) for melting experiment data at 3GPa (black) and 7GPa (grey) The experimental data are taken from Walter et al., (1998).

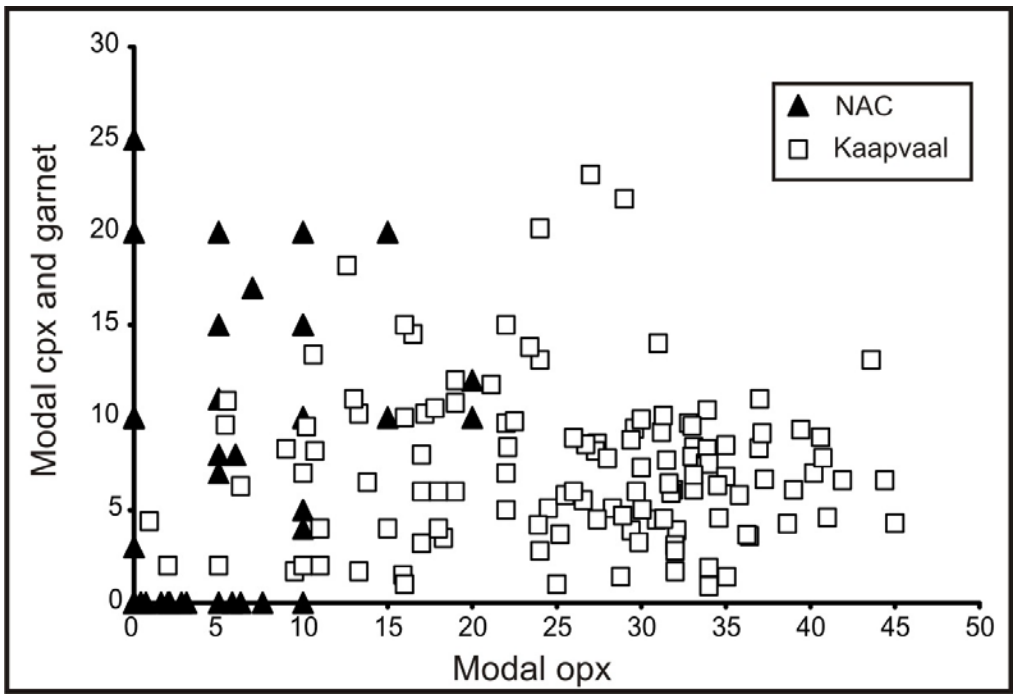

Figure 3.2.

Variation of modal cpx+garnet with modal opx for a range of samples from the Kaapvaal craton and NAC (Bizzarro and Stevenson 2003; Simon et al. 2003; Gibson et al. 2008; Simon et al. 2008; Wittig et al. 2008; Sand et al. 2009).

olivine Mg numbers greater than 91.2 that contain abundant cpx and garnet (Fig. 3.1.); inconsistent with a residual origin for these phases.

This apparent "excess" cpx could be added from at least two different processes. The spatial association of cpx and garnet with orthopyroxene (opx) in a number of samples has led some authors to suggest that the cpx and garnet could be the products of exsolution from high T opx (Cox et al. 1987; Canil 1992; Saltzer et al. 2001). Garnet and cpx are thought to exsolve from opx by the reaction 'high-T opx→ garnet + cpx + low-T opx' (Cox et al. 1987; Canil 1992; Saltzer et al. 2001). However, if exsolution of garnet and cpx from opx is the dominant process by which cpx and garnet are added to the lithospheric mantle there should a positive correlation between modal abundances of opx and garnet+cpx (Canil 1992). This is not observed in datasets from the Kaapvaal craton or the NAC (Fig. 3.2.). While processes such as exsolution and polybaric melting may affect these trends, they are so scattered, especially at moderate to high olivine Mg numbers, that it seems unlikely that melting and cooling can produce the spread.

The preferred hypothesis for the addition of cpx and garnet to the depleted lithospheric mantle is by crystallisation from one or more metasomatic melts (van Achterbergh et al. 2001; Pearson and Nowell 2002; Gregoire et al. 2003; Simon et al. 2003). We present a detailed trace element and isotope study of cpx and garnet in two garnet lherzolites from two contrasting cratons: the NAC and the Kaapvaal craton, discussed below, in order to address this issue. We aim to show that it is possible to identify the processes that add both the cpx and

garnet to the mantle lithosphere in both the NAC and the Kaapvaal craton. These processes can be tracked through time and can be extrapolated to give a broader picture of the temporal and spatial evolution of the lithospheric mantle.

The metasomatic addition of cpx and garnet has implications for lithosphere evolution. Cpx and garnet are important hosts for Sr and REE in the lithospheric mantle and therefore the addition of these phases to the lithosphere will exercise the dominant control on the geochemical evolution of the lithosphere through time (Pearson and Nowell 2002). The Sr budget, for example, will be dominated by the garnet addition until the cpx is added. The addition of cpx, and especially garnet, has a strong influence on the physical properties of the mantle lithosphere including density; one of the most important in terms of stability. The addition of these phases can increase the density of the mantle lithosphere by more than 2% (Schutt and Lesher 2006). It is therefore critical to understand the origin and timing of cpx and garnet addition if we are to understand the potential temporal controls on the chemical and physical evolution of the lithosphere.

3.1.2. CONSTRAINTS ON CRATONIC PERIDOTITE MINERALOGY: THE KAAPVAAL VERSUS THE NORTH ATLANTIC CRATON

Most pioneering early work on cratonic peridotites was carried out on the Kaapvaal craton due to the ready availability of samples through mining (Nixon et al. 1963; Gurney et al. 1975; Harte et al. 1975; Nixon and Boyd 1975). However it has become apparent in recent years, as the database of xenoliths

from a range of cratons has become available, that the Kaapvaal lithospheric mantle may not be typical (Rudnick et al. 1994; Pearson et al. 2003; Bernstein et al. 2007; Simon et al. 2008). The Kaapvaal mantle contains significantly higher proportions of opx, reflected in lower modal olivine contents (Fig. 3.3.), than the other cratons (e.g. Canil 1992; Simon et al. 2008). The origin of this high opx content is thought to be due to the addition of SiO_2-rich fluid (Kelemen et al. 1998), perhaps in an Archean subduction zone (Kesson and Ringwood 1989; Lee 2004; Gibson et al. 2008; Simon et al. 2008). The relationship between average olivine Mg number and modal olivine abundance from a range of cratons (Fig. 3.3.) illustrates that the silica enrichment that affects the Kaapvaal craton can be observed to varying extents in the Siberian and Tanzanian cratons (Rudnick et al. 1994; Bernstein et al. 2007; Pearson and Wittig 2008). In contrast, peridotites from the NAC have very low opx contents. These plot towards the end of the oceanic trend and, interestingly, with a similar olivine Mg number and modal olivine content to depleted dunites from the Iwanaidaike ophiolite massif (Pearson and Wittig 2008). This peridotite massif is the product of Mesozoic partial melting above a supra-subduction zone and therefore is thought to be representative of mantle that has undergone extensive melt depletion under shallow, wet conditions (Kubo 2002). The xenoliths studied here are from the NAC (Pyramidfels, Greenland) and the Kaapvaal craton (Bultfontein, South Africa) and therefore represent the two end members in the spectrum of opx contents of cratonic peridotite lithosphere. In addition to opx enrichment, other xenoliths provide evidence of extensive metasomatism of the Kaapvaal lithosphere, at least in the regions sampled by kimberlites. This metasomatism is expressed by the presence of MARID (xenoliths containing

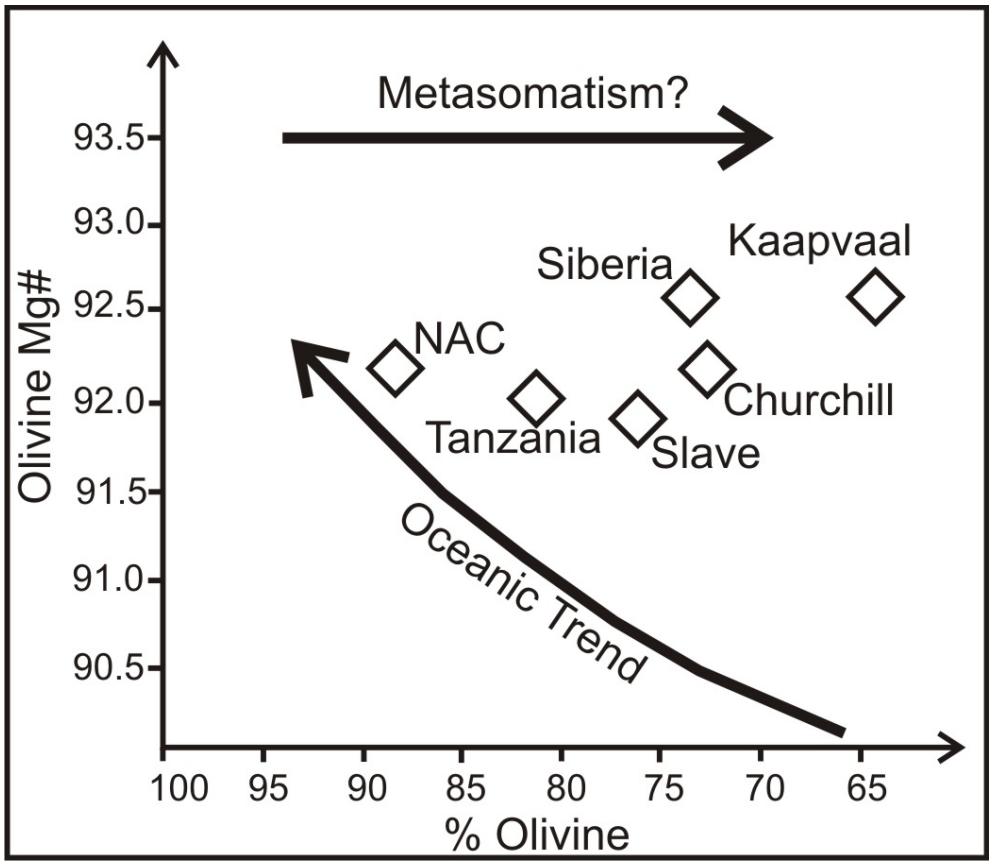

Figure 3.3.

'Boyd' plot showing the variation of mean olivine Mg# with the mean modal percent (by wt) of olivine in low temperature peridotite xenoliths from a range of cratons (adapted from Pearson and Wittig, 2008). Peridotites that are residual after melting should, in theory, plot at the end of the oceanic trend. Metasomatism, due to the addition of Si-rich melt/fluids, can lead to opx enrichment which decreases the modal abundance of olivine.

mica, amphibole, rutile, ilmentite and diopside) and other xenoliths, with abundant mica and amphibole, from kimberlites the Kaapvaal craton (Dawson 1984; Erlank et al. 1987; Gregoire et al. 2003). No such metasomatic rocks have been observed to date from the NAC lithosphere, suggesting that there has been significantly more metasomatism in the Kaapvaal craton (Bernstein et al. 2007; Pearson and Wittig 2008).

3.2. SAMPLES

3.2.1. LOCATION

The Greenland peridotite xenolith we selected for study is from the Pyramidfels region of S.W. Greenland on the southern edge of the NAC. These xenoliths are found in sills (Emeleus and Andrews 1975) that are broadly of kimberlitic composition but technically are ultra-mafic lamprophyres (UML). These sills, dated at 164Ma (Heaman 2005), are intruded into the Pyramidfjeld granite complex of Palaeoproterozoic Ketildian age. The xenolith distribution is heterogeneous and the majority of xenoliths are dunites with rare garnet lherzolites (Wittig et al. 2008). There are very few crustal xenoliths and therefore the sills are concluded to be non-explosive and emplaced at lower crustal levels (Hutchinson et al. 2007).

The xenolith (JMK) from the Kaapvaal craton, South Africa, was collected from the Boshoff Road Dumps near Kimberley, South Africa, and is probably

sourced from the Bultfontein kimberlite pipe. The Bultfontein kimberlite pipe has been dated at 84±0.9Ma using Rb-Sr isochron techniques on phlogopite megacrysts (Kramers et al. 1983). Xenoliths from this location, although not this sample, have been the focus of many previous studies (Nixon and Boyd 1975; Boyd 1989; Canil 1992; Saltzer et al. 2001).

A small number of analyses have also been carried out on a garnet lherzolite, M9, from Lesotho. Detail of this xenolith including location, petrography and mineral chemistry can be found in Simon et al.(2003; 2008).

3.2.2. PETROGRAPHY

3.2.2.1. Bultfontein

This xenolith, JMK, is a coarse, equant garnet lherzolite and was primarily chosen because of the abundance of large and relatively crack free cpx (Fig. C.1.). The xenolith contains olivine (78.6%; all modal abundance values estimated from image analysis), opx (4.6%), cpx (7.1%), garnet (9.7%) and minor amounts of phlogopite (<0.1%). The olivine is primarily coarse, up to 10mm, but has re-crystallised into a fine groundmass along grain boundaries. However these boundaries still preserve the original textural equilibration of the olivine grains with dihedral angles close to 120º. As observed for other Kaapvaal xenoliths, the opx crystals tend to be associated with either cpx or garnet, rarely occurring just with olivine. Opx is much more abundant in this

xenolith than in the samples from Greenland, reflecting the relative Si-enrichment of the Kaapvaal lithosphere (Kesson and Ringwood 1989; Lee 2004; Simon et al. 2008). The cpx crystals, as mentioned before, are large (up to 5mm) and have rounded boundaries and in some cases appear to be embayed or possibly interstitial to the olivine. The 'spongey' rims that have been reported from other Kaapvaal xenoliths (Simon et al. 2003) are not observed in this xenolith. Garnet crystals show a range in size from 2mm to 10mm and a wide spectrum of alteration, with some being very fresh and almost crack free and others showing an abundance of cracks. Kelyphite rims are only observed in a very small number of grains close to the edge of the xenolith. There is no optical evidence of infiltration of kimberlite melt.

3.2.2.2. Greenland

Garnet-bearing xenoliths are uncommon at Pyramidfels on the southern edge of the NAC, partly because the lithosphere is thought to be thinner towards the south, compared to further north (Sand et al. 2009). The majority of xenoliths from this locality are therefore spinel lherzolites, harzburgites and dunites. The Greenland xenolith studied here, G-06-07Z (Fig. D.1.), is a coarse, equant, garnet lherzolite comprising of cpx (6.0%; all modal abundance values estimated from image analysis), opx (1.6%), garnet (including kelyphite 5.0%) and olivine (87.1%). Minor amounts of phlogopite (<0.2%) and spinel (<0.1%) are present in the kelyphite rims surrounding the garnets. There are also rims of small, round spinel grains around the edge of the kelyphite rims. The garnets have been extensively kelyphytised and in some cases are almost completely

replaced. The kelyphite boundary is thinner along garnet-cpx boundaries than garnet-olivine boundaries. There is minimal alteration to serpentine along olivine grain boundaries away from the infiltrating kimberlite melt.

The cpx crystals range from 2mm to 5mm in size and are rounded and embayed. There is no association between cpx and any other mineral phases although there are some cpx crystals included within the garnet. There is minimal alteration of the cpx either along cracks or along the grain boundaries. 'Spongey' rims are also not observed in this xenolith.

The edge of the xenolith is embayed and kimberlite melt can be seen infiltrating the xenolith along olivine grain boundaries. Phlogopite is observed crystallising in some places where the kimberlite has infiltrated the xenolith.

Data are also presented from a spinel lherzolite, sample G-06-07Y (Fig. D.1.). This coarse, equant spinel lherzolite comprises predominantly of olivine (85%; all modal abundance values estimated from image analysis) and cpx (9.9%) with minor amounts of phlogopite (4.7%) and spinel (0.4%). The olivine (crystals ranging from 2mm to 5mm in size) has been altered to serpentine around the grain boundaries but the crystal cores remain relatively unaltered. The olivine crystal boundaries have dihedral angles close to 120º indicating that they are in textural equilibrium.

The cpx and phlogopite both occur as 'clots' where a number of crystals have grown in a discrete area often associated with an altered vein (1-2mm wide) that

cuts through the thin section. This vein predominantly contains phlogopite although some patches of quenched melt are observed. The cpx and phlogopite are spatially closely related. The phlogopite crystals (2-3mm in size) show a range from euhedral to subhedral crystal forms and are found as inclusions in cpx. The cpx (2-5mm in size) is predominantly interstitial with rounded and embayed edges as well as containing round inclusions of olivine. The cpx crystals are altered and show a large number of fine cracks throughout and bands of melt inclusions.

No opx was observed in the thin section. There is a small proportion of spinel in the centre of a clot of phlogopite. The spinel crystals show rounded and bulbous edges.

3.2.3. MINERAL CHEMISTRY

Representative major element compositions of the minerals for both locations are located in Table C.1. and D.1.

3.2.3.1. Bultfontein

This garnet lherzolite (JMK) contains chrome diopside with a high Cr number of 30. The red garnets are Cr-pyrope and are classified, by their Ca (average 4.41wt% CaO) and Cr (average 3.79wt% Cr_2O_3) contents, as G9 or lherzolitic garnets indicating that they have equilibrated with cpx (Schulze 2003; Grütter et

al. 2004). Garnet is pyrope (71% pyrope) with minor components of almandine (18%) and grossular (12%).

Olivine has a Mg number ([Mg/[Mg+Fe]]*100) of 91.6, close to the global average of 92.6 for cratonic mantle (Bernstein et al. 2007; Pearson and Wittig 2008). This is comparable to other olivine from the Kaapvaal craton (Pearson et al. 2003; Bernstein et al. 2007; Pearson and Wittig 2008).

The clinopyroxene is Cr diopside in composition and has a Mg number of 91.3 and a Cr number of 30.3. These values are similar to those observed in other cratonic garnet peridotites respectively (Pearson et al. 2003).

The opx is enstatite (92% enstatite, 7% ferrosilite, 1% wollastonite) and has a higher Mg number (average 92.6) than the corresponding olivine.

No major element core to rim zoning is observed among or within any of the mineral phases and the composition of each mineral phase is homogeneous throughout the xenolith.

3.2.3.2. Greenland

The olivine from both Greenland xenoliths has a Mg number of 89.6, which is significantly lower than the olivine from Bultfontein and the average of 92.6 for cratonic peridotite xenoliths (Bernstein et al. 2007; Pearson and Wittig 2008). However, this olivine Mg number is not typical of mantle xenoliths from

Greenland where the majority of samples analysed by Sand et al. (2009; from localities further north) show a range on olivine Mg number from 88 to 94, with most samples between 91 and 93 (Pearson and Wittig 2008).

Cpx in the garnet lherzolite sample (G-06-07Z) is Cr diopside with an average Mg number of 91.1, slightly higher than the olivine, and a Cr number of 25.5. The spinel lherzolite (G-06-07Y), on the other hand, has an average Mg number of 90.8 and a much higher Cr number of 88.3. These values, as with the samples from the Kaapvaal Craton, are similar to those observed in other garnet and spinel facies lherzolites (Boyd et al. 1999; Pearson et al. 2003).

Opx in the garnet lherzolite (G-06-07Z) is predominantly enstatite (91% enstatite, 9% ferrosilite and 1% wollastonite) and, as with JMK, has a higher Mg number (average 91.6) than the corresponding olivine. The spinel lherzolite does not contain opx.

Garnets in the garnet lherzolite (JMK) are pyrope (71% pyrope) garnet with minor almandine (17%) and grossular (12%) components. The garnet Ca (average 4.62wt% CaO) and Cr (average 2.11wt% Cr_2O_3) contents classify them as G9 (Schulze 2003; Grütter et al. 2004) or lherzolitic garnets.

There is no major element zoning or variation observed within or among the individual mineral phases.

3.2.4. GEOTHERMOBAROMETRY

In order to estimate the pressure and temperature that these xenoliths equilibrated at it is first important to assess the degree to which the major elements are in equilibrium (Smith 1999). Mantle xenoliths are bought to the surface relatively quickly and it is therefore assumed, in the majority of cases, that mantle minerals will remain in major element equilibrium and reflect mantle conditions (Smith 1999). However, there are examples of dis-equilibrium with the most commonly cited evidence being major element zoning between the core and rim of individual mineral crystals (e.g. Griffin et al. 1989; Griffin et al. 1996; Shimizu et al. 1997c). Estimates of diffusion coefficients, at a specific temperature, for the cations used in thermobarometry are poorly constrained and are dependant on factors such as pressure, crystallographic direction, oxygen fugacity and composition (Griffin et al. 1996; Brenker and Brey 1997). In pyroxenes, for example, substantially slower diffusion has been observed for Al and Cr than for Fe, Mg and Ca with the diffusion rates varying by four orders of magnitude (Smith and Barron 1991; Witt-Eickschen et al. 1993; Ozawa and Takahashi 1995; Smith and Riter 1997). The cores of these minerals may therefore be equilibrated for some cations and not others. However this can be circumvented by using rim compositions, which are much more likely to be in equilibrium, for pressure and temperature estimates.

In the samples presented here there was no major element zoning observed among any of the mineral phases and therefore the minerals are assumed to be

in equilibrium. This is supported by evidence from the Ca and Cr (a slower diffusing cation) that indicates that the garnet and cpx are in equilibrium with each other.

3.2.4.1. Bultfontein

Temperature and pressure estimates have been calculated from six thin sections from the same xenolith (Table C.2.). The pressure estimates range from 52.2kbar to 55.1kbar (MacGregor 1974) with temperatures ranging from 1136ºC to 1183ºC (Brey and Kohler 1990; Brey et al. 2009). This is within the range observed from this area and the sample plots close to the typical Kaapvaal geotherm which corresponds to a 40 to 42mWm^{-2} geotherm (Stachel et al. 2003; Simon et al. 2008). The coincidence of the pressure and temperature estimates from these xenoliths with the geotherm confirms the previous conclusion that these xenoliths are in major element equilibrium.

3.2.4.2. Greenland

Pressure and temperature estimates for a suite of xenoliths from Pyramidfels have been calculated along with a geotherm for this area by Nielsen et al. (2008). The garnet lherzolite presented yields equilibration conditions of 947ºC (Brey and Kohler 1990; Brey et al. 2009) and 34.5kbar (MacGregor 1974). This is within the range observed from the few other garnet lherzolites from this area (Sand et al. 2009).

3.3. METHOD

3.3.1. SAMPLING

In-situ sampling of the cpx for trace element and Sr isotope analysis was carried out by micro-drilling on 100μm thick sections using the procedure outlined by Charlier et al. (2006) using a New Wave MircoMill at NCIET, Durham University, UK. The cores of crystals were drilled where possible and any cracks, that might contain any potential alteration, were avoided. The drilled powder was collected in 18mΩ MilliQ water (MQ), dried and weighed to allow accurate determination of trace element concentrations. The drilled weights ranged from 0.035mg to 0.143mg.

The garnets, and associated cpx, were picked to allow determination of isotopic compositions. In order to ensure that the garnet and cpx pairs were closely associated a polished block, approximately 5mm thick, of each xenolith was prepared and the garnet and surrounding cpx was cut out in approximately 1cm^2 sections (see Figure C.2. for garnet locations). These sections each contained only one garnet and were then crushed separately in an agate mill that was cleaned between samples to avoid any cross contamination. Clean garnet aggregates, of different fragments (to ensure enough analyte for analysis), and individual cpx were hand picked from the coarse crush. All fragments selected were bound by fractures. The sample weights ranged from 0.029mg to 0.405mg for the cpx and 0.36mg to 52.79mg for the garnet. The mineral separates were

leached in MQ in an ultrasonic bath for 30min and then again in fresh MQ for 30min again. Separates were then leached in UpA ('Ultra-purity acid') 6N HCl at 50ºC for 30 min before being rinsed in MQ. The chips were checked again optically before being dissolved.

Whole rock samples were also prepared by removing any potential kimberlite on the xenolith surface before crushing to a powder. Approximately 100mg was dissolved for isotope and trace element analysis. A number of leaching experiments were carried out on the whole rock powders and the results of these are summarised in Table C.6. and Table D.6.

3.3.2. CHEMISTRY

The picked and drilled mineral separates and whole rock samples were both dissolved using the same method (scaled up for the larger samples), outlined by Charlier et al. (2006) and Klein BenDavid and Pearson (2009). UpA acids were used to dissolve all mineral separate samples to minimise blanks. A 10% aliquot, by mass, was taken for trace element analysis by ICP-MS. The remaining 90% was processed through micro Sr columns as outlined by Charlier et al. (2006) using cleaned Sr-spec resin. The eluant from the Sr column was collected and processed through cation columns using Bio-Rad AG50W-X8 200-400 mesh cation exchange resin to isolate the REE fraction for Nd isotope analysis (Dowall et al. 2003).

3.3.3. ICP MASS SPECTROMETRY (ICP-MS)

The trace element aliquot was diluted in 500ul of 3% UpA HNO_3 for the drilled and picked samples or 50ml (TD 3% HNO_3) for the whole rock samples and analysed for 21 trace elements using the ThermoFisher Element II at NCIET. The parameters used are similar to those outlined in Font et al. (2008). Accuracy and repeatability of the trace element concentrations are 10% or better (Table A.8.) and are given in Harlou et al. (2009).

3.3.4. LASER-ABLATION ICP MASS SPECTROMETRY (LA-ICP-MS)

In-situ trace element concentrations in the garnet, cpx and opx were analysed for 25 trace elements using a Perkin-Elmer Elan DRC II at the University of Cambridge, UK. These analyses were ablated using a 213nm wavelength UP213 New Wave laser (interfaced to a Perkin-Elmer Elan DRC II ICP-MS) at an energy density between 6 and 7 Jcm^{-2} and a pulse repetition rate of 10Hz resulting in craters with a diameter of 100μm. The ICP-MS data acquisition settings were dependant on the concentration of the elements in the samples, and for this study dwell times were typically 10 to 50ms.

For all data, NIST 610 was used for calibration of element sensitivity. Calibration accuracy was verified by analysing NIST 612 or 614 as an unknown sample and recoveries were typically 90 to 110% of the values published by Pearce et al. (1997). The CaO content of each sample was used for internal

standard normalisation of the trace element signals. ICP-MS drift during the analytical session was less than 10% (Table A.9.).

The data were processed and concentrations calculated using Glitter Software (GEMOC, Australia). This allows precise selection of blanks, signals and visualisation of the quality of the data.

3.3.5. THERMAL IONISATION MASS SPECTROMETRY (TIMS)

Sr isotope ratios for the drilled and picked samples were determined on the ThermoFisher Triton at NCIET, Durham University, UK. Purified Sr was loaded onto Re filaments using a TaF_5 activator. Sr was analysed with a static multi-collection routine with each analysis consisting of 200 ratios with an integration time of 4 seconds per ratio. Sr isotope ratios were corrected for mass fractionation using an $^{86}Sr/^{88}Sr$ ratio of 0.1194 and an exponential law. The reproducibility for 3ng NBS 987 standards (these yield a similar beam size to the majority of the samples analysed here, typically between 0.5 and 3Vof ^{88}Sr) that were run in different sessions (the polarity of the Triton switches between positive and negative ion mode - a session refers to a period of time when the Triton was in positive ion mode) are summarised in Table A.1 and given in detail in Table A.2. The mass of Sr analyte for each sample varied from 1ng to 20ng for the drilled cpx and from 5ng to over 100ng for the picked mineral separates. The average total procedural Sr blank was 17pg (±18 2sd, n=22) although this varied between 27pg and 1pg of Sr. The total procedural blank is typically less than 0.1% of the Sr in the sample for each batch of chemistry

processed (Table A.7.). Sr isotope ratios were not blank corrected as this correction is less than the analytical uncertainty.

3.3.6. MULTICOLLECTOR ICP MASS SPECTROMETRY (MC-ICPMS)

Following chemistry, whole rock Sr and all Nd fractions (whole rock and mineral separates) were dissolved in 3% HNO_3 and analysed on the ThermoFisher Neptune MC-ICPMS at NCIET, Durham University, UK. Samples were aspirated using an ESI PFA-50 nebulizer in conjunction with a 'cinnabar' micro-cyclonic borosilicate spray chamber. The basic analytical method used for each element on the Neptune comprises a static multi-collection routine of 1 block of 50 cycles with an integration time of 4sec per cycle; total analysis time 3.5mins.

Using the PFA-50 nebuliser, cinnabar spray chamber and a normal H skimmer cone, the sensitivity for Nd on the Neptune is 60-80V total Nd ppm^{-1} at an uptake rate of 90µl min^{-1}. Instrumental mass bias was corrected for using a $^{146}Nd/^{145}Nd$ ratio of 2.079143 (equivalent to the more commonly used $^{146}Nd/^{144}Nd$ ratio of 0.7219) and an exponential law. The $^{146}Nd/^{144}Nd$ ratio is used for correcting mass bias since at Durham Nd isotopes are measured on a total REE-cut from the cation columns and this is the only Ce- and Sm-free stable Nd isotope ratio. This approach requires a correction for isobaric interferences from Sm on ^{144}Nd, ^{148}Nd and ^{150}Nd. The correction used is based on the method outlined in Nowell & Parrish (2002) and Nowell et al., (2008). The accuracy of the Sm correction method during analysis of a total REE

fraction is demonstrated by repeat analyses of the USGS BHVO-1 std, which yield an average $^{143}Nd/^{144}Nd$ ratio of 0.512982±0.000007 (13.5ppm 2SD, n=13) after Sm correction; essentially identical to the TIMS ratio of 0.512986±0.000009 (17.5ppm 2SD; n=19) obtained by Weis et al. (2005) on a pure Nd separate. Average signal size for the ^{146}Nd in the standards was 3.2±0.7 V and was 6.4±7.4V for the samples. The samples were analysed in a single analytical session during which the average $^{143}Nd/^{144}Nd$ value of 0.511104±0.000008 (16.5ppm; n=9) for the in-house standard J&M and an average value of $^{143}Nd/^{144}Nd$ value of 0.511104±0.000011 (22.2ppm; n=8) for the Sm-doped in-house standard J&M (used to monitor the offline Sm correction). The standard details are summarised in Table A.5. These values are comparable to the long-term value reported by (Pearson and Nowell 2005). Sample data are reported relative to a J&M value of 0.511110 (equivalent to a La Jolla value of 0.511862; Royse et al., 1998).

Using the PFA-50 nebuliser, cinnabar spray chamber and a normal H skimmer cone, the sensitivity for Sr on the Neptune is typically ~60V total Sr ppm^{-1} at an uptake rate of 90µl min^{-1}. Prior to analysis a small aliquot was first tested to establish the Sr concentration of each sample by monitoring the size of the ^{84}Sr beam (the ^{88}Sr was too high in non-diluted aliquots to measure directly) from which a dilution factor was calculated to yield a beam of approximately 20V ^{88}Sr. Instrumental mass bias was corrected for using an $^{88}Sr/^{86}Sr$ ratio of 8.375209 (the reciprocal of the $^{86}Sr/^{88}Sr$ ratio of 0.1194) and an exponential law. The samples were analysed in a single session during which the average $^{87}Sr/^{86}Sr$ value for NBS987 (with ^{88}Sr = 20V) was 0.710258±0.000010 (7ppm

2SD; n=7). Details of these standard values are summarised in Table A.3. Sample data are reported relative to an NBS 987 value of 0.71024 (Thirlwall 1991).

3.3.7. ELECTRONPROBE MICROANALYSER (EPMA)

Olivine, opx, cpx and garnet were all analysed for major element concentrations using a Cameca SX100 Electonprobe microanalyser at the University of Cambridge, UK, with a beam voltage of 15kv, a current of 10nA for the major elements and 100nA for the trace elements and a beam diameter of 1μm. Further details are summarised in Table A.10.

3.4. RESULTS

The geochemical data for the mineral separates and the whole rock samples can be found in Appendices C and D.

3.4.1. BULK ROCK GEOCHEMISTRY

3.4.1.1. Mantle Xenoliths

Garnet lherzolites from Bultfontein and Greenland were analysed for whole rock trace elements as well as Sr and Nd isotope ratios. The whole rock trace

element pattern for the Bultfontein garnet lherzolite ($[La/Yb]_N$ = 5.68; Fig. 3.4(a)) is slightly enriched in incompatible elements relative to primitive mantle, but less so than the Greenland samples ($[La/Yb]_N$ = 25.50; Fig. 3.4(b)). In contrast to the Bultfontein peridotite, the Greenland peridotite trace element pattern shows a positive peak for Sr, with a Sr concentration of 116ppm.

The whole rock sample from Bultfontein has a high $^{87}Rb/^{86}Sr$ ratio of 0.252 and an initial $^{87}Sr/^{86}Sr$ ratio of 0.705707 (±0.000014; Fig. 5). The whole rock Greenland garnet lherzolite xenolith has a lower $^{87}Rb/^{86}Sr$ value of 0.117 and initial $^{87}Sr/^{86}Sr$ ratio of 0.706260 (±0.000007; Fig. 6).

3.4.1.2. Host Rock

Bulk rock kimberlite analyses for Bultfontein have been taken from the literature (Le Roex et al. 2003) and are plotted in Fig. 3.4(a). The trace element patterns are enriched, much more so than the mantle xenolith, with negative peaks in Sr and Pb. Two whole rock analyses of the Bultfontein kimberlite have been taken from the literature and have initial Sr isotope ratios of 0.703985 and 0.705370 (Becker and Le Roex 2006).

Six UML (Fig. 3.4(b)) samples from Greenland, hosts to the xenoliths, were analysed for whole rock trace elements and Sr and Nd isotopes. The six analyses all show similar trace element LREE/HREE enriched patterns enrichment, with $[La/Yb]_N$ ratios ranging from 86 to 116 (Fig. 3.4(b)). There

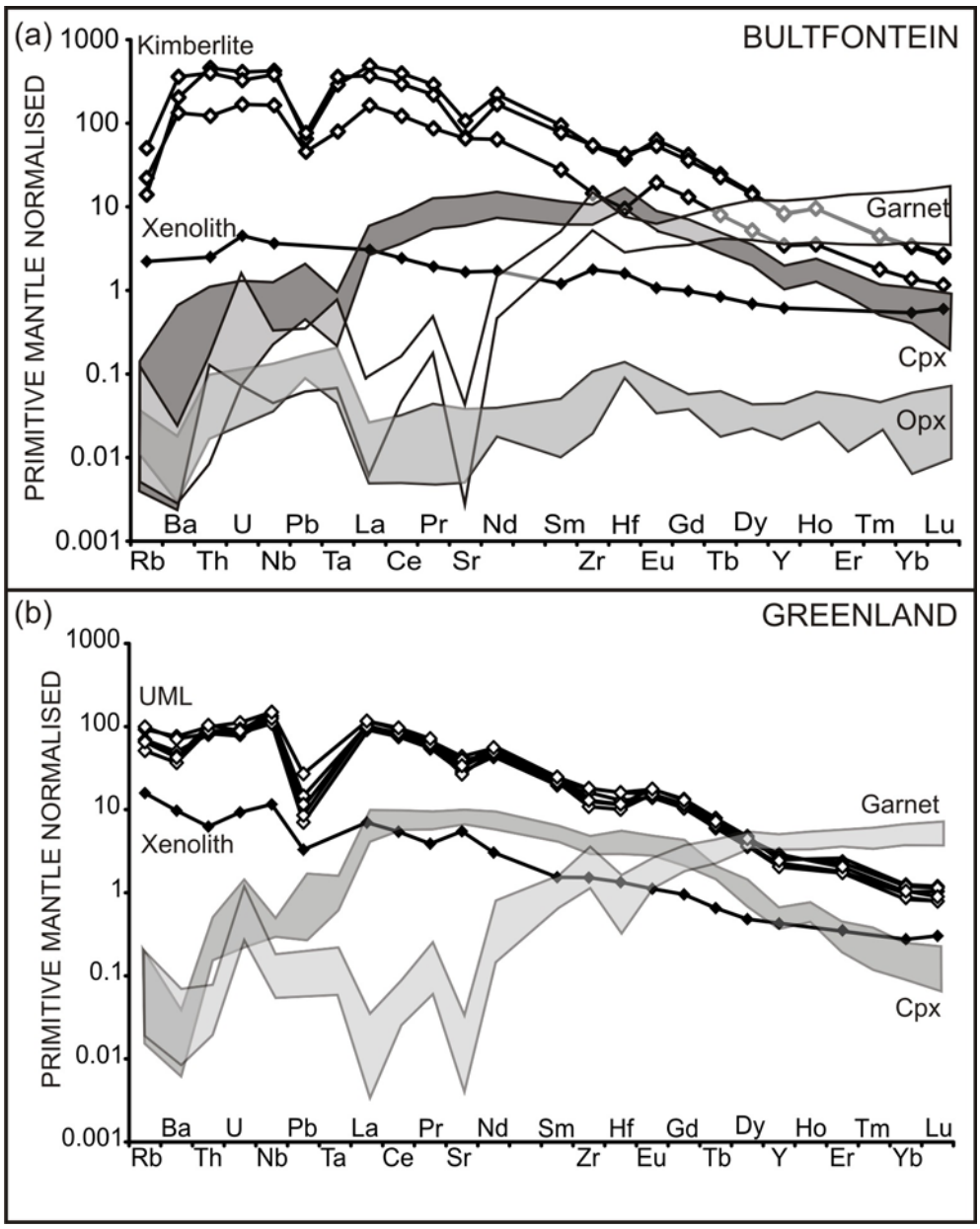

Figure 3.4

(a) *Primitive mantle normalised (Sun and McDonough 1989) multi-element plots for the whole rock peridotite xenolith (JMK) from Bultfontein. The whole rock kimberlite analyses are taken from Le Roex et al. (2003). The fields depict the analyses of opx, garnet and cpx taken from the same sample, shown for reference.*

(b) *Primitive mantle normalised (Sun and McDonough 1989) multi-element plots for the whole rock peridotite xenolith (G-06-07Z) and the host UML from Greenland. The fields depict the analyses of garnet and cpx taken from the same sample, shown for reference.*

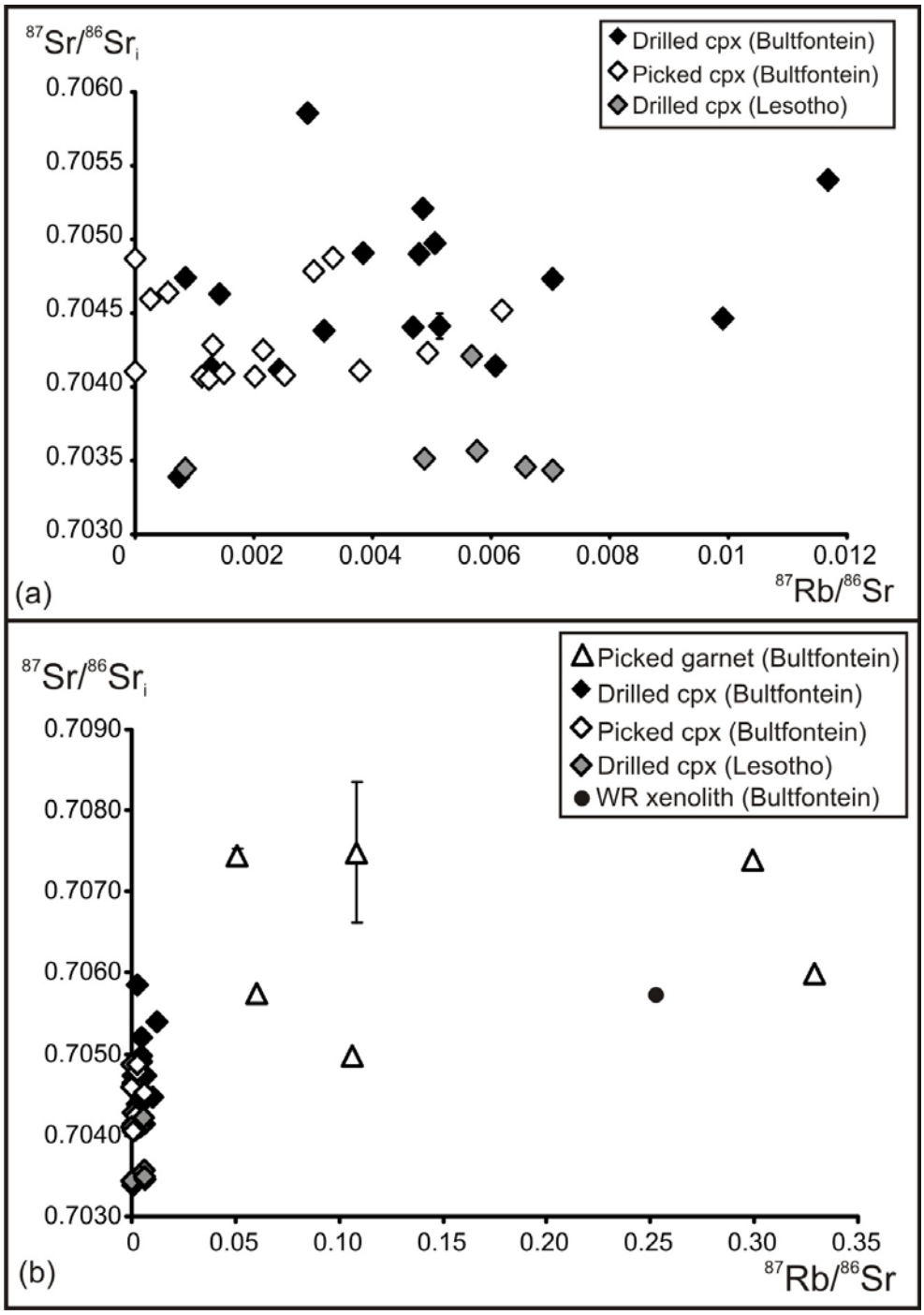

Figure 3.5.

(a) *Initial $^{87}Sr/^{86}Sr$ values for the drilled and picked cpx from Bultfontein (sample JMK) and Lesotho (M9) plotted against $^{87}Rb/^{86}Sr$ ratios.*

(b) *Initial $^{87}Sr/^{86}Sr$ values for the picked and drilled cpx with the picked garnet as well as the whole rock peridotite xenolith plotted against $^{87}Rb/^{86}Sr$.*

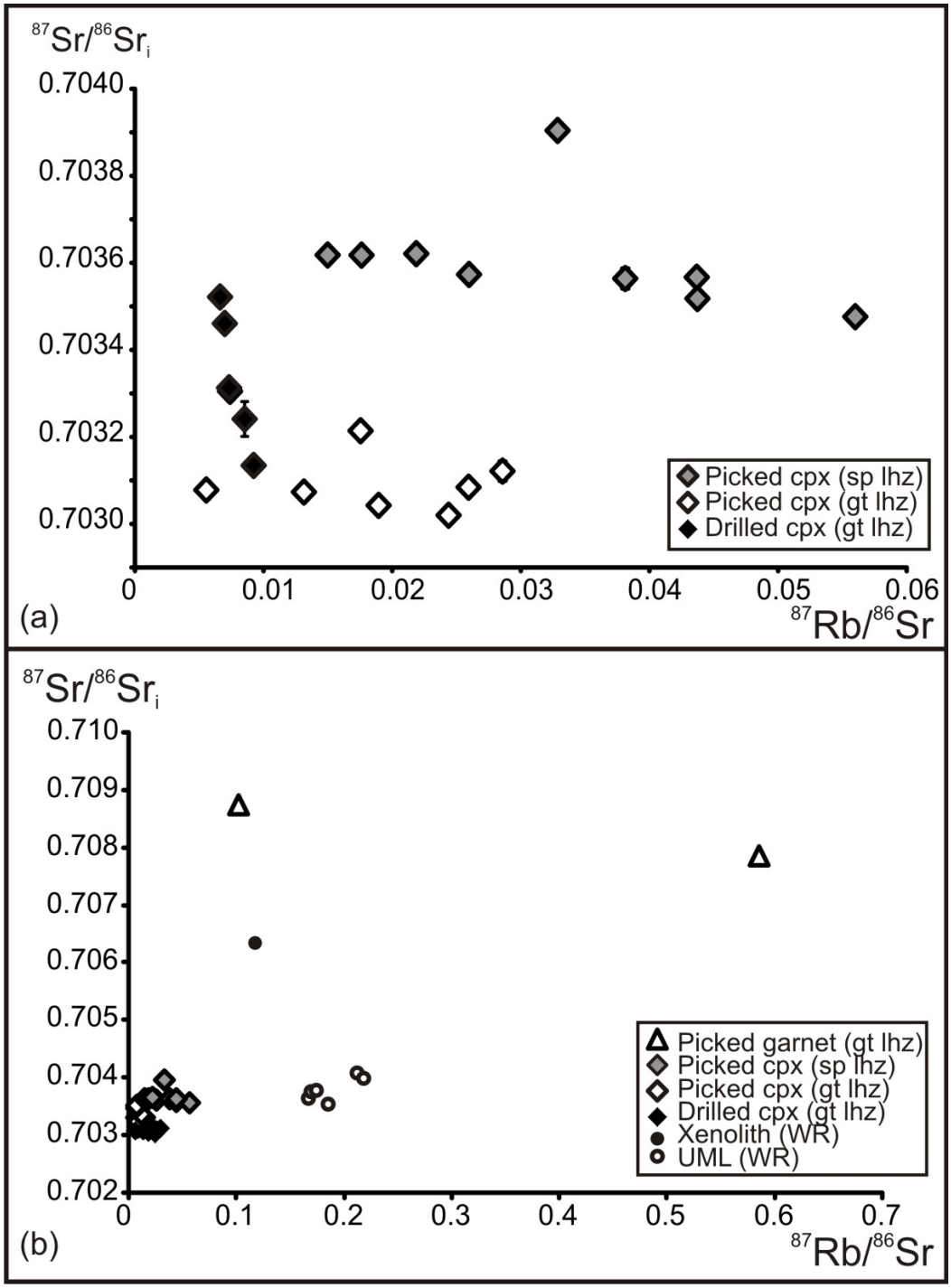

Figure 3.6.

(a) *Initial $^{87}Sr/^{86}Sr$ values for the drilled and picked cpx from Greenland garnet lherzolite (G-06-07Z) and the spinel lherzolite (G-06-07Y) plotted against $^{87}Rb/^{86}Sr$ ratios.*

(b) *Initial $^{87}Sr/^{86}Sr$ values for the picked and drilled cpx with the picked garnet as well as the whole rock peridotite xenolith and the whole rock UML plotted against $^{87}Rb/^{86}Sr$.*

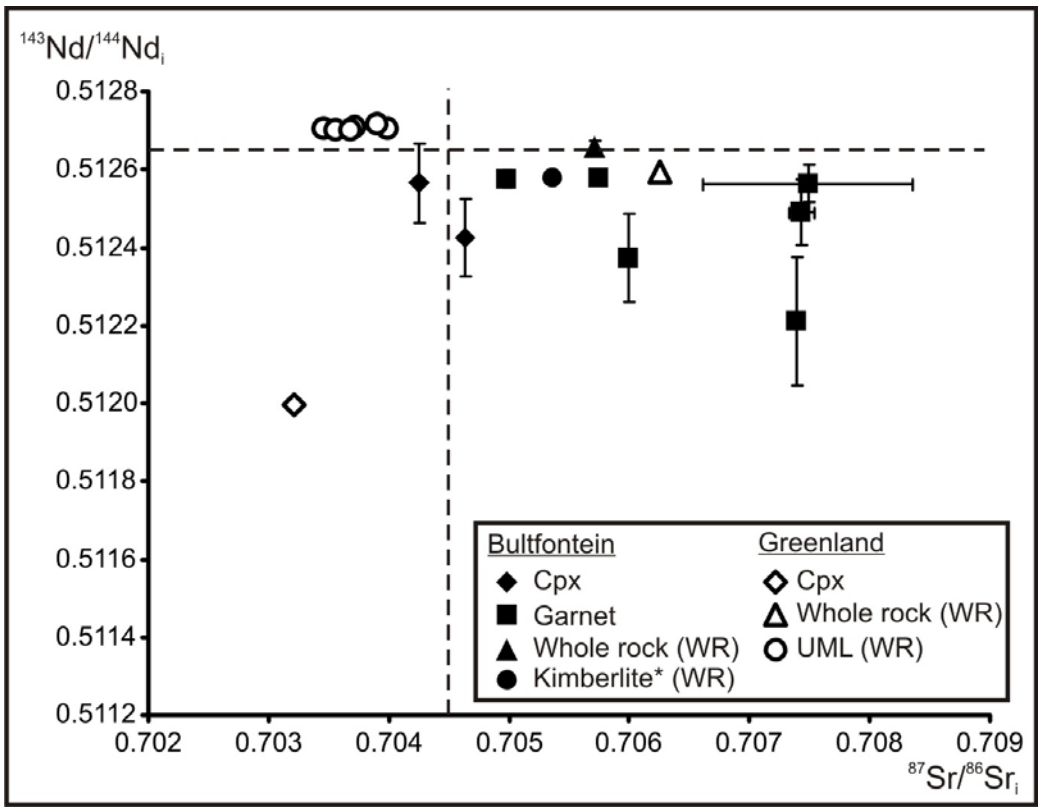

Figure 3.7.

$^{143}Nd/^{144}Nd_i$ against $^{87}Sr/^{86}Sr_i$ for the cpx, garnet, whole rock (WR) peridotite xenolith and the host Bultfontein kimberlite (taken from Le Reox et al., 2003) for the garnet lherzolite xenolith from Bultfontein (JMK) in the black symbols. The cpx data along with the whole rock peridotite xenolith and the host UML are also plotted in the open symbols.

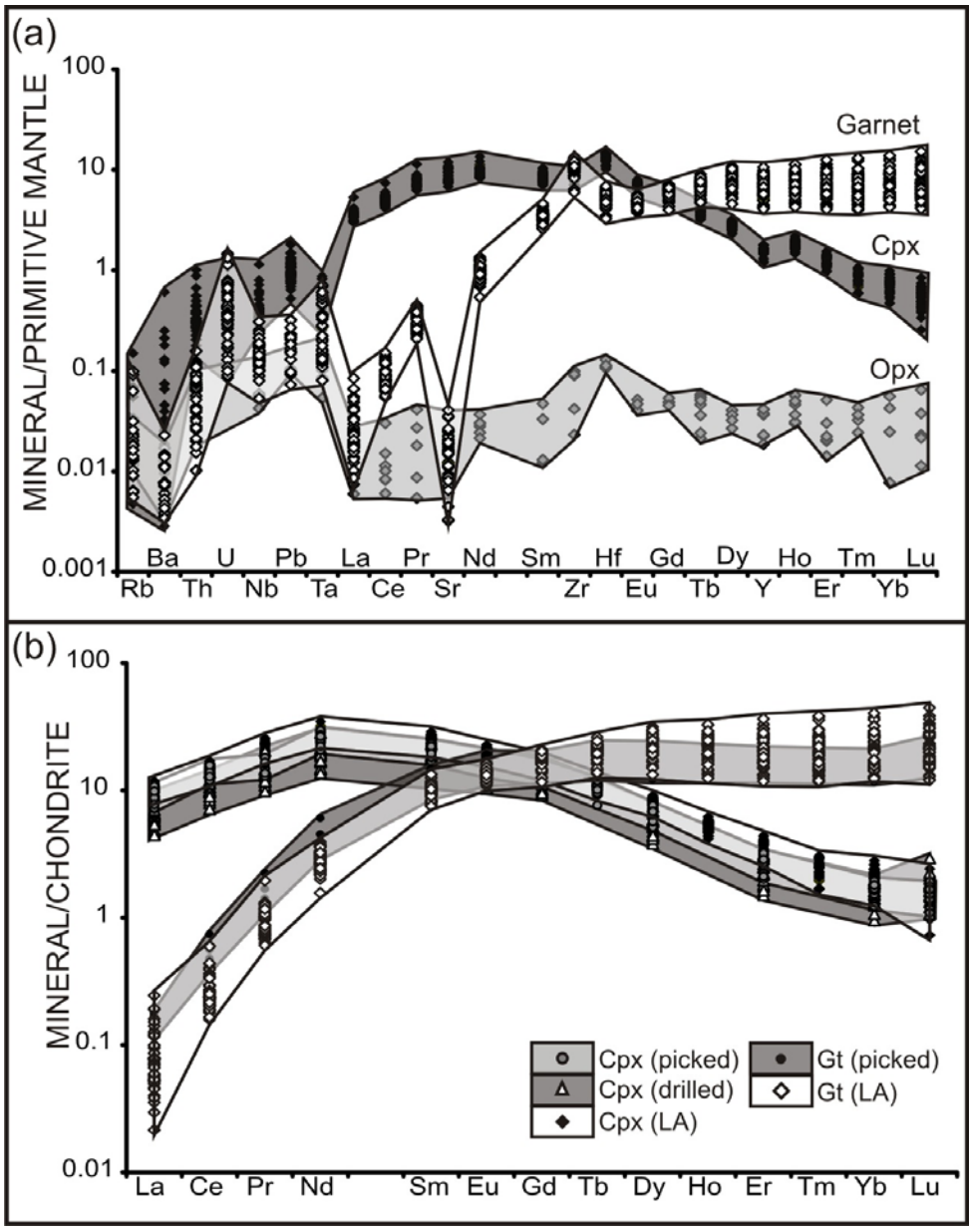

Figure 3.8.

(a) *Primitive normalised (Sun and McDonough 1989) multi-element plots for the laser ablation data for the garnet, cpx and opx from the Bultfontein garnet lherzolite (JMK).*

(b) *Chondrite normalised (Sun and McDonough 1989) REE plots for the cpx and garnet that have been picked and drilled as well as those analysed by laser ablation.*

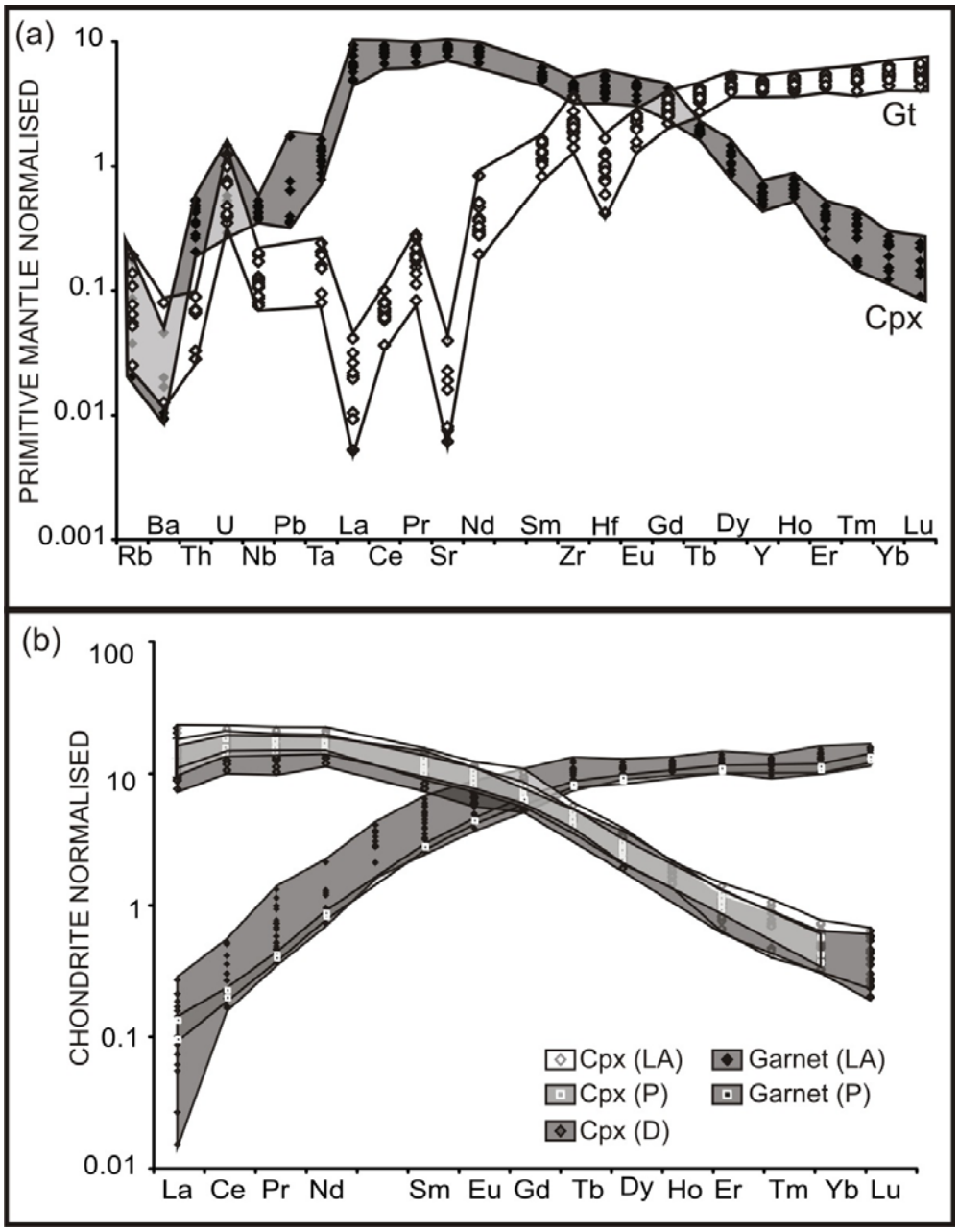

Figure 3.9.

(a) *Primitive normalised (Sun and McDonough 1989) multi-element plots for the laser ablation data for the garnet and cpx from the Greenland garnet lherzolite (G-06-07Z).* ***(b)*** *Chondrite normalised (Sun and McDonough 1989) REE plots for the cpx and garnet that have been picked and drilled as well as those analysed by laser ablation*

is a slight anomaly in Sr in the UML which has Sr concentrations ranging from 565ppm to 921ppm. There is also a slight dip in Zr-Hf in some of the analyses with $[Hf/Eu]_N$ ranging from 0.66 to 1.04.

The Greenland UML has a range in $^{87}Rb/^{86}Sr$ from 0.166 to 0.218, and $^{147}Sm/^{144}Nd$ from 0.085 to 0.094, which is within the range observed in other UML from the NAC (Tappe et al. 2004). The small range in initial Sr isotope ratios (0.703454 to 0.703996) does not correlate with $^{87}Rb/^{86}Sr$ and is within the range of Sr isotope ratios observed in the Greenland cpx (Fig. 3.6.). The UML whole rock analyses show a range in $^{143}Nd/^{144}Nd_i$ from 0.512701 to 0.512714 (Fig. 3.7.).

3.4.2. BULTFONTEIN GARNET LHERZOLITE (JMK)

In-situ analyses show that the Bultfontein garnet lherzolite cpx are LREE enriched (average $[La/Ce]_N$ = 5.10) with a hump in the MREE (Fig. 3.8(b)). This trace element pattern is typical of those first found in low temperature Kaapvaal peridotites by Shimizu et al. (1975) The LA-ICP-MS data did not reveal any consistent trace element zoning within or among the cpx crystals, consistent with the major element data. The multi-element plot (Fig. 3.8(a)) shows that these cpx do not have the negative Hf-Zr anomaly which is often observed in cpx that have been metasomatised by a carbonatite melt (Blundy and Dalton 2000). Although the inter-element fractionation in the cpx is consistent, the element concentrations do vary, with Sr for example, showing a range from 144ppm to 276ppm with an average of 192ppm (LA data). The

other trace element concentrations show a similar relative range. These variations do not correlate with crystal size, shape or any other textural parameter although it is difficult to constrain textural parameters using the two dimensional slices provided by the thin section. There is, however, no consistent variation observed between the core and rim of the cpx crystals. The range in trace element concentrations observed here are consistent with those from other LA-ICP-MS studies (Ionov et al. 2002; Schmidberger et al. 2003).

The garnet crystals all show the same LREE-depleted patterns (Fig. 3.8.; average $[La/Ce]_N = 0.20$) which is typical of garnet that is in equilibrium with cpx (Shimizu 1975). This is consistent with the major element data which classify these garnets as G9 or lherzolitic. The most notable feature of these garnets is a large negative trough for Sr, typical of mantle garnets (Pearson et al. 2003). The multi-element plot shows that the patterns, as with the cpx, do not show any variation among the garnet crystals and no consistent zoning is observed. However, like the cpx there is a range in element concentrations with Nd, for example, ranging from 0.7ppm to 1.9ppm with an average of 1.3ppm (LA data). This variation does not correlate with the shape, size or colour of the garnets in the thin section.

A number of altered cracks were analysed for trace elements using LA-ICP-MS in order to characterise the alteration and therefore eliminate any samples that might have become contaminated. The 'cracks' show very different REE patterns which are flatter ($[La/Ce]_N = 1.3$) due to the higher concentration of

LREE. Therefore the few garnet analyses that showed a slight kick to higher La values were deemed to be contaminated and were rejected.

Opx crystals were also analysed by LA-ICP-MS but the concentrations were close to limit of quantification for a number of elements. The trace element patterns that can be plotted show flat REE concentrations with a slight peak in Th and U (Fig. 3.8(b)).

Cpx shows a limited variation in $^{87}Rb/^{86}Sr$ from less than 0.001 to 0.012 with an average of 0.003 (Fig. 3.5.). These values are within a similar range to $^{87}Rb/^{86}Sr$ values for cpx mineral separates from MARID suite xenoliths from Bultfontein which show a range in $^{87}Rb/^{86}Sr$ from 0.005 to 0.0291 (Kramers et al. 1983). The garnet samples on the other hand show a wider range in $^{87}Rb/^{86}Sr$ from 0.051 to 0.329, consistent with other analyses of garnet mineral separates from Kaapvaal mantle xenoliths, which show a range from 0.035 to 1.095 (Basu and Tatsumoto 1980; Richardson et al. 1985; Erlank et al. 1987; Gunther and Jagoutz 1994; Simon et al. 2003; Bedini et al. 2004; Simon et al. 2008)

The small range observed in $^{87}Rb/^{86}Sr$ is not reflected in the $^{87}Sr/^{86}Sr_i$ values for the cpx from this sample (Fig. 3.5.). The drilled and picked cpx crystals both show a wide range in $^{87}Sr/^{86}Sr_i$ from 0.703389 to 0.705856. The broad range in $^{87}Sr/^{86}Sr_i$ of the cpx mineral separates from mantle xenoliths brought to the surface in kimberlites from across the Kaapvaal craton which show a range from 0.702257 to 0.708301 (Basu and Tatsumoto 1980; Richardson et al. 1985;

Erlank et al. 1987; Gunther and Jagoutz 1994; Pearson et al. 1995a; Simon et al. 2003; Bedini et al. 2004; Simon et al. 2008). The sampled cpx from this xenolith is therefore well within this overall range but displays a large proportion of it from a single sample. Despite the large variation in $^{87}Sr/^{86}Sr_i$ among the Bultfontein xenolith cpx there is no isochronous relationship.

The cpx from this sample shows a range of $^{143}Nd/^{144}Nd_i$ of 0.512425 and 0.512565 which is within the range previously reported for cpx analysed from Bultfontein mantle xenoliths (Richardson et al. 1985; Simon et al. 2008). Garnet shows a range in $^{143}Nd/^{144}Nd_i$ from 0.512210 and 0.512579 (Fig. 3.7.). There is no isochronous relationship between the cpx and garnet.

3.4.3. LESOTHO GARNET LHERZOLITE (M9)

A small number of cpx crystals were analysed from M9 (Simon et al. 2003; Simon et al. 2008) that showed a range in $^{87}Rb/^{86}Sr$ from 0.001 to 0.007 and, in contrast to the JMK, a very limited range in $^{87}Sr/^{86}Sr_i$ from 0.703434 to 0.704209 (Fig. 3.5.).

3.4.4. GREENLAND GARNET LHERZOLITE (G-06-07Z)

In-situ analyses of cpx show that, as with most on-craton peridotites (Shimizu 1975; Pearson et al. 2003), cpx is LREE enriched with $[La/Yb]_N$ ratios ranging from 20 to 50 reflecting a range in La concentrations (Fig. 3.9.). This cpx,

unlike the cpx from Bultfontein, has a relatively flat chondrite normalised REE pattern from La through to Nd (average $[La/Nd]_N$ = 0.8). The REE patterns from both the picked and drilled cpx show the same range as do those analysed by LA-ICP-MS (Fig. 3.9.). The multi-element plots show no negative Zr-Hf anomalies. The trace element patterns of the cpx from this xenolith are consistent with each other but there is some scatter in concentrations with Sr, for example, ranging from 162ppm to 200ppm. This is smaller than the range observed in the cpx from Bultfontein but may partly be attributed to fewer crystals being analysed from Greenland. Another significant different between the cpx from these two localities is that the cpx from Greenland has significantly higher Rb concentrations, ranging up to 0.1ppm (compared to values an order of magnitude lower in the Bultfontein sample).

The bulk garnet analyses and those analysed by LA-ICP-MS show the same LREE depleted patterns with $[La/Yb]_N$ ratios ranging from 0.001 to 0.02. This variation can be attributed to the range in La values as opposed to a range in Yb ratios. The picked garnet shows a more restricted range than the *in-situ* garnet analyses but this is probably because only two garnets were picked compared to 13 LA analyses made. There was no consistent variation in trace element concentrations between the core and rim analyses.

The Greenland garnet multi-element patterns were also filtered for contamination using the analyses of kelyphite from the Bultfontein sample. Only one garnet analysis was found to have anomalously high LREE abundances and was rejected.

Cpx from the Greenland garnet lherzolite shows elevated $^{87}Rb/^{86}Sr$ values, ranging from 0.006 to 0.029 (Fig. 3.6.), when compared with the cpx from Bultfontein and other localities (Richardson et al. 1985; Pearson 1999). However, the elevated Rb concentrations are confirmed by all three methods used to analyse the cpx and were also found by Wittig et al. (2008) for cpx from Greenland xenoliths suites. The two garnet analyses show different $^{87}Rb/^{86}Sr$ values of 0.102 and 0.588 which, as with the cpx, are elevated when compared to the $^{87}Rb/^{86}Sr$ values for the garnet from Bultfontein (Fig. 3.6.).

The range in initial $^{87}Sr/^{86}Sr$ observed in the cpx is much more limited and less radiogenic (0.703020 to 0.703522, n=13) than that observed for the Bultfontein xenolith (JMK; Fig. 3.6.). These values, however, are more typical of global mantle cpx (Pearson 1999).

Two garnet separates were analysed from the garnet lherzolite and the initial $^{87}Sr/^{86}Sr$ ratios are 0.708749 (±0.000020) and 0.707849 (±0.000033). These are more radiogenic than the garnet analyses from Bultfontein but, as with the Bultfontein xenolith they show no correlation with Rb/Sr values.

Nd isotope data are sparse for this xenolith as the sample is much smaller and the cpx and garnet are less abundant. The one cpx analysis has an $^{143}Nd/^{144}Nd_i$ of 0.511995 and the single garnet analysis is 0.512594 (Fig. 3.7.). These two points do not define an isochron with a reasonable age.

3.4.5. GREENLAND SPINEL LHERZOLITE (G-06-07Y)

Picked cpx fragments from a spinel lherzolite show higher $^{87}Rb/^{86}Sr$ ratios than the garnet lherzolite from the same locality, ranging from 0.015 to 0.056. This can be attributed to the lack of garnet, which preferentially partitions the Rb over the cpx (Blundy and Dalton 2000). The cpx was also found to be more radiogenic than the garnet lherzolite, with a range in initial $^{87}Sr/^{86}Sr$ from 0.703559 to 0.703953. There is no isochronous relationship observed among the cpx (Fig. 3.6.).

3.5. DISCUSSION

3.5.1. EVIDENCE FOR METASOMATIC ADDITION OF CPX AND GARNET

3.5.1.1. Initial mineralogy of the depleted residua

Olivine Mg number, less susceptible to the effects of cryptic and modal metasomatism than whole rock Mg-Al-Si (e.g. Herzberg 2004), is one of the more reliable proxies used to quantify the degree of melt extraction experienced by the Archean lithospheric mantle (Bernstein et al. 2006). The range of global olivine Mg numbers for cratonic peridotites is relatively small, with an average of 92.6, corresponding to approximately 35% melt extraction (Bernstein et al.

2006), with the upper limits of the range indicating melt removal of up to 40 or even 50% (Pearson and Wittig 2008). Although Fe addition, via cryptic metasomatism, can lower olivine Mg numbers and partly mask the melting signature (Danchin 1979; Griffin et al. 2003) these estimates are thought to be reliable on a global scale and are consistent with depletion estimates of more than 30% from other proxies such as HREE abundances (Pearson and Wittig 2008).

The average Mg number of olivine in the Bultfontein peridotite xenolith is 91.6, indicating melt depletion of approximately 30%, which is towards the lower end of the range for typical low-T Kaapvaal peridotites. This indicates that there has possibly been a small degree of cryptic metasomatism affecting the olivine in this sample.

The xenolith from Greenland however shows more evidence of cryptic metasomatism as the olivine Mg number is 89.6, considerably lower than the average for NAC peridotites of 92.2 (Pearson and Wittig 2008). This average corresponds to 30% to 40% melt extraction (Bizzarro and Stevenson 2003; Bernstein et al. 2007; Pearson and Wittig 2008). However Wittig et al (2008) did identify a large spread in olivine Mg numbers in NAC peridotites, from 83 to 93 (Pearson and Wittig 2008). This indicates that while the majority of NAC xenoliths have been minimally affected by metasomatism, a small subset may reflect significant interaction of the depleted lithospheric mantle with Archean high-FeO mafic or ultramafic melts which would be capable of crystallising

olivine with Mg numbers as low as 86 (Bizzarro and Stevenson 2003; Wittig et al. 2008).

To establish the amount of residual cpx and garnet that should remain following initial melt extraction in cratonic peridotites, it is important to determine at what pressure the melting takes place. There is significant evidence from HREE abundances that the majority of this melt extraction from the lithospheric mantle is shallow, occurring at around 3GPa (Kelemen et al. 1998; Canil 2004; Wittig et al. 2008). Although this is the general consensus, some authors propose, based on Fe contents, that the depth of melting starts much deeper, in a plume-related setting (Aulbach et al. 2007; Griffin et al. 2009). For shallow melting, at the depletion levels indicated for the Bultfontein xenolith, then garnet and cpx are over-represented as melting experiments show that cpx and garnet are both exhausted after about 10 to 23% melting (Walter 1998). However if the melting was initiated at a greater depth, at 7GPa for example, then cpx is exhausted by about 38 to 46% melting but garnet persists to 60 to 65% melting (Walter 1998). In this study we consider the evidence for deep melting to be equivocal because the low bulk Fe contents of cratonic peridotites can be lowered by opx addition (Lee 2004; Simon et al. 2008).

3.5.1.2. Metasomatic versus exsolution origin for cpx and garnet

If the cpx and garnet in typical cratonic peridotites is not residual then it must have been added by a later process. Two such processes are commonly cited: exsolution from opx and modal metasomatism. The exsolution hypothesis is

based on the observation that there is often a close spatial relationship among opx, cpx and garnet (Cox et al. 1987; Canil 1992; Saltzer et al. 2001). However, as discussed in the introduction (Fig. 2), there is no correlation between the modal abundance of opx with garnet+cpx for a database of peridotite xenoliths from the Kaapvaal craton and the NAC (see caption for references). This relationship is particularly poor for the NAC where opx is significantly less modally abundant and therefore these peridotites should, if exsolution is a dominant process, have significantly lower cpx and garnet abundances. This is not the case (Fig. 3.2.).

The mass balance for the peridotites presented in this study, especially for the Bultfontein sample, would require a very large modal abundance of opx in the residue in order to generate the observed cpx and garnet abundances. Simple modelling of the opx-cpx solvus, for example, suggests that high-T opx would exsolve approximately 8% cpx, by mass, on cooling from 1650ºC to 1400ºC (Brey and Huth 1984; Walter 1998). Therefore a modal abundance of 89% high-T opx would be required in the bulk rock residue to generate the observed abundance of cpx in the Bultfontein peridotite merely by exsolution. A high-T opx abundance of 75% is required to generate the observed cpx by exsolution in the Greenland xenolith. These estimates are clearly unrealistic and incompatible with predictions from melting experiments that indicate that after 30 to 40% melt extraction there would be between 15 and 30% opx remaining (Walter 1998). A further problem with deriving either cpx or garnet from exsolution of opx is that opx has relatively low trace element abundances, especially the REE, as during melting most trace elements are incompatible

(partition coefficients range from 0.0003 for La to 0.114 for Lu (Schwandt and McKay 1998)). It is therefore unlikely that exsolution of cpx and garnet from opx would generate the incompatible enriched trace element patterns observed in these minerals from either locality (Simon et al. 2003). Therefore we conclude that although exsolution of garnet and cpx from opx is a process that occurs in the lithospheric mantle, it is not the dominant mechanism by which cpx and garnet are generated in these samples.

The alternative origin for the cpx and garnet in cratonic peridotites is a metasomatic origin where these phases have crystallised from a percolating metasomatic melt (Erlank et al. 1987; Shimizu et al. 1997a; van Achterbergh et al. 2001; Pearson and Nowell 2002; Gregoire et al. 2003; Simon et al. 2003; Burgess and Harte 2004; Simon et al. 2008). It has been noted in previous studies that cpx that has undergone melt depletion will be LREE depleted whereas the majority of cpx from cratonic mantle xenoliths are LREE-enriched (Shimizu 1975; Pearson and Nowell 2002). Although this LREE enrichment could be the result of recent overprinting of pre-existing depleted cpx this would be expected to result in zoning which is not observed. Therefore the trace element patterns observed in the cpx from Greenland and Bultfontein are consistent with those that would be expected if the cpx had crystallised from a metasomatic melt.

3.5.2. RELATIVE TIMING OF CPX AND GARNET ADDITION

3.5.2.1. Controls on trace element and isotopic equilibrium

In order to assess the timing of garnet and cpx addition to the lithospheric mantle it is first important to understand whether these minerals crystallised together or in different events. In the simplest scenario, both minerals would crystallise at the same time from a single melt. If this is the case then it would be expected that both the garnet and cpx would be in equilibrium both, in terms of their trace elements and isotopic ratios (Shimizu et al. 1997b; Pearson 1999; Simon et al. 2003). Trace element equilibrium can be assessed by examining the partition coefficients between the garnet and cpx and comparing these to experimentally determined values (e.g. Simon et al. 2003). These relationships may be complicated by later cryptic effects but as both phases would experience the same history the trace elements should re-equilibrate, although this is dependant on the diffusivities of individual elements.

The assessment of isotopic equilibrium is less straightforward than that of trace element equilibrium. In theory, if both the cpx and garnet crystallise at the same time and from the same melt, the two minerals should, at the time of crystallisation, have the same isotopic composition as the melt. Once the temperature of the system drops below the blocking temperature, radiogenic decay products will cease to be lost by diffusion and, in the case of Sr, garnet (with a higher Rb/Sr ratio) will become significantly more radiogenic with time

whereas the cpx (with very low Rb/Sr) will only become slightly more radiogenic in its $^{87}Sr/^{86}Sr$ ratio. These two should then define an isochron that reflects the timing of decrease below the blocking temperature. Bedini et al. (2004) have suggested a more complex scenario that depends on different element diffusivities. These authors studied Sm-Nd and Lu-Hf systematics in cpx and garnet from low temperature garnet peridotite xenoliths from South Africa. These data revealed that both the Sm-Nd and Lu-Hf systems remain open under the thermal conditions of the lithospheric mantle and there is evidence for continuous diffusion of radiogenic Nd and Hf out of the garnet through intergranular exchange to surrounding mineral phases or fluid. Slower diffusing cations, in this case Hf, will record older ages than faster diffusing cations, such as Nd. This decoupling of Hf from Nd is more noticeable in garnets than in pyroxene (Bedini et al. 2004). The study of Bedini et al. (2004) did not extend to the Rb-Sr system but as Sr diffusivities are higher than those for Nd it is assumed that this system will also be 'leaky'. It is therefore difficult to use these systems to constrain the age of metasomatism in the lithospheric mantle and any mineral isochrons must be interpreted with caution.

Despite the complexities introduced by the concept of 'leaky chronometers', a number of studies have found that Rb-Sr and Sm-Nd two and three mineral isochrons that appear to record geologically meaningful ages. In these cases it is the age of eruption of the volcanic host that bought the xenolith to the surface (Richardson et al. 1985; Walker et al. 1989; Pearson et al. 1995b; Pearson 1999). If the concept of leaky chronometer in the lithosphere is valid, then these isochrons that reflect the eruption age must either mean that both/all minerals

formed together, immediately prior to eruption, from the same/similar melts or, that a melt associated with the host volcanism totally overprinted all minerals analysed and re-set the isotope clock.

Other examples indicate that the cpx and garnet were added at different times and this would have different implications for the trace element and isotopic equilibration (Gunther and Jagoutz 1994). The time over which the two minerals would equilibrate is dependant on the diffusivity of the trace element in garnet and cpx. Diffusivities are strongly dependant on temperature and vary according to crystallographic direction. Sr diffusivities have been calculated for the fastest axis of diffusion for both garnet and cpx (Sneeringer et al. 1984; Shimizu and Sobolev 1995). Diffusivities are typically of the order of $1x10^{-16}cms^{-1}$ at 1000ºC and 20kbar in cpx (Sneeringer et al. 1984) and $4.4x10^{-17}cms^{-1}$ in garnet, at 1000ºC (Shimizu and Sobolev 1995). The samples studied here both equilibrated in terms of rapidly diffusing major elements, at around 1000ºC and therefore it is possible to calculate how long it would take for cpx and garnet to equilibrate using Fick's Law ($x = \sqrt{Dt}$ where t=time, D=diffusivity, x=distance). For example, if the distance between the cores of the cpx and garnet crystals is 1cm, then Sr concentrations should completely equilibrate between the two phases in the order of 200Ma (Sneeringer et al. 1984; Shimizu and Sobolev 1995). Isotopic diffusion, or self-diffusion, is thought to occur an order of magnitude faster than trace element diffusion (Bedini et al. 2004) and therefore isotopic equilibrium should be reached in approximately tens of millions and years.

3.5.2.2. Inter-mineral trace element equilibration in the Bultfontein and Greenland peridotite xenoliths

The partition coefficients between adjacent cpx and garnet crystals have been calculated for a suite of trace elements using the laser ablation data in order that rim measurements could be compared (Fig. 3.10.). The data were compared with a set of natural partition coefficients calculated from a well-equilibrated garnet pyroxenite from Kakanui, New Zealand (Zack et al. 1997). These partition coefficients are similar to others taken from different suites that include peridotite (Hauri et al. 1994; Glaser et al. 1997; Eggins et al. 1998; Green et al. 2000); but were chosen because the equilibration conditions, 920ºC (Zack et al. 1997), are similar, in terms of temperature, to those observed at both Bultfontein, 1150ºC, and Greenland, 947ºC. The main difference between the samples presented here and the garnet pyroxenite is that the pyroxenite contains amphibole. This may therefore be expected to lead to some discrepancies between the two sets of garnet-cpx partition coefficients in terms of Nb (Ionov et al. 2002).

The cpx and garnet in the Bultfontein peridotite show a range of inter-mineral partition coefficients that are plotted to show the relative percent difference compared to those observed by Zack et al. (1997). There are some significant differences in terms of the calculated partition coefficients for Nb, U and Th but these may be attributed to the presence of amphibole in the pyroxenite. The largest relative percentage difference observed in the calculated partition coefficients for the REE is for the HREE (e.g. mean percentage difference for

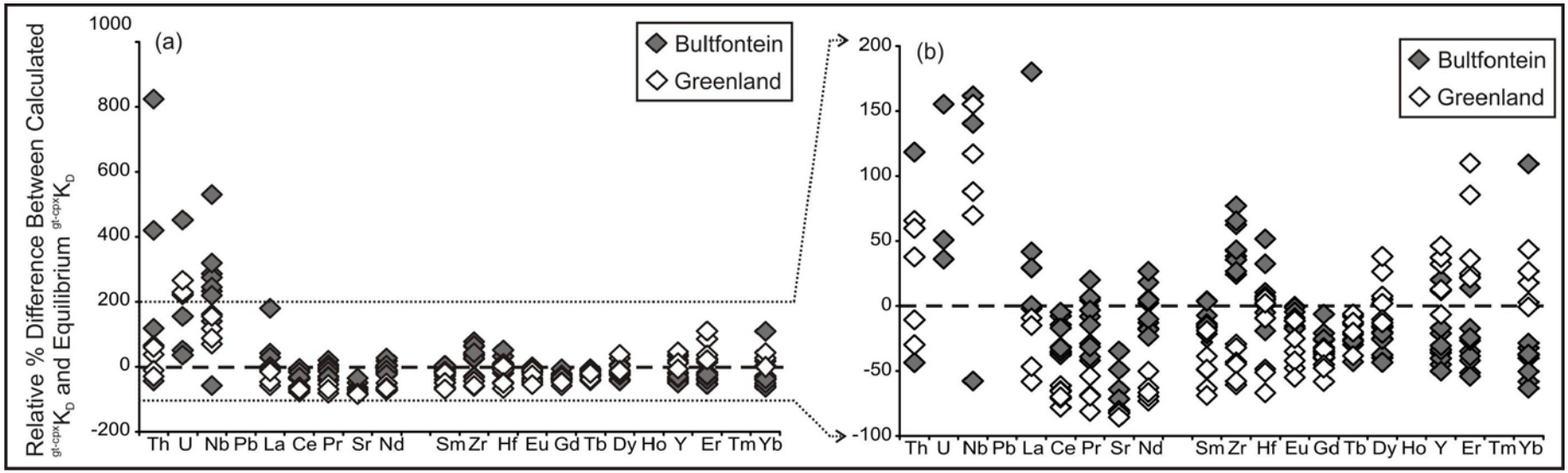

Figure 3.10.

(a) *The relative percentage difference between the calculated partition coefficients for adjacent cpx and garnet crystals (using laser ablation data) and equilibrium partition coefficients (Zack et al. 1997) for a range of elements for xenoliths from both locations.*

(b) *A more detailed plot of the same data within the range outlined by the dashed lines in (a).*

Yb is -42%). It is also important to note that there are significant differences in the garnet-cpx partition coefficients for Sr with a mean $^{gt\text{-}cpx}D_{Sr}$ of 0.002 for Bultfontein compared to 0.005 for Zack et al (1997). These relationships mimic those found by Simon et al. (2003)

The partitioning of trace elements between cpx and garnet in the garnet lherzolite from Greenland are less equilibrated than those from Bultfontein as they show a larger deviation from those in Zack et al. (1997; Fig. 3.10.). There are distinct differences in the slope of the REE with a mean $[D_{Ce}/D_{Yb}]$ of $3.6x10^{-4}$ compared to $1.37x10^{-3}$ from Zack et al. (1997). There are also significant differences in the LREE partitioning between the garnet and cpx, with the mean $^{gt\text{-}cpx}D_{Ce}$ for Bultfontein being 0.008 compared to 0.025 for Zack et al. (1997). The Greenland lherzolite minerals are even further out of equilibrium than those from Bultfontein in terms of Sr, with the mean $^{gt\text{-}cpx}D_{Sr}$ being 0.001 compared to 0.005 for Zack et al. (1997). However, despite this trace element disequilibrium, the lack of major element zoning indicates that the major elements have more closely approved equilibrium (section 3.2.4); probably due to higher diffusivities for major element cations.

The calculated cpx-garnet partition coefficients suggest that the two garnet lherzolites we have studied have experienced differing degrees of trace element equilibration. The cpx and garnet in the Greenland lherzolite are less equilibrated than those in the sample from Bultfontein. This may partly be attributed to the lack of direct contact between the cpx and garnet in the garnet lherzolite from Greenland and thus diffusion distances are much greater. The

lack of trace element equilibration in both samples suggests that the cpx and garnet cannot have been added at the same time from one melt, as this should result in trace element equilibration. The apparent disequilibrium therefore suggests that either the cpx and garnet were added by different melts at different times or that the disequilibrium is caused by the melt composition changing due to chromatographic effects (e.g. Burgess and Harte 2004). The latter is unlikely as these minerals are spatially related and it is unlikely that chromatographic effects would fractionate trace element ratios over a millimetre scale. The trace element measurements were made on the rims of crystals and were less than 1mm apart. Using Fick's Law and a conservative distance of 2 mm (1mm in the garnet and 1mm in the cpx) then the Sr should have equilibrated in approximately 10Myr by solid state diffusion, even if they were initially not in equilibrium. This implies that at least one of the phases is a recent addition to the mantle, added within less than 10Myr of being entrained in the kimberlite.

3.5.2.3. Isotopic equilibration in the Bultfontein and Greenland xenoliths

In order to assess the isotopic equilibration of the cpx and garnet in these samples we have plotted two mineral isochrons for both the Sr and Nd isotope systems from adjacent garnet and cpx crystals (Fig. 3.11. and Table 3.1.). The cpx and garnet were picked as chips from a $1cm^2$ section of a polished slab of each of the garnet lherzolite samples, containing only one garnet. This ensured that the garnet and cpx would be spatially related and thus be more likely to be in equilibrium.

The cpx and garnet from the Bultfontein lherzolite were closer to trace element equilibration than those in the Greenland lherzolite which would imply that this sample is more likely to have approached inter-mineral isotopic equilibrium. However Sr and Nd two mineral isochrons do not give consistent ages for the same, adjacent, garnet-cpx pair (Fig. 3.11., Table 3.1.). The Sm-Nd and Rb-Sr systems both give implausible two point isochron ages, 63Ma (younger than the 90Ma eruption age) and 5633Ma (greater than the age of the earth) respectively (Fig. 3.11.; Table. 3.1.). This same relationship is seen for all the garnet and cpx pairs where an age was determined for both isotope systems. This therefore suggests significant dis-equilibrium within the isotope systematics of these two minerals. A similar lack of isotopic equilibrium has been observed in peridotite xenoliths from Lesotho (Richardson et al. 1985; Simon et al. 2008), for example, where negative 'isochrons' have also been observed (Richardson et al. 1985; Simon et al. 2008). There is no correlation between the isotopic ratio of the garnets (the dominant control on 'age') and Sr or Nd concentrations, ruling out a simple mixing relationship between two melts for instance.

There are a number of possible explanations for why the cpx and garnet are not in isotopic equilibrium. Richardson et al. (1985) observed negative isochronous relationships in a coarse, phlogopite-bearing garnet-spinel lherzolite from Lesotho. Richardson et al. (1985) suggested that these isochronous relationships were generated by a late addition of an exotic metasomatic component without isotopic equilibration. This could explain the isotopic relationships observed here. However, this model assumes pre-existing garnet

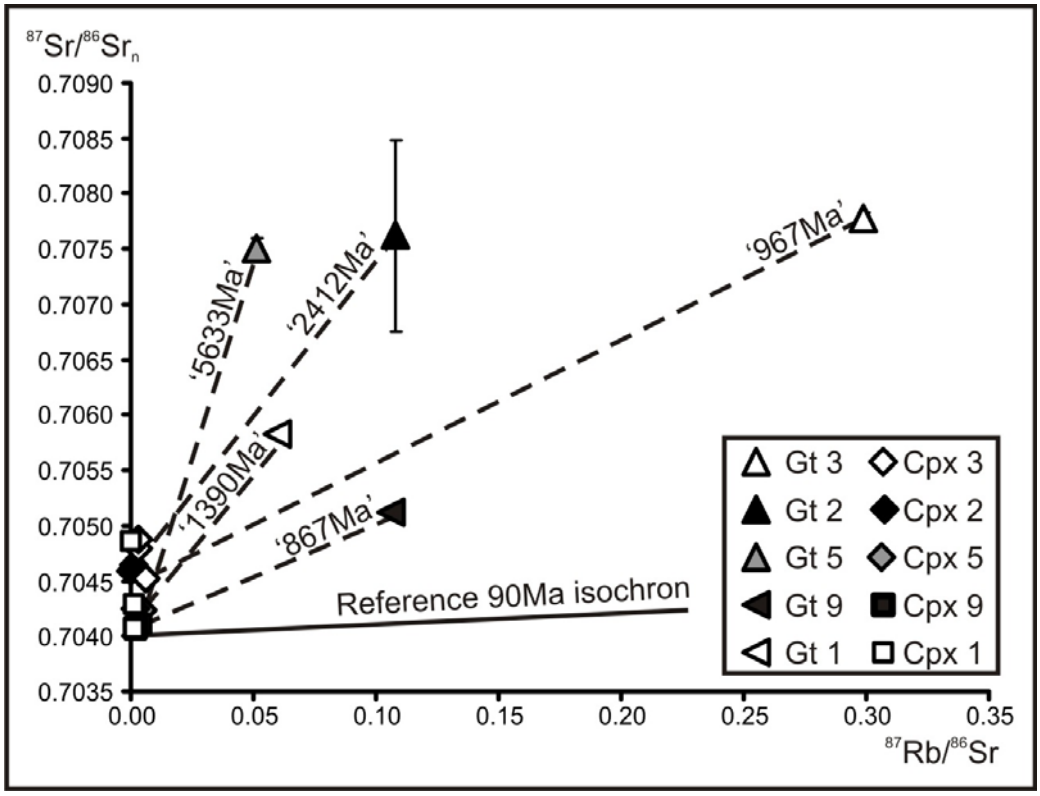

Figure 3.11.

An 'isochron plot' of the measured $^{87}Sr/^{86}Sr$ ratios against $^{87}Rb/^{86}Sr$ for adjacent garnet and cpx pairs with the 'age' labelled on the tie line.

	Kimberlite age (Ma)	Cpx-Gt Rb-Sr 'age' (Ma)		Cpx- Gt Sm-Nd 'age' (Ma)	
Bultfontein					
Gt 1	90	1390	±44		
Gt 2	90	2412	±705	139	±53
Gt 3	90	967	±19		
Gt 5	90	5633	±207	63	±70
Gt 9	90	867	±33		
Greenland					
G-06-07	164	748	±5		

Table 3.1.

Table of the two mineral isochron 'ages' for adjacent cpx and garnet crystals for both the Rb-Sr and Sm-Nd systems for the garnet lherzolite xenoliths from Bultfontein (JMK) and Greenland (G-06-07Z). The ages from the Bultfontein garnet lherzolite are all from within the same xenolith.

and cpx, perhaps as residual phases and hence cannot explain the over – abundance of these mineral phases in depleted rocks. An alternative explanation is proposed by Gunther and Jagoutz (1994) which suggests that the inverse cpx-garnet isochrons in Kimberley xenoliths could be attributed to the garnets forming from a precursor mineral with a lower Sm/Nd ratio, such as amphibole. The garnet would therefore inherit the unradiogenic Nd isotope ratio of this phase. However in the Bultfontein peridotite studied here the Nd isotope ratios of the garnets are more radiogenic than the cpx unlike the sample studied by Gunther and Jagoutz (1994). The explanation preferred, on the basis of the data presented here, is that the cpx and garnet were added at different times during different melt infiltration events with the cpx being a more recent addition. Isotopic equilibrium through 'self-diffusion' between the cores of adjacent minerals is thought to be an order of magnitude faster than trace element equilibration. Therefore the Sr isotopic dis-equilibrium between adjacent cpx and garnet crystals cannot be preserved longer than approximately 20Myr (Sneeringer et al. 1984). This timescale is further reduced to less than 10Myr if only Sr isotopic equilibration between adjacent cpx crystals is considered because diffusion rates are faster in cpx. This would therefore imply that the isotopic variation observed in the cpx could not persist for longer than about 10Myr before inclusion in the kimberlite, supporting a recent origin for the cpx.

The Sr isotope compositions for the cpx do provide some indication of a recent origin. The measured initial Sr isotope ratios are within the range observed in present day OIBs and are therefore consistent with a recent convecting mantle

origin. In contrast, the garnet is much more radiogenic, suggesting significant in growth of radiogenic Sr and/or addition by a melt with a more exotic Sr isotope ratio. The negative (i.e. future) depleted mantle Nd model ages yields negative 'ages' for the garnets do not offer precise age information but are also indicative of a complex history that could involve crystallisation from a melt with enriched Nd isotope characteristics.

3.5.3. NATURE OF THE PARENTAL MELT COMPOSITION

The trace element and isotope data support the cpx and garnet, in both garnet lherzolites studied here, being added at different times by different melts. Trace element partitioning data can then be used in order to identify the parental melts that they crystallised from respectively. This technique relies on equilibration between the garnet or cpx and the melt. In the two garnet lherzolites the cpx and garnet have already been shown to be out of trace element equilibrium with each other and therefore it is implicit that there is also likely to be some misfit in solid-liquid equilibration. This therefore means that a perfect match between melts predicted using experimentally derived partition coefficients and natural melts is unlikely. A best fit approach will therefore be used. The isotope data can then be used to further constrain the source region of these melts as isotopes are not fractionated by magmatic processes. The addition of cpx, the most recent phase to crystallise, is considered first.

3.5.3.1. Cpx parental melt

The cpx is enriched in incompatible elements implying that the host melt was a small fraction melt. In order to identify the exact nature of this melt a range of partition coefficients for kimberlite (Keshav et al. 2005), carbonatite (Blundy and Dalton 2000; Adam and Green 2001; Klemme et al. 2002) and basalt (Hauri and Hart 1997) melts have been used (Fig. 3.12. and 3.13.). The resulting melts show both a range in trace element patterns and abundances that reflect the range in partition coefficients (Fig. 3.12.). This compositional dependence means that the absolute concentrations of the calculated melts cannot provide definitive constraints on the parent but the presence of absence of strong inter-element fractionation is likely to be more indicative. The calculated "equilibrium" melts have been compared to trace element patterns of kimberlites (Fig. 3.12(a); Le Roex et al. 2003), carbonatites (Fig. 3.12(b); Bizimis et al. 2003) and a typical ocean island basalt (Fig. 3.12(c); OIB; Sun and McDonough 1989). Carbonatite melts can be ruled out as possible parental melts in both localities as the cpx do not have the striking negative Zr-Hf anomaly seen in natural carbonatite or cpx formed from them (Hauri and Hart 1994). In addition the melt calculated, using carbonatite partition coefficients, has a large positive Sr anomaly which is not observed in trace element patterns in carbonatites (Fig. 3.12(b)). There is also a poor match between the calculated parental melt to cpx, using basalt partition coefficients, and the trace element patterns of OIB. The $[La/Yb]_N$ ratio of typical OIB (normalised to primitive mantle) is 12.3 (Sun and McDonough 1989) whereas the calculated "basalt" melt has an average $[La/Yb]_N$ ratio of 53.0 for the Bultfontein lherzolite and 269 for the Greenland lherzolite. There are additional differences in Zr and Hf

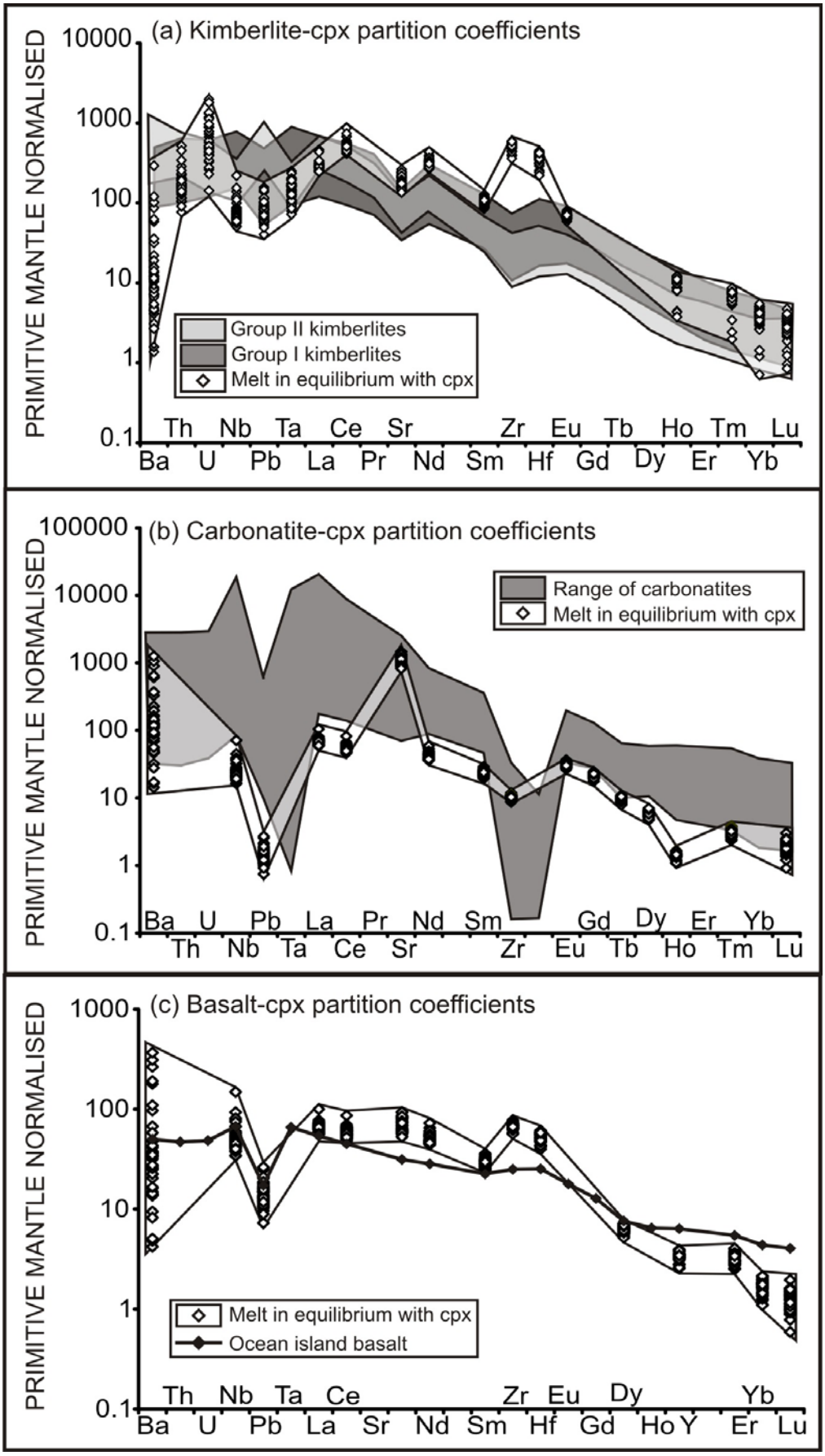

Figure 3.12. *(see overleaf)*

Figure 3.12.

(a) *Primitive mantle normalised (Sun and McDonough 1989) multi-element plot of the melts predicted to be in equilibrium with the cpx in the garnet lherzolite from Bultfontein (JMK) using kimberlite melt-cpx partition coefficients (Keshav et al. 2005). The fields of Group I and Group II kimberlites are shown for reference (Becker and Le Roex 2006).*

(b) *Primitive mantle normalised (Sun and McDonough 1989) multi-element plot of the melts predicted to be in equilibrium with the cpx in the garnet lherzolite from Bultfontein (JMK) using carbonatite melt-cpx partition coefficients (Blundy and Dalton 2000; Adam and Green 2001; Klemme et al. 2002). The fields of a range of naturally occurring carbonatites are shown for reference (Bizimis et al. 2003).*

(c) *Primitive mantle normalised (Sun and McDonough 1989) multi-element plot of the melts predicted to be in equilibrium with the cpx in the garnet lherzolite from Bultfontein (JMK) using basalt melt-cpx partition coefficients (Hauri and Hart 1997). A representative trace element pattern of an OIB basalt is shown for reference (Sun and McDonough 1989).*

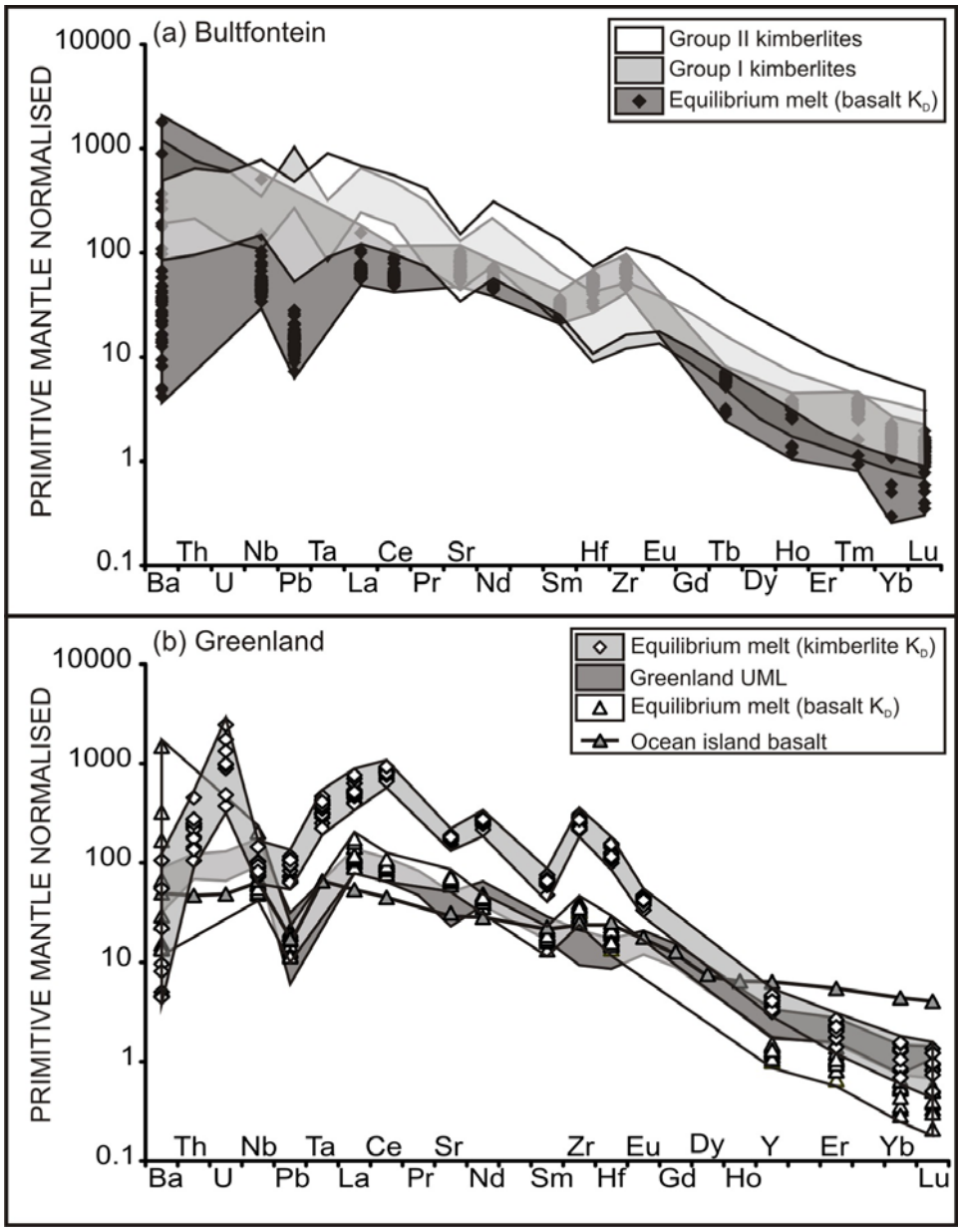

Figure 3.13.

(a) *Primitive mantle normalised (Sun and McDonough 1989) multi-element plot of melts predicted to be in equilibrium with cpx for the garnet lherzolite from Bultfontein (JMK) using basalt melt-cpx partition coefficients (Hauri and Hart 1997). Representative fields of Group I and Group II kimberlites (Becker and Le Roex 2006) from South Africa are shown for reference.*

(b) *Primitive mantle normalised (Sun and McDonough 1989) multi-element plot of melts predicted to be in equilibrium with cpx for the garnet lherzolite from Greenland (G-06-07) using basalt melt-cpx partition coefficients (Hauri and Hart 1997) and kimberlite melt-cpx partition coefficients (Keshav et al. 2005). Multi-element plots of the host Greenland UML are shown for reference along with a representative pattern from an OIB (Sun and McDonough 1989).*

which show a positive anomaly in the predicted melts whereas such anomalies are not observed in OIB trace element patterns.

A closer match is found between the range of kimberlite melts (or UML in the case of the Greenland xenolith) and the calculated melt parental to cpx using kimberlite partition coefficients (Fig. 3.12(a); Keshav et al. 2005). There are still discrepancies, such as the elevated Zr-Hf in the predicted melt that is not observed in kimberlites. However Hf and Zr are both slow diffusing cations and therefore take longer to reach equilibrium than other species. As such, small differences in the calculated and natural melts may not be significant. The REE are a better fit, with the average calculated melt for the Bultfontein cpx showing a $[La/Yb]_N$ ratio of 94.8. This compares closely to Group I kimberlites which have a wide range of $[La/Yb]_N$ ratios from 86.9 to 325.7. The calculated melt for the Greenland cpx which has an average $[La/Yb]_N$ ratio of 489.9 compared to 102 in the UML. Kimberlite trace element patterns are highly variable and can be influenced by incorporation of lithospheric mantle and crust which may explain some of the differences between the calculated and natural melt, especially HREE which are though to be elevated by crustal addition (Le Roex et al. 2003; Dowall 2004). It is also likely that the metasomatic melt will fractionate and evolve as it crystallises cpx and therefore this may also explain some of the discrepancies (Ionov et al. 2002; Burgess and Harte 2004). Partitioning experiments and equilibrium are difficult to achieve in carbonate and water-rich systems that may approximate to kimberlite melts and it is possible that partition coefficients derived for simple basalt systems are the most accurate. A closer fit between the calculated melts and natural kimberlites

is obtained using basalt partition coefficients to model the melt in equilibrium with the cpx (Fig. 3.13.). This provides a much closer fit with kimberlite trace element patterns for the Bultfontein cpx and with the host UML trace elements for the Greenland cpx. While recognising the problems of using equilibrium partition coefficients in estimating parental magmas it seems inescapable that the melt is probably a small degree melt of approximately kimberlite composition which is LREE-enriched with high La/Yb ratios. On this basis, kimberlite, or 'proto-kimberlite' magma (or UML in the case of Greenland), is the most likely melt that has recently "equilibrated" with the cpx.

The range in Sr isotope values observed in the cpx from the Bultfontein lherzolite would be consistent with addition from a Group I kimberlite magma. This is supported by probability density function (PDF) plots of global cpx and Group I kimberlite Sr isotope ratios which show significant overlap (Fig. 3.14.). The $^{87}Sr/^{86}Sr_i$ values for the host Bultfontein kimberlite range from 0.703985 to 0.705370 (Becker and Le Roex 2006) which is within the range observed for the cpx. The Sr isotope ratio of the primary kimberlite magma is likely to be less radiogenic than the measured value, again due to incorporation of continental crust which increases the Sr isotope ratio of the magma (Mitchell 1986; Woodhead et al. 2009). The significant Sr isotope variation observed in cpx from the Bultfontein peridotite could be attributed to different generations of kimberlite magma that have interacted to differing extents with metasomatised lithosphere. The Kaapvaal craton has experienced has been Group I kimberlite activity since at least 1200Ma (Premier) and therefore cpx addition could be associated with any Group I kimberlite activity through the evolution of the

cratonic lithosphere. The evidence from the Bultfontein peridotites, however, points to a more recent origin which may be related to the host kimberlite.

The Greenland peridotite cpx show a very limited range in $^{87}Sr/^{86}Sr_i$ (0.703559 to 0.703953), compared to the Bultfontein cpx. The Greenland range is within the, also limited, range of the host UMLs (0.703454 to 0.703996). The small range of Sr isotope ratios observed in both the host rocks and the cpx from Greenland probably reflects the less metasomatised nature of the Greenland lithospheric mantle compared to the Kaapvaal lithosphere. The Greenland lithosphere therefore represents a simpler system and is probably more typical of lithospheric mantle throughout history than the Kaapvaal lithosphere (e.g. Bernstein et al. 2006; Wittig et al. 2008).

In summary the geochemical signatures of cpx from two studied lherzolites from both South Africa (Kaapvaal Craton) and Greenland (NAC) are consistent with addition of cpx from melts closely related to their host rocks.

3.5.3.2. Garnet parental melt

A combination of the trace element and Sr isotopic dis-equilibrium in the lherzolites from both the Kaapvaal craton and the NAC indicate that the two minerals have not formed together. The garnet may have interacted with more

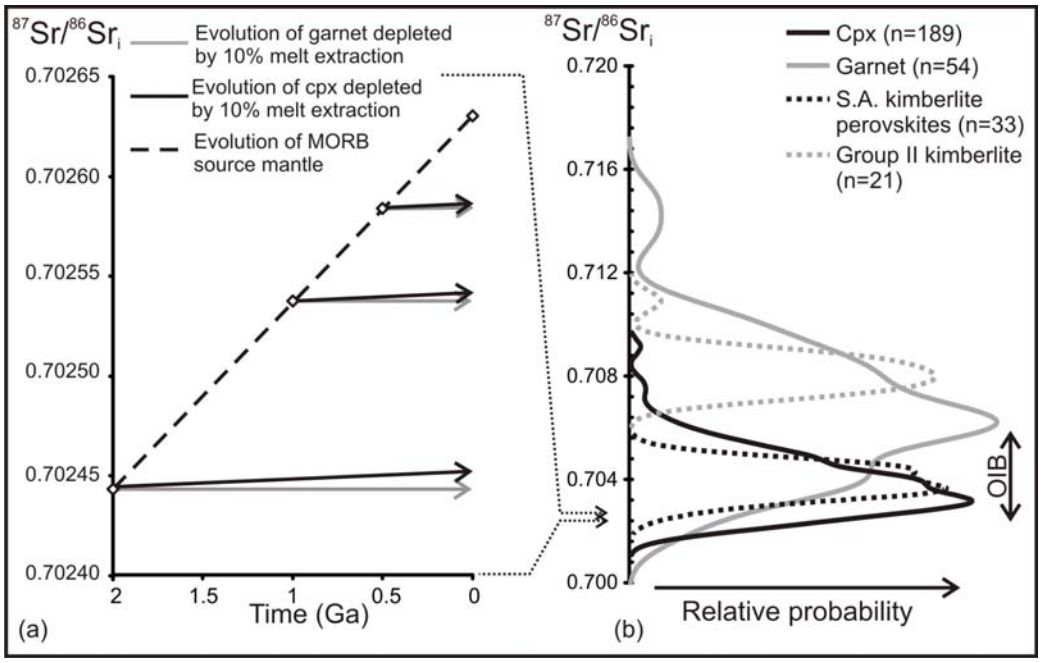

Figure. 3.14.

(a) *The modelled evolution of garnet (grey) and cpx (black) that is predicted for a residue, following melt depletion of a MORB-source mantle at 2Ga, 1Ga or 0.5Ga. The $^{87}Rb/^{86}Sr$ ratios are those predicted following 10% melt extraction (Hellebrand et al. 2002).*

(b) *A PDF plot of the observed $^{87}Sr/^{86}Sr_i$ ratios for cpx and garnet from on-craton settings (Richardson et al. 1985; Gunther and Jagoutz 1994; Pearson et al. 1995a; Pearson et al. 1995b; Schmidberger et al. 2001; Schmidberger et al. 2002; Bedini et al. 2004; Carlson et al. 2004; Simon et al. 2008; Klein-BenDavid and Pearson 2009) as well as those from Group I kimberlite groundmass perovskite (a better estimate of the primary kimberlite composition) and Group II kimberlites (Le Roex et al. 2003).*

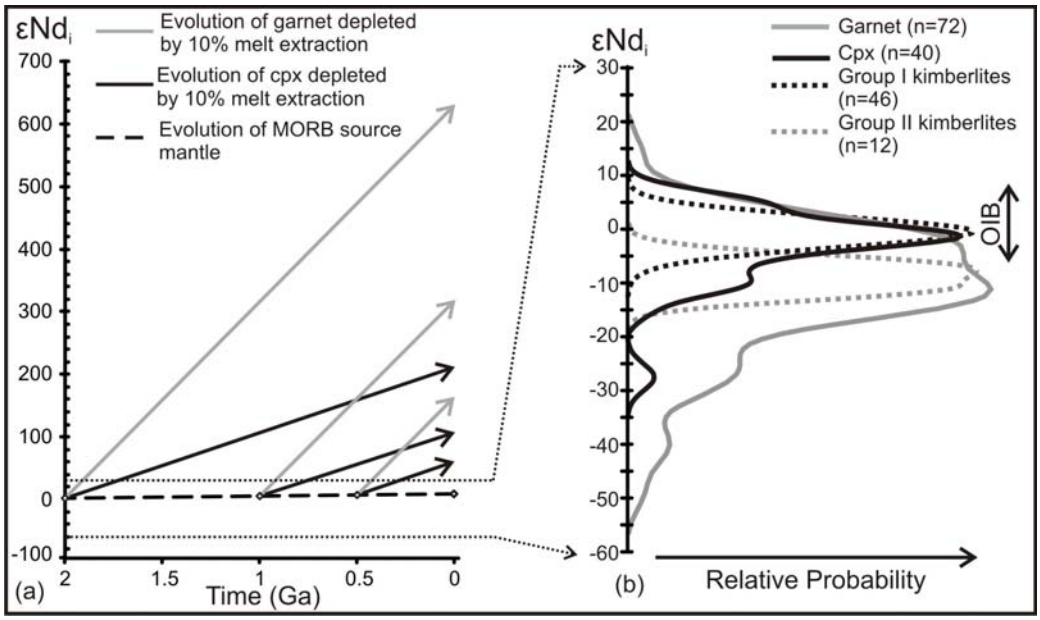

Figure. 3.15.

(a) *The modelled evolution of garnet (grey) and cpx (black) that predicted for a residue following melt depletion of a MORB-source mantle at 2Ga, 1Ga or 0.5Ga. The $^{147}Sm/^{143}Nd$ ratios are those predicted following 10% melt extraction (Hellebrand et al. 2002).*

(b) *A PDF plot of the observed εNd_i values for cpx and garnet from on-craton settings (Richardson et al. 1985; Gunther and Jagoutz 1994; Pearson et al. 1995a; Pearson et al. 1995b; Schmidberger et al. 2001; Schmidberger et al. 2002; Bedini et al. 2004; Carlson et al. 2004; Simon et al. 2008; Klein-BenDavid and Pearson 2009) as well as those from Group I and Group II kimberlites from South Africa (Le Roex et al. 2003).*

than one metasomatic melt which makes it difficult to use trace element compositions to establish the parental melt. This, as with the approach taken with the cpx, introduces some uncertainty to applying equilibrium partition coefficients to estimate melts. However the calculated trace element patterns are broadly consistent with each other implying that the garnets may have all been overprinted by a similar melt and indicating that a parental melt, or the last melt the garnet equilibrated with, must have been LREE-enriched using any set of partition coefficients.

Sr isotope compositions can be used to further constrain the origin of the garnet parental melt. Garnets in mantle xenoliths show a wide range of Sr isotopes but are typically more radiogenic than the co-existing cpx (Fig. 3.14.). This is partly the result of radiogenic in-growth due to the higher Rb/Sr ratios of garnet than cpx but this relationship is preserved when initial ratios are considered. Garnets from the Bultfontein xenolith show a wide range in $^{87}Sr/^{86}Sr_i$ that do not conform to an isochron (Fig. 3.11.). This isotope heterogeneity could suggest that they have been added by different melts at different times. It is also possible that they were added by the same melt that was either heterogeneous or that the garnets have subsequently been overprinted to differing extents by different melts. The low Sr contents of the garnets make them susceptible to such interaction. It is not possible using the data presented here to differentiate between these options. However, we note that no zoning in elemental concentrations is observed.

In the case of the Bultfontein xenoliths the Sr isotope ratios of the garnets (0.70498 to 0.70749) overlap with the lower end of the range of Group II kimberlites (0.7072 to 0.7109; Nowell et al. 2004; Becker and Le Roex 2006), Group II kimberlite magmatism predates the main phase of Cretaceous Group I kimberlite eruptions (including the Bultfontein host) in the Kaapvaal craton. The Group II kimberlites (sometimes referred to as orangeites; Mitchell 1986) have a significantly more radiogenic Sr isotope signature than the Group I, or basaltic, kimberlites (Nowell et al. 2004; Becker and Le Roex 2006). Group II kimberlites are thought to originate from sources within the mantle lithosphere that are enriched in minerals, such as phlogopite, derived from ancient metasomatism (Becker and Le Roex 2006; Coe et al. 2009; Woodhead et al. 2009). The radiogenic Sr isotope compositions of the Bultfontein garnets could therefore have been the result of crystallisation from melts related to Group II kimberlites. Evidence of the infiltration of Group II kimberlite melts beneath Bultfontein comes the presence of MARID xenoliths at Bultfontein that contain zircons yielding U-Pb ages of 120Ma, the age of Group II kimberlite magmatism (Konzett et al. 1998). Most of the Bultfontein garnets are less radiogenic than the Group II kimberlite range and this maybe because the whole rock kimberlite analyses are more radiogenic due to the incorporation of crust or due to partial re-equilibration of the garnet with later Group I kimberlite magmatism that crystallised the cpx. The significant range in $^{87}Sr/^{86}Sr$ observed in the garnets from the Bultfontein xenolith that is less than 10cm in diameter, indicates that overprinting from the recent Group I kimberlite magmatism may be heterogeneous.

No Group II kimberlite magmatism has been recorded in the crust at Greenland lamproites occur in West Greenland, intruded at 1374Ma, that have a range of $^{87}Sr/^{86}Sr_i$ from 0.70473 to 0.70615 (Tappe et al. 2007). If these values are forward modelled from their eruption age to the present day using $^{87}Rb/^{86}Sr$ measured in garnets from the Greenland peridotite (0.101 and 0.584), a range in garnet $^{87}Sr/^{86}Sr$ of 0.70674 to 0.717656 would result. This spans the measured $^{87}Sr/^{86}Sr$ values for the Greenland garnets and is a strong indication that the lamproite magmatism could have been responsible for the crystallisation of the garnets in the mantle lithosphere in the Proterozoic. However the trace element signature of the garnets has been overprinted more recently by the host kimberlite magma that crystallised the cpx prior to eruption.

3.6. IMPLICATIONS

3.6.1. CRATONIC MANTLE EVOLUTION

The evidence presented here outlines a complex evolution for the lithospheric mantle sampled by kimberlitic melts. This sequence starts with highly depleted cratonic lithosphere (Bernstein et al. 2007) that is converted to harzburgite by the addition of opx (Kelemen et al. 1992; Rudnick et al. 1994; Kelemen et al. 1998) probably during the Archean (Fig 16 A ; Simon et al. 2008). Alternatively, opx could be added by "autometasomatism" due to the production of Si-rich fluids during melting (Pearson and Wittig 2008). The extent of the

opx addition varies and seems most intense in the lithosphere beneath the Kaapvaal craton and least intense in the still largely dunitic NAC (Fig. 3.15.).

The resulting harzburgites then experience garnet addition by infiltration of lamproite/Group II kimberlite melts (Fig. 3.16.). These additions occur at different times associated with their respective magmas (Fig. 3.16.). This suggests that globally the process of garnet addition is heterogeneous and location specific, depending on the activity and mobility of enriched, small degree lithospheric melts.

The cpx is then a recent addition to the garnet harzburgite, associated with the host magma (Fig. 15; Shimizu et al. 1997b) and converts harzburgite to lherzolite, as proposed by van Achterbergh et al. (2002), Pearson and Nowell (2002), Simon et al. (2003) and Gregoire et al. (2003). The parental melt to cpx in kimberlite magma in the case of the lherzolites from the Kaapvaal craton, and is an UML magma in the case of peridotites from NAC. The addition of both garnet and cpx is thought to occur through melt-wallrock reactions (e.g. Foley 1992) and therefore is only associated with the melt veins leading to a localised distribution as oppose to wholesale alteration of the lithospheric mantle. The majority of the lithospheric mantle is likely to remain as depleted dunites or opx-enriched harzburgites in some cases (Bernstein et al. 2007).

We can now examine how widely applicable this model of cpx and garnet addition is. A global database of initial Sr and Nd isotope analyses has been

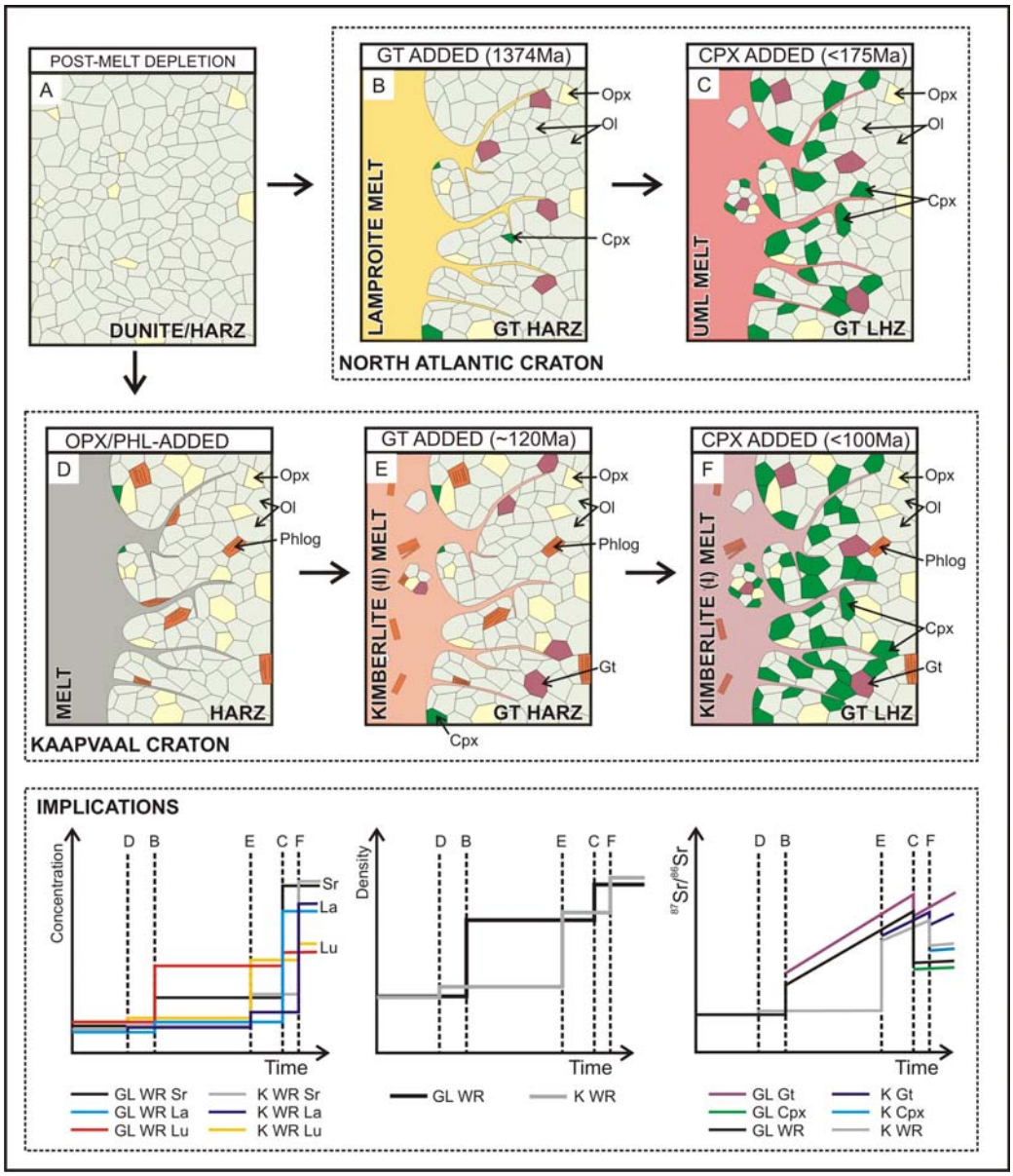

Figure 3.16. *(see overleaf)*

Figure 3.16.

Schematic diagram to summarise the mineralogical evolution of the lithospheric mantle in both the Kaapvaal craton (A, D, E, F) and the NAC (A, B, C) and the implications that would have on the fertility, density and Sr isotope evolution.

***(A)** A schematic image of the peridotite mantle after melt depletion. The majority of the lithospheric mantle is concluded to still be a depleted dunite/harzburgite (harz) residue.*

***(B)** Illustrates the addition of garnet to the NAC lithospheric mantle, potentially by a lamproite magma at 1374Ma. This addition is localised melt-wall rock reactions.*

***(C)** Illustrating the addition of cpx to the lithospheric mantle beneath the NAC by the UML magma, relatively recently (<175Ma). This addition is localised to melt-wallrock reactions and therefore only the peridotite immediately adjacent to the vein would be altered to a garnet lherzolite (gt lhz).*

***(D)** This illustrates the potential addition of opx and phlogopite (phlog) associated with an ancient metasomatic event. The extent of this metasomatism is unknown and beyond the scope of this paper. This has modified the peridotite lithospheric mantle from a depleted dunite/harz to a harz and is thought to affect different cratons to differing extents.*

***(E)** Illustrating the addition of garnet proposed to be by Group II kimberlite magma (~120Ma or associated with an earlier episode of activity). This addition is localised to melt-wall rock reactions and therefore has not affected the whole of the lithospheric mantle. This process may add minor amounts of cpx in some locations as well.*

***(F)** The most recent addition to lithospheric mantle peridotites in the Kaapvaal craton is cpx, related to the Group I kimberlite activity (<100Ma or associated with an earlier episode of activity).*

The bottom panel summarises the consequences of this evolution in modal mineralogy in terms of fertility (where the concentrations of different representative elements are plotted), density and the Sr isotope evolution of the garnet, cpx and the whole rock (WR).

compiled from cpx and garnet mineral separate data cratonic peridotites (Fig. 3.14. and 3.15.). These data have been plotted as probability density function plots (PDF) to illustrate the distribution of isotopic data (Fig. 3.14. and 3.15.). The PDF plots of the initial Sr and epsilon Nd ratios of bulk cpx separates show distinct and narrow peaks at $^{87}Sr/^{86}Sr$ of 0.7032 and εNd of 0. In both isotope systems, global cratonic cpx compositions are within the range observed for present day OIB and Group I kimberlite, supporting a recent origin from melts derived from the convecting mantle origin.

The Rb/Sr and Sm/Nd ratios of cpx from a peridotite that has experienced approximately 10% melt extraction have been modelled (Hellebrand et al. 2002) in order to predict the isotopic composition of depleted mantle cpx that would remain following melt extraction at a range of ages (Fig. 3.14. and 3.15.). Only moderate degrees of melt extraction have been modelled. These results indicate that, in the case of Sr, residual cpx would show a very limited range in Sr isotope compositions and while the low $^{87}Sr/^{86}Sr$ values of the depleted cpx fall within the mode of cratonic cpx, this model cannot explain the many values that are more radiogenic than 0.7027 (Fig. 3.14.). The modelling of Nd isotope evolution is even more revealing; and shows that if cpx was residual from as little as 10% melting, depending on the age, it would rapidly evolve, to increasingly positive epsilon Nd values, up to +213 (Fig. 3.15.; if the melt was extracted at 2Ga). This is inconsistent with observations as the range in epsilon Nd in cpx from cratonic lherzolites is very limited, with the vast majority of cpx plotting between +10 and -20. Some of the more elevated $^{87}Sr/^{86}Sr$ and low εNd values (less than -10) indicate either long-term enriched compositions, or

formation from melts originating from old enriched lithospheric sources, but the majority of cpx compositions can be explained by more recent formation, probably from melts associated with the host kimberlite.

Initial Sr and epsilon Nd data from garnet mineral separate data has been plotted in the same way as the cpx. A key observation is that the cpx and garnet, for both Sr and Nd, show different peak in the statistical distribution of their Sr and Nd initial isotope ratios. This implies that globally, as well as for the samples presented here, garnet and cpx are, in most cases, added by different events. There is some overlap in garnet and cpx isotope values indicating that either some garnet has been completely overprinted by melts that added the cpx, or that in some locations (e.g. where complete isotopic equilibration is observed), some garnet may have been added along with the cpx. The peaks in isotope composition for the garnet data ($^{87}Sr/^{86}Sr_i$=0.7062; epsilon Nd_i=-10) are broader than those for cpx and not as well defined. This suggests that garnet addition is more complex and, as with the two samples presented here, varies between different cratons. As with the cpx the initial Sr and epsilon Nd values of residual garnet remaining after 10% melt extraction at a range of ages has been plotted (Fig. 3.14. and 3.15.). This shows that, as with the cpx, the observed garnet values are not consistent with an ancient residual origin. The garnet compositions are much more easily reconciled by long-term evolution with low Sm/Nd and high Rb/Sr, or, via formation from melts originating from ancient enriched sources. Recently, Klein BenDavid and Pearson (2009) have identified some diamond-forming fluids as having very enriched Sr and Nd isotopic

compositions and have suggested that these may be significant metasomatic agents in the deeper lithosphere.

3.6.2. BULK COMPOSITION OF THE LITHOSPHERE AND ITS POTENTIAL AS A MAGMA SOURCE

The geochemical evolution of the lithosperic mantle is determined by the modal mineralogy. A harzburgitic residue, dominated by olivine and opx, remaining after melt extraction, would be extremely depleted in both major and trace elements (Fig. 3.16.). The addition of garnet, at different times depending on the craton concerned, would increase the relative fertility in some areas of the lithospheric mantle, in particular the HREE abundances would be increased, and to a lesser extent the LREE. As garnet would, in a garnet harzburgite, be the main host for Sr and Nd then the whole rock would be dominated by the isotopic composition of the garnet (Fig. 3.16.). However, even though the isotopic composition of some of these garnet-bearing peridotites are very enriched, the overall levels of incompatible elements is low, making them unlikely magma sources (Pearson and Nowell 2002). The recent addition of cpx would have the effect again increasing the relative fertility of the lithospheric mantle, especially in Sr and the LREE (Fig. 3.16.). The Sr budget, and to some extent the Nd budget, of the whole rock would be dominated by the cpx leading to a decrease in the Sr isotope ratio of the garnet lherzolite compared to the garnet harzburgite (Fig. 3.16.). Even in these re-fertilised lherzolites, overall incompatible element concentrations are generally less than primitive mantle values (Pearson and Nowell 2002).

The addition of garnet and cpx to the lithospheric mantle is likely to be localised to melt vein activity and therefore is not a wholesale alteration of the lithosphere. This therefore means that mantle xenolith and mineral concentrate data, brought up as inclusions in kimberlite or other magmas, may only represent the mantle immediately beneath the host volcanism. Hence caution should be exercised when extrapolating this data to the lithospheric mantle as a whole.

As pointed out by Pearson and Nowell (2002) lithospheric peridotite isotopic compositions are dominated by those similar to convecting mantle compositions, with many being similar to the MORB and OIB sources. Hence the continental lithospheric mantle, even beneath cratons, should not be necessarily regarded as an enriched reservoir, on the basis of the xenolith sample base. It contains pods characterised by enriched isotope compositions, but it is not dominated by them. These characteristics may arise because metasomatic veining by recent melts has overprinted any ancient signatures. So we may expect more "enriched" isotope signatures away from recent kimberlite veins. Nonetheless, even where enriched isotopic signatures are likely to persist, we should not equate this signature to enrichment in incompatible elements unless within metasomes dominated by phases such as amphibole and mica.

3.6.3. DYNAMICAL IMPLICATIONS

Cpx and, especially garnet, are relatively dense phases (e.g. density of garnet at 3GPa is 3.61Mgm^{-3} compared to 3.25Mgm^{-3} for olivine; Schutt and Lesher, 2006) which contain abundant Al and Ca compared to olivine and opx. Schutt and Lesher (2006) have modelled the effect on bulk density of varying the modal abundance of these phases as they are removed, by melt extraction, where the varying composition of the mineral phases as well as the modes is taken into consideration. This modelling shows that the density change resulting from removal, or in the case of metasomatism addition, of these phases is dependant on pressure. The maximum bulk density change resulting from the removal or addition of cpx is 2.1%. Such a large change in density would have a significant bearing on the dynamic stability of the lithosphere if the change affected the whole lithosphere. However, it is clear from this and earlier studies that the addition of cpx is likely to be relatively recent, associated with the kimberlite, and although this will cause a density change in the lithosphere it will be very localised, probably to a small area proximal to melt veins. The addition of garnet is more significant. It is difficult to determine a clear picture of garnet addition from geochemistry as there have been subsequent overprinting events, such as the addition of later cpx. The garnet could therefore have been added over a period of time, continuously, or more likely in steps. The simplest option has been summarised in Fig. 3.16. where the garnet is added in one event that is older than the cpx. This addition would have a more significant impact on lithospheric density but again is probably added relatively locally as opposed to wholesale throughout the lithospheric mantle.

3.7. CONCLUSIONS

1. Very high olivine Mg numbers of Archean lithospheric mantle peridotites are consistent with melt extraction between 30 to 40%, well beyond the point of depletion of both cpx and garnet at pressures less than 3GPa. Nonetheless, many samples of cratonic peridotites have significant cpx and garnet contents. There is insufficient opx in most lithospheric peridotites to account for these phases via exsolution from a high temperature, high pressure precursor. Therefore if a low pressure melting model is correct, the garnet and cpx observed within most cratonic peridotite cannot have a residual or exsolution origin.
2. The high incompatible trace element concentrations in the cpx as well as the high modal abundance of both phases in the Kaapvaal and NAC peridotites can be explained via a model where these phases crystallise from a melt.
3. The lack of trace element and isotopic equilibrium between the cpx and garnet cannot be preserved for periods longer than approximately 10Ma, implying that the phases were added at different times. Cpx is the most recent addition, with Sr and Nd isotope signatures are similar to present day convecting mantle values. In contrast garnets are more isotopically diverse.
4. The melts predicted to be in equilibrium with the cpx vary depending on the partition coefficients chosen but the most likely parental melts are kimberlite-suite magmas. The larger range of Sr isotope values in cpx from Kaapvaal peridotites compared to those from NAC peridotites

reflects the more heterogeneous and metasomatised nature of the lithospheric mantle in the Kaapvaal craton. The kimberlite magma interacts with this lithosphere and diversifies its geochemical signature.

5. The picture of garnet introduction is more complicated and it is not possible to use the trace element patterns to 'see through' the most recent overprinting by the kimberlite magmatism. The radiogenic Sr isotope compositions of some garnets from the Kaapvaal craton are attributed to metasomatic addition by the older Group II kimberlites. Garnets within a NAC peridotite from Greenland also have radiogenic Sr isotope signatures that can be attributed to formation during lamproite magmatism in West Greenland at 1374Ma.
6. The recent addition of cpx associated with the kimberlite magmatism in two contrasting on-craton settings suggests that this is a common process that can be applied to most cratonic settings. This is supported by the global similarity of cratonic peridotite cpx Sr and Nd isotope data and Group I kimberlites.
7. The recent crystallisation of cpx from infiltrating melts has implications for the geochemical fertility of the lithospheric mantle through time because cpx is an important host for REE and Sr. On evidence of this and other studies (van Achterbergh et al. 2001; Pearson and Nowell 2002; Gregoire et al. 2003; Simon et al. 2008) lherzolitic cratonic peridotites are a relatively recent phenomenon, evolving from depleted dunites and harzburgites. These pre-cursers were depleted in incompatible elements. Even the subsequent "metasomatic" lherzolites remain depleted relative to "fertile mantle" (Pearson and Nowell 2002).

8. Continental lithospheric mantle has experienced a long-lived and complex mineralogical evolution, beginning with opx addition though garnet addition to more recent cpx introduction. This is achieved via the interaction with at least three different parental melts and explains the highly complex nature of continental lithospheric mantle geochemistry.

3.8. REFERENCES

Adam, J. and Green, T. (2001). "Experimentally determined partition coefficients for minor and trace elements in peridotite minerals and carbonatitic melt, and their relevance to natural carbonatites." European Journal of Mineralogy 13(5): 815-827.

Aulbach, S., Griffin, W. L., Pearson, N. J., O'Reilly, S. Y. and Doyle, B. J. (2007). "Lithosphere formation in the central Slave Craton (Canada): plume subcretion or lithosphere accretion?" Contributions to Mineralogy and Petrology 154(4): 409-427.

Basu, A. R. and Tatsumoto, M. (1980). "Nd isotopes in selected mantle-derived rocks and their minerals and their implictations for mantle evolution." Contributions to Mineralogy and Petrology 75: 43-54.

Becker, M. and Le Roex, A. P. (2006). "Geochemistry of South African on- and off-craton, Group I and Group II kimberlites: Petrogenesis and source region evolution." Journal of Petrology 47(4): 673-703.

Bedini, R. M., Blichert-Toft, J., Boyet, M. and Albarede, F. (2004). "Isotopic constraints on the cooling of the continental lithosphere." Earth and Planetary Science Letters 223(1-2): 99-111.

Bernstein, S., Hanghoj, K., Kelemen, P. B. and Kent Brooks, C. (2006). "Ultra-depleted, shallow, cratonic mantle beneath West Greenland: dunitic xenoliths from Ubekendt Ejland." Contributions to Mineralogy and Petrology 152: 335-347.

Bernstein, S., Kelemen, P. B. and HanghÃ¸j, K. (2007). "Consistent olivine Mg# in cratonic mantle reflects Archean mantle melting to the exhaustion of orthopyroxene." Geology 35(5): 459-462.

Bizimis, M., Salters, V. J. M. and Dawson, J. B. (2003). "The brevity of carbonatite sources in the mantle: evidence from Hf isotopes." Contributions to Mineralogy and Petrology 145(3): 281-300.

Bizzarro, M. and Stevenson, R. K. (2003). "Major element composition of the lithospheric mantle under the North Atlantic craton: Evidence from

peridotite xenoliths of the Sarfartoq area, southwestern Greenland." Contributions to Mineralogy and Petrology 146(2): 223-240.

Blundy, J. and Dalton, J. (2000). "Experimental comparison of trace element partitioning between clinopyroxene and melt in carbonate and silicate systems, and implications for mantle metasomatism." Contributions to Mineralogy and Petrology 139(3): 356-371.

Boyd, F. R. (1989). "Compositional Distinction between Oceanic and Cratonic Lithosphere." Earth and Planetary Science Letters 96(1-2): 15-26.

Boyd, F. R., Pearson, D. G. and Mertzman, S. A. (1999). Spinel-facies peridotites form the Kaapvaal root. Proceedings of the 7th International Kimberlite Conference. Gurney, J. J., Gurney, J. L., Pascoe, M. D. and Richardson, S. H. Cape Town, South Africa, Red Roof Design. The J.B. Dawson Volume**:** 40-48.

Brenker, F. E. and Brey, G. P. (1997). "Reconstruction of the exhumation path of the Alpe Arami garnet-peridotite body from depths exceeding 160 km." Journal of Metamorphic Geology 15(5): 581-592.

Brey, G. and Huth, J. (1984). The enstatite-diopside solvus to 60kbar. Kimberlites II: The mantle and crust-mantle relationships., Proceedings of the third international kimberlite conference. Developments in Petrology, Elsevier.

Brey, G. P. and Kohler, T. (1990). "Geothermobarometry in 4-Phase Lherzolites .2. New Thermobarometers, and Practical Assessment of Existing Thermobarometers." Journal of Petrology 31(6): 1353-1378.

Brey, G. P., Bulatov, V. K. and Girnis, A. V. (2009). "Geobarometry for peridotites: experments in simple and natural systems from 6 to 10GPa." Journal of Petrology 49(1): 3-24.

Burgess, S. R. and Harte, B. (2004). "Tracing lithosphere evolution through the analysis of heterogeneous G9-G10 garnets in peridotite xenoliths, II: REE chemistry." Journal of Petrology 45(3): 609-634.

Canil, D. (1992). "Orthopyroxene stability along the peridotite along the peridotite solidus and the origin of cratonic lithosphere beneath Southern Africa." Earth and Planetary Science Letters 111(1): 83-95.

Canil, D. (2004). "Mildly incompatible elements in peridotites and the origins of mantle lithosphere." Lithos 77(1-4): 375-393.

Carlson, R. W., Irving, A. J., Schulze, D. J. and Hearn, B. C. (2004). "Timing of Precambrian melt depletion and Phanerozoic refertilization events in the lithospheric mantle of the Wyoming Craton and adjacent Central Plains Orogen." Lithos 77(1-4): 453-472.

Charlier, B. L. A., Ginibre, C., Morgan, D., Nowell, G. M., Pearson, D. G., Davidson, J. P. and Ottley, C. J. (2006). "Methods for the microsampling and high-precision analysis of strontium and rubidium isotopes at single crystal scale for petrological and geochronological applications." Chemical Geology 232(3-4): 114-133.

Coe, N., Le Roex, A. P., Gurney, J., Pearson, D. G. and Nowell, G. M. (2009). "Petrogenesis of the Swartruggens and Star Group II kimberlite dyke swarms, South Africa: constraints from whole rock geochemistry " Contributions to Mineralogy and Petrology 156(5): 627-652.

Cox, K. G., Smith, M. R. and Beswtherick, S. (1987). Textural studies of garnet lherzolites: evidence of exsolution origin from high-temperature harzburgites. Mantle Xenoliths. Nixon, P. H., John Wiley and Sons Ltd.**:** 537-550.

Danchin, R. V. (1979). Mineral and bulk chemistry of garnet lherzolite and garnet harzburgite xenoliths from the Premier Mine, South Africa. The Mantle Sample: Inclusions in Kimberlites and Other Volcanics. Boyd, F. R. and Meyer, H. O. A. Washington, D.C. , American Geophysical Union**:** 104-126.

Dawson, J. B. (1984). Contrasting types of upper-mantle metasomatism. Kimberlite II: The mantle and crust-mantle relationships. Kornprobst, J. Amsterdam, Elsevier**:** 289-294.

Dowall, D. (2004). Elemental and isotopic geochemistry of kimberlites from the Lac de Gras field, Northwest Territories, Canada. Department of Earth Sciences. Durham, Durham University. PhD.

Dowall, D. P., Nowell, G. M. and Pearson, D. G. (2003). "Chemical pre-concentration procedures for high-precision analysis of Hf-Nd-Sr isotopes in geological materials by plasma ionisation multi-collector mass spectrometry (PIMMS) techniques." Plasma Source Mass Spectrometry: Applications and Emerging Technologies: 321-337.

Eggins, S. M., Rudnick, R. L. and McDonough, W. F. (1998). "The composition of peridotites and their minerals: A laser-ablation ICP-MS study." Earth and Planetary Science Letters 154(1-4): 53-71.

Emeleus, C. H. and Andrews, J. R. (1975). "Mineralogy and petrology of kimberlite dyke and sheet intrusions and included peridotite xenoliths from South-West Greenland." Physics and Chemistry of The Earth 9: 179-197.

Erlank, A. J., Waters, F. G., Hawkesworth, C. J., Haggerty, S. E., Allsopp, H. L. and Menzies, M. A. (1987). Evidence for mantle metasomatism in peridotite nodules from the Kimberley Pipes, South Africa. Mantle Metasomatism. Menzies, M. A. and Hawkesworth, C., Academic Press**:** 221-312.

Foley, S. (1992). "Vein-plus-wall-rock melting mechanisms in the lithosphere and the origin of potassic alkaline magmas." Lithos 28(3-6): 435-453.

Font, L., Davidson, J. P., Pearson, D. G., Nowell, G. M., Jerram, D. A. and Ottley, C. J. (2008). "Sr and Pb isotope micro-analysis of plagioclase crystals from Skye Lavas: an insight into open-system processes in a flood basalt Province." Journal of Petrology 49(8): 1449-1471.

Gibson, S. A., Malarkey, J. and Day, J. A. (2008). "Melt Depletion and Enrichment beneath the Western Kaapvaal Craton: Evidence from Finsch Peridotite Xenoliths." Journal of Petrology 49(10): 1817-1852.

Glaser, S. M., Foley, S. F. and Gunther, D. (1997). Trace element compositions of minerals in garnet and spinel peridotite xenoliths from the Vitim volcanic field, Transbaikalia, eastern Siberia, Cambridge, Massachusetts.

Green, T. H., Blundy, J. D., Adam, J. and Yaxley, G. M. (2000). "SIMS determination of trace element partition coefficients between garnet, clinopyroxene and hydrous basaltic liquids at 2-7.5 GPa and 1080-1200 degrees C." Lithos 53(3-4): 165-187.

Gregoire, M., Bell, D. R. and Le Rouex, A. P. (2003). "Garnet lherzolites from the Kaapvaal craton (South Africa): Trace element evidence for a metasomatic history." Journal of Petrology 44(4): 629-657.

Griffin, W. L., Smith, D., Boyd, F. R., Cousens, D. R., Ryan, C. G., Sie, S. H. and Suter, G. F. (1989). "Trace-Element Zoning in Garnets from

Sheared Mantle Xenoliths." Geochimica et Cosmochimica Acta 53(2): 561-567.

Griffin, W. L., Smith, D., Ryan, C. G., OReilly, S. Y. and Win, T. T. (1996). "Trace-element zoning in mantle minerals: Metasomatism and thermal events in the upper mantle." Canadian Mineralogist 34: 1179-1193.

Griffin, W. L., O'Reilly, S. Y., Natapov, L. M. and Ryan, C. G. (2003). "The evolution of lithospheric mantle beneath the Kalahari Craton and its margins." Lithos 71(2-4): 215-241.

Griffin, W. L., O'Reilly, S. Y., Alfonso, J. C. and Begg, G. C. (2009). "The Composition and Evolution of Lithospheric Mantle: a Re-evaluation and itsTectonic Implications." Journal of Petrology 50: 1185-1204.

Grütter, H. S., Gurney, J. J., Menzies, A. H. and Winter, F. (2004). "An updated classification scheme for mantle-derived garnet, for use by diamond explorers." Lithos 77(1-4): 841-857.

Gunther, M. and Jagoutz, E. (1994). Isotopic disequilibria (Sm/Nd, Rb/Sr)between minerals of coarse grained, low temperature peridotites from Kimberley floors, southern Africa. Proceedings of the 5th International Kimberlite Conference, Brazil.

Gurney, J. J., Harte, B. and Cox, K. G. (1975). Mantle xenoliths in the Matsoku kimberlite pipe. Physics and Chemistry of the Earth 9. Ahrens, L. H., Dawson, J. B., Duncan, A. R. and Erlank, A. J., Pergamon Press.

Harlou, R., Pearson, D. G., Nowell, G. M., Ottley, C. J. and Davidson, J. P. (2009). "Combined Sr isotope and trace element analysis of melt inclusions at sub-ng levels using micro-milling, TIMS and ICPMS." Chemical Geology 260(3-4): 254-268.

Harte, B., Cox, K. G. and Gurney, J. J. (1975). Petrography and geological history of upper mantle xenoliths from the Matsoku kimberlite pipe. Physics and Chemistry of the Earth 9. Ahrens, L. H., Dawson, J. B., Duncan, A. R. and Erlank, A. J., Pergamon Press.

Hauri, E. H. and Hart, S. R. (1994). "Constraints on Melt Migration from Mantle Plumes - a Trace-Element Study of Peridotite Xenoliths from Savaii, Western-Samoa." Journal of Geophysical Research-Solid Earth 99(B12): 24301-24321.

Hauri, E. H., Wagner, T. P. and Grove, T. L. (1994). "Experimental and natural partitioning of Th, U, Pb and other trace elements between garnet, clinopyroxene and basaltic melts." Chemical Geology 117(1-4): 149-166.

Hauri, E. H. and Hart, S. R. (1997). "Rhenium abundances and systematics in oceanic basalts." Chemical Geology 139(1-4): 185-205.

Heaman, L. (2005). Patterns of kimberlite emplacement - the importance of robust geochronology. Workshop on Greenland's diamond potential, Copenhagen, GEUS.

Hellebrand, E., Snow, J. E., Hoppe, P. and Hofmann, A. W. (2002). "Garnet-field melting and late-stage refertilization in 'residual' abyssal peridotites from the Central Indian Ridge." Journal of Petrology 43(12): 2305-2338.

Herzberg, C. (2004). "Geodynamic information in peridotite petrology." Journal of Petrology 45(12): 2507-2530.

Hutchinson, M. T., Nielsen, L. J. and Bernstein, S. (2007). "P-T history of kimberlite-hosted garnet lherzolites from South-West Greenland." Geological Survey of Denmark and Greenland Bulletin 13: 45-48.

Ionov, D. A., Bodinier, J. L., Mukasa, S. B. and Zanetti, A. (2002). "Mechanisms and sources of mantle metasomatism: Major and trace element compositions of peridotite xenoliths from Spitsbergen in the context of numerical modelling." Journal of Petrology 43(12): 2219-2259.

Kelemen, P. B., Dick, H. J. B. and Quick, J. E. (1992). "Formation of harzburgite by pervasive melt rock reaction in the upper mantle." Nature 358(6388): 635-641.

Kelemen, P. B., Hart, S. R. and Bernstein, S. (1998). "Silica enrichment in the continental upper mantle via melt/rock reaction." Earth and Planetary Science Letters 164(1-2): 387-406.

Keshav, S., Corgne, A., Gudfinnsson, G. H., Bizimis, M., McDonough, W. F. and Fei, Y. (2005). "Kimberlite petrogenesis: Insights from clinopyroxene-melt partitioning experiments at 6 GPa in the CaO-MgO-Al2O3-SiO2-CO2 system." Geochimica et Cosmochimica Acta 69(11): 2829-2845.

Kesson, S. E. and Ringwood, A. E. (1989). "Slab mantle interactions 2: The formation of diamonds." Chemical Geology 78(2): 97-118.

Klein-BenDavid, O. and Graham Pearson, D. (2009). "Origins of subcalcic garnets and their relation to diamond forming fluids--Case studies from Ekati (NWT-Canada) and Murowa (Zimbabwe)." Geochimica et Cosmochimica Acta 73(3): 837-855.

Klein-BenDavid, O. and Pearson, D. G. (2009). "Origins of subcalcic garnets and their relation to diamond forming fluids--Case studies from Ekati (NWT-Canada) and Murowa (Zimbabwe)." Geochimica et Cosmochimica Acta 73(3): 837-855.

Klemme, S., Blundy, J. D. and Wood, B. J. (2002). "Experimental constraints on major and trace element partitioning during partial melting of eclogite." Geochimica et Cosmochimica Acta 66(17): 3109-3123.

Konzett, J., Armstrong, R. A., Sweeney, R. J. and Compston, W. (1998). "The timing of MARID metasomatism in the Kaapvaal mantle: An ion probe study of zircons from MARID xenoliths." Earth and Planetary Science Letters 160(1-2): 133-145.

Kramers, J. D., Roddick, J. C. M. and Dawson, J. B. (1983). "Trace element and isotope studies on veined, metasomatic and 'MARID' xenoliths from Bultfontein, South Africa." Journal Name: Earth Planet. Sci. Lett.; (Netherlands); Journal Volume: 65:1: Medium: X; Size: Pages: 90-106.

Kubo, K. (2002). "Dunite formation processes in highly depleted peridotite: Case study of the Iwanaidake peridotite, Hokkaido, Japan." Journal of Petrology 43(3): 423-448.

Le Roex, A. P., Bell, D. R. and Davis, P. (2003). "Petrogenesis of group I kimberlites from Kimberley, South Africa: Evidence from bulk-rock geochemistry." Journal of Petrology 44(12): 2261-2286.

Lee, C. T. A. (2004). Geochemical/petrologic constraints on the origin of cratonic mantle, Montreal, CANADA, Amer Geophysical Union.

MacGregor, I. D. (1974). "The system MgO-Al2O3-SiO2-olubility of Al2O3 in enstatite for spinel and garnet peridotite compositions." American Mineralogist 59: 110-119.

Mitchell, R. H. (1986). Kimberlites: Mineralogy, Geochemistry, and Petrology, Plenum Press.

Nielsen, L. J., Hutchinson, M. T. and Malarkey, J. (2008). "Geothermal constraints from kimberlite-hosted garnet lherzolites from southern Greenland." 9th International Kimberlite Conference Extended Abstract: 9IKC-A-00047

Nixon, P. H., von Knorring, O. and Rooke, J. M. (1963). "Kimberlites and associated inclusions: a mineralogical and geochemical study." American Mineralogist 48: 1090-1132.

Nixon, P. H. and Boyd, F. R. (1975). "Mantle evolution based on studies of kimberilte nodules from Southern Africa."

Nowell, G. M. and Parrish, R. R. (2002). Simultaneous acquisition of isotope compositions and parent/daughter ratios by non-isotope dilution solution-mode Plasma ionisation Multi-collector Mass Spectrometry (PIMMS). Plasma Source Mass Spectrometry The New Millenium**:** 298-310.

Nowell, G. M., Pearson, D. G., Bell, D. R., Carlson, R. W., Smith, C. B., Kempton, P. D. and Noble, S. R. (2004). "Hf isotope systematics of kimberlites and their megacrysts: New constraints on their source regions." Journal of Petrology 45(8): 1583-1612.

Nowell, G. M., Luguet, A., Pearson, D. G. and Horstwood, M. S. A. (2008). "Precise and accurate 186Os/188Os and 187Os/188Os measurements by multi-collector plasma ionisation mass spectrometry (MC-ICP-MS) part I: Solution analyses." Chemical Geology 248(3-4): 363-393.

Ozawa, K. and Takahashi, N. (1995). " P-T history of a mantle diapir - the Horoman Peridotite Complex, Hokkaido, Northern Japan." Contributions to Mineralogy and Petrology 120(3-4): 223-248.

Pearce, N. J. G., Perkins, W. T., Westgate, J. A., Gorton, M. P., Jackson, S. E., Neal, C. R. and Chenery, S. P. (1997). "A compilation of new and published major and trace element data for NIST SRM 610 and NIST SRM 612 glass reference materials." Geostandards Newsletter-the Journal of Geostandards and Geoanalysis 21(1): 115-144.

Pearson, D. G., Carlson, R. W., Shirey, S. B., Boyd, F. R. and Nixon, P. H. (1995a). "Stabilization of Archean Lithospheric Mantle - a Re-Os

Isotope Study of Peridotite Xenoliths from the Kaapvaal Craton." Earth and Planetary Science Letters 134(3-4): 341-357.

Pearson, D. G., Shirey, S. B., Carlson, R. W., Boyd, F. R., Pokhilenko, N. P. and Shimizu, N. (1995b). "Re-Os, Sm-Nd, and Rb-Sr isotope evidence for thick Archean lithospheric mantle beneath the Siberian craton modified by multistage metasomatism." Geochimica et Cosmochimica Acta 59(5): 959-977.

Pearson, D. G. (1999). Evolution of the cratonic lithospheric mantle: an isotopic perspective. Mantle petrology: field observations and high pressure experiments. Bertka, C. M., Mysen, B. O. and Fei, Y., Geological Society of London. Special Publication, No. 6**:** 57-78.

Pearson, D. G. and Nowell, G. M. (2002). "The Continental Lithospheric Mantle: Characteristics and Significance as a Mantle Reservoir." Philosophical Transactions: Mathematical, Physical and Engineering Sciences 360(1800): 2383-2410.

Pearson, D. G., Canil, D. and Shirey, S. B., Eds. (2003). Mantle sample included in volcanic rocks: xenoliths and diamonds. Treatise on Geochemistry: The Mantle and Core, Elsevier.

Pearson, D. G. and Nowell, G. M. (2005). Accuracy and precision in plasma ionisation multi-collector mass spectrometry: constraints from neodymium and hafnium isotope measurements. Plasma Source Mass Spectrometry, Current Trends and Future Developments, Special Publication of the Royal Society of Chemistry. Holland, G. and Bandura, D. R.**:** 284-314.

Pearson, D. G. and Wittig, N. (2008). "Formation of Archaean continental lithosphere and its diamonds: the root of the problem." Journal of the Geological Society 165: 895-914.

Richardson, S. H., Erlank, A. J. and Hart, S. R. (1985). "Kimberlite-Borne Garnet Peridotite Xenoliths from Old Enriched Subcontinental Lithosphere." Earth and Planetary Science Letters 75(2-3): 116-128.

Royse, K. R., Kempton, P. D. and Darbyshire, D. P. F. (1998). Procedure for the analysis for Rb-Sr and Sm-Nd isotopes at the NERC isotope geosciences laboratory. NERC Isotope Geosciences Laboratory Report Series. No. 121.

Rudnick, R., Mcdonough, W. F. and Orpin, A. (1994). Northern Tanzanian peridotite xenoliths: A comparison with Kaapvaal peridotites and inferences on metasomatic interactions. Proceedings of the Fifth International Kimberlite Conference. Meyer, H. O. A. and Leonardos, O. H. Brazil. Kimberlites, related rocks and mantle xenoliths.

Saltzer, R. L., Chatterjee, N. and Grove, T. L. (2001). "The Spatial Distribution of Garnets and Pyroxenes in Mantle Peridotites: Pressure-Temperature History of Peridotites from the Kaapvaal Craton." J. Petrology 42(12): 2215-2229.

Sand, K. K., Waight, T. E., Pearson, D. G., Nielsen, T. F. D., Makovicky, E. and Hutchison, M. T. (2009). "The lithospheric mantle below southern West Greenland: A geothermobarometric approach to diamond potential and mantle stratigraphy." Lithos 112(Supplement 2): 1155-1166.

Schmidberger, S. S., Simonetti, A. and Francis, D. (2001). "Sr-Nd-Pb isotope systematics of mantle xenoliths from Somerset Island kimberlites: Evidence for lithosphere stratification beneath Arctic Canada." Geochimica et Cosmochimica Acta 65(22): 4243-4255.

Schmidberger, S. S., Simonetti, A., Francis, D. and Gariepy, C. (2002). "Probing Archean lithosphere using the Lu-Hf isotope systematics of peridotite xenoliths from Somerset Island kimberlites, Canada." Earth and Planetary Science Letters 197(3-4): 245-259.

Schmidberger, S. S., Simonetti, A. and Francis, D. (2003). "Small-scale Sr isotope investigation of clinopyroxenes from peridotite xenoliths by laser ablation MC-ICP-MS - implications for mantle metasomatism." Chemical Geology 199(3-4): 317-329.

Schulze, D. J. (2003). "A classification scheme for mantle-derived garnets in kimberlite: a tool for investigating the mantle and exploring for diamonds." Lithos 71(2-4): 195-213.

Schutt, D. L. and Lesher, C. E. (2006). "Effects of melt depletion on the density and seismic velocity of garnet and spinel lherzolite." Journal of Geophysical Research-Solid Earth 111(B5): -.

Schwandt, C. S. and McKay, G. A. (1998). "Rare earth element partition coefficients from enstatite/melt synthesis experiments." Geochimica et Cosmochimica Acta 62(16): 2845-2848.

Shimizu, N. (1975). "Rare earth elements in garnets and clinopyroxenes from garnet lherzolite nodules in kimberlites." Earth and Planetary Science Letters 25(1): 26-32.

Shimizu, N. and Sobolev, N. V. (1995). "Young peridotitic diamonds from the Mir kimberlite pipe." Nature 375(6530): 394-397.

Shimizu, N., Pokhilenko, N. P., Boyd, F. R. and Pearson, D. G. (1997a). "Geochemical characteristics of mantle xenoliths from Udachnaya kimberlite pipe." Geologiya I Geofizika 38(1): 194-205.

Shimizu, N., Sobolev, N. V. and Yefimova, E. S. (1997b). "Chemical heterogeneity of garnet inclusions and juvenility of peridotite diamonds from Siberia." Geologiya I Geofizika 38(2): 337-352.

Shimizu, N., Sobolev, N. V. and Yefimova, E. S. (1997c). "Chemical heterogeneities of inclusion garnets and juvenile character of peridotitic diamonds from Siberia." Russian Geology and Geophysics 38(2): 356-372.

Simon, N. S. C., Irvine, G. J., Davies, G. R., Pearson, D. G. and Carlson, R. W. (2003). "The origin of garnet and clinopyroxene in "depleted" Kaapvaal peridotites." Lithos 71(2-4): 289-322.

Simon, N. S. C., Carlson, R. W., Pearson, D. G. and Davies, G. R. (2008). "The origin and evolution of the Kaapvaal cratonic lithospheric mantle." Journal of Petrology 48: 589-625.

Smith, D. and Barron, B. R. (1991). "Pyroxene-garnet equilibration during cooling in the mantle." American Mineralogist 76(11-12): 1950-1963.

Smith, D. and Riter, J. C. A. (1997). "Genesis and evolution of low-Al orthopyroxene in spinel peridotite xenoliths, Grand Canyon field, Arizona, USA." Contributions to Mineralogy and Petrology 127(4): 391-404.

Smith, D. (1999). Temperatures and pressures of mineral equiliration in peridotite xenoliths: Review, discussion, and implictaions. Mantle petrology: Field observations and high pressure experimentation: A tribute to Francis R. (Joe) Boyd. Fei, Y., Bertka, C. M. and Mysen, B. O., The Geochemical Society. Special Publication No. 6 171-188.

Sneeringer, M., Hart, S. R. and Shimizu, N. (1984). "Strontium and Samarium Diffusion in Diopside." Geochimica Et Cosmochimica Acta 48(8): 1589-1608.

Stachel, T., Harris, J. W., Tappert, R. and Brey, G. P. (2003). "Peridotitic diamonds from the Slave and the Kaapvaal cratons--similarities and differences based on a preliminary data set." Lithos 71(2-4): 489-503.

Sun, S. S. and McDonough, W. F. (1989). "Chemical and isotopic systematics of oceanic basalts: implications for mantle composition and processes." Geological Society, London, Special Publications 42(1): 313-345.

Tappe, S., Jenner, G. A., Foley, S. F., Heaman, L., Besserer, D., Kjarsgaard, B. A. and Ryan, B. (2004). "Tomgat ultramafic lamprophyres and their relation to the north Atlantic alkaline province." Lithos 76(1-4): 491-518.

Tappe, S., Foley, S. F., Stracke, A., Romer, R. L., Kjarsgaard, B. A., Heaman, L. M. and Joyce, N. (2007). "Craton reactivation on the Labrador Sea margins: 40Ar/39Ar age and Sr-Nd-Hf-Pb isotope constraints from alkaline and carbonatite intrusives." Earth and Planetary Science Letters 256(3-4): 433-454.

Thirlwall, M. (1991). "Long term reproducibility of multicollector Sr and Nd ratio analyses." Chemical Geology (Isotope Science Section) 94: 85-104.

van Achterbergh, E., Griffin, W. L. and Stiefenhofer, J. (2001). "Metasomatism in mantle xenoliths from the Letlhakane kimberlites: estimation of element fluxes." Contributions to Mineralogy and Petrology 141(4): 397-414.

van Achterbergh, E., Griffin, W. L., Ryan, C. G., O'Reilly, S. Y., Pearson, N. J., Kivi, K. and Doyle, B. J. (2002). "Subduction signature for quenched carbonatites from the deep lithosphere." Geology 30(8): 743-746.

Walker, R. J., Carlson, R. W., Shirey, S. B. and Boyd, F. R. (1989). "Os, Sr, Nd, and Pb Isotope Systematics of Southern African Peridotite Xenoliths - Implications for the Chemical Evolution of Subcontinental Mantle." Geochimica et Cosmochimica Acta 53(7): 1583-1595.

Walter, M. J. (1998). "Melting of garnet peridotite and the origin of komatiite and depleted lithosphere." Journal of Petrology 39(1): 29-60.

Weis, D., Kieffer, B., Maerschalk, C., Pretorius, W. and Barling, J. (2005). "High-precision Pb-Sr-Nd-Hf isotopic characterization of USGS BHVO-1 and BHVO-2 reference materials." Geochemistry Geophysics Geosystems 6: 10.

Witt-Eickschen, G., Seck, H. A. and Reys, C. (1993). "Multiple Enrichment Processes and their Relationships in the Subcrustal Lithosphere Beneath the Eifel (Germany)." J. Petrology 34(1): 1-22.

Wittig, N., Pearson, D. G., Webb, M., Ottley, C. J., Irvine, G. J., Kopylova, M., Jensen, S. M. and Nowell, G. M. (2008). "Origin of cratonic lithospheric mantle roots: A geochemical study of peridotites from the North Atlantic Craton, West Greenland." Earth and Planetary Science Letters 274(1-2): 24-33.

Woodhead, J. D., Hergt, J., Phillips, D. and Paton, C. (2009). "African kimberlites revisited: In-situ Sr isotope analysis of groundmass perovskite." Lithos 112(Supplement 1): 311-317.

Zack, T., Foley, S. F. and Jenner, G. A. (1997). "A consistent partition coefficient set for clinopyroxene, amphibole and garnet from laser ablation microprobe analysis of garnet pyroxenites from Kakanui, New Zealand. ." Neues Jarbuch Fur Mineralogie. Abhandlungen 172(1): 23-41.

Chapter 4:

GEOCHEMICAL DISSECTION OF A KIMBERLITE AND OLIVINE MELILITITE: TRACKING MAGMATIC EVOLUTION AND CONSTRAINING THE RELATIONSHIP BETWEEN KIMBERLITES AND THE LOW-Cr MEGACRYSTS SUITE.

4.1. INTRODUCTION

The elemental (Kjarsgaard et al., 2009) and isotopic (e.g. Nowell et al. 2004; Pearson and Wittig 2008) composition of primary kimberlite magma has long been a subject of debate. The frequent occurrence of crustal fragments within hypabyssal and volcaniclastic kimberlite is a clear indication of the importance of crustal contamination in modifying the kimberlite magma. Sr isotope ratios are a powerful tool that can be used to fingerprint magma source regions as they are sensitive to crustal contamination but are not fractionated by magmatic processes such as crystallisation. In the case of kimberlites, the primary magma is ubiquitously contaminated by material from the lithospheric mantle and crust both as xenoliths/xenocryts and by wallrock-melt reactions (Mitchell 1986; Mitchell 2008). Incorporation of mantle fragments (Fig. 4.1.), however, typically does not have a significant impact on the Sr isotope composition of the kimberlite as Sr concentrations are low (Pearson et al. 2003) and the isotopic ratio is similar to convecting mantle melts. Addition of Archean crust with higher Sr concentrations and significantly more radiogenic ratios can mask the 'primary' kimberlite signature resulting in more radiogenic whole rock analyses than would be expected from a mantle melt (Fig. 4.1.).

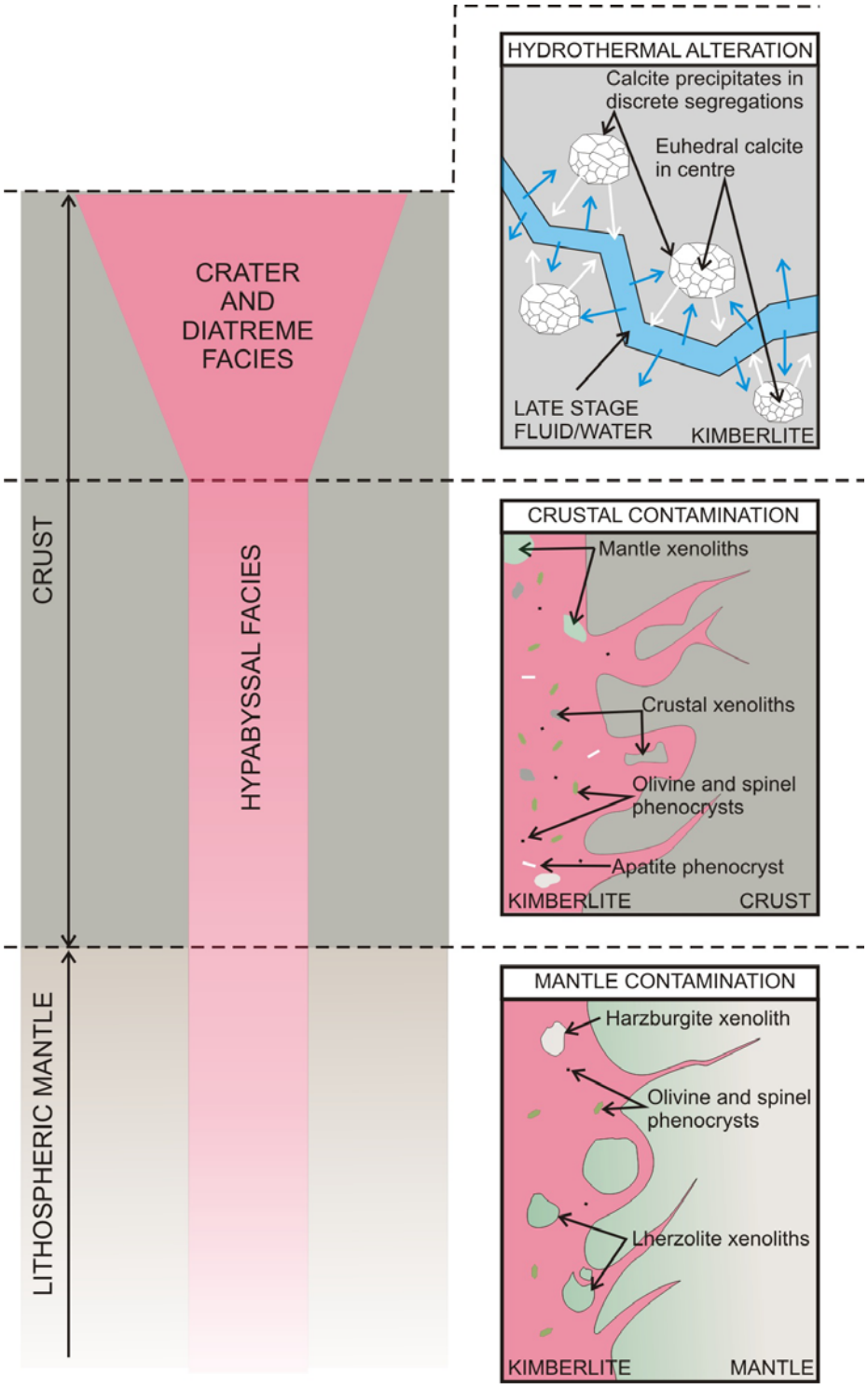

Figure 4.1.

A schematic illustration of the processes that affect the kimberlite magma as it intrudes the lithosphere. The entrainment of lithospheric mantle has a minimal effect on the Sr isotope composition of the kimberlite as the Sr compositions are low. However the entrainment of crust and late stage hydrothermal alteration associated with emplacement can both potentially introduce significant radiogenic Sr.

Historically, hypabyssal kimberlites were sampled to avoid crustal contamination as they were regarded as minimally contaminated (Smith et al. 1983). However, recent studies of hypabyssal root zone kimberlites indicate that in some instances crustal material can be intimately mixed with kimberlite (e.g. Sparks et al. 2006; Mitchell 2008). While contamination by macroscopic crustal xenoliths can mostly be avoided by careful sample selection or hand picking, these procedures cannot remove the effects of crustal assimilation into the kimberlite magma (Kjarsgaard et al. 2009). Hydrothermal alteration (Fig. 4.1.), associated with syn- and post-emplacement processes, further complicates whole rock analysis, as the kimberlite fluids may interact with groundwater and/or wallrock, which typically contain more radiogenic Sr (Mitchell 1986; Walters et al. 2006).

Perovskite ($CaTiO_3$), a kimberlite groundmass mineral phase, is thought to be relatively robust to alteration and has been used extensively to date kimberlites via the U-Pb system (Kramers and Smith 1983; Heaman 1989) and can also yield Sr and Nd isotope data (Heaman 1989). The high concentration of Sr in perovskites (typically over 1000ppm; Heaman 1989) has recently been exploited to constrain the 'primary' kimberlite initial $^{87}Sr/^{86}Sr$ because crustal fragments are avoided (Paton et al. 2007b). It has been suggested that direct LA ICP-MS analyses of kimberlite perovskite provides a better constraint on the initial Sr isotope ratio of the kimberlite magma than whole rock Sr isotope data (Paton et al. 2007a; Paton et al. 2007b; Kamenetsky et al. 2009; Woodhead et al. 2009). However, the temperature and pressure range over which perovskite (or most kimberlite mineral phases) crystallises is poorly constrained. Perovskite

may, therefore, crystallise after a significant amount of crust has already been assimilated into the magma. So, while *in-situ* analysis of perovskite has been a significant step forward, this single phase approach may not reveal the true initial Sr isotope ratio of the uncontaminated magma. A more detailed multi-phase approach is therefore required to resolve some of these issues and constrain to what extent perovskite and other mineral phases record the $^{87}Sr/^{86}Sr_i$ ratio of the evolving kimberlite magma.

In order to better understand the kimberlite system, we first present a geochemical dissection of an olivine melilitite from Saltpetre Kop (SPK), South Africa. This sample (with the exception of melilite) contains a similar suite of mineral phases to those observed in kimberlite, but has apparently experienced a less complex history, with few visible indicators of crustal incorporation. It is also relatively fresh in comparison to most kimberlites. These data are compared to an analogue study on a sample from the hypabyssal Jos kimberlite dyke. For both samples, a range of mineral phases (olivine, melilite, perovskite, phlogopite, calcite, apatite) have been analysed for trace elements and Sr isotope ratios using high precision TIMS techniques. The low concentration of Sr, and variable Rb/Sr ratios for olivine and phlogopite precludes LA-ICP-MS analysis.

Constraining the primary Sr isotope signature of the kimberlite magma is vital to better understanding processes in the lithospheric mantle such as metasomatism as well as diamond and megacryst formation which have

previously been linked to the kimberlite magma (Erlank et al. 1987; Schrauder et al. 1996; Davies et al. 2001; Simon et al. 2003; Nowell et al. 2004; Tomlinson et al. 2005; Zedgenizov et al. 2007; Klein-BenDavid et al. 2009). The relationship between the low-Cr megacrysts suite, carried in the kimberlite load, and the kimberlite magma has been long debated. Nowell et al (2004) observed that there is a significant overlap in Nd (Fig. 4.2.) and Hf isotope ratios between the megacrysts suite and the whole rock kimberlite analyses and therefore concluded that the two were genetically related. However there is some offset in terms of Sr isotope ratios between the two (Fig. 4.2.) which has been used to argue against such a link (Davies et al. 2001). Therefore characterising the 'true' Sr isotope composition of the primary kimberlite magma would better constrain this relationship. This also has implications for the diamond genesis. Recent analytical advances have made it possible to analyse the trace element composition, and in some cases isotope ratios, of diamond forming fluids, trapped as inclusions. This has led some authors to suggest a link between these diamond forming fluids and a primary kimberlite magma (Schrauder et al. 1996; Tomlinson et al. 2005; Zedgenizov et al. 2007; Klein-BenDavid et al. 2009).

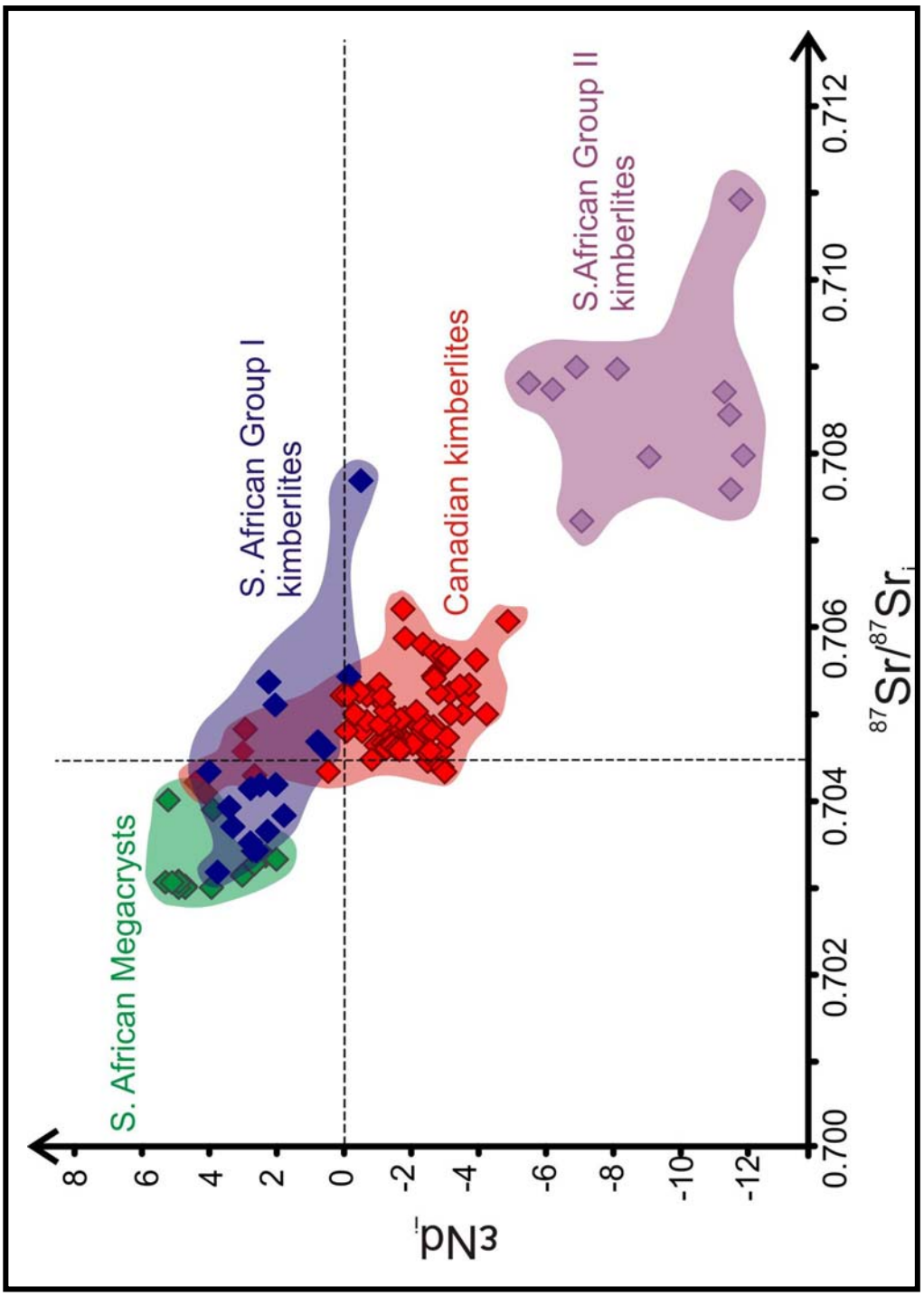

Figure 4.2.

Plot of initial Sr isotope ratios against epsilon Nd for whole rock analyses of Group I and Group II kimberlites from South Africa (Becker and Le Roex 2006) along with data from the low-Cr megacryst suite, also from South Africa (Nowell et al. 2004 and references therein.). Canadian whole rock kimberlite data (Dowall 2004) are plotted for reference.

4.2. METHOD

The majority of minerals analysed in this study, with the exception of melilite and some calcite, were hand picked (see Appendices E and F for images of picked minerals) following heavy liquid separation. The olivine, perovskite and phlogopite were first leached in 3N HCl for 30min at 40ºC and then in 18mΩ MilliQ water (MQ) for 60min at 60ºC. The leachates were collected and analysed for trace element concentrations and Sr isotope ratios. The apatite was not leached as apatite dissolves readily in weak acid. However the picked apatite did not show any visible grain boundary contamination and the concentration of Sr is sufficiently high that any contamination was assumed to have a minimal effect. The mineral separates were then re-picked after leaching, to remove any minerals that had visible grain boundary contamination, and weighed. For the melilitite sample (SPK) individual, apatite grains were photographed and the weight calculated from the volume using LAS (Leica Application Suite) software to a resolution of 2μm, as they were too small to weigh.

Apatite from the Jos kimberlite sample is only present in very low modal abundances and tended to break up when the sample was crushed. In order to address this problem a recently developed technique was employed which disaggregates the hand sample along grain boundaries leading to better preservation of individual crystals. This sample was processed at CNT Mineral Consulting Inc., Ottawa, Canada using a CNT Spark-2 electric pulse

disaggregator with a 1mm EPD sieve on a 393g piece of fresh rock (after sawing off the weathered portions). This was then further processed using a CNT HS-11 hydroseparator, followed by magnetic separation. The apatite was hand picked from the non-magnetic, 45μm to 75μm fraction. A number of calcite segregations were also hand picked from the 150μm to 212μm non-magnetic fraction, processed in the same way.

Melilite phenocrysts (from SPK) and calcite segregations (from Jos) were sampled using *in-situ* micro-drilling on 50μm thick sections following the procedure outlined in Charlier et al (2006), using a New Wave MicroMill at NCIET, Durham University, UK. Care was taken to avoid any potential contamination along cracks or grain boundaries. The drilled powder was collected in MQ, dried down and weighed to allow accurate determination of trace element concentrations. The drilled weights varied from 3μg to 120μg.

The picked mineral separates and drilled samples were processed using micro-Sr dissolution chemistry. A 10% aliquot, by mass, was taken for trace element analysis and the remaining 90% was put through micro-Sr columns as outlined in Charlier et al (2006) using cleaned Sr-spec resin. Romil triple distilled "UpA" grade acids were used throughout. For a small number of samples the eluant from the Sr column chemistry was collected and processed through cation columns, following the method outlined by Dowall et al. (2003), to isolate the REE for Nd isotope analysis.

The trace element aliquot was dissolved in 485µl of UpA 3%HNO_3 and analysed for 21 trace elements using the ThermoFisher Element II ICPMS at NCIET, Durham University, UK. The parameters used were similar to those given in Font et al (2006). Accuracy and repeatability of the trace element concentrations using the aliquotting technique are 10% or better and are given in Harlou et al (2009). A summary of the standard reproducibility for the analyses presented here are in Table A.8. The trace element concentrations were used to filter data where leaching was not successful in removing grain boundary contaminations (details of the leachate concentrations can be found in the Appendices E and F).

Sr isotope ratios (for the picked and drilled samples) were analysed using the ThermoFisher Triton Thermal Ionisation Mass Spectrometer (TIMS) at NCIET, Durham University, UK. The samples were loaded onto Re filaments using a TaF_5 activator. Sr was analysed with a static multi-collection routine with each analysis consisting of 200 ratios with an integration time of 4 seconds per ratio. Sr isotope ratios were corrected for mass fractionation using an $^{86}Sr/^{88}Sr$ ratio of 0.1194 and an exponential law. The average $^{87}Sr/^{86}Sr$ ratio for 3ng loads of the NBS987 standard (yielding beam sizes that are typical of the smaller sample sizes analysed here), over the period of this study, was 0.710246±14 (19.7ppm 2SD;n=19). The standard values analysed over the period of study are summarised in Table A.1. and given in detail in Table A.2. Sample values were normalised to a standard value of 0.710240 (Thirlwall 1991). The mass of Sr analyte varied from 1ng to over 100ng for the minerals from Jos and from 1 to 30ng for the SPK mineral separates. The leachates were also analysed for Sr

isotopes and contained 20ng to 400ng of Sr. The average total procedural Sr blank was 15pg (±12 2sd, n=14) and is less than 1% of the analysed Sr in each of the processed batches of chemistry. The details of the blanks analysed for each batch of chemistry analysed is summarised in Table A.7.

Following chemistry, whole rock Sr and all Nd fractions (whole rock and mineral separates) were dissolved 3% HNO_3 and analysed on the ThermoFisher Neptune MC-ICPMS (Multi Collector ICP Mass Spectrometer) at NCIET, Durham University, UK. Samples were aspirated using an ESI PFA-50 nebulizer in conjunction with a 'cinnabar' micro-cyclonic borosilicate spray chamber. The basic analytical method used for each element on the Neptune comprises a static multi-collection routine of 1 block of 50 cycles with an integration time of 4sec per cycle; total analysis time 3.5mins.

Using the PFA-50 nebuliser, cinnabar spray chamber and a normal H skimmer cone, the sensitivity for Nd on the Neptune is 60-80V total Nd ppm^{-1} at an uptake rate of 90µl min^{-1}. Instrumental mass bias was corrected for using a $^{146}Nd/^{145}Nd$ ratio of 2.079143 (equivalent to the more commonly used $^{146}Nd/^{144}Nd$ ratio of 0.7219) and an exponential law. The $^{146}Nd/^{145}Nd$ ratio is used for correcting mass bias since at Durham Nd isotopes are measured on a total REE-cut from the cation columns and this is the only Ce and Sm-free stable Nd isotope ratio. This approach requires a correction for isobaric interferences from Sm on ^{144}Nd, ^{148}Nd and ^{150}Nd. The correction used is based on the method outlined in Nowell and Parrish (2002) and Nowell et al. (2008).

The accuracy of the Sm correction method during analysis of a total REE fraction is demonstrated by repeat analyses of the USGS BHVO-1 std, which yield an average $^{143}Nd/^{144}Nd$ ratio of 0.512982±0.000007 (13.5ppm 2SD, n=13) after Sm correction; essentially identical to the TIMS ratio of 0.512986±0.000009 (17.5ppm 2SD; n=19) obtained by Weis et al. (2005) on a pure Nd separate. Average signal size for the ^{146}Nd in the standards was 2.8±0.1 V and was 0.16±0.26V for the samples. The samples were analysed in a single analytical session during which the average $^{143}Nd/^{144}Nd$ value of 0.511116±0.000010 (19.7ppm 2SD; n=7) for the in-house standard J&M and an average value of $^{143}Nd/^{144}Nd$ value of 0.511117±0.000016 (31.7ppm 2SD; n=6) for the Sm-doped in-house standard J&M (used to monitor the offline Sm correction). Details of these standards can be found in Tables A.5. and A.6. These values are comparable to the long-term value reported by Pearson and Nowell (2005). Sample data are reported relative to a J&M value of 0.511110 (equivalent to a La Jolla value of 0.511862, Royse et al., 1998).

Modal abundance data were collected using a quantitative SEM based method on a QEMSCAN at the Colorado School of Mines, USA, following the procedure outlined by Benvie et al (2007) and Hoal et al (2009) with a 12μm resolution.

The major elements analyses were analysed using a four spectrometer Cameca Camebax MBX electron microprobe by wavelength dispersive x-ray analysis

method (WDX) at the Earth Sciences Department, Carleton University, Ottawa. The operating conditions are summarised in Table A.11.

4.3. SAMPLES

4.3.1 SAMPLE DESCRIPTION

4.3.1.1. Saltpetre Kop (SPK)

Olivine melilitites are alkali, ultramafic volcanic rocks that are found in a range of continental tectonic settings often associated with rifts (Dunworth and Wilson 1998) The sample presented here is from a satellite plug of the Saltpetre Kop volcano in the Western Cape, South Africa (DeWet 1975) that has been dated at 72.5 (± 1.2) and 76.8 (±1.3) Ma using K-Ar dating of whole rock powder and phlogopite separates respectively (Duncan et al. 1978). The olivine melilitites at Saltpetre Kop occur as pipes and dykes on the edge of the main volcanic centre that consists of potassic trachyte cabonatite and associated pyroclastic deposits. The complex intrudes through the Early to mid Proterozoic Namaqua-Natal mobile belt (DeWet 1975; Janney et al. 2002). The SPK melilitite was selected because it is extremely fresh with excellent preservation of all phases, including melilite.

4.3.1.2. Jos Kimberlite

The Jos kimberlite is exposed as a 1-2m wide hypabyssal dyke on Somerset Island, Nunavut, Canada (Mitchell and Meyer 1980). The kimberlite dyke intrudes a Silurian platform carbonate sequence that overlies Archean crust (Kjarsgaard et al. 2009). The matrix contains few country rock xenoliths or ultramafic xenoliths although mantle minerals from disaggregated xenoliths are observed (Mitchell and Meyer 1980). The Jos intrusion has been dated to about *ca.* 98Ma using the U-Pb dating on perovskites technique (Kjarsgaard and Heaman, unpublished). The Jos kimberlite was selected for study because it exhibits minimal crustal contamination or late stage hydrothermal alteration and is extremely fresh with excellent preservation of all mineral phases.

4.3.2. PETROGRAPHY AND MINERAL CHEMISTRY

In order to assess the sequence in which mineral crystallisation might record the progressive crustal contamination of the solidifying magma it is necessary to first understand the petrography (Fig. 4.3., 4.4., 4.5. and 4.6.). False colour QEMSCAN images illustrating spatial mineral relations are located in Fig. E.1. and F.1. Quantitative mineral modes calculated from the QEMSCAN images are given in Fig. 4.3. and 4.5.

4.3.2.1. Saltpetre Kop

The petrography and mineral chemistry of the Saltpetre Kop olivine melilite has been studied in detail by Boctor and Yoder (1986). New microprobe analyses of melilite, monticellite and wollastonite, combined with the data from Boctor and Yoder (1986), are listed in Table E.1. The sample shows bands on a centimeter scale where the melilite has been altered (Fig. E.1.). These bands probably represent areas where fluid has passed through the sample and were avoided in this study. Olivine (19%; forsterite content ranging from 85 to 89) and Sr-bearing melilite (16%; 0.33 to 0.36wt% SrO) occur as early forming phenocrysts (Fig. 4.4.) within a fine-grained groundmass predominantly composed of high-Sr (0.45 to 0.53wt% SrO) melilite (14%), Sr-poor (<0.02wt% SrO) monticellite (11%), phlogopite (9%), sodalite (7%) and nepheline (5%) with minor amounts of spinel (4%), perovskite (3%), apatite (3%) and wollastonite (0.18wt% SrO; Fig. 4.3.). Olivine, melilite and spinel co-crystallised as the earliest mineral phases (Fig. 4.4.). Euhedral olivine phenocrysts, up to 4mm in size, contain melt inclusions decorating growth zones within the crystal (Fig. 4.4(a)). A number of olivine phenocrysts show irregular, late-stage monticellite overgrowths (Fig. 4.4(b)), but there is little evidence of serpentenisation (Fig. 4.3., 4.4). Melilite is the next phase to crystallise and forms euhedral to subhedral rectangular lathes with spinel inclusions towards the rim (Fig. 4.3., 4.4(c)). The presence of fresh melilite rules out significant post-emplacement alteration as melilite is readily altered to calcite (Mahotkin et al. 2000). Euhedral, brown perovskite (20μm-50μm) is

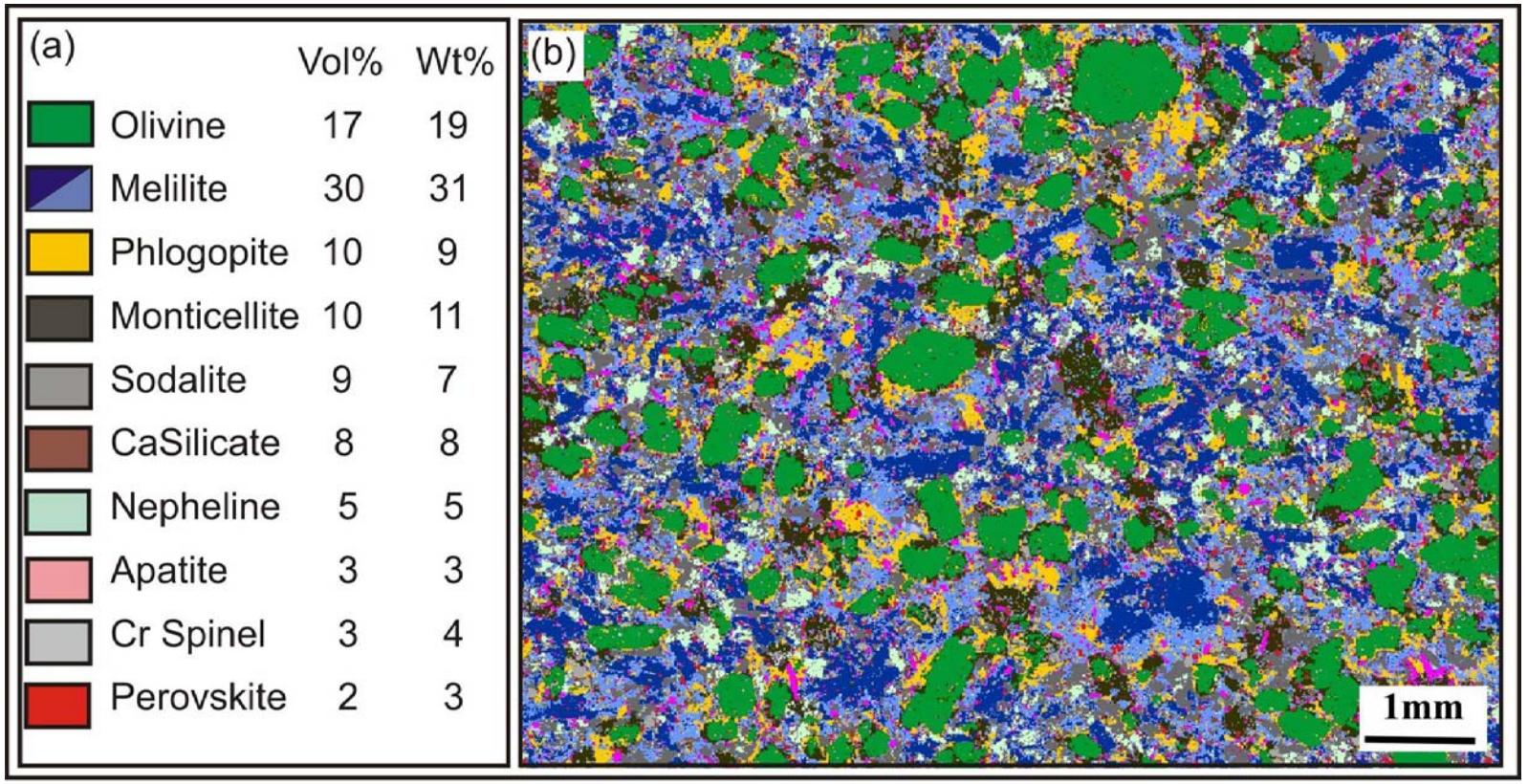

Figure. 4.3.

(a) *The modal abundance of the minerals are listed by volume % (from the image) and this has been converted to weight % using mineral density data (Deer et al. 1992).*

(b) *The QEMSCAN image of an area of the thin section and the minerals are labelled according to the key in (a). The two shades of blue for the melilite refer to melilite (dark blue) and an alteration product (light blue) that is assumed to have formed from the breakdown of melilite.*

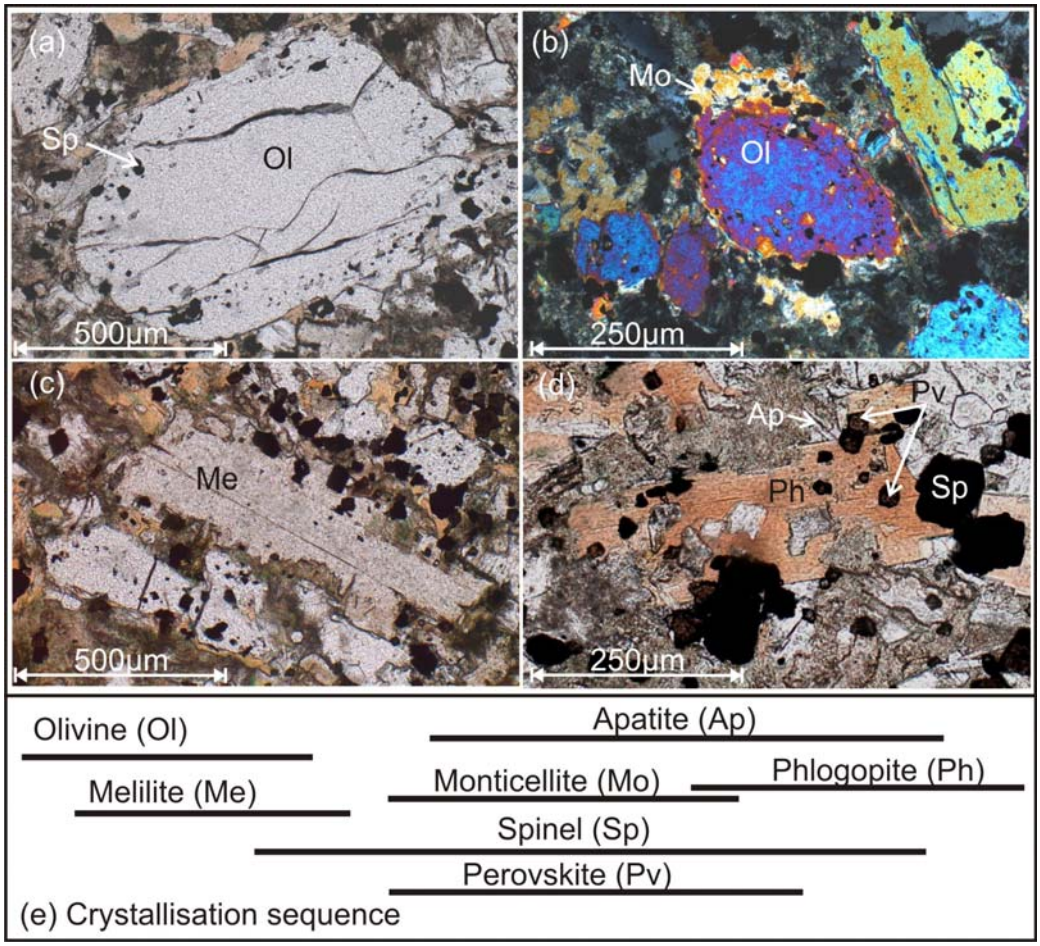

Figure 4.4.

Photomicrographs of SPK illustrating mineral relationships.

(a) *A euhedral olivine (ol) phenocryst with a growth zone containing melt inclusions and spinel (sp) crystals.*

(b) *A cross polarised image of an olivine crystal with a low birefringence monticellite (mo) overgrowth.*

(c) *A rectangular lathe of melilite (me) with spinel inclusions towards the rim.*

(d) *A phlogopite (ph) crystal with inclusions of both spinel and perovskite (pv). Apatite (ap) is also shown.*

(e) *Crystallisation order determined from petrography.*

found both in the groundmass and as inclusions in phlogopite (Fig. 4.4(a)) and is the next mineral phase to crystallise. It is difficult to distinguish the order of crystallisation for apatite as it is found as lathes (~100μm in length) in the groundmass (Fig. 4.4(d)) and is not included within other phases making it difficult to establish when it crystallised. There is some post-emplacement alteration in the groundmass of the groundmass melilite to zeolite phases.

It was not possible to sample the other groundmass phases (e.g. wollastonite) as they were too small to be sampled by drilling and did not survive the crushing process. However as these mineral phases crystallise late it is concluded that there would be minimal Sr remaining in the melt after phases such as perovskite and apatite had crystallised. These mineral phases are therefore deemed not to be significant contributors to the Sr budget.

4.3.2.2. Jos Kimberlite

Defining a crystallisation sequence for kimberlites is complex due to the significant xenocryst load and potential post-emplacement alteration (Mitchell 1986). The mineralogy of Jos has been previously described in detail by Mitchell and Meyer (1980). Microprobe analyses of olivine, perovskite, apatite and calcite are listed in Table F.1. The major element composition of phlogopite and spinel are taken from Mitchell and Meyer (1980). The Jos kimberlite (Fig. 4.5. and 4.6.) is minimally serpententised compared to many kimberlites (Fig. F.1.) removing some of the uncertainty created by interpreting altered phases. Olivine occurs as both angular to anhedral macrocrysts (up to

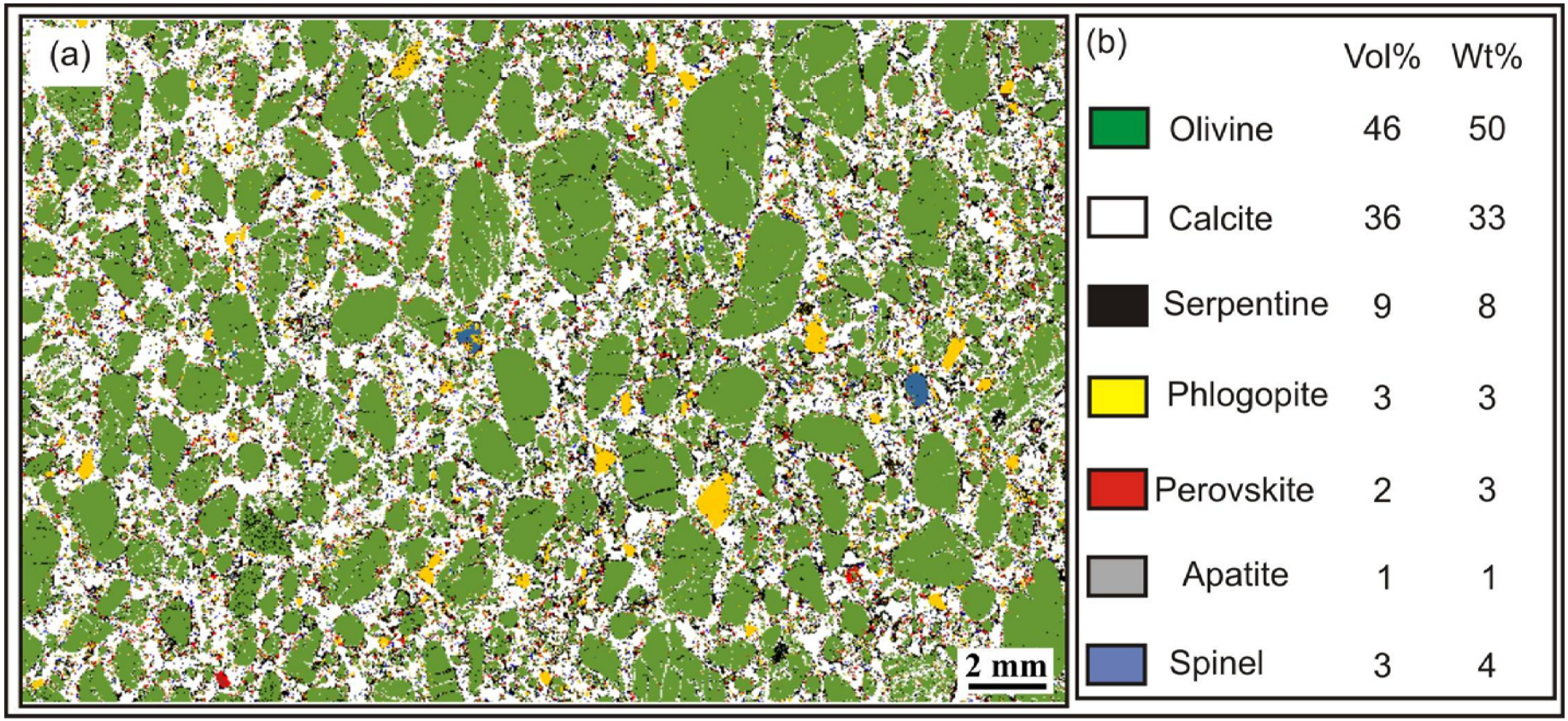

Figure. 4.5.

(a) *QEMSCAN image of a thin section of the hypabyssal Jos kimberlite. The colours correspond to the key in (b).*

(b) *The modal abundances of the different mineral phases listed by volume % (from the image) which has been converted to weight % using densities from Deer et al. (1992).*

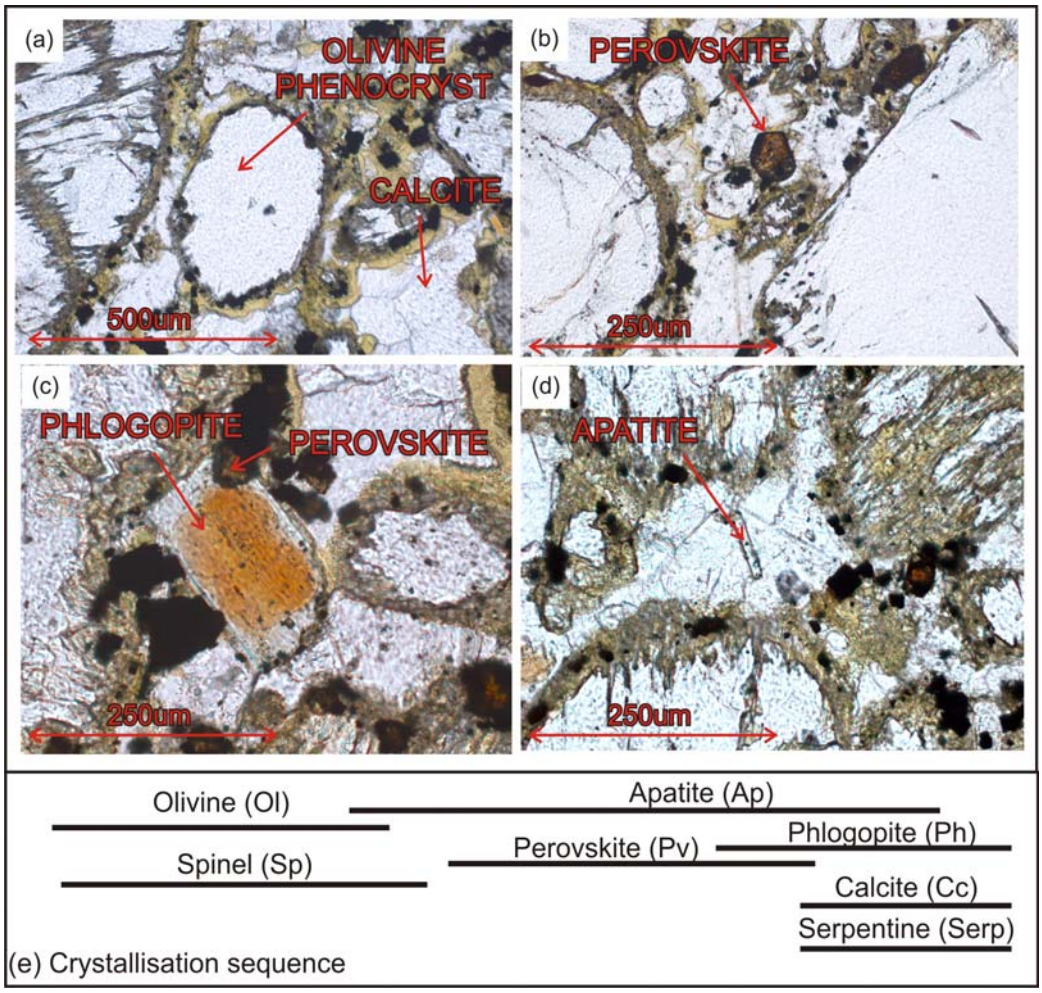

Figure 4.6.

Photomicrographs of a thin section taken from a sample of the Jos kimberlite.

(a) *A euhedral olivine phenocryst, rimmed with a small layer of serpentine. A calcite segregation can be seen in the bottom right corner.*

(b) *Euhedral perovskite in the kimberlite groundmass.*

(c) *Perovskite included in the rim of groundmass phlogopite which has a colourless rim of phlogopite with more of a kinshitalite composition.*

(d) *A euhedral crystal of apatite in the centre of a calcite segregation.*

(e) *Crystallisation sequence determined from the petrography.*

5mm), which are interpreted as xenocrysts, as they have forsterite-rich (with forsterite contents ranging from 91.3 to 92.8) core compositions. The rims of these anhedral marcocrysts are slightly more Fe-rich and of near constant composition (forsterite composition ranging from 88.7 to 90.3). Euhedral to subhedral olivine phenocrysts (100 to 1000μm; Fig. 4.6(a) and Fig. 4.7(d)) have variable core compositions (forsterite composition ranging from 84.7 to 92.3) with near constant rim compositions (forsterite contents ranging from 88.7 to 90.3) that are similar to the rims on the olivine xenocrysts. Phenocrystal olivine and Cr-rich, low-Ti spinel are interpreted to be the earliest, co-crystallising mineral phases.

The crystallisation order is more difficult to distinguish for the other mineral phases in the Jos kimberlite. Anhedral phlogopite macrocrysts (Fig. 4.6(c)), interpreted as megacrysts (1 to 3mm), have high-Ti (3.47-4.89wt% TiO_2) and low-Ba (<0.33wt% BaO) cores which have magnesium number ranging from 86 to 89. These macrocrysts are strongly zoned, with medial zones of moderate Ti and Ba contents (~2wt% TiO2, 0.35 to 4.39wt% BaO) and Mg numbers ranging from 89 to 92. The outer rims are low-Ti (<0.42wt% TiO2), high-Ba (>18wt% BaO) and have a high Mg number of 95. Small euhedral phenocrysts (<1mm) and groundmass (<200μm) phlogopite crystals have low-Ti, moderate-Ba cores, and very low-Ti, very high-Ba rims with very high Mg numbers (94.8 to 96.3). The phenocrysts and groundmass micas zoning trends are typical of archetypal kimberlite (i.e. phlogopite-kinoshitalite solid solution zoning towards the end-member kinoshitalite).

Apatite is sparsely distributed in the Jos kimberlite (modal abundance is 1%). It occurs in three morphologies (Fig. 4.7): (1) euhedral prisms (~50μm) with distinct core, moat (containing serpentine) and rim textures similar to that observed in kimberlite 'atoll' spinels (Fig. 4.7(b)); (2) euhedral prisms (~50μm, Fig. 4.7(d)); and (3) rare elongate tabular (100 to 200μm in length) zoned crystals (Fig. 4.7(a)). Apatite is observed in the groundmass, in calcite – serpentine segregations (Fig. 4.6(d) and 4.7(b)), within calcite, and rarely within rims of olivine crystals (Fig. 4.7(c)). There is no obvious correlation between apatite composition and morphology and all apatite crystals contain 0.33-0.57 wt% SrO.

Perovskite (Fig. 4.6(b) and 4.7(c)), found as simply zoned, brown, euhedral to subhedral crystals (<20μm-50μm), is interpreted as the next phase to crystallise. It is found in the groundmass as individual crystals, inter-grown with low-Cr-high-Ti spinel, and as inclusions in phlogopite and calcite. It is also observed as an overgrowth on rare Mg-ilmenite megacrysts. Perovskite cores are Na-, LREE-, Ta-enriched as compared to rim compositions. No systematic variation in core to rim Sr content is observed, with concentrations ranging from 0.17 to 0.30 wt% SrO.

The last phases to crystallise are calcite and serpentine. The resulting groundmass is predominantly composed of calcite, observed as elongate tabular laths, euhedral to subhedral grains and anhedral interlocking grains. The calcite

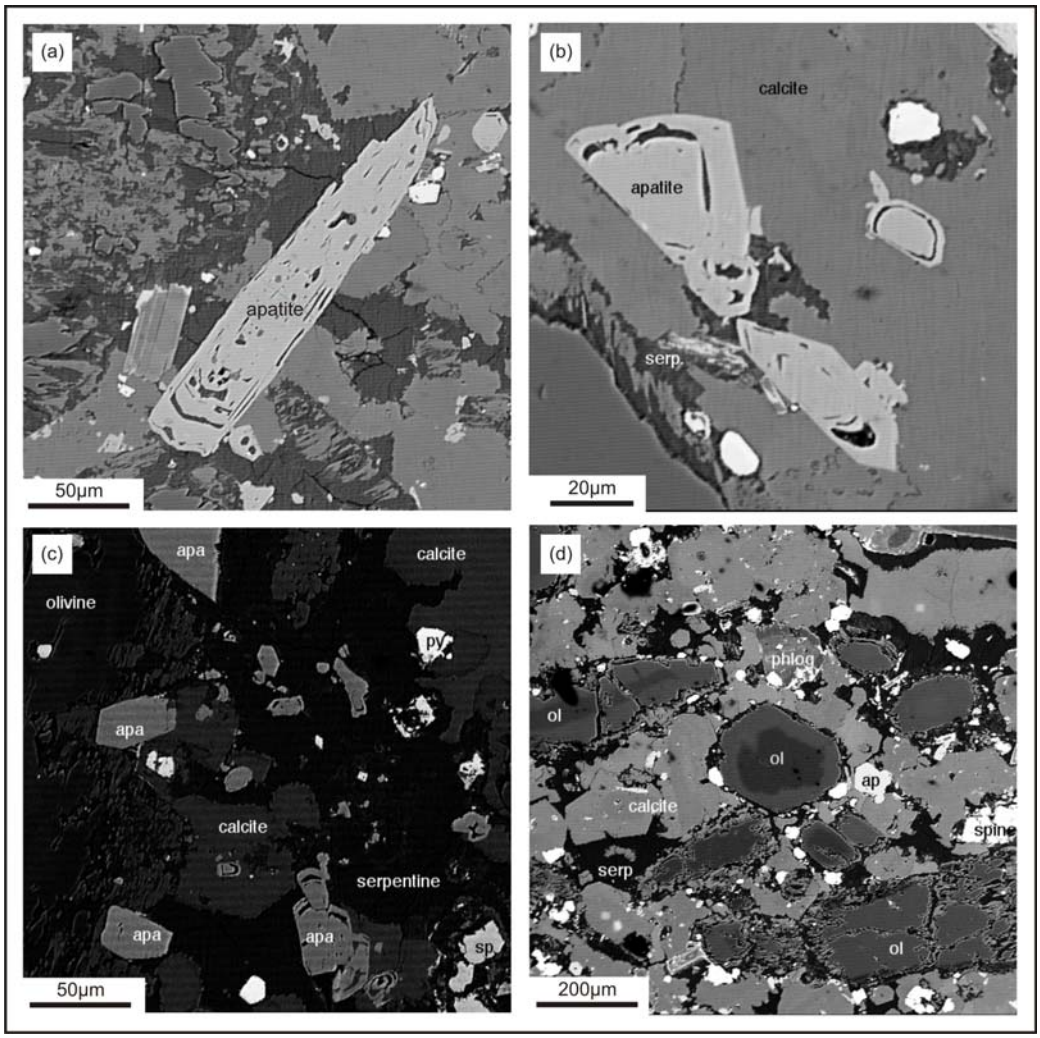

Figure 4.7.

SEM images (taken at Carleton University, Ottawa, Canada) of a thin section of the Jos kimberlite illustrating the different morphologies of apatite.

(a) *A zoned crystal of tabular apatite.*

(b) *Apatite crystal in a calcite-serpentine matrix showing a distinct dark serpentine (serp) moat illustrating at least two generations of apatite growth.*

(c) *Image of the groundmass illustrating coarser euhedral apatite (apa) crystal within the rim of an olivine crystal (to the left) compared to an apatite crystal showing a serpentine moat with an apatite atoll, located in the calcite-serpentine matrix.*

(d) *Zoned olivine (ol) phenocryst, pictured in the centre, in a claicte and serpentine (serp) matrix. A zoned phlogopite (phlog) crystal is also illustrated.*

crystals are typically 50-200μm in size (Fig. 4.6(d) and 4.7.). The tabular- and euhedral/subhedral-shaped grains are interpreted as being of products of magmatic crystallisation, whereas the anhedral grains are thought to represent precipitates from lower temperature carbohydrothermal fluids (Wilson et al. 2007). There is a good correlation between morphology and composition with the anhedral calcite grains containing low-Sr, low-Ba and high-Mg, high-Fe compositions (Fig. 4.10.). The tabular- and euhedral/subhedral-shaped grains on the other hand have high-Sr, high-Ba and low-Mg, low-Fe compositions. The magmatic calcite crystals contain 0.71 to 1.02wt% SrO; anhedral carbohydrothermally precipitated calcite grains have 0.19 to 0.52wt% SrO.

4.4. RESULTS

4.4.1. ELEMENTAL BUDGETS

4.4.1.1. Saltpetre Kop

Representative trace element patterns of the mineral phases from SPK are enriched relative to primitive mantle (Fig. 4.8.). The phenocrystal olivine has the lowest trace element concentrations and is the least LREE enriched, with a $[La/Yb]_N$ ratio of 35 compared to 108 for the whole rock. Trace element partition coefficients between olivine and silicate melt range from $1x10^{-2}$ for Yb to $1x10^{-5}$ for the LREE and Sr (Beattie 1994). Therefore the analysed trace

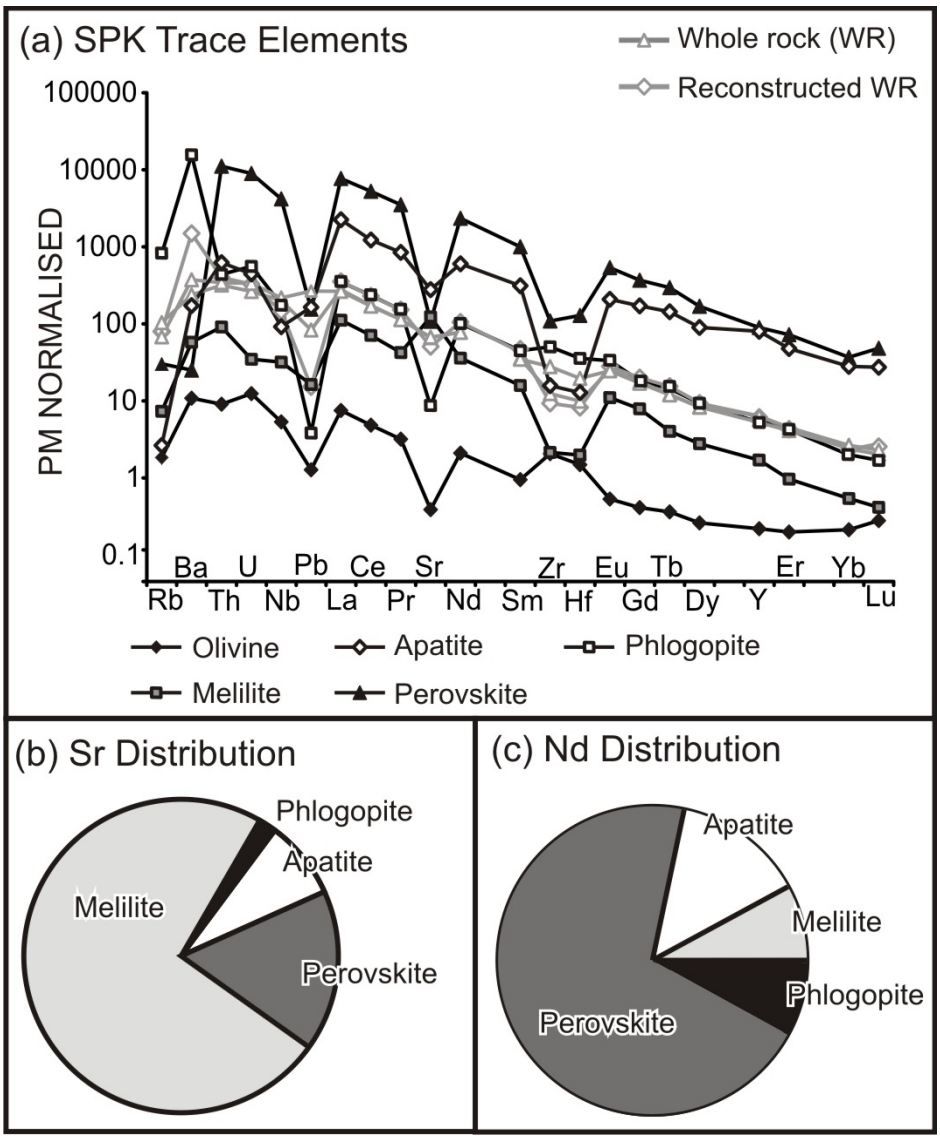

Figure 4.8.

(a) *Multi-element trace element plot for representative mineral analyses normalised to primitive mantle (PM; Sun and McDonough 1989). These are compared to whole rock analyses (Janney et al. 2002) and the reconstructed whole rock analysis from the mineral and modal abundance data. The uncertainties on most of the mineral phases are less than 2% but for the apatite the uncertainty is 25%.*

(b) *Distribution of Sr among the analysed mineral phases calculated from quantitative model abundance data (QEMSCAN) and mineral trace element concentrations. The values are normalised to 100%.*

(c) *Distribution of Nd among the analysed mineral phases calculated from quantitative model abundance data (QEMSCAN) and mineral trace element concentrations. The values are normalised to 100%.*

element budget is likely to be strongly influenced by the melt inclusions observed in the olivine phenocrysts. Provided these melts are, for the most part, isolated during olivine crystallisation, they provide an accurate reflection of the 'early' melt composition (Ramos and Reid 2005; Jackson and Hart 2006; Harlou et al. 2009).

Apatite and perovskite, both accessory phases, have the highest trace element concentrations (Fig. 4.8.), significantly higher than the whole rock. Perovskite is the most LREE enriched phase with a $[La/Yb]_N$ ratio of 209 and the trace element pattern observed here is similar to other kimberlitic perovskites that have been analysed (Jones 1987; Heaman 1989; Yang et al. 2009).

Phlogopite has similar trace element concentrations (Fig. 4.8.) and patterns to the whole rock with the exception of Ba, Sr and the HFSE. High Ba concentrations are typical of mantle and kimberlitic phlogopites (Pearson et al. 2003) whereas very high Ba concentrations are typical of kimberlite phlogopite (Mitchell 1995; this study). Trace element concentrations in the melilite are relatively low with the exception of Sr which is very high, yielding a large primitive mantle normalised positive anomaly compared to the negative peak observed in the other analysed mineral phases. This is supported by analyses of SrO of melilites from other olivine melilititie samples (Dunworth and Wilson 1998).

The whole rock trace element budget has been reconstructed from the mineral trace element and quantitative modal abundance data (Fig. 4.8.). The match between the reconstructed and measured whole rock data is relatively good although the reconstructed patterns slightly overestimate the LREE. This is probably due to the likely variability in mineral compositions (observed, for example, in analyses of kimberlitic perovskite from Jos). The high peak in Ba in the reconstructed whole rock is attributed to phlogopite which, from the microprobe data, is very variable and only one composition is used in this reconstruction. The relative similarity of the reconstructed primitive mantle normalised trace element patterns with the measured pattern implies minimal grain boundary contamination and minimal incorporation of trace elements in other mineral phases not analysed here.

The high Sr content of melilite combined with a high modal abundance means that the whole rock Sr budget is dominated by the melilite (Fig. 4.8, 75%). Apatite (18%) and perovskite (6%) make up the majority of the remaining whole rock Sr budget.

The Nd budget (Fig. 4.8(c)) has also been estimated for this sample and is dominated, in this case, by perovskite (62%) followed by apatite (18%), melilite (11%) and phlogopite (9%).

4.4.1.2. Jos Kimberlite

The minerals from the Jos kimberlite show a large range in trace element concentration with La, for example, ranging from less than 1ppm in the xenocrystal olivine to over 3500ppm in the perovskite. Trace elements patterns of olivine (Fig. 4.9.), as with the olivine in SPK, are likely to represent an integrated signal of olivine plus any magmatic inclusions but the majority of the incompatible elements primarily reside in the melt inclusions. This is reflected in the more elevated elemental concentrations in the phenocrystal olivine which has a higher density of observed magmatic inclusions. Trace element patterns for the phenocrystal olivine from both localities have similar patterns although HREE concentrations are higher in SPK than Jos.

Perovskite shows the most elevated trace element concentrations (Fig. 4.9.) and therefore is a dominant control on the whole rock trace elements. The perovskite ($[La/Yb]_N$ = 597) is significantly more LREE enriched than the whole rock ($[La/Yb]_N$ = 146). These variations in La/Yb ratios reflect variations in HREE concentrations as $[La/Nd]_N$ ratios show very little variation between any of the mineral phases and the whole rock (average $[La/Nd]_N$ = 2.8, range 2.4 to 3.4).

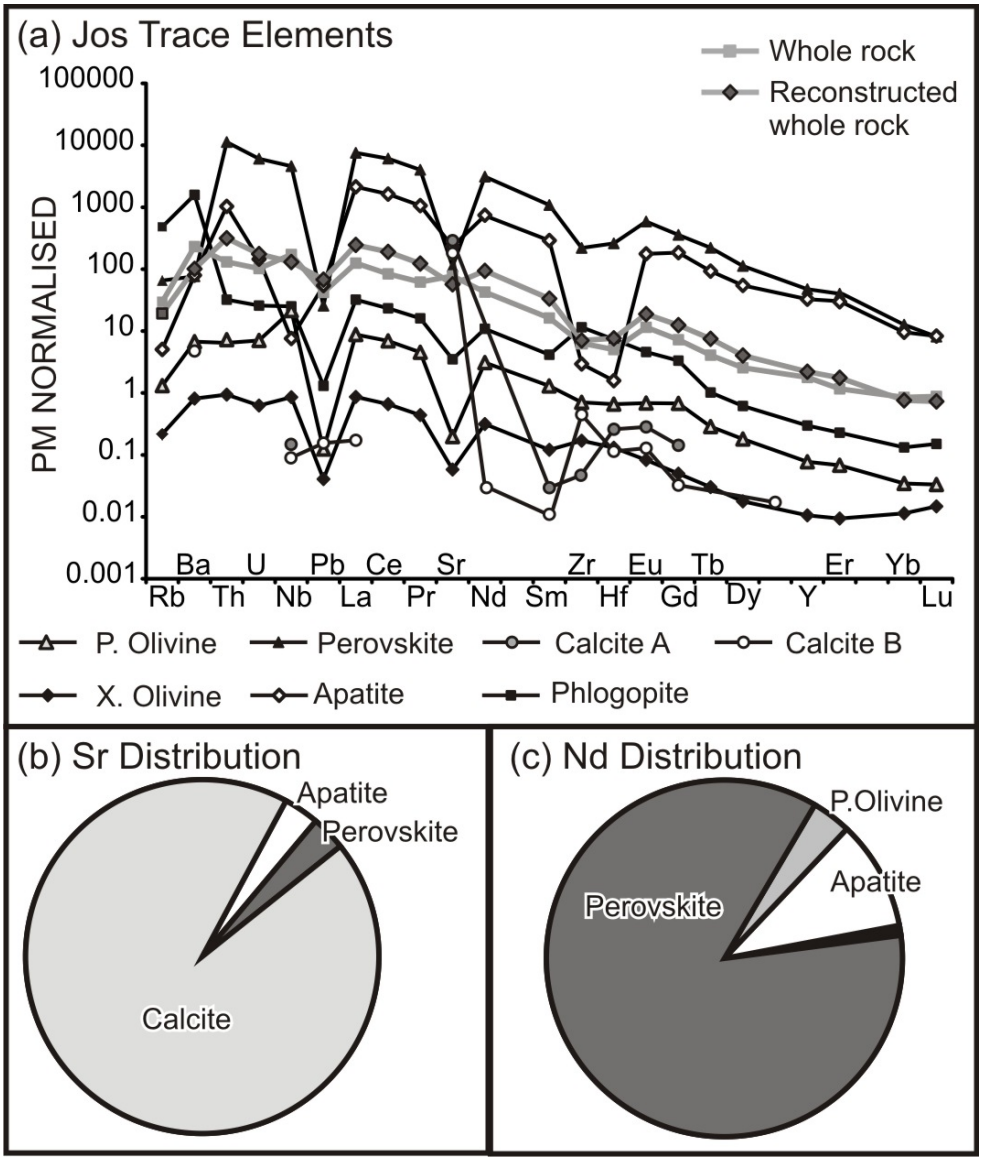

Figure 4.9.

(a) *Multi-element trace element plot for representative mineral analyses normalised to primitive mantle (Sun and McDonough 1989). These are compared to whole rock analyses and the reconstructed whole rock analysis from the mineral and modal abundance data.*

(b) *Distribution of Sr among the analysed mineral phases calculated from quantitative model abundance data (QEMSCAN) and mineral trace element concentrations. These values are normalised to 100%*

(c) *Distribution of Nd among the analysed mineral phases calculated from quantitative model abundance data (QEMSCAN) and mineral trace element concentrations. These values are normalised to 100%.*

The trace element concentrations in the apatite (Fig. 4.9.) are not as high as those in the perovskite, with the exception of Sr. The multi-element pattern is LREE-enriched ($[La/Yb]_N$ = 223) but has a significantly shallower slope than the perovskite and whole rock analyses due to high HREE concentrations. A noticeable feature of the apatite multi-element pattern is the large negative Hf-Zr anomaly.

It was not possible to drill or pick individual calcite crystals and therefore the drilled and picked results represent a whole segregation that will contain more than one morphology of calcite. On the basis of Sr/Ba ratios each segregation can be shown to be dominated by one morphology (Fig. 4.10.). These have been classified as high Sr/Ba calcite A, dominated by anhedral calcite (on the basis of the probe data) and low Sr/Ba calcite B which is dominated by tabular and euhedral to subhedral calcite and is interpreted as magmatic calcite. The concentrations of other trace elements are very low in calcite A although calcite B contains some LREE-enrichment. As observed in the probe data the Sr concentrations are very variable with calcite A containing much higher Sr concentrations than calcite B.

The whole rock trace elements have been reconstructed using representative trace element concentrations and the quantitative modal abundances calculated from the QEMSCAN images. Although the patterns are consistent for each mineral the concentrations vary. This may explain the discrepancy in terms of concentrations between the reconstructed and measured whole rock but more

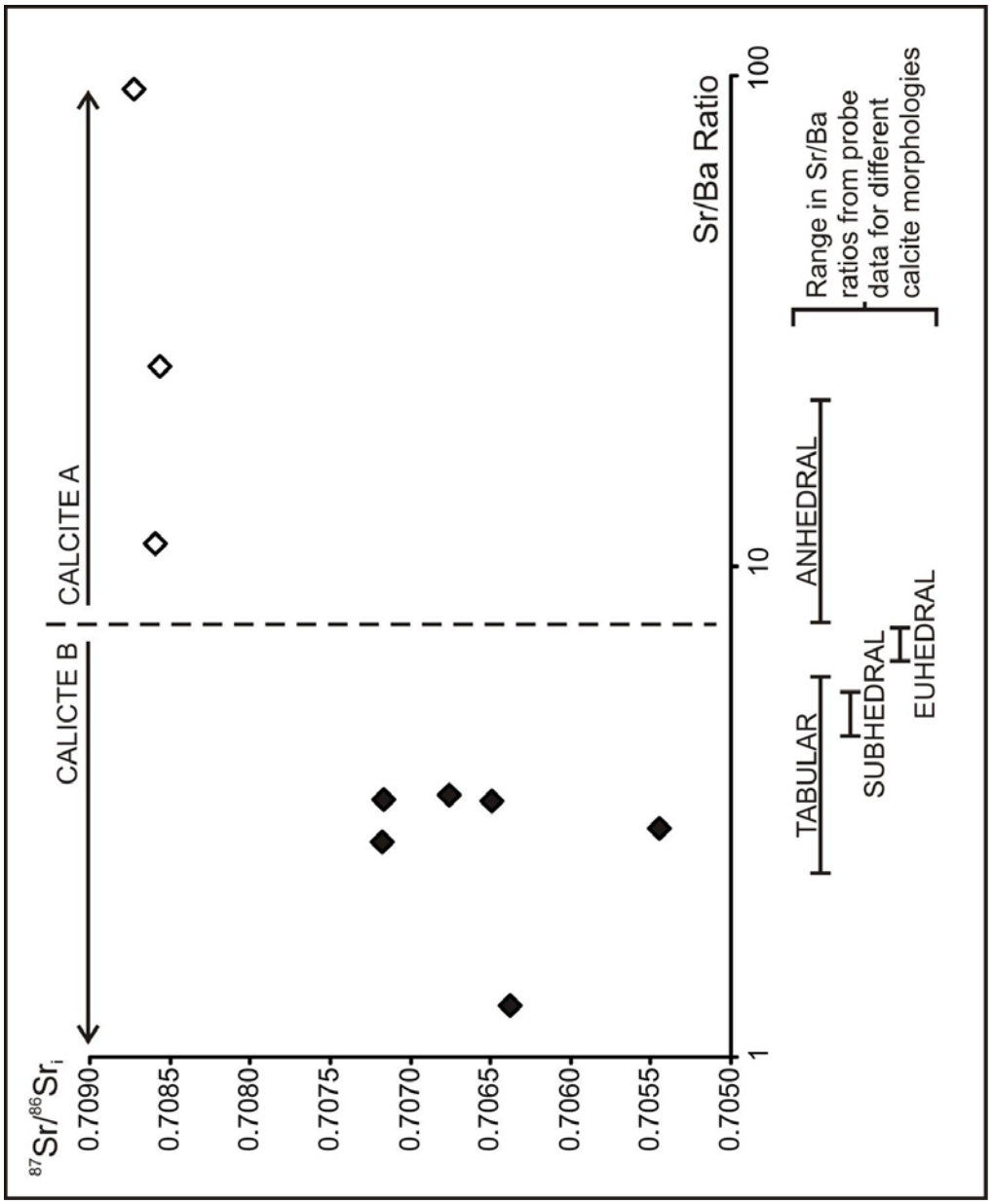

Figure 4.10.

Plot of initial $^{87}Sr/^{86}Sr$ value against Sr/Ba ratios for drilled and picked calcite segregations, illustrating the difference between calcite A and B as described in the text. Range in Sr/Ba ratios from microprobe data for the different morphologies of calcite are illustrated below the plot.

importantly the patterns are similar. The Sr in the reconstructed whole rock pattern is dominated by calcite, which is variable both in terms of concentration and in terms of the multi-element patterns. This may explain the discrepancies in terms of LREE-enrichment and Sr between the reconstructed and measured whole rock trace element data.

All of the minerals, with the exception of calcite, show a negative chondrite normalised Sr anomaly (Fig. 4.9.) which is not evident in the kimberlite trace element pattern. The Sr budget of the analysed minerals, as with the melilitite, is dominated by one phase, calcite (94%). Hence calculated trace element budgets are critically dependent on the calcite abundance and small variations on a macro scale may cause differences between measured and calculated values (e.g. Wilson et al. 2007). Perovskite (3%) and apatite (3%) also contribute to the whole rock budget and in a system with significantly less calcite these phases would become more dominant. The Nd budget, as with SPK, is dominated by perovskite (85%) with a small contribution from apatite (10%). The other analysed mineral phases contain the remaining 5% of the available Nd budget (Fig. 4.9(c)).

4.4.2. ISOTOPE VARIATION

4.4.2.1. Saltpetre Kop

Acid leachates from each phase were analysed for Sr isotopes, where possible, and were found to be within error of the mineral that was leached. Therefore grain boundary contamination had little effect on the Sr isotope ratio (see Appendix E). The two phenocrysts phases, olivine and melilite, have the least radiogenic initial $^{87}Sr/^{86}Sr$ and are within uncertainty of the whole rock (Fig 4.11; Janney et al. 2002). This is not surprising as melilite, which dominates the whole rock Sr budget, shows the smallest range in $^{87}Sr/^{86}Sr_i$ (0.70425 to 0.70428, n=5) and therefore the overlap between the melilite and the two whole rock analyses (0.70423 and 0.70425, (Janney et al. 2002)) is a reflection of this influence. The two composite (multi grain) perovskite analyses are within uncertainty of each other but are slightly more radiogenic than the whole rock. The range in $^{87}Sr/^{86}Sr_i$ increases to more radiogenic values in the later crystallising phases with individual apatite crystals showing a range from 0.70422 to 0.70448 (n=4). The two phlogopite analyses show the largest range in $^{87}Sr/^{86}Sri$ from 0.704321 to 0.704926.

The analysed phases display a significant range in $^{87}Rb/^{86}Sr$ from 0.001 in the apatite to 8.35 in the phlogopite. This variation does show an isochronous relationship with the measured $^{87}Sr/^{86}Sr$ but there are complications associated

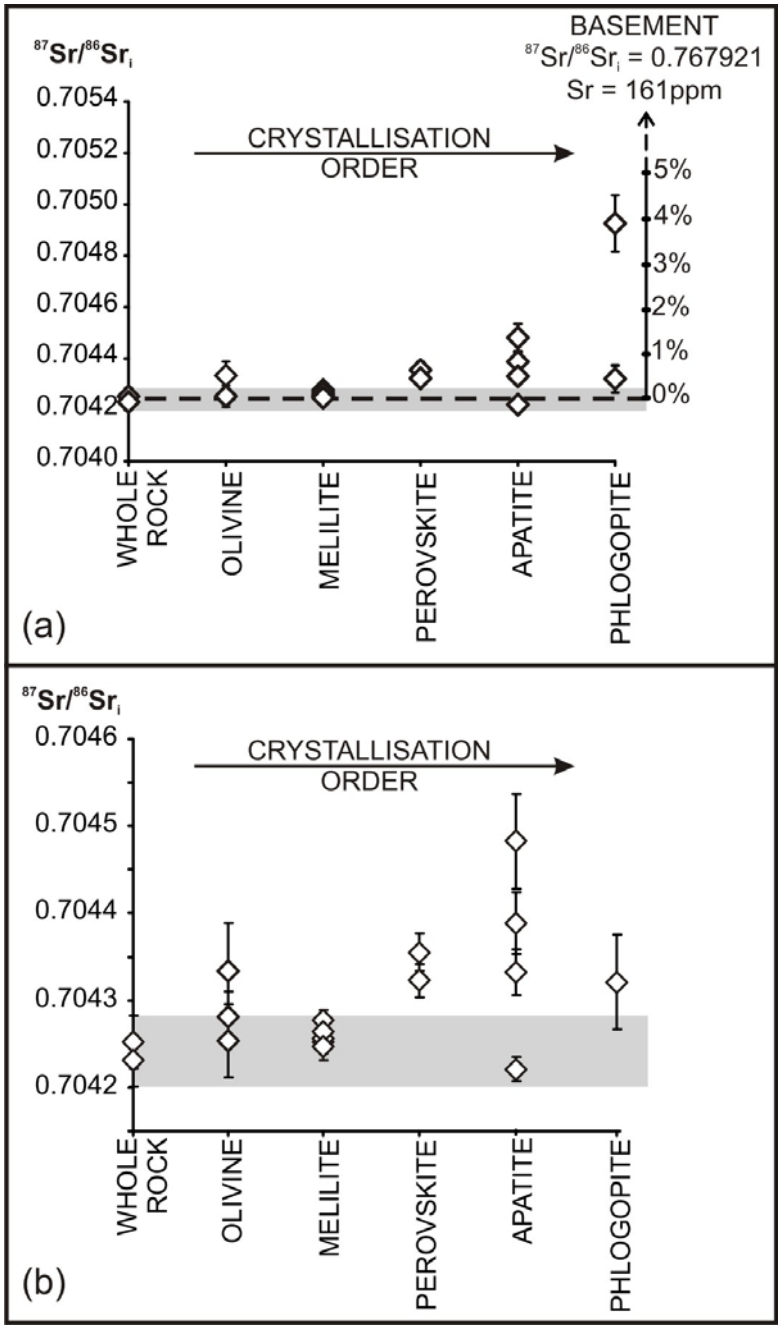

Figure 4.11.

(a) *Plot showing the $^{87}Sr/^{86}Sr_i$ values of the mineral phases and the whole rock (grey shaded band) for the olivine melilitite. The error bars represent ±2SE and are smaller than the symbol where not displayed. The crystallisation order moves from left to right. The results of simple two component mixing between the magma and the Proterozoic basement are shown to the right (see text for details).*

(b) *A more detailed plot of the same data illustrating the variation between the individual analyses of the mineral phases with the whole rock variation illustrated by the grey band. Again the error bars represent 2SE and the crystallisation order progresses from left to right.*

with calculating as age derived in this manner which are discussed in section 4.5.3.

4.4.2.2. Jos Kimberlite

The minerals from the Jos kimberlite show significantly more variation than those from the melilitite, with the majority of the minerals being significantly less radiogenic than the whole rock ($^{87}Sr/^{86}Sr_i$ = 0.706226; Fig. 4.12.). The least radiogenic phase is xenocrystal olivine with an $^{87}Sr/^{86}Sr_i$ of 0.704789 (±62 2σ). This unradiogenic signature is similar to whole rock and cpx initial $^{87}Sr/^{86}Sr$ data from low temperature mantle xenoliths from the Nikos kimberlite (Somerset Island) which show a range from 0.703776 to 0.706632 (Fig. 4.13; Schmidberger et al. 2003) indicating that the xenocrysts could originate within the lithospheric mantle beneath Somerset Island. The euhedral phenocrystal olivine is marginally more radiogenic than the xenocrystal olivine. The $^{87}Sr/^{86}Sr_i$ of the phenocrystal olivine represents the average $^{87}Sr/^{86}Sr$ of the magmatic inclusions assumed to be present within the olivine (Jackson and Hart 2006; Harlou et al. 2009).

Both individual and composite grains of perovskite were analysed. The two composite analyses (7 to 10 grains) are within uncertainty ($^{87}Sr/^{86}Sr_i$=0.704919 and 0.704920). However the individual grains analysed showed a range in $^{87}Sr/^{86}Sr_i$ from 0.704855 to 0.705269. An additional perovskite was found to be more radiogenic ($^{87}Sr/^{86}Sr_i$=0.705615) than the others and it also had an

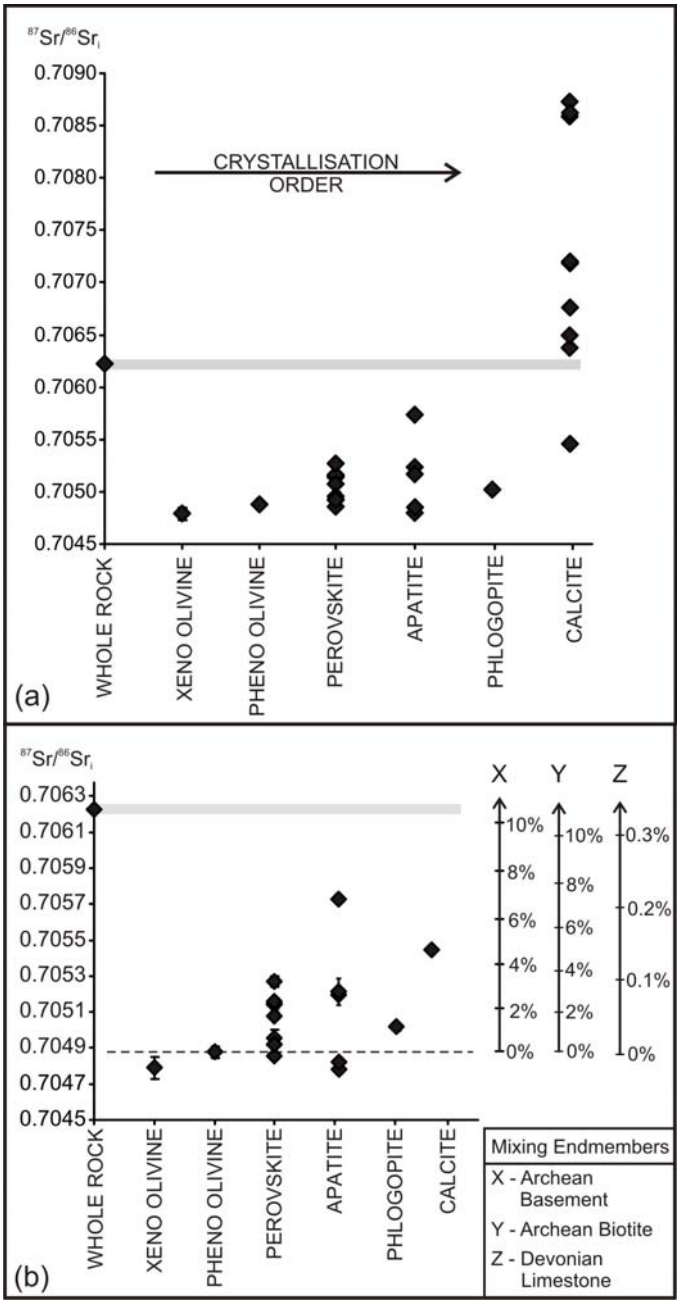

Figure 4.12

(a) *Plot of showing the $^{87}Sr/^{86}Sr_i$ variation between the mineral phases analysed from the Jos kimberlite along with the whole rock (black diamond and grey band). The symbols are larger than the errors on the analyses. The crystallisation order progresses from left to right.*

(b) *A more detailed view of the mineral $^{87}Sr/^{86}Sr_i$ variation with the whole rock again shown in the black diamond and grey shaded band. The error bars represent 2SE. The results of simple two component mixing of a proto-kimberlite melt with the Archean basement (X; wholesale melting); with a melt formed from Archean biotite (Y) and with limestone (Z); see the text for more details.*

elevated $^{87}Rb/^{86}Sr$ ratio of 0.033 compared to an average of 0.008 for the other samples. This elevated $^{87}Rb/^{86}Sr$ is attributed to high Rb present in fluid inclusions that may result from deuteric alteration of the crystal rim and, as such, this sample was rejected.

The apatite shows the largest range in $^{87}Sr/^{86}Sr_i$ from 0.704787 (comparable to the xenocrystic olivine) to 0.705726.

The sampled calcite segregations show a wide range of $^{87}Sr/^{86}Sr_i$ values from 0.705447 to 0.708725. These values correlate with Sr/Ba ratios (Fig. 4.10.) and therefore the more radiogenic segregations, with Sr/Ba values over 10, are thought to be dominated by anhedral calcite which crystallised from carbohydrothermal fluids (calcite A). The $^{87}Sr/^{86}Sr$ values of these calcites are comparable to the limestone country rock (0.708813) and therefore may reflect interaction with this endmember via hydrothermal alteration. The segregations which have Sr/Ba ratios less than about 10 are more likely to reflect segregations that are dominated, to differing extents, by magmatic calcite (calcite B).

Nd isotopes were analysed for the perovskite, where there was significant analyte (Fig. 4.13.). The Nd results for the perovskite overlapped the whole rock values and the composition of a low-T peridotite xenolith suite from the Nikos kimberlite, also on Somerset Island (Fig. 4.13.).

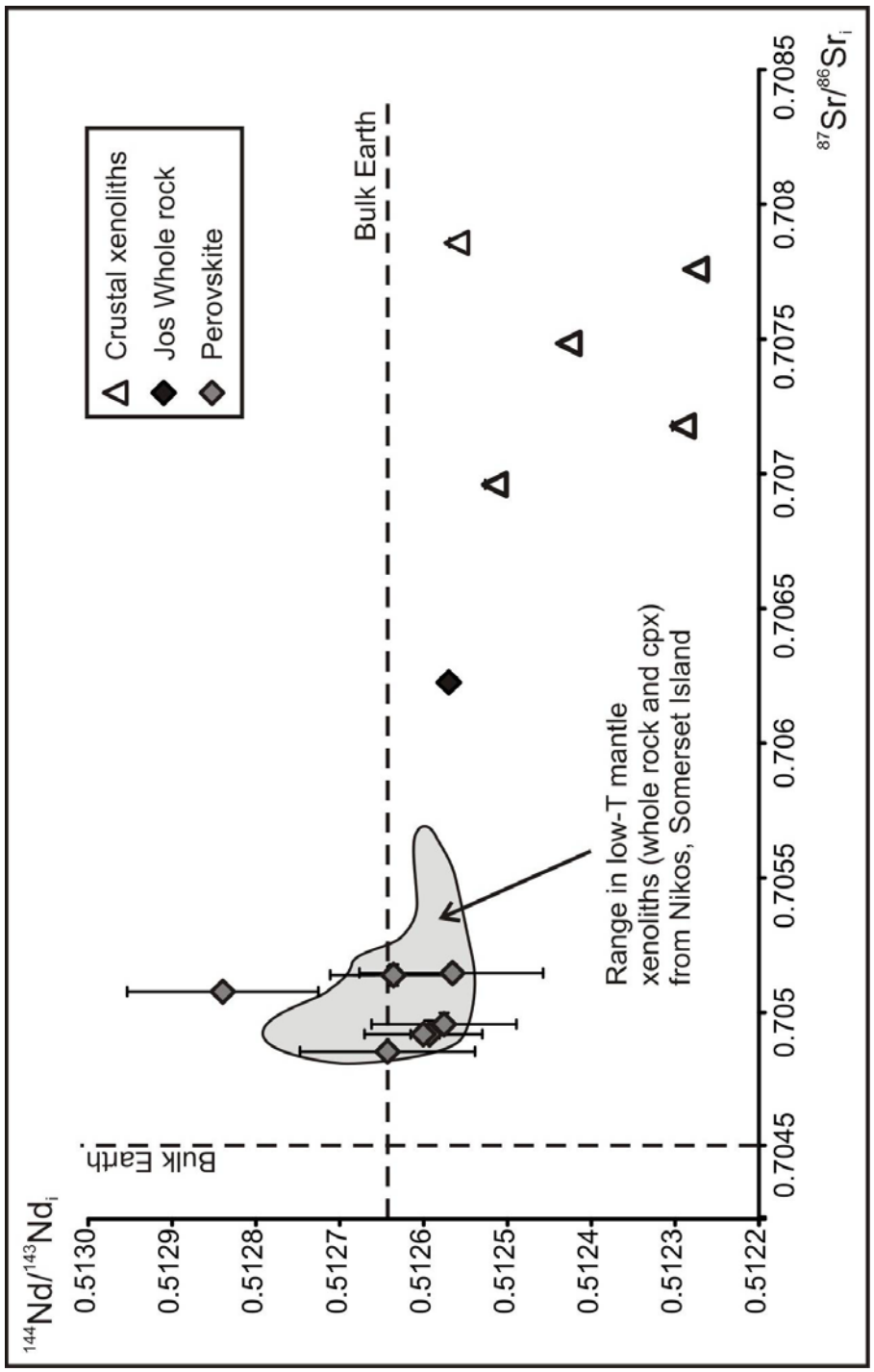

Figure 4.13.

Plot of initial Nd and Sr isotope ratios for perovskite and whole rock analyses from the Jos kimberlite. A number of analyses from crustal xenoliths found in a sample of Selatiavik (Somerset Island) kimberlite core (known for the high preservation of crustal xenoliths) are shown for reference. The grey field outlines the region where whole rock and cpx mineral separate data, taken from low-T peridotite mantle xenoliths from the Nikos kimberlite (Schmidberger et al. 2003), plot.

4.5. DISCUSSION

4.5.1. CONSTRAINING THE CRUSTAL CONTRIBUTION

Crustal assimilation through melt-wallrock reactions is a common process found in a wide range of magmatic rocks (e.g. Aitcheson and Forrest 1994; Davidson et al. 2006). Studies of zoned plagioclase phenocrysts in basaltic systems indicate that in this environment contamination can be complex and occur multiple times due to magma recharge (Davidson et al. 2006). In basaltic systems AFC (assimilation-fractional crystallisation) modelling can be used to investigate the degree of crustal assimilation. Given that the SPK melilitite and Jos kimberlite, from a macroscopic perspective, appear to be (1) minimally crustally contaminated, and (2) not highly fractionated to a nephelinite (for SPK) or aphanitic kimberlite (for Jos), batch mixing is used to approximate the amount of crustal addition.

Crustal assimilation occurs at all levels of the crust but is greatest when the temperature difference between the ascending magma and the crust are smallest i.e. in the deep crust. The mass of crust that can be assimilated into 'highly' alkaline basalts, compared to the mass of crystals fractionated is greatest in the first 70ºC to 95ºC of magma cooling as the magma ascends though the crust (Reiners et al. 1995). In kimberlite, olivine is the first phase to crystallise (>1200C; Mitchell 2008), along with Cr spinel, and this is thought to occur predominantly while the magma is passing through the lithospheric mantle

(Mitchell 2008). The lithospheric mantle has a very low Sr content and an $^{87}Sr/^{86}Sr_i$ which, from the xenocrystal olivine, is similar to the Sr isotopic composition of the primary kimberlite magma and therefore addition of this material has no effect on the magma composition in terms of Sr. This is reflected by the low $^{87}Sr/^{86}Sr_i$ value of the phenocrystal olivine. The zoning in the olivine phenocrysts indicates that olivine crystallisation is an ongoing process and therefore the rims may be in equilibrium with a slightly contaminated magma. The groundmass phases, however, are interpreted to have crystallised at higher crustal levels from a magma which may have undergone crustal more significant crustal contamination.

Simple two component mixing models can be used to assess the amount of crustal contamination required in order to generate the variation observed in the Sr ratio of minerals from SPK. The olivine melilitite intrudes through the Proterozoic Namaqua-Natal mobile belt (Janney et al. 2002) and a borehole in the vicinity of Saltpetre Kop yielded megacrystic granites at a depth of 2493m with an $^{87}Sr/^{86}Sr_{75Ma}$ of 0.767921 and a Sr concentration of 161ppm (Eglington and Armstrong 2003). Despite the SPK melilitite having over seven times more Sr than the basement the extreme difference in $^{87}Sr/^{86}Sr_i$ means that even minor crustal assimilation will have a significant impact on the isotopic signature of the melt (Fig. 4.11. and Fig. 4.14.). The observed range in $^{87}Sr/^{86}Sr_i$ in the apatite and phlogopite can be explained by a maximum addition of 5% of the granite basement to a melt with a similar composition to the olivine and melilite (Fig. 4.11. and Fig. 4.14.). It is difficult to constrain the influence of this

basement on the early crystallising olivine and melilite but the similarity in $^{87}Sr/^{86}Sr_i$ of both these phases indicates that it is likely to be minimal.

Unravelling the effects of crustal contamination is more complicated in kimberlitic systems as more processes are involved (Mitchell 1986). The phenocrystal olivine (crystallising >1200 ºC) has a low initial $^{87}Sr/^{86}Sr$ and reflects a mineral phase that has undergone minimal contamination (Fig. 4.12.). The perovskite crystals (suggested to crystallise between 1000ºC and 800ºC; (Mitchell 2008)), on the other hand, show a wide range of $^{87}Sr/^{86}Sr_i$ from values similar to the olivine up to 0.705269 (Fig. 4.12.). This suggests that the perovskite is crystallising over a period of time while progressive assimilation of the crust into the kimberlite magma is occurring. Hence, while perovskite records Sr isotope ratios that are less influenced by the crust that the whole rock, the earlier crystallising olivine, the majority of which is thought to crystallise before emplacement (Mitchell 2008), should provide a more accurate view of the isotopic composition of the unmodified magma. The mineral phase that records the most information, both about the source region as well as crustal contamination, is apatite (Fig. 4.12.). The data presented here would therefore imply that apatite crystallises over a wider temperature range than previously thought and in this case records the least radiogenic Sr isotope signature.

The Jos kimberlite intrudes through Archean basement on Somerset Island but no analyses are available from this location and therefore analyses of similar basement from nearby Baffin Island are used to estimate the amount of crustal

contamination. A two component mixing model between typical Archean basement (Fig. 4.12(b); X) from a Baffin Island granitoid with an $^{87}Sr/^{86}Sr_{98Ma}$ of 0.770862 and a Sr concentration of 177ppm (Harlou 2007) was mixed with an estimated kimberlite melt ($^{87}Sr/^{86}Sr_i$ value of 0.704879 from the phenocrystal olivine and a Sr concentration of 1000ppm taken from Dowall (2004)). The range in Sr isotope composition observed for individual perovskites can be explained with less than 4% crustal addition whereas the range in apatite $^{87}Sr/^{86}Sr_i$ values would require around 7% crustal addition. The crustal melt however is more likely to be predominantly composed of more fusible minerals such as mica as oppose to whole sale melting of the basement. Thus the addition of biotite (Fig. 4.12(b); Y) via preferential assimilation from Archean granitoids has also been modelled. The Sr concentration of biotite is variable but a value of 20ppm is used here, taken from analyses of biotites (within granites from the Kaapvaal craton (Barton and Vanreenen 1992)). Although the concentration of Sr is very low, the Sr isotopic ratio of mica is extremely high. Mixing between mica ($^{87}Sr/^{86}Sr_{98Ma}$ = 1.2532) and the kimberlite melt therefore indicates that an addition of less than 4% mica would be needed to explain the range observed in the perovskites or 6% to explain the Sr isotope range observed in the apatite analyses. The Jos kimberlite dyke intrudes through Silurian limestone and contains some limestone xenoliths. The addition of this lithology (Fig. 4.12(b); Z) to 'primary' kimberlite magma has also been modelled and only 0.2 to 0.3% assimilation of this limestone would be required (Fig. 4.12.). Crustal assimilation will occur at multiple levels in the crust and therefore it is not possible to exactly constrain the degree of crustal assimilated but the results of this simple modelling implies that an addition of less than 10%

of crustal material would be required to generate the observed range in Sr isotopes in the apatite. Once again it is clear that while the perovskite contains significantly less radiogenic Sr than the whole rock kimberlite, this phase has seen the influence of crustal contamination. A more accurate view of the uncontaminated kimberlite magma can be obtained from phenocrystal olivine which, despite the low Sr concentrations, records relatively low $^{87}Sr/^{86}Sr_i$ values. However, as with SPK, the mineral phase that records the most information, both about the source region and crustal contamination is apatite. Apatite was thought to crystallise relatively late (>650ºC but after perovskite, spinel and olivine; Mitchell, 2008) but this study would indicate, both from the petrography (apatite included in early olivine rims as well as in the late forming calcite-serpentine segregations) and the Sr isotope data (Fig. 4.14.) that apatite may have crystallised over a much larger temperature window. This may be due to the elevated phosphorous content of kimberlite magma compared to other, more basaltic, systems.

4.5.2. KIMBERLITE-MANTLE Sr ISOTOPIC RELATIONSHIPS

The potential of perovskites to provide a better constraint on the initial $^{87}Sr/^{86}Sr$ of kimberlites than the whole rock has recently been exploited (Heaman 1989; Paton et al. 2007a; Kamenetsky et al. 2009; Woodhead et al. 2009). Paton et al (2007a) used LA-ICP-MS on perovskites from two Indian kimberlite fields, which were indistinguishable in terms of whole rock Sr isotope data. The

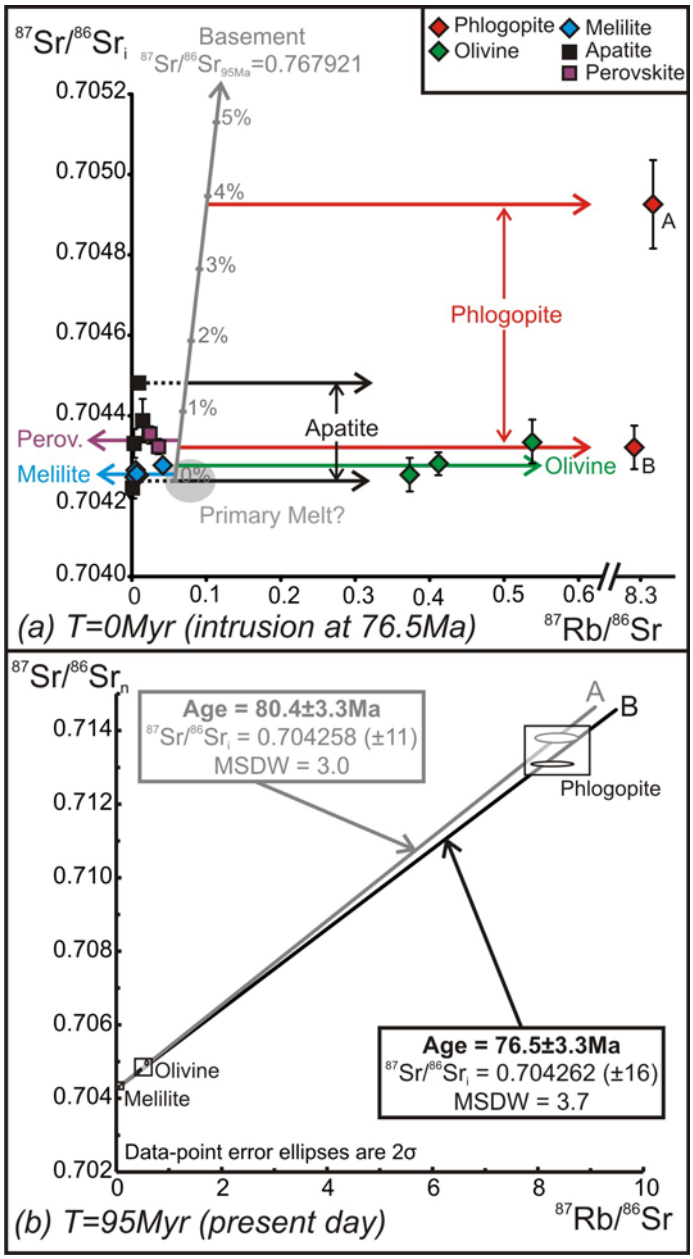

Figure 4.14.

(a) *A plot of the initial (at the time of emplacement 76.5Ma) $^{87}Sr/^{86}Sr$ ratio against $^{87}Rb/^{86}Sr$ (note the break in the x axis) of the individual minerals from the olivine melilitite (SPK). A mixing line between the primary melt and the basement in plotted for reference and the points when the minerals crystallised (with their own $^{87}Rb/^{86}Sr$ values) throughout the process of crustal assimilation is shown by the arrows.*

(b) *An isochron plot using the normalised $^{87}Sr/^{86}Sr$ values (at the present day) illustrating the different ages that can be obtained using the two different phlogopite analyses that have been affected to differing extents by crustal assimilation (as illustrated in (a)).*

perovskite data could be used to distinguish between the two fields and indicated that there were two slightly different sources with significantly lower $^{87}Sr/^{86}Sr$ than suggested by the whole rock hosts. The success of this study was aided by the fact that the kimberlites, from this locality, were significantly altered and this generated significant radiogenic Sr in the whole rock over the 1.2Ga since their eruption. Perovskites, on the other hand, has low Rb/Sr and therefore require only a very minor age correction over 1.2Ga. Furthermore they are relatively robust to alteration. The application of LA-ICP-MS has been extended to a number of South African kimberlites where the differences between the whole rock and perovskite Sr analyses, although evident, are less dramatic (Woodhead et al. 2009). Nonetheless, it is clear that perovskites provide a better constraint than whole rock data on the $^{87}Sr/^{86}Sr$ composition of the 'primary' kimberlite magma.

The data we have presented in this study shows that there is a range in $^{87}Sr/^{86}Sr_i$ values in perovskites from a single sample of the 98Ma Jos kimberlite. This range is attributed to progressive crustal assimilation occurring as the perovskite is crystallising from the magma. This indicates that perovskites do not necessarily give the closest approximation to the source composition. The range in $^{87}Sr/^{86}Sr$ between crystals, although resolvable above uncertainty using TIMS, would not be resolvable in LA-ICP-MS studies and it is therefore important to analyse a number of crystals to characterise the range in $^{87}Sr/^{86}Sr$.

Kimberlite magma (originating in the convecting mantle) has been implicated, from trace element data, as a likely metasomatic agent responsible for the addition of cpx (the dominant host for Sr in the peridotite) to the lithospheric mantle (Gregoire et al. 2003; Simon et al. 2003). However there is a degree of mismatch between Sr isotope values observed from mantle cpx (from peridotite xenoliths) and those from whole rock kimberlite analyses. However the new data from the Jos phenocrystal olivine is within the range observed for cpx and whole rock mantle xenoliths from Somerset Island (Schmidberger et al. 2001) and therefore this data would support a closer link between the kimberlite, as a metasomatic agent, and modal metasomatism in the lithospheric mantle.

4.5.3 KIMBERLITE - MEGACRYST- DIAMOND RELATIONSHIPS

An additional aspect of our data, when combined with recently published perovskite data is that it allows a closer examination of the relationship between kimberlite and the low-Cr megacryst suite. The relationship of megacrysts and the kimberlite magma has long been debated (e.g. Jones 1987; Hops et al. 1992; Davies et al. 2001; Nowell et al. 2004; Kopylova et al. 2009). This debate centers on whether there is a genetic link between the kimberlite magma and the megacryst suite (Jones 1987; Nowell et al. 2004; Kopylova et al. 2009) or whether the two are independent of each other (Davies et al. 2001). A key piece of evidence that has been used to argue against megacrysts crystallising from kimberlites is that megacrysts have less radiogenic Sr isotope ratios than whoel rock kimberlite analyses (Fig. 2; Davies et al. 2001) despite both showing a

similar range in Nd and Hf isotope ratios (Nowell et al. 2004). Nowell et al (2004) argued that the difference in Sr is related to the greater susceptibility of kimberlite whole rock $^{87}Sr/^{86}Sr_i$ to alteration and contamination. The new data presented here as well as the new perovskite data supports this hypothesis. The majority of published low-Cr megacryst Sr isotope data comes from southern African Group I kimberlites where new perovskite Sr isotope data are now available (Woodhead et al. 2009). A compilation of this new data, with corresponding megacryst data, shows that although the megacrysts show a wide range of $^{87}Sr/^{86}Sr_i$ values, there is a significant overlap with the perovskite data (Fig. 4.15.). In the case of Monastery, where all three types of data are available, the early forming megacrysts again show a range in initial $^{87}Sr/^{86}Sr$ but the cpx megacrysts are similar to the estimate from the perovskite. The later crystallising ilmenite megacrysts extend to more radiogenic values and Nowell et al (2004) suggest that at this stage the megacryst magma has interacted with the lithospheric mantle.

A further piece of evidence used to argue against a close link between megacrysts and their host kimberlite is the disagreement between the REE patterns of the melts that are predicted to be in equilibrium with low-Cr megacryst suite and the host kimberlite. Davies et al. (2001) observed that the REE patterns of the melt predicted to be in equilibrium with clinopyroxene (cpx) megacrysts included in the Gideon kimberlite, Namibia, would have chondrite normalised $[La/Yb]_N$ ratios of about 20, much lower than the host kimberlite ($[La/Yb]_N$ from 90 to 110). However if new partition coefficients for REE partitioning between cpx and a kimberlite melt are used the resulting

predicted melt would have $[La/Yb]_N$ ratios ranging from 134 to 158, more comparable to the kimberlite. Furthermore assimilation of crust into a kimberlite magma has been shown to increase the concentration of HREE in the melt (Dowall 2004), thus reducing the $[La/Yb]_N$ ratio of the contaminated kimberlite magma. The true $[La/Yb]_N$ ratio of the primary kimberlite magma would therefore be higher leading to a larger degree of overlap between the melts predicted from the megacrysts and the host kimberlite magma. The trace element composition of the primary kimberlite magma could potentially be better constrained using the mineral data here if experimental constraints on partitioning were developed. Therefore these data remove key arguments against an intimate link between the kimberlite magma and the low-Cr megacryst suite.

Recent trace element studies on fluid micro-inclusions found in diamonds, thought to reflect the fluid the diamond grew from, have been shown to have trace element patterns similar to kimberlites or carbonatites. This had led some authors to suggest a genetic relationship between some diamond forming fluids and kimberlite magmas (e.g. Klein-BenDavid et al. in press and references therein.). However crustal contamination affects the trace element composition of whole rock kimberlite analyses (Dowall 2004) and although the experimental partitioning data is not yet available for kimberlite minerals and their melts the data presented here could, eventually, help clarify the true trace element composition of the kimberlite magma. The data presented here as well as the new perovskite data confirm that the primary Sr isotope ratio of the kimberlite magmas tends to have convecting mantle Sr isotope values. The Sr

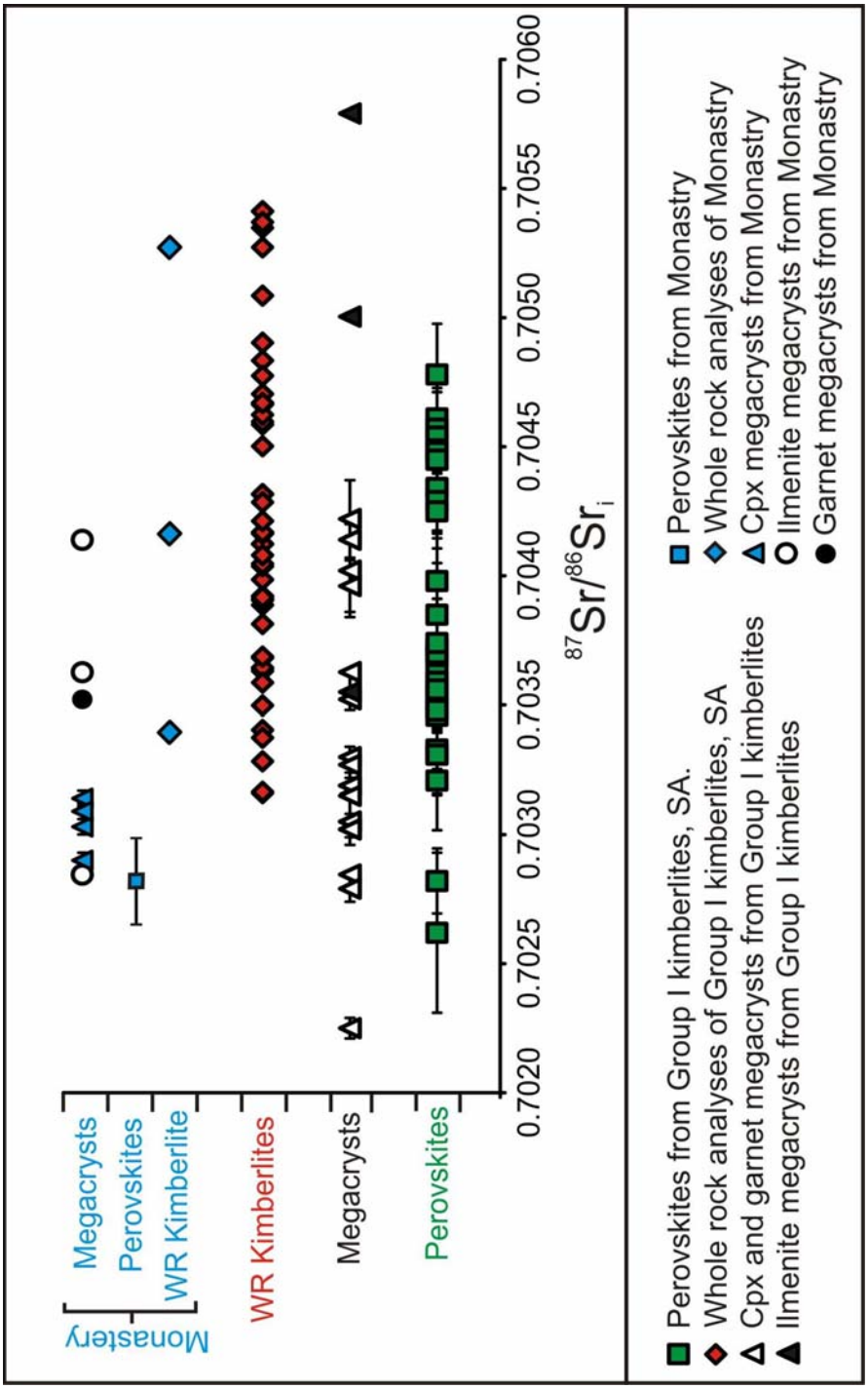

Figure 4.15.

Plot of initial $^{87}Sr/^{86}Sr$ values for megacrysts (Nowell et al. 2004), Group I kimberlites (Becker and Le Roex 2006) and perovskites (Woodhead et al. 2009) from South Africa. The same data is also plotted just for the Monastery Pipe, South Africa (same data sources).

isotope composition of the diamond forming fluids show a wide range from such convecting mantle values up to more radiogenic ratios which has lead Klein BenDavid (in press; and references therein) to argue that kimberlite or carbonatite melts had a role in diamond formation.

4.5.3. Rb-Sr GEOCHRONOLOGY

Rb-Sr isochrons have been widely used to date igneous rocks including kimberlites (e.g. Smith et al. 1985; Creaser et al. 2004). A requirement of this method is that the initial isotopic ratios of all the mineral phases being used are within uncertainty when they crystallise. Therefore any progressive crustal contamination that occurs while the minerals are crystallising will change the resulting $^{87}Sr/^{86}Sr_i$ value of those minerals and thus causes scatter on the isochron diagram. Davidson et al (2005) showed that it is possible for limited variation in the initial Sr ratio to be obscured in an isochron that appears to be statistically valid. In order to assess the validity of any isochron it is critical to assess sample petrography and if possible corroborate with an external age estimate.

The minerals from the olivine melilitite scatter around an isochron which yields a slope equivalent to an age of 77.4 ± 2.6Ma (MSDW = 23). This age is within error of the K-Ar age, although the absolute age is slightly older. This older Rb/Sr age is probably a result of including data that have been affected by crustal contamination (Davidson et al. 2005), which produces the high MSDW

(a function of scatter). If we select phases/analyses that appear to have been least affected by contamination or alteration, i.e. only the melilite, olivine and one of the phlogopite analyses then the absolute ages reduces to 76.0 ± 3.3Ma and the MSWD is reduced to 3.7 (Fig. 4.14(b)). This age is therefore in closer agreement with the K-Ar age. If this is repeated and the isochron plotted using the phlogopite analysis that has been affected by crustal contamination the age increases to 80.7Ma ± 3.2Ma (MSWD=3.0; Fig. 4.14(b)). This illustrates the importance of phlogopite, as the high Rb/Sr phase, in constraining the age. It is also important to note that K-Ar ages are also affected by crustal contamination as addition of old crust can add radiogenic Ar to the magma.

These results have implications for kimberlite geochronology studies using the Rb-Sr system on macrocrystic and/or phenocrystal and groundmass phlogopites. In the present study, phlogopite certainly exhibits significant variation. An application of this technique which uses Rb-Sr isotope data from macrocrystic phlogopite combined with the range in Rb/Sr ratios to calculate an age from an Rb-Sr isochron (e.g. Creaser et al. 2004). However in some cases a single phlogopite crystal is used to calculate a "model age". In this case is it is important to be able to distinguish between xenocrystal and phenocrystal phlogopite which, as shown in this study, is not always straightforward. If the phlogopite was a phenocryst then assumptions about the initial value could be misleading if that phlogopite had crystallised after significant crustal contamination had occurred. Therefore crustal contamination is a key issue in understanding and interpreting Rb/Sr and K/Ar ages.

4.6. CONCLUSIONS AND IMPLICATIONS

1. In contrast to previous LA-ICP-MS studies these high precision TIMS data presented in this study identify a significant range in initial Sr isotope ratios amongst mineral phases as well as among individual grains of the same phase, e.g. perovskite. These ranges reflect the effects of crustal contamination and therefore although perovskite provides a closer approximation to the kimberlite source region than the whole rock it may have also been affected by some contamination. We suggest that apatite offers the most potential despite the analytical challenge it presents.

2. The data presented here, combined with published perovskite data, allows for a more accurate comparison between the parental kimberlite magma and the low-Cr megacrysts suite. This comparison reveals a strong overlap in Sr isotopic compositions, supporting previous Nd and Hf isotopic studies, and implying a close genetic link between the two.

3. This study has revealed highly variable $^{87}Sr/^{86}Sr_i$ ratios in different phases (especially phlogopite) that indicate that caution is required when using phlogopite to determine Rb-Sr ages. This applies especially to single crystal model emplacement ages.

4.7. REFERENCES

Aitcheson, S. J. and Forrest, A. H. (1994). "Quantification of Crustal Contamination in Open Magmatic Systems." Journal of Petrology 35(2): 461-488.

Barton, J. M. and Vanreenen, D. D. (1992). "The Significance of Rb-Sr Ages of Biotite and Phlogopite for the Thermal History of the Central and Southern Marginal Zones of the Limpopo Belt of Southern Africa and the Adjacent Portions of the Kaapvaal Craton." Precambrian Research 55(1-4): 17-31.

Beattie, P. (1994). "Systematics and Energetics of Trace-Element Partitioning between Olivine and Silicate Melts - Implications for the Nature of Mineral Melt Partitioning." Chemical Geology 117(1-4): 57-71.

Becker, M. and Le Roex, A. P. (2006). "Geochemistry of South African on- and off-craton, Group I and Group II kimberlites: Petrogenesis and source region evolution." Journal of Petrology 47(4): 673-703.

Benvie, B. (2007). "Mineralogical imaging of kimberlites using SEM-based techniques." Minerals Engineering 20(5): 435-443.

Boctor, N. Z. and Yoder, H. S. (1986). "Petrology of Some Melilite-Bearing Rocks from Cape-Province, Republic of South Africa - Relationship to Kimberlites." American Journal of Science 286(7): 513-539.

Charlier, B. L. A., Ginibre, C., Morgan, D., Nowell, G. M., Pearson, D. G., Davidson, J. P. and Ottley, C. J. (2006). "Methods for the microsampling and high-precision analysis of strontium and rubidium isotopes at single crystal scale for petrological and geochronological applications." Chemical Geology 232(3-4): 114-133.

Creaser, R. A., Grutter, H., Carlson, J. and Crawford, B. (2004). "Macrocrystal phlogopite Rb-Sr dates for the Ekati property kimberlites, Slave Province, Canada: evidence for multiple intrusive episodes in the Paleocene and Eocene." Lithos 76(1-4): 399-414.

Davidson, J., Charlier, B. and Hora, J. M. (2005). "Mineral isochrons and isotopic fingerprinting: Pitfalls and promises." Geology 33(1): 29-32.

Davidson, J. P., Font, L., Charlier, B. L. A. and Tepley, F. J. (2006). "Mineral-scale Sr isotope variation in plutonic rocks - a tool for unravelling the evolution of magma systems." Transactions of the Royal Society of Edinburgh-Earth Sciences 97: 357-367.

Davies, G. R., Spriggs, A. J. and Nixon, P. H. (2001). "A non-cognate origin for the Gibeon kimberlite megacryst suite, Namibia: Implications for the origin of Namibian kimberlites." Journal of Petrology 42(1): 159-172.

Deer, W. A., Howie, R. A. and Zussman, J. (1992). An introduction to the rock-forming minerals, Pearson.

DeWet, J. J. (1975). "Carbonatites and related rocks at Saltpetre Kop, Sutherland, Cape Province." Annals, University of Stellenbosch (Series A1) 1: 193-232.

Dowall, D. (2004). Elemental and isotopic geochemistry of kimberlites from the Lac de Gras field, Northwest Territories, Canada. Department of Earth Sciences. Durham, Durham University. PhD.

Dowall, D. P., Nowell, G. M. and Pearson, D. G. (2003). "Chemical pre-concentration procedures for high-precision analysis of Hf-Nd-Sr isotopes in geological materials by plasma ionisation multi-collector mass spectrometry (PIMMS) techniques." Plasma Source Mass Spectrometry: Applications and Emerging Technologies: 321-337.

Duncan, R. A., Hargraves, R. B. and Brey, G. P. (1978). "Age, paleomagnetism and chemistry of melilite basalts in the Southern Cape, South Africa." Geological Magazine 115(5): 317-396.

Dunworth, E. A. and Wilson, M. (1998). "Olivine melilitites of the SW German Tertiary Volcanic Province: mineralogy and petrogenesis." Journal of Petrology 39(10): 1805-1836.

Eglington, B. M. and Armstrong, R. A. (2003). "Geochronological and isotopic constraints on the Mesoproterozoic Namaqua-Natal Belt: evidence from deep borehole intersections in South Africa." Precambrian Research 125(3-4): 179-189.

Erlank, A. J., Waters, F. G., Hawkesworth, C. J., Haggerty, S. E., Allsopp, H. L. and Menzies, M. A. (1987). Evidence for mantle metasomatism in peridotite nodules from the Kimberley Pipes, South Africa. Mantle

Metasomatism. Menzies, M. A. and Hawkesworth, C., Academic Press**:** 221-312.

Font, L., Davidson, J. P., Pearson, D. G., Nowell, G. and Ottely, C. (2006). "Detailed histories of magma transfer and contamination in a flood basalt province - a Sr isotope micro-sampling study of Skye basalts." Geochimica et Cosmochimica Acta 70(18): A181-A181.

Gregoire, M., Bell, D. R. and Le Rouex, A. P. (2003). "Garnet lherzolites from the Kaapvaal craton (South Africa): Trace element evidence for a metasomatic history." Journal of Petrology 44(4): 629-657.

Harlou, R. (2007). Understanding magma genesis through analysis of melt inclusions: application of innovative micro-sampling techniques. Department of Earth Sciences. Durham, Durham Univeristy. PhD.

Harlou, R., Pearson, D. G., Nowell, G. M., Ottley, C. J. and Davidson, J. P. (2009). "Combined Sr isotope and trace element analysis of melt inclusions at sub-ng levels using micro-milling, TIMS and ICPMS." Chemical Geology 260(3-4): 254-268.

Heaman, L. M. (1989). "The nature of the subcontinental mantle from Sr-Nd-Pb isotopic studies on kimberlitic perovskite." Earth and Planetary Science Letters 92(3-4): 323-334.

Hoal, K. O., Appleby, S. K., Stammer, J. G. and Palmer, C. (2009). "SEM-based quantitative mineralogical analysis of peridotite, kimberlite, and concentrate." Lithos In Press, Accepted Manuscript.

Hops, J. J., Gurney, J. J. and Harte, B. (1992). "The Jagersfontein Cr-Poor Megacryst Suite - Towards a Model for Megacryst Petrogenesis." Journal of Volcanology and Geothermal Research 50(1-2): 143-160.

Jackson, M. G. and Hart, S. R. (2006). "Strontium isotopes in melt inclusions from Samoan basalts: Implications for heterogeneity in the Samoan plume." Earth and Planetary Science Letters 245(1-2): 260-277.

Janney, P. E., Le Roex, A. P., Carlson, R. W. and Viljoen, K. S. (2002). "A chemical and multi-isotope study of the Western Cape olivine melilitite province, South Africa: Implications for the sources of kimberlites and the origin of the HIMU signature in Africa." Journal of Petrology 43(12): 2339-2370.

Jones, R. A. (1987). Strontium and neodymium isotopic and rare earth element evidence for the genesis of megacrysts in kimberlites of southern Africa. Mantle Xenoliths. Nixon, P. H., Wiley**:** 711.

Kamenetsky, V. S., Maas, R., Kamenetsky, M. B., Paton, C., Phillips, D., Golovin, A. V. and Gornova, M. A. (2009). "Chlorine from the mantle: Magmatic halides in the Udachnaya-East kimberlite, Siberia." Earth and Planetary Science Letters In Press, Corrected Proof.

Kjarsgaard, B. A., Pearson, D. G., Tappe, S., Nowell, G. M. and Dowall, D. P. (2009). "Geochemistry of hypabyssal kimberlites from Lac de Gras, Canada: Comparisons to a global database and applications to the parent magma problem." Lithos 112(Supplement 1): 236-248.

Klein-BenDavid, O., Pearson, D. G., Nowell, G. M., Ottley, C. J., McNeill, J. C. R. and Cartigny, P. (2009). "Mixed fluid sources involved in diamond growth constrained by Sr-Nd-Pb-C-N isotopes and trace elements." Earth and Planetary Science Letters in press.

Klein-BenDavid, O., Pearson, D. G., Nowell, G. M., Ottley, C. J., McNeill, J. C. R. and Cartigny, P. (in press). "Mixed fluid sources involved in diamond growth constrained by Sr-Nd-Pb-C-N isotopes and trace elements." Earth and Planetary Science Letters.

Kopylova, M. G., Nowell, G. M., Pearson, D. G. and Markovic, G. (2009). "Crystallization of megacrysts from protokimberlitic fluids: Geochemical evidence from high-Cr megacrysts in the Jericho kimberlite." Lithos 112(Supplement 1): 284-295.

Kramers, J. D. and Smith, C. B. (1983). "A Feasibility Study of U-Pb and Pb-Pb Dating of Kimberlites Using Groundmass Mineral Fractions and Whole-Rock Samples." Isotope Geoscience 1(1): 23-38.

Mahotkin, I. L., Gibson, S. A., Thompson, R. N., Zhuravlev, D. Z. and Zherdev, P. U. (2000). "Late Devonian diamondiferous kimberlite and alkaline picrite (Proto-kimberlite?) - Magmatism in the Arkhangelsk Region, NW Russia." Journal of Petrology 41(2): 201-227.

Mitchell, R. H. and Meyer, H. O. A. (1980). "Mineralogy of micaceous kimberlite from the Jos dyke, Somerset Island, N.W.T." Canadian Mineralogist 18: 241-250.

Mitchell, R. H. (1986). Kimberlites: Mineralogy, Geochemistry, and Petrology, Plenum Press.

Mitchell, R. H. (1995). Kimberlites, Orangeites, and Related Rocks. New York, Plenum.

Mitchell, R. H. (2008). "Petrology of hypabyssal kimberlite: relevance to primary magma compositions." Journal of Volcanology and Geothermal Research 174: 1-8.

Nowell, G. M. and Parrish, R. R. (2002). Simultaneous acquisition of isotope compositions and parent/daughter ratios by non-isotope dilution solution-mode Plasma ionisation Multi-collector Mass Spectrometry (PIMMS). Plasma Source Mass Spectrometry The New Millenium**:** 298-310.

Nowell, G. M., Pearson, D. G., Bell, D. R., Carlson, R. W., Smith, C. B., Kempton, P. D. and Noble, S. R. (2004). "Hf isotope systematics of kimberlites and their megacrysts: New constraints on their source regions." Journal of Petrology 45(8): 1583-1612.

Nowell, G. M., Luguet, A., Pearson, D. G. and Horstwood, M. S. A. (2008). "Precise and accurate 186Os/188Os and 187Os/188Os measurements by multi-collector plasma ionisation mass spectrometry (MC-ICP-MS) part I: Solution analyses." Chemical Geology 248(3-4): 363-393.

Paton, C., Hergt, J. M., Phillips, D., Woodhead, J. D. and Shee, S. R. (2007a). "New insights into the genesis of Indian kimberlites from the Dharwar Craton via in situ Sr isotope analysis of groundmass perovskite." Geology 35(11): 1011-1014.

Paton, C., Woodhead, J. D., Hergt, J. M., Phillips, D. and Shee, S. (2007b). "Strontium isotope analysis of kimberlitic groundmass perovskite via LA-MC-ICP-MS." Geostandards and Geoanalytical Research 31(4): 321-330.

Pearson, D. G., Canil, D. and Shirey, S. B., Eds. (2003). Mantle sample included in volcanic rocks: xenoliths and diamonds. Treatise on Geochemistry: The Mantle and Core, Elsevier.

Pearson, D. G. and Nowell, G. M. (2005). Accuracy and precision in plasma ionisation multi-collector mass spectrometry: constraints from neodymium and hafnium isotope measurements. Plasma Source Mass

Spectrometry, Current Trends and Future Developments, Special Publication of the Royal Society of Chemistry. Holland, G. and Bandura, D. R.**:** 284-314.

Pearson, D. G. and Wittig, N. (2008). "Formation of Archaean continental lithosphere and its diamonds: the root of the problem." Journal of the Geological Society 165: 895-914.

Ramos, F. C. and Reid, M. R. (2005). "Distinguishing melting of heterogeneous mantle sources from crustal contamination: Insights from Sr isotopes at the phenocryst scale, Pisgah Crater, California." Journal of Petrology 46(5): 999-1012.

Reiners, P. W., Nelson, B. K. and Ghiorso, M. S. (1995). "Assimilation of Felsic Crust by Basaltic Magma - Thermal Limits and Extents of Crustal Contamination of Mantle-Derived Magmas." Geology 23(6): 563-566.

Royse, K. R., Kempton, P. D. and Darbyshire, D. P. F. (1998). Procedure for the analysis for Rb-Sr and Sm-Nd isotopes at the NERC isotope geosciences laboratory. NERC Isotope Geosciences Laboratory Report Series. No. 121.

Schmidberger, S. S., Simonetti, A. and Francis, D. (2001). "Sr-Nd-Pb isotope systematics of mantle xenoliths from Somerset Island kimberlites: Evidence for lithosphere stratification beneath Arctic Canada." Geochimica et Cosmochimica Acta 65(22): 4243-4255.

Schmidberger, S. S., Simonetti, A. and Francis, D. (2003). "Small-scale Sr isotope investigation of clinopyroxenes from peridotite xenoliths by laser ablation MC-ICP-MS - implications for mantle metasomatism." Chemical Geology 199(3-4): 317-329.

Schrauder, M., Koeberl, C. and Navon, O. (1996). "Trace element analyses of fluid-bearing diamonds from Jwaneng, Botswana." Geochimica et Cosmochimica Acta 60(23): 4711-4724.

Simon, N. S. C., Irvine, G. J., Davies, G. R., Pearson, D. G. and Carlson, R. W. (2003). "The origin of garnet and clinopyroxene in "depleted" Kaapvaal peridotites." Lithos 71(2-4): 289-322.

Smith, B. H. S., Skinner, E. M. and Clement, C. R. (1983). "Further Data on the Occurrence of Pectolite in Kimberlite." Mineralogical Magazine 47(342): 75-78.

Smith, C. B., Allsopp, H. L., Kramers, J. D., Hutchinson, G. and Rodick, J. C. (1985). "Emplacement ages of Jurassic-Cretaceous South African kimberlites by the Rb-Sr method on phlogopite and whole rock samples." Transactions of the Geological Society of South Africa 88: 249-266.

Sparks, R. S. J., Baker, L., Brown, R. J., Field, M., Schumacher, J., Stripp, G. and Walters, A. (2006). "Dynamical constraints on kimberlite volcanism." Journal of Volcanology and Geothermal Research 155(1-2): 18-48.

Sun, S. S. and McDonough, W. F. (1989). "Chemical and isotopic systematics of oceanic basalts: implications for mantle composition and processes." Geological Society, London, Special Publications 42(1): 313-345.

Thirlwall, M. (1991). "Long term reproducibility of multicollector Sr and Nd ratio analyses." Chemical Geology (Isotope Science Section) 94: 85-104.

Tomlinson, E., De Schrijver, I., De Corte, K., Jones, A. P., Moens, L. and Vanhaecke, F. (2005). "Trace element compositions of submicroscopic inclusions in coated diamond: A tool for understanding diamond petrogenesis." Geochimica et Cosmochimica Acta 69(19): 4719-4732.

Walters, A. L., Phillips, J. C., Brown, R. J., Field, M., Gernon, T., Stripp, G. and Sparks, R. S. J. (2006). "The role of fluidisation in the formation of volcaniclastic kimberlite: Grain size observations and experimental investigation." Journal of Volcanology and Geothermal Research 155(1-2): 119-137.

Weis, D., Kieffer, B., Maerschalk, C., Pretorius, W. and Barling, J. (2005). "High-precision Pb-Sr-Nd-Hf isotopic characterization of USGS BHVO-1 and BHVO-2 reference materials." Geochemistry Geophysics Geosystems 6: 10.

Wilson, M. R., Kjarsgaard, B. A. and Taylor, B. (2007). "Stable isotope composition of magmatic and deuteric carbonate phases in hypabyssal kimberlite, Lac de Gras field, Northwest Territories, Canada." Chemical Geology 242(3-4): 435-454.

Woodhead, J. D., Hergt, J., Phillips, D. and Paton, C. (2009). "African kimberlites revisited: In-situ Sr isotope analysis of groundmass perovskite." Lithos 112(Supplement 1): 311-317.

Yang, Y.-H., Wu, F.-Y., Wilde, S. A., Liu, X.-M., Zhang, Y.-B., Xie, L.-W. and Yang, J.-H. (2009). "In-situ perovskite Sr-Nd isotopic constraints on the petrogenesis of the Ordovician Mengyin kimberlites in the North China Craton." Chemical Geology 264(1-4): 24-42.

Zedgenizov, D. A., Rege, S., Griffin, W. L., Kagi, H. and Shatsky, V. S. (2007). "Composition of trapped fluids in cuboid fibrous diamonds from the Udachnaya kimberlite: LAM-ICPMS analysis." Chemical Geology 240(1-2): 151-162.

Chapter 5:

DISCUSSION AND CONCLUSIONS

5.1. INTRODUCTION

This chapter aims to summarise and draw together the conclusions of the previous three chapters in order to resolve the questions that were asked in the introduction. The first section, 5.2, discusses the metasomatic addition of cpx and garnet to the lithospheric mantle (Table 5.1) and the implications arising from this. The second section, 5.3, addresses the primary composition of kimberlite magma and the relationship between this, the low-Cr megacrysts suite and the metasomatic addition of cpx.

Modal metasomatic mineral addition	Age estimate	Suggested Parental Magma
Off-craton lithospheric mantle		
Cpx	**Relatively recent**	**Convecting mantle melt such as a carbonatite**
Middle Atlas	*Within 5Myr of emplacement (2Ma)*	*Carbonatite (not the host basalt)*
On-cration lithospheric mantle		
Cpx	**Relatively recent**	**Kimberlite-type melt related to the host magma**
Greenland	*Within 10Myr of emplacement (168Ma)*	*UML*
Bultfontein	*Within 10Myr of emplacement (90Ma)*	*Group I kimberlite*
Garnet	**Older than cpx addition**	**Lamproite-type melt**
Greenland	*>1327Ma*	*Lamproite*
Bultfontein	*>120Ma*	*Group II kimmberlite*

Table 5.1. *Summary of the parental melts responsible for the modal metasomatic additions of cpx and garnet to the lithospheric mantle.*

5.2. METASOMATISM

5.2.1. METASOMATIC ADDITION OF CPX TO THE LITHOSPHERIC MANTLE

The issue of metasomatic addition of cpx to the lithospheric mantle has been addressed in on- and off-craton settings, in Chapters 2 and 3 respectively. The trace element and isotope data from the samples studied supports the preliminary hypotheses drawn from melting experiments and melt estimates that the cpx is a metasomatic addition (e.g. Pearson and Nowell 2002). A common feature among the cpx in these samples is that, although their trace element *patterns* are similar within each xenolith, there are significant variations in their *concentrations*, including Sr. These variations, at mantle temperatures, should be equilibrated over approximately 10 to 65Myr, depending on the length scale. This therefore implies that the cpx is a recent metasomatic addition to lithospheric mantle in both on- and off-craton settings. The metasomatic agent, however, varies between the localities (Table 5.1). In the case of the off-craton Atlas xenoliths the cpx compositions are consistent with recent addition, or re-equilibration, with a carbonatite melt (Chapter 2; Table 5.1). This is not the basaltic magma that bought these xenoliths to the surface. The xenoliths from Greenland and South Africa, on the other hand, reflect addition by the host magma (UML or kimberlite), although this is complicated by the issues associated with tracing the parental kimberlite magma (Chapter 3; Table 5.1). These issues are discussed more fully in section 5.3.

The data from the detailed studies carried out here are compared with a global database of Sr and Nd isotope data from bulk cpx separates (see Chapter 2 for data sources). This shows that, on a PDF plot, there is a narrow and well-defined peak in cpx Sr and Nd isotope data for off-craton xenoliths which is with the range observed in OIBs (Hofmann 2003). This distribution is therefore inconsistent with an ancient origin of cpx via long term enrichment or depletion in the lithospheric mantle as both these processes would introduce significant isotopic variation leading to a broader peak (in a PDF plot) and greater spread in global Sr and Nd isotopic data than is observed. The data are more consistent in off-craton settings with cpx being a recent to the lithospheric mantle. For on-craton settings the picture is less clear. There is still a distinctive peak in terms of Sr and Nd, when global data are plotted on PDF plots, which overlap with present day convecting mantle values. This implies that, as with the off-craton cpx, the majority of the cpx is inconsistent with long term enrichment or depletion and is therefore also likely to have a recent origin. However there are some localities, such as the xenolith from Bultfontein, where a larger spread in the Sr isotope values is observed towards more radiogenic values. This variation is concluded to be the result of infiltration of the xenolith by isotopically heterogeneous melts which, although originating in the convecting mantle, have incorporated components from the lithospheric mantle that have experienced more ancient metasomatism (e.g. phlogopite). An example of such fluid/melt interaction in the lithospheric mantle and subsequent isotope diversity is provided by the isotopic diversity recorded by diamond forming fluids (Klein-BenDavid and Pearson 2009; Klein-BenDavid et al. in press). Such processes

could therefore account for the Sr isotope and trace element variations observed in the cpx from Bultfontein. This explanation is preferred as it does not invoke an ancient origin for the cpx which has been shown to be unlikely due to the variation observed in concentration and Sr isotope values between adjacent cpx crystals, inconsistent with long residence times.

The global distribution of Nd isotopes in cratonic cpx shows a close correlation with whole rock Nd data for Group I kimberlites. The kimberlite whole rock Sr data are complicated by crustal contamination (addressed in more detail in section 5.3) and therefore the peak in the whole rock kimberlite Sr data is not in close agreement with the cratonic cpx. However if the kimberlite data is adjusted to lower Sr isotope values, to account for the prevalent crustal contamination, then the kimberlite Sr data would be consistent with the Nd and trace element data and overlap with the cpx. This therefore implies that the majority of cpx found in peridotite xenoliths entrained in kimberlites has been recently added by, or equilibrated with, the 'primary' kimberlite magma. These conclusions are summarised in Fig. 5.1.

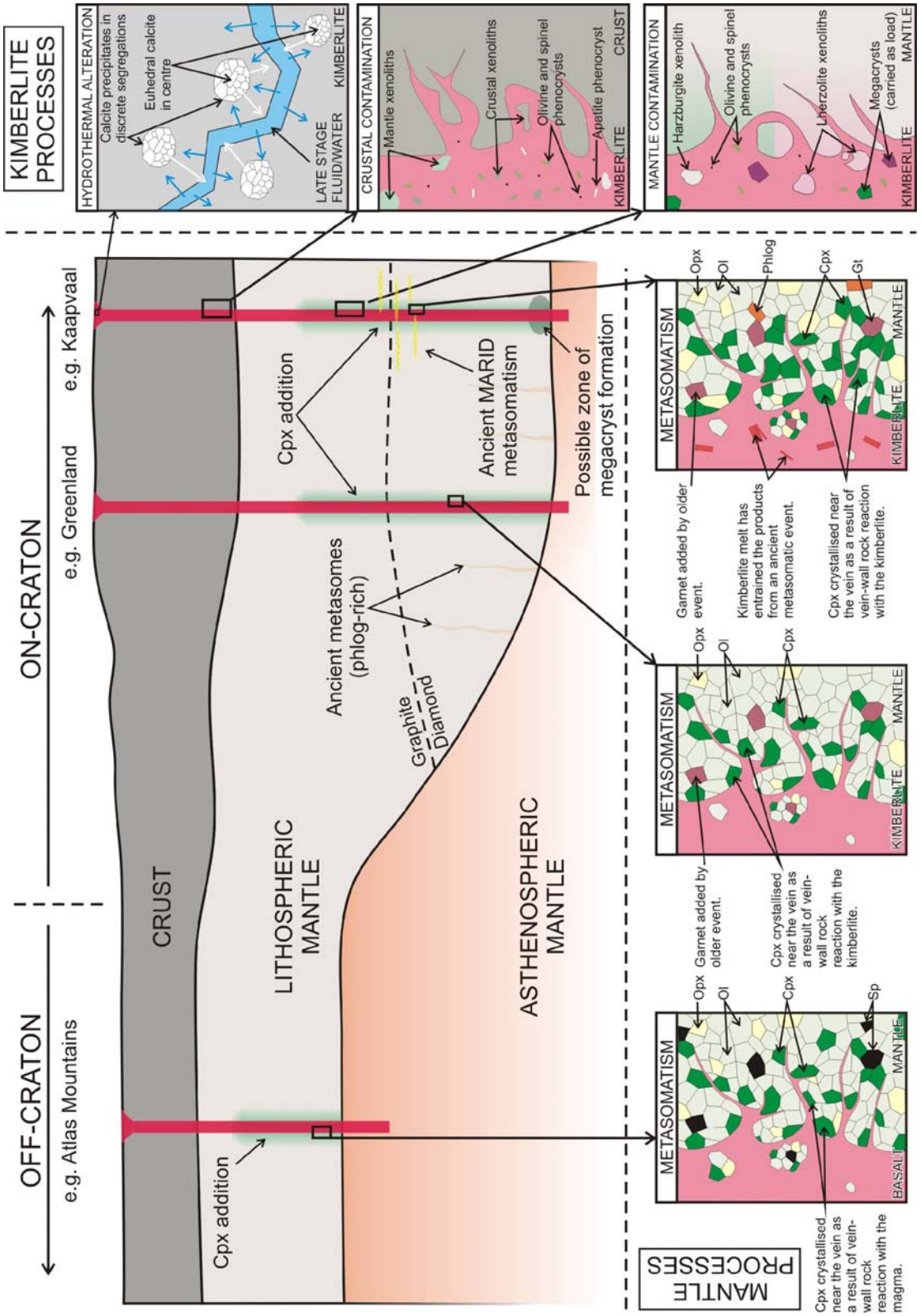

Figure 5.1. *A schematic diagram illustrating the process both in the peridote mantle in on- and off-craton settings as well as in lithospheric mantle more akin to the lithosphere beneath the NAC and the Kaapvaal craton. These processes are thought to be localised and related to melt-wallrock reactions. The processes that affect the kimberlite whole rock are also illustrated. Kimberlite magma is closely related to cpx addition and the crystallisation of megacrysts in cratonic lithospheric mantle.*

5.2.2. METASOMATIC ADDITION OF GARNET TO CRATONIC LITHOSPHERIC MANTLE

The metasomatic addition of cpx to the lithospheric mantle has now been established. In on-craton settings, where melt depletion estimates are in excess of 30% (e.g. Pearson and Wittig 2008), and melting is shallow (less than 3GPa) garnet is also predicted to be exhausted from the residue thus implying that the garnet now present in cratonic peridotites also has a metasomatic origin (Chapter 3). The garnet and cpx are not in trace element or isotopic equilibrium and therefore cannot have been added in the same event. The cpx, on the basis of trace element and isotopic variation between adjacent crystals, is assumed to be a relatively recent addition and therefore, as the two are added by different events, the garnet must be an older addition. It is not possible to accurately date garnet addition using the isotope data as the garnet and cpx have not equilibrated and there is no isochronous relationship between the individual garnets analysed. The addition of garnet is complicated as it has been overprinted by the event that added the cpx and probably others. In the case of the Bultfontein peridotite (JMK), studied here, the garnet composition is compatible with formation from earlier Group II kimberlite magmatism. However in Greenland there are no Group II kimberlites and the garnet is concluded to have crystallised from lamproite magmas. This type of volcanism was active in the area around 1374Ma (Tappe et al. 2007) and, using the measured garnet Rb/Sr ratios, it is possible to generate the observed radiogenic Sr isotope ratios in the garnets by lithospheric residence, since formation from lamproite magmas in the Mid-Proterozoic.

The isotopic signature of garnet in cratonic peridotites is thus more varied, with a more complex signature than the cpx. This is reflected in a PDF plot of global garnet initial Sr and Nd isotope values for cratonic garnets from around the world. This shows a much broader PDF distribution of isotopic signatures, with a less defined peak than the corresponding cpx PDF plots. The garnet is more radiogenic, in terms of Sr, than the cpx with low-Ca, high-Cr garnets in particular having very radiogenic isotopes (Klein-BenDavid and Pearson 2009). This may in part be the result of higher Rb/Sr ratios in garnet compared with cpx which would, over time, lead to more radiogenic $^{87}Sr/^{86}Sr$ values. However the dominant reason for this spread is that the parental magma from which the garnet formed was characterised by significantly more radiogenic Sr. The isotopic composition of the garnet-forming melt may have been related to melts derived from ancient metasomatism such as Group II kimberlites or lamproites such melts have been clearly linked to the formation of low-Ca, high-Cr garnet associated with diamonds and hence to diamond forming fluids (Klein-BenDavid et al. in press). In the majority of cratons this enriched component, in the form of phlogopite-rich metasomes, is thought to be mostly removed by previous melting episodes by the time that the majority of cpx is added and therefore cpx tends to have a more typical mantle signature. This is not the case in Bultfontein where some of these metasomatic components seems to have been incorporated into the melt that crystallised the cpx. This observation is consistent with previous work that suggests that the Kaapvaal cratonic lithosphere has undergone significantly more metasomatism than other cratons, such as the NAC (e.g. Simon et al. 2008; Fig. 5.1).

5.2.3. IMPLICATIONS

The recent addition of cpx to the lithosphere has implications for the geochemical and geophysical evolution of the lithosphere (addressed in Chapters 2 and 3). Cpx, as well as garnet, are important hosts for incompatible trace elements such as REE and Sr in the lithospheric mantle. Therefore the addition of these phases is a dominant control on the fertility and incompatible element inventory of the lithospheric mantle. In the case of cratonic lithosphere the cpx was added recently by a precursor melt to the host volcanism. In this case the addition of cpx is likely to be localised to the wallrock around melt veins associated with this volcanism. This cpx addition would therefore only have affected a relatively small area of the lithospheric mantle (Fig. 5.1). It is difficult to constrain to what extent the magma has infiltrated the lithospheric mantle and not reached the surface and so these may be many such vein like structures in the cratonic lithospheric mantle (Fig. 5.1). Nonetheless, the distribution of metasomatic cpx is unlikely to be uniform. The xenolith suites are therefore biased towards cpx-bearing peridotites found around wallrocks to veins and hence may not be representative of the bulk of the lithosphere which is likely to be dominated by depleted harzburgite and dunite lithology (Pearson et al. 2003). One implication of this is that true bulk lithospheric stratigraphy determined from mineral concentrate data (e.g. Griffin et al. 2009) will only represent the lithospheric stratigraphy in a relatively localised area of lithosphere related to the passage of the host melt.

The addition of both garnet and cpx to lithospheric mantle has significant implications for the geochemical evolution of the lithospheric mantle. The addition of garnet, a host for the HREE, is location specific and would re-enrich the lithospheric mantle to some extent. However, cpx is the dominant host for Sr and the LREE in the mantle and it is the addition of this phase that will have the most significant effect on how enriched the lithosphere is perceived to be. The conclusions drawn here indicate that the majority of cpx was added relatively recently to the lithospheric mantle which implies that the current enrichment, as represented by lherzolites, is a recent phenomenon and the lithospheric mantle may not have been a geochemically relatively enriched source through time. This was recognised by Pearson and Nowell (2002) who presented the bulk incompatible trace element abundances of lithospheric peridotites on a cpx-free basis. The most incompatible enriched peridotites have restricted bulk-earth/convecting mantle Sr and Nd isotope compositions. There are cratonic lithospheric mantle peridotites with very extreme isotope compositions but such rocks tend to have very low incompatible element contents and are not viable sources for incompatible element enriched magmas. The greatest incompatible enrichment and isotopic diversity is observed in mica-rich metasomes, not in the peridotites.

The addition of garnet and cpx also has implications for the geophysical evolution of the lithospheric mantle. This is because cpx, and especially garnet, are relatively dense phases. These effects have been modelled by Schutt and Lesher (2006), including the effects of mineral chemistry as well as the modal abundance on density. They modelled the effects of melt extraction from a

fertile lherzolite, resulting in a buoyant depleted harzburgite. However, if this was reversed so that the garnet and cpx were being added to a depleted residue, as is shown by this study, this model could be used to reflect metasomatic processes. The results of this modelling show that the addition of cpx to the lithospheric mantle can increase the density by from 0.6% to 2.1%, depending on pressure and starting composition. It has been suggested in some cratons, such as in the North China Craton, that the lack of isostatic equilibration could be explained by recent delamination (Gao et al. 2002). The addition of cpx is restricted to wallrock-vein interactions and therefore has a limited extent and is unlikely to have been sufficient to cause delamination but it may have been a contributing factor.

5.3. KIMBELITE MAGMATISM

5.3.1. TRACING THE PRIMARY SR ISOTOPE RATIO OF KIMBERLITE MAGMAS

The issue of the primary composition of the kimberlite magma, which is responsible for the cpx addition, is addressed in Chapter 4. This addresses the fundamental question of what the Sr isotope composition of the primary, uncontaminated kimberlite magma is and its relation to metasomatic activity in the lithospheric mantle. The novel approach used in this study has shown that it is possible to track and 'see through' the effects of crustal. This multiphase approach was, in part, possible due to a new disaggregation technique which

breaks the rock sample along grain boundaries thus increasing the preservation of friable mineral phases such as apatite.

The initial study used an olivine melilitite as a simpler analogue. The Sr content of the whole rock is dominated by the melilite, a phenocryst phase, and therefore accurately reflects the source composition. However the later forming phases show a wider spread to more radiogenic Sr isotope values indicating that there has been a small degree of crustal contamination during crystallisation (modelled to be up to 4%). This study also showed that perovskite is not the least radiogenic phase, in terms of Sr, and is therefore not truly representative of the source region despite being routinely chosen for LA studies. This would imply that, in this case, perovskite is crystallises later then previously thought and after the magma has been affected by crustal contamination. Apatite on the other hand, shows a wide range, from values similar to the olivine and melilite up to more radiogenic values. This indicates that apatite is crystallising throughout the magma evolution and therefore recording more information both about the source region as well as the crustal contamination than any other mineral phase.

The kimberlite sample (Jos), similarly dissected, proved to be more complex. The whole rock kimberlite is relatively radiogenic with an initial Sr isotope ratio of 0.706226. The Sr budget is dominated, in the Jos kimberlite, by late crystallising calcite. The calcite has a wide range of Sr isotope values and although some of the calcite is thought to have a magmatic origin the majority is more likely to have crystallised/precipitated from a late stage fluid that may

have interacted with groundwater (Fig. 5.2). The calcite Sr isotopic composition dominates the whole rock analysis and therefore neither are truly reflective of the source composition. The phenocryst olivine, on the other hand, is one of the least radiogenic phases and is within the range of Sr isotope values observed in present day convecting mantle melts. This is therefore more likely to reflect the composition of the primary kimberlite magma. The perovskite, as with SPK, shows a range of Sr isotope values from those similar to the olivine to more radiogenic values that can be explained by up to 4% crustal assimilation. This shows that, as with SPK, the perovskite is not necessarily the best phase to characterise the kimberlite source region as it appears to crystallise after some degree of crustal assimilation. Apatite is the least radiogenic Sr isotope phase analysed but extends to radiogenic values that are consistent with crustal assimilation of up to 8%. This suggests that apatite crystallises throughout the magma evolution and is the best phase to both constrain the source region and to trace the crustal assimilation (Fig. 5.2.).

5.3.2. THE LINK BETWEEN KIMBERLITE MAGMA, METASOMATISM AND MEGACRYSTS

The link between kimberlite magma, the low-Cr megacryst suite that characterises many kimberlites and metasomatic melts has been addressed in Chapter 4, and to some extent in Chapter 3. These are long-standing issues that are important to resolve if we are to better understand kimberlite genesis and their effects on the lower cratonic lithospheric mantle. One of the principle arguments for a non-cognate origin of the low-Cr megacryst suite is the

difference in their Sr isotope composition from kimberlites. This is despite a close overlap in terms of Nd and Hf isotopes between the low-Cr megacryst suite and kimberlites (Nowell et al. 2004). The new kimberlite data presented here, along with LA perovskite data, confirm the hypothesis that whole rock kimberlite Sr analyses overestimate the Sr isotope composition of the primary kimberlite magma. These new data remove this argument against a genetic origin therefore implying that the two are related. The nature of this relationship cannot be deduced from these data but it is likely that either the megacrysts crystallised from stalled kimberlite magma or due to melt-wallrock reactions with the peridotite mantle.

In Chapter 3 the evidence from trace element patterns implied that kimberlite magma, as well as potentially crystallising the low-Cr megacrysts suite, is also thought to be responsible for the metasomatic addition of cpx to the lithospheric mantle. There is a mismatch observed between the whole rock Sr isotope ratios of the host kimberlite and those of the cpx. The range of Sr isotope values observed in the cpx, however, does overlap with the new kimberlite mineral and perovskite Sr data which is more representative of the primary kimberlite magma. In the Jos kimberlite, for example, the early crystallising mineral phases have Sr isotope values that overlap with mantle cpx analysed from Somerset Island peridotite xenoliths (from the same craton). Therefore both the megacrysts and the cpx in peridotite are concluded to have both crystallised from the primary kimberlite magma. This work therefore strongly suggests that the kimberlite magma is responsible for a range of processes within the lithospheric mantle (Fig. 5.1).

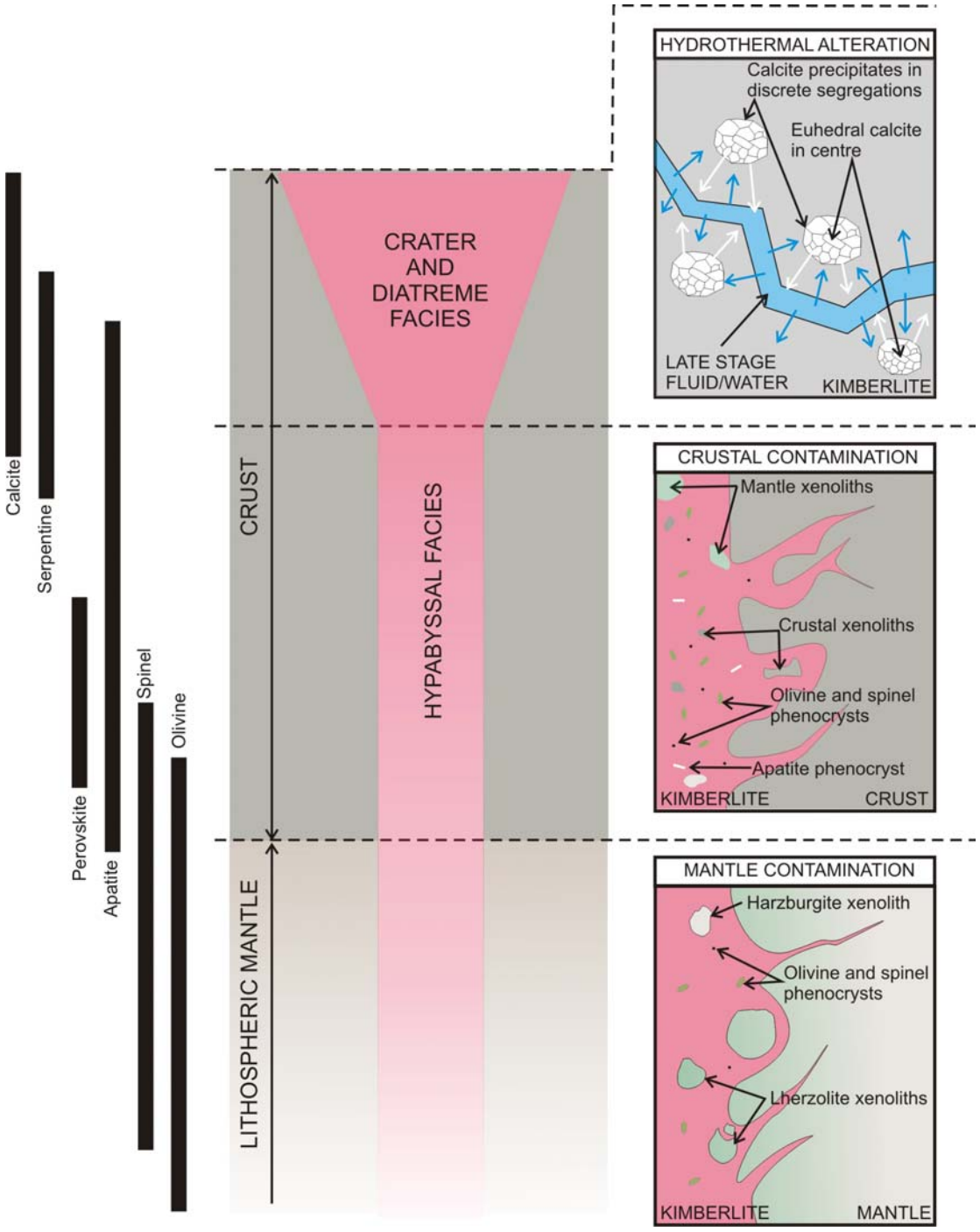

Figure 5.2. *A schematic diagram illustrating the processes that affect a kimberlite as it moves to the surface and erupts. The proposed sequence of crystallisation within the kimberlite magma is based on petrography and isotope geochemistry.*

5.4. FURTHER WORK

The mantle xenolith studies have revealed some interesting results and the techniques used here could be employed in future studies. However in the majority of cases it is predicted that there will be limited Sr isotope variation, although systems such as U-Pb and Sm-Nd may provide more information. Wittig et al. (in revision), for example used the U-Pb system to provide age constrains on the metasomatism in the Middle Atlas. This study has provided some broad time constraints on metasomatic activity in the lithospheric mantle using diffusion coefficients in adjacent crystals. This could be further constrained however using trace element concentration profiles across crystal boundaries leading to more accurate distance estimates than those used here. The shape of calculated diffusion profiles, which could be estimated using an ion probe, would also provide information about the extent to which the crystals have equilibrated. These could potentially be used to assess the time scales over which certain elements diffusively equilibrate between the garnet and the cpx under mantle conditions. This method has been used to assess residence times of crystals in magma chambers (Martin et al. 2008) and could potentially be adapted to this situation.

The kimberlite study provides ample opportunity for further work. The novel approach used here allows a more detailed insight into kimberlite geochemistry than previous work on single phase or whole rock data. This can therefore be used on a range of kimberlite samples to investigate whether the conclusions

drawn here can be more widely applied. Hypabyssal kimberlite was selected for this study as it is thought to be less contaminated than other facies based on observations of crustal xenoliths. However how much the amount of crust assimilated into the magma varies between the difference facies is unknown. Therefore the microsampling approach used here could potentially be extended to study a kimberlite pipe where it would be possible to sample the hypabyssal, diatreme and crater facies. The alteration of the latter two would make this challenging but phases such as perovskite should still be preserved. This could also be extended to kimberlite pipes where there are several distinct generations of magma intrusion in order to investigate whether the degree of crustal assimilation varies.

A detailed study, like the one presented for Jos, could be extended to include serpentine. There is currently an on going debate about the origin of serpentine and whether it is a primary magmatic phase (Mitchell 1986) or the product of hydrothermal alteration (Sparks et al. 2006). This debate is predominantly based on petrographic and experimental data but the two hypothesises should be distinguishable using radiogenic, and especially stable, isotope analyses. Serpentine that is magmatic should, in theory have a mantle signature whereas serpentine produces via hydrothermal alteration due to interaction with groundwater should have a more crustal signature. This could potentially be complicated if the serpentine is magmatic and has crystallised from late stage kimberlite fluids which may have interacted to some extent with groundwater. It was possible however to distinguish between the two generations of calcite in the Jos kimberlite and therefore, despite the microsampling challenge (the

serpentine would need to be drilled as it does not survive crushing), isotope analyses of serpentine may resolve the debate on its origin.

Both apatite and calcite showed significant Sr isotope variation as well as morphological variations which could not be exploited with the methods used here. However an ion probe study on these two phases (potentially possible due to the low Rb concentrations, high Sr concentrations as resolving the ^{87}Rb interference is not possible, and large ranges in isotope values) would allow a more accurate correlation between the different crystal morphologies and the respective Sr isotopic composition. This would potentially constrain the link between morphology and Sr isotope composition that has been inferred from the data presented here. Exley et al. (1983) have previously carried out an ion probe study on calcite from kimberlite which did resolve Sr isotope variations. A detailed *in-situ* study of Sr isotope ratio variation in calcite, such as the one proposed, would potentially reveal more information about hydrothermal alteration processes as well as characterising individual crystals (Exley and Jones 1983; Wilson et al. 2007). This would be further strengthened by stable isotope analyses that would clearly distinguish between magmatic calcite and calcite that has a closer affinity to the crust (Wilson et al. 2007).

5.5. REFERENCES

Exley, R. A. and Jones, A. P. (1983). "87Sr/86Sr in kimberlitic carbonates by ion microprobe: Hydrothermal alteration, crustal contamination and relation to carbonatite." Contributions to Mineralogy and Petrology 83(3): 288-292.

Gao, S., Rudnick, R. L., Carlson, R. W., McDonough, W. F. and Liu, Y.-S. (2002). "Re-Os evidence for replacement of ancient mantle lithosphere beneath the North China craton." Earth and Planetary Science Letters 198(3-4): 307-322.

Griffin, W. L., O'Reilly, S. Y., Alfonso, J. C. and Begg, G. C. (2009). "The Composition and Evolution of Lithospheric Mantle: a Re-evaluation and itsTectonic Implications." Journal of Petrology 50: 1185-1204.

Hofmann, A. W., Ed. (2003). Sampling mantle heterogeneity through oceanic basalts: isotopes and trace elements. Treatise on Geochemistry: The Mantle and Core, Elsevier.

Klein-BenDavid, O. and Pearson, D. G. (2009). "Origins of subcalcic garnets and their relation to diamond forming fluids--Case studies from Ekati (NWT-Canada) and Murowa (Zimbabwe)." Geochimica et Cosmochimica Acta 73(3): 837-855.

Klein-BenDavid, O., Pearson, D. G., Nowell, G. M., Ottley, C. J., McNeill, J. C. R. and Cartigny, P. (in press). "Mixed fluid sources involved in diamond growth constrained by Sr-Nd-Pb-C-N isotopes and trace elements." Earth and Planetary Science Letters.

Martin, V. M., Morgan, D. J., Jerram, D. A., Caddick, M. J., Prior, D. J. and Davidson, J. P. (2008). "Bang! Month-Scale Eruption Triggering at Santorini Volcano." Science 321(5893): 1178-.

Mitchell, R. H. (1986). Kimberlites: Mineralogy, Geochemistry, and Petrology, Plenum Press.

Nowell, G. M., Pearson, D. G., Bell, D. R., Carlson, R. W., Smith, C. B., Kempton, P. D. and Noble, S. R. (2004). "Hf isotope systematics of

kimberlites and their megacrysts: New constraints on their source regions." Journal of Petrology 45(8): 1583-1612.

Pearson, D. G. and Nowell, G. M. (2002). "The Continental Lithospheric Mantle: Characteristics and Significance as a Mantle Reservoir." Philosophical Transactions: Mathematical, Physical and Engineering Sciences 360(1800): 2383-2410.

Pearson, D. G., Canil, D. and Shirey, S. B., Eds. (2003). Mantle sample included in volcanic rocks: xenoliths and diamonds. Treatise on Geochemistry: The Mantle and Core, Elsevier.

Pearson, D. G. and Wittig, N. (2008). "Formation of Archaean continental lithosphere and its diamonds: the root of the problem." Journal of the Geological Society 165: 895-914.

Schutt, D. L. and Lesher, C. E. (2006). "Effects of melt depletion on the density and seismic velocity of garnet and spinel lherzolite." Journal of Geophysical Research-Solid Earth 111(B5): -.

Simon, N. S. C., Carlson, R. W., Pearson, D. G. and Davies, G. R. (2008). "The origin and evolution of the Kaapvaal cratonic lithospheric mantle." Journal of Petrology.

Sparks, R. S. J., Baker, L., Brown, R. J., Field, M., Schumacher, J., Stripp, G. and Walters, A. (2006). "Dynamical constraints on kimberlite volcanism." Journal of Volcanology and Geothermal Research 155(1-2): 18-48.

Tappe, S., Foley, S. F., Stracke, A., Romer, R. L., Kjarsgaard, B. A., Heaman, L. M. and Joyce, N. (2007). "Craton reactivation on the Labrador Sea margins: 40Ar/39Ar age and Sr-Nd-Hf-Pb isotope constraints from alkaline and carbonatite intrusives." Earth and Planetary Science Letters 256(3-4): 433-454.

Wilson, M. R., Kjarsgaard, B. A. and Taylor, B. (2007). "Stable isotope composition of magmatic and deuteric carbonate phases in hypabyssal kimberlite, Lac de Gras field, Northwest Territories, Canada." Chemical Geology 242(3-4): 435-454.

Wittig, N., Pearson, D. G., Baker, J., Duggen, S. and Hoernle, K. (in revision). "Tracing the metasomatic and magmatic evolution of continental mantle roots with Rb-Sr, SM-Nd, Lu-Hf and U-Pb and Th-Pb isotopes: a case

study of Middle Atlas (Morocco) peridotite xenoliths." Geochimica et Cosmochimica Acta.

Appendix A:

STANDARD DATA

Table A.1(a) *Summary of 3ng NBS987 standard data run on the Triton (TIMS) during the period the data were analysed. These values, according to the batch number, were used to normalise the measured Sr isotope ratios to the accepted values. JM refers to Jacqueline Malarkey. All JM standard data is located in Table A.2.*

Triton Session	Batch Numbers Analysed	3ng NBS987 Standard Variation							
		JM				All users			
		$^{87}Sr/^{86}Sr$ Value	2sd abs	2sd (ppm)	n	$^{87}Sr/^{86}Sr$ Value	2sd abs	2sd (ppm)	n
Aug 2007 - Sept 2007	M30, M33, M35, M41, M42	0.710245	0.000025	35.0	15	0.710245	0.000028	39.9	65
NB. Cup configuration changed									
Nov 2007 - Dec 2007	M44, M46, M48, M49	0.710240	0.000010	13.5	12	0.710237	0.000011	15.9	25
Feb 2008	M52, M53, M54	0.710236	0.000012	16.7	7	0.710236	0.000012	17.3	16
June 2008- Aug 2008	M56, M57, M58, 103	0.710240	0.000013	18.7	18	0.710239	0.000016	22.2	47
Jan 2009 - Feb 2009	M67, M68, M75, M76, M77, M81	0.710247	0.000014	19.7	19	0.710247	0.000015	20.8	32
Aug 2009 - Sept 2009	JOS	0.710247	0.000007	10	2	0.710248	0.000018	24.8	11

Table A.1(b) *Summary of all NBS987 standard data run on the Triton (TIMS) during the period the data were analysed. These values, according to the batch number, were used to normalise the measured Sr isotope ratios to the accepted values. JM refers to Jacqueline Malarkey. All JM standard data is located in Table A.2.*

Triton Session	Batch Numbers Analysed	600ng, 12ng, 6ng, 3ng and 1ng NBS987 Standard Variation							
		JM				All users			
		$^{87}Sr/^{86}Sr$ Value	2sd abs	2sd (ppm)	n	$^{87}Sr/^{86}Sr$ Value	2sd abs	2sd (ppm)	n
Aug 2007 - Sept 2007	M30, M33, M35, M41, M42	0.710242	0.000022	33.2	29	0.712045	0.000032	45.1	98
NB. Cup configuration changed									
Nov 2007 - Dec 2007	M44, M46, M48, M49	0.710240	0.000010	13.5	12	0.710242	0.000017	24.2	44
Feb 2008	M52, M53, M54	0.710236	0.000012	16.7	7	0.710237	0.000017	23.9	39
June 2008- Aug 2008	M56, M57, M58, 103	0.710240	0.000012	17.2	24	0.710239	0.000016	22.4	58
Jan 2009 - Feb 2009	M67, M68, M75, M76, M77, M81	0.710246	0.000013	18.5	34	0.710246	0.000018	17.3	75
Aug 2009 - Sept 2009	JOS	0.710248	0.000010	14.3	4	0.710249	0.000019	26.1	38

Table A.2. *Summary of all Triton NBS987 standards run by Jacqueline Malarkey for the past three years. The reproducibility during each session is summarised in Table A.1.*

Std Size (ng)	Date	Mag no.	Repeat?	Std	Method File	Filament	Activator	84Sr/86Sr c	1SE	87Sr/86Sr corrected	1SE	# accepted ratios
Nov 2006 (no samples run)												
600	20/11/2006	354	No	NBS987	Sr 1	Ta	H3PO4	0.056853	0.000001	**0.710232**	0.000004	172(180)
600	20/11/2006	354	No	NBS987	Sr 1	Ta	H3PO4	0.056489	0.000001	**0.710227**	0.000004	172(180)
600	20/11/2006	354	No	NBS987	Sr 1	Ta	H3PO4	0.056495	0.000001	**0.710228**	0.000003	175(180)
600	20/11/2006	354	No	NBS987	Sr 1	Ta	H3PO4	0.056492	0.000001	**0.710226**	0.000002	171(180)
600	21/11/2006	354	No	NBS987	Sr 1	Ta	H3PO4	0.056493	0.000001	**0.710220**	0.000003	167(180)
600	21/11/2006	354	No	NBS987	Sr 1	Ta	H3PO4	0.056494	0.000001	**0.710229**	0.000003	173(180)
600	21/11/2006	354	No	NBS987	Sr 1	Ta	H3PO4	0.056493	0.000001	**0.710225**	0.000003	171(180)
600	21/11/2006	354	No	NBS987	Sr 1	Ta	H3PO4	0.056494	0.000001	**0.710235**	0.000003	172(180)
600	21/11/2006	354	No	NBS987	Sr 1	Ta	H3PO4	0.056492	0.000001	**0.710229**	0.000003	173(180)
600	21/11/2006	354	No	NBS987	Sr 1	Ta	H3PO4	0.056492	0.000001	**0.710227**	0.000003	172(180)
600	21/11/2006	354	No	NBS987	Sr 1	Ta	H3PO4	0.056490	0.000001	**0.710224**	0.000003	175(180)
600	21/11/2006	354	No	NBS987	Sr 1	Ta	H3PO4	0.056493	0.000001	**0.710228**	0.000003	172(180)
600	21/11/2006	354	No	NBS987	Sr 1	Ta	H3PO4	0.056495	0.000001	**0.710233**	0.000003	174(180)
600	21/11/2006	354	No	NBS987	Sr 1	Ta	H3PO4	0.056494	0.000001	**0.710226**	0.000003	174(180)
Aug 2007-Sept 2007 (NB cup configuration changed)												
600	03/08/2007	414	Yes	NBS987	Sr2	Ta	H3PO4	0.056494	0.000001	**0.710252**	0.000003	171/180
600	03/08/2007	414	Yes	NBS987	Sr2	Ta	H3PO4	0.056595	0.000001	**0.710240**	0.000003	172/180
600	03/08/2007	414	Yes	NBS987	Sr2	Ta	H3PO4	0.056496	0.000001	**0.710240**	0.000003	171/180
600	03/08/2007	414	Yes	NBS987	Sr2	Ta	H3PO4	0.056498	0.000001	**0.710236**	0.000003	171/180
600	03/08/2007	414	Yes	NBS987	Sr2	Ta	H3PO4	0.056495	0.000001	**0.710228**	0.000003	172/180
12	06/08/2007	415	No	NBS987	Sr2	Re	TaF5	0.056494	0.000002	**0.710228**	0.000005	173/180
12	06/08/2007	415	No	NBS987	Sr2	Re	TaF5	0.005650	0.000002	**0.710235**	0.000006	172/180
12	06/08/2007	415	No	NBS987	Sr2	Re	TaF5	0.056496	0.000003	**0.710228**	0.000007	173/180
6	06/08/2007	415	No	NBS987	Sr2	Re	TaF5	0.056470	0.000007	**0.710231**	0.000010	169/180
6	06/08/2007	415	No	NBS987	Sr2	Re	TaF5	0.056487	0.000002	**0.710252**	0.000007	172/180
3	06/08/2007	415	No	NBS987	Sr2	Re	TaF5	0.056502	0.000005	**0.710232**	0.000008	169/180
3	06/08/2007	415	No	NBS987	Sr2	Re	TaF5	0.056489	0.000006	**0.710228**	0.000011	175/180
3	07/08/2007	415	No	NBS987	Sr2	Re	TaF5	0.056473	0.000006	**0.710249**	0.000001	174/180
3	07/08/2007	415	No	NBS987	Sr2	Re	TaF5	0.056515	0.000065	**0.710269**	0.000012	172/180
6	07/08/2007	415	No	NBS987	Sr2	Re	TaF5	0.056492	0.000003	**0.710237**	0.000007	173/180
6	10/08/2007	417	No	NBS987	Sr2	Re	TaF5	0.056504	0.000004	**0.710235**	0.000009	173/180
3	10/08/2007	417	No	NBS987	Sr2	Re	TaF5	0.056507	0.000004	**0.710245**	0.000008	174/180
3	12/08/2007	417	No	NBS987	Sr2	Re	TaF5	0.056512	0.000021	**0.710248**	0.000012	175/180
6	12/08/2007	417	No	NBS987	Sr2	Re	TaF5	0.056484	0.000004	**0.710233**	0.000009	170/180

Table A.2.continued

Std Size (ng)	Date	Mag no.	Repeat?	Std	Method File	Filament	Activator	84Sr/86Sr c	1SE	87Sr/86Sr corrected	1SE	# accepted ratios
Aug 2007-Sept 2007 (NB cup configuration changed)												
3	13/08/2007	417	No	NBS987	Sr2	Re	TaF5	0.056519	0.000006	**0.710250**	0.000010	169/180
6	13/08/2007	417	No	NBS987	Sr2	Re	TaF5	0.056486	0.000005	**0.710250**	0.000008	172/180
3	17/08/2007	419	No	NBS987	Sr2	Re	TaF5	0.056490	0.000007	**0.710255**	0.000012	172/180
3	17/08/2007	419	No	NBS987	Sr2	Re	TaF5	0.056458	0.000006	**0.710236**	0.000011	172/180
3	18/08/2007	419	No	NBS987	Sr2	Re	TaF5	0.056491	0.000008	**0.710241**	0.000012	173/180
3	18/08/2007	419	No	NBS987	Sr2	Re	TaF5	0.056511	0.000007	**0.710228**	0.000012	172/180
NB. Changed from 18 blocks to 20 blocks												
3	03/09/2007	424	No	NBS987	Sr2	Re	TaF5	0.005650	0.000003	**0.710245**	0.000007	191/200
3	03/09/2007	424	No	NBS987	Sr2	Re	TaF5	0.056519	0.000011	**0.710264**	0.000015	189/200
3	03/09/2007	424	No	NBS987	Sr2	Re	TaF5	0.056507	0.000006	**0.710249**	0.000009	190/200
3	03/09/2007	424	No	NBS987	Sr2	Re	TaF5	0.056520	0.000006	**0.710243**	0.000011	191/200
Nov 2007- Dec 2007												
3	39416	457	No	NBS987	Sr2	Re	TaF5	0.056490	0.000002	**0.710236**	0.000005	188/200
3	30/11/2007	457	No	NBS987	Sr2	Re	TaF5	0.056490	0.000002	**0.710236**	0.000005	188/200
3	30/11/2007	457	No	NBS987	Sr2	Re	TaF5	0.056490	0.000006	**0.710241**	0.000009	190/200
3	01/12/2007	458	No	NBS987	Sr2	Re	TaF5	0.056488	0.000004	**0.710239**	0.000008	190/200
3	02/12/2007	458	No	NBS987	Sr2	Re	TaF5	0.056485	0.000004	**0.710246**	0.000008	191/200
3	06/12/2007	460	No	NBS987	Sr2	Re	TaF5	0.056489	0.000005	**0.710244**	0.000009	194/207
3	06/12/2007	460	No	NBS987	Sr2	Re	TaF5	0.056492	0.000003	**0.710238**	0.000006	195/200
3	07/12/2007	461	No	NBS987	Sr2	Re	TaF5	0.056461	0.000004	**0.710233**	0.000008	191/200
3	07/12/2007	461	No	NBS987	Sr2	Re	TaF5	0.056474	0.000004	**0.710241**	0.000008	193/200
3	08/12/2007	461	No	NBS987	Sr2	Re	TaF5	0.056462	0.000006	**0.710240**	0.000010	191/200
3	12/12/2007	463	No	NBS987	Sr2	Re	TaF5	0.056482	0.000005	**0.710250**	0.000008	190/200
3	12/12/2007	463	No	NBS987	Sr2	Re	TaF5	0.056498	0.000003	**0.710236**	0.000007	192/200
Feb 2008												
3	14/02/2008	484	No	NBS987	Sr2	Re	TaF5	0.056462	0.000002	**0.710241**	0.000006	193/200
3	14/02/2008	484	No	NBS987	Sr2	Re	TaF5	0.056490	0.000003	**0.710238**	0.000006	189/200
3	15/02/2008	484	No	NBS987	Sr2	Re	TaF5	0.056502	0.000003	**0.710244**	0.000005	190/200
3	15/02/2008	484	No	NBS987	Sr2	Re	TaF5	0.056497	0.000002	**0.710227**	0.000005	190/200
3	18/02/2008	485	No	NBS987	Sr2	Re	TaF5	0.056490	0.000003	**0.710239**	0.000006	189/200
3	18/02/2008	485	No	NBS987	Sr2	Re	TaF5	0.056480	0.000002	**0.710229**	0.000005	189/200
3	19/02/2008	485	No	NBS987	Sr2	Re	TaF5	0.056482	0.000002	**0.710234**	0.000005	189/200

Table A.2.continued

Std Size (ng)	Date	Mag no.	Repeat?	Std	Method File	Filament	Activator	84Sr/86Sr c	1SE	87Sr/86Sr corrected	1SE	# accepted ratios
June 2008 - Aug 2008												
600	02/06/2008	508	No	NBS987	Sr2	Re	TaF5	0.056493	0.000001	**0.710237**	0.000003	188/200
600	02/06/2008	508	No	NBS987	Sr2	Re	TaF5	0.056493	0.000001	**0.710243**	0.000004	191/200
600	02/06/2008	508	No	NBS987	Sr2	Re	TaF5	0.056942	0.000001	**0.710236**	0.000002	191/200
600	02/06/2008	508	No	NBS987	Sr2	Re	TaF5	0.056962	0.000003	**0.710242**	0.000002	191/200
600	02/06/2008	508	No	NBS987	Sr2	Re	TaF5	0.056685	0.000003	**0.710233**	0.000003	189/200
600	02/06/2008	508	No	NBS987	Sr2	Re	TaF5	0.056495	0.000001	**0.710245**	0.000003	190/200
3	02/06/2008	508	No	NBS987	Sr2	Re	TaF5	0.056490	0.000022	**0.710237**	0.000005	190/200
3	02/06/2008	508	No	NBS987	Sr2	Re	TaF5	0.056485	0.000002	**0.710234**	0.000006	193/200
3	02/06/2008	508	No	NBS987	Sr2	Re	TaF5	0.056485	0.000003	**0.710234**	0.000006	194/200
3	02/06/2008	508	No	NBS987	Sr2	Re	TaF5	0.056485	0.000003	**0.710245**	0.000006	191/200
3	03/06/2008	508	No	NBS987	Sr2	Re	TaF5	0.056492	0.000003	**0.710238**	0.000006	189/200
3	03/06/2008	508	No	NBS987	Sr2	Re	TaF5	0.056495	0.000002	**0.710226**	0.000005	190/200
3	03/06/2008	508	No	NBS987	Sr2	Re	TaF5	0.056491	0.000002	**0.710246**	0.000004	186/200
3	04/06/2008	509	No	NBS987	Sr2	Re	TaF5	0.056484	0.000002	**0.710245**	0.000005	191/200
3	04/06/2008	509	No	NBS987	Sr2	Re	TaF5	0.056498	0.000003	**0.710248**	0.000065	94/101
3	05/06/2008	509	No	NBS987	Sr2	Re	TaF5	0.056482	0.000003	**0.710238**	0.000005	194/200
3	05/06/2008	509	No	NBS987	Sr2	Re	TaF5	0.056487	0.000003	**0.710239**	0.000006	190/200
3	11/06/2008	510	No	NBS987	Sr2	Re	TaF5	0.056489	0.000002	**0.710241**	0.000006	141/149
3	11/06/2008	510	No	NBS987	Sr2	Re	TaF5	0.056497	0.000003	**0.710237**	0.000006	194/200
3	12/06/2008	510	No	NBS987	Sr2	Re	TaF5	0.056488	0.000002	**0.710246**	0.000004	189/200
3	12/06/2008	510	No	NBS987	Sr2	Re	TaF5	0.056489	0.000002	**0.710243**	0.000006	191/200
3	22/07/2008	518	No	NBS987	Sr2	Re	TaF5	0.056497	0.000002	**0.710254**	0.000005	194/200
3	22/07/2008	518	No	NBS987	Sr2	Re	TaF5	0.056501	0.000003	**0.710245**	0.000006	189/200
3	05/08/2008	519	No	NBS987	Sr2	Re	TaF5	0.056494	0.000003	**0.710233**	0.000006	193/200
Jan 2009 - Feb 2009												
600	26/01/09	573	No	NBS987	Sr2	Ta	HPO4	0.056491	0.000001	**0.710246**	0.000003	192/200
600	26/01/09	573	No	NBS987	Sr2	Ta	HPO4	0.056487	0.000001	**0.710247**	0.000003	190/200
600	26/01/09	573	No	NBS987	Sr2	Ta	HPO4	0.056492	0.000001	**0.710248**	0.000003	193/200
600	26/01/09	573	No	NBS987	Sr2	Ta	HPO4	0.056492	0.000002	**0.710231**	0.000005	193/200
600	26/01/09	573	No	NBS987	Sr2	Ta	HPO4	0.056495	0.000002	**0.710234**	0.000005	192/200
600	26/01/09	573	No	NBS987	Sr2	Ta	HPO4	0.056490	0.000004	**0.710248**	0.000003	192/200
600	26/01/09	573	No	NBS987	Sr2	Ta	HPO4	0.056490	0.000001	**0.710248**	0.000005	143/150
600	26/01/09	573	No	NBS987	Sr2	Ta	HPO4	0.056490	0.000001	**0.710246**	0.000003	195/200
600	26/01/09	573	No	NBS987	Sr2	Ta	HPO4	0.056491	0.000002	**0.710250**	0.000004	194/200
600	26/01/09	573	No	NBS987	Sr2	Ta	HPO4	0.056488	0.000001	**0.710245**	0.000003	197/200
12	27/01/09	573	No	NBS987	Sr2	Re	TaF5	0.056487	0.000002	**0.710241**	0.000004	192/200
12	27/01/09	573	No	NBS987	Sr2	Re	TaF5	0.056490	0.000001	**0.710249**	0.000004	192/200

Table A.2.continued

Std Size (ng)	Date	Mag no.	Repeat?	Std	Method File	Filament	Activator	84Sr/86Sr c	1SE	87Sr/86Sr corrected	1SE	# accepted ratios
Jan 2009 - Feb 2009												
6	27/01/09	573	No	NBS987	Sr2	Re	TaF5	0.056490	0.000002	**0.710239**	0.000006	192/200
6	27/01/09	573	No	NBS987	Sr2	Re	TaF5	0.056482	0.000003	**0.710245**	0.000006	189/200
6	27/01/09	573	No	NBS987	Sr2	Re	TaF5	0.056488	0.000002	**0.710256**	0.000005	190/200
3	27/01/09	573	No	NBS987	Sr2	Re	TaF5	0.056491	0.000003	**0.710243**	0.000006	188/200
3	27/01/09	573	No	NBS987	Sr2	Re	TaF5	0.056497	0.000003	**0.710246**	0.000006	192/200
3	27/01/09	573	No	NBS987	Sr2	Re	TaF5	0.056458	0.000003	**0.710248**	0.000007	192/200
3	28/01/09	574	No	NBS987	Sr2	Re	TaF5	0.056479	0.000005	**0.710255**	0.000009	192/200
3	29/01/09	574	No	NBS987	Sr2	Re	TaF5	0.056483	0.000003	**0.710249**	0.000005	192/200
3	29/01/09	574	No	NBS987	Sr2	Re	TaF5	0.056481	0.000006	**0.710253**	0.000006	199/200
3	04/02/09	576	No	NBS987	Sr2	Re	TaF5	0.056487	0.000003	**0.710237**	0.000007	192/200
3	04/02/09	576	No	NBS987	Sr2	Re	TaF5	0.056490	0.000005	**0.710239**	0.000008	185/200
3	05/02/09	576	No	NBS987	Sr2	Re	TaF5	0.056488	0.000004	**0.710233**	0.000007	190/200
3	05/02/09	576	No	NBS987	Sr2	Re	TaF5	0.056484	0.000005	**0.710239**	0.000006	188/200
3	06/02/09	577	No	NBS987	Sr2	Re	TaF5	0.056487	0.000003	**0.710243**	0.000006	191/200
3	06/02/09	577	No	NBS987	Sr2	Re	TaF5	0.056494	0.000004	**0.710259**	0.000008	193/200
3	07/02/09	577	No	NBS987	Sr2	Re	TaF5	0.056483	0.000008	**0.710250**	0.000017	104/109
3	07/02/09	577	No	NBS987	Sr2	Re	TaF5	0.056486	0.000002	**0.710243**	0.000005	192/200
3	02/03/09	585	No	NBS987	Sr2	Re	TaF5	0.056499	0.000003	**0.710244**	0.000006	190/200
3	02/03/09	585	No	NBS987	Sr2	Re	TaF5	0.056497	0.000002	**0.710250**	0.000005	191/200
3	03/03/09	585	No	NBS987	Sr2	Re	TaF5	0.056494	0.000003	**0.710248**	0.000005	191/200
3	03/03/09	585	No	NBS987	Sr2	Re	TaF5	0.056493	0.000003	**0.710257**	0.000006	190/200
3	04/03/09	586	No	NBS987	Sr2	Re	TaF5	0.056477	0.000003	**0.710246**	0.000006	188/200
Aug 2009 - Sept 2009												
3	17/09/09	647	Yes	NBS987	Sr2	Re	TaF5	0.056504	0.000006	**0.710249**	0.000010	193/200
3	17/09/09	647	No	NBS987	Sr2	Re	TaF5	0.056492	0.000002	**0.710244**	0.000005	191/200
1	17/09/09	647	No	NBS987	Sr2	Re	TaF5	0.056485	0.000004	**0.710243**	0.000007	190/200
1	17/09/09	647	No	NBS987	Sr2	Re	TaF5	0.056490	0.000004	**0.710254**	0.000008	189/200

Table A.3. *Summary of NBS987 standard data run on the Neptune(PIMS) during the period the data were analysed. These values, according to the batch number, were used to normalise the measured Sr isotope ratios to the accepted values.*

Date	Batch Numbers Analysed	NBS987			
		$^{87}Sr/^{86}Sr_m$	2sd abs	2sd (ppm)	n
15/10/2008	92, 110	0.710258	0.000005	7.0	7
01/04/2009	111, 112, 113	0.710248	0.000020	27.9	12
23/04/2009	116	0.710241	0.000010	14.7	8

Table A.4. *Details of NBS987 standards run.*

Run No	Sample Name	87Sr/86Sr	1SE	Int (V) 88Sr	Int (mV) 85Rb
15/10/2008					
6	NBS 987	0.710257	0.000004	22.5	0.08
7	NBS 987	0.710263	0.000006	22.6	0.05
8	NBS 987	0.710258	0.000004	22.8	0.05
9	NBS 987	0.710259	0.000005	22.8	0.05
15	NBS 987	0.710255	0.000005	22.1	0.04
21	NBS 987	0.710257	0.000005	20.9	0.06
24	NBS 987	0.710259	0.000051	20.8	0.05
01/04/2009					
9	NBS987	0.710244	0.000005	11.7	0.18
10	NBS987	0.710238	0.000006	11.7	0.19
11	NBS987	0.710250	0.000008	11.6	0.17
12	NBS987	0.710234	0.000006	11.7	0.18
18	NBS987	0.710273	0.000007	11.4	0.17
19	NBS987	0.710245	0.000008	11.4	0.17
25	NBS987	0.710253	0.000006	11.3	0.17
31	NBS987	0.710255	0.000006	11.4	0.17
37	NBS987	0.710247	0.000007	12.3	0.18
43	NBS987	0.710241	0.000007	12.3	0.18
46	NBS987	0.710249	0.000007	12.3	0.19
47	NBS987	0.710245	0.000005	12.3	0.18
23/04/2009					
5	NBS987	0.710252	0.000004	23.0	0.23
6	NBS987	0.710236	0.000005	23.1	0.22
7	NBS987	0.710239	0.000005	21.6	0.22
8	NBS987	0.710245	0.000004	21.2	0.22
14	NBS987	0.710239	0.000005	22.7	0.23
15	NBS987	0.710242	0.000004	22.7	0.22
20	NBS987	0.710239	0.000005	23.1	0.23
21	NBS988	0.710237	0.000003	23.2	0.23

Table A.5. *Summary of J&M as well as Sm-doped J&M (corrected offline for Sm interferences) standard data run on the Neptune (PIMS) during the period the data were analysed. These values, according to the batch number, were used to normalise the measured Nd isotope ratios to the accepted value.*

Date	Batch Numbers Analysed	J&M				Sm doped J&M			
		$^{143}Nd/^{144}Nd_m$	2sd abs	2sd (ppm)	n	$^{143}Nd/^{144}Nd_m$	2sd abs	2sd (ppm)	n
28/05/2008	M58	0.511103	0.000013	24.9	2	0.511112	0.000009	18.5	3
22/10/2008	M56, M57, M67, 92,96,108,110	0.511104	0.000008	16.5	9	0.511104	0.000011	22.2	8
31/03/2009	M76, M77, M81, 113	0.511116	0.000010	19.7	7	0.511117	0.000016	31.7	6

Table A.6. *Full details J&M and Sm-doped J&M standards run.*

Run Sequence	Sample Name	143Nd/144Nd	1SE	Int (V) 146Nd	Int (mV) 147Sm
28/05/2008					
7	J&M	0.511107	0.000009	1.17	0.01
8	J&M	0.511098	0.000007	1.17	0.01
9	Sm doped J&M	0.511108	0.000009	1.40	235
10	Sm doped J&M	0.511110	0.000010	1.40	236
16	Sm doped J&M	0.511117	0.000008	1.38	231
22/10/2008					
1	J&M	0.511103	0.000006	3.43	0.07
2	J&M	0.511099	0.000005	3.46	0.07
3	J&M	0.511106	0.000007	3.45	0.07
11	J&M	0.511102	0.000007	3.35	0.16
18	J&M	0.511106	0.000006	3.11	0.16
26	J&M	0.511096	0.000007	3.18	0.12
33	J&M	0.511108	0.000006	3.45	0.10
40	J&M	0.511103	0.000006	3.35	0.16
45	J&M	0.511109	0.000005	2.42	0.60
4	Sm doped J&M	0.511109	0.000006	2.16	470
5	Sm doped J&M	0.511104	0.000006	2.19	478
12	Sm doped J&M	0.511100	0.000007	1.95	424
21	Sm doped J&M	0.511109	0.000007	1.82	396
27	Sm doped J&M	0.511096	0.000005	1.96	430
34	Sm doped J&M	0.511109	0.000007	2.14	452
41	Sm doped J&M	0.511110	0.000007	1.85	396
46	Sm doped J&M	0.511098	0.000009	1.36	286
31/03/2009					
1	J&M	0.511114	0.000006	2.85	0.06
2	J&M	0.511124	0.000005	2.85	0.06
3	J&M	0.511118	0.000005	2.86	0.06
11	J&M	0.511113	0.000006	2.80	0.07
18	J&M	0.511118	0.000007	2.78	0.07
25	J&M	0.511114	0.000007	2.72	0.06
32	J&M	0.511108	0.000006	2.69	0.06
4	Sm doped J&M	0.511109	0.000007	2.83	236
5	Sm doped J&M	0.511117	0.000005	2.84	237
12	Sm doped J&M	0.511115	0.000006	2.79	232
19	Sm doped J&M	0.511131	0.000006	2.80	233
26	Sm doped J&M	0.511118	0.000007	2.75	227
33	Sm doped J&M	0.511109	0.000007	2.71	223

Table A.7. *Summary of total procedural blanks (TPB) for each batch of chemistry processed for Sr isotope analysis (n refers to number of blanks in the chemistry batch). The average mass of Sr analyte (ng) that was analysed for Sr isotope ratios is shown and the blank contribution calculated as a percentage of this. The mass of Sr analyte in each batch did show considerable variation but this gives an indication of blank levels.*

Batch #	TPB (pg)	n	Average Sr in sample (ng)	Blank Contribution %
M30	20.3	2	28.9	0.07
M33	12	3	10.0	0.12
M35	0.9	3	11.7	0.01
M41	11.3	3	11.2	0.10
M42	9.7	4	11.3	0.09
Change 3% HNO3 made with UPA water as oppose to MilliQ				
M44	13.2	2	75.1	0.02
M46	20.4	4	11.2	0.18
M48	26.8	3	8.6	0.31
M49	22.3	2	11.8	0.19
M52	19.3	2	7.8	0.25
M53	13.6	2	17.3	0.08
M54	15.2	3	34.8	0.04
M56	14.6	7	16.7	0.09
M57	20.5	3	12.3	0.17
M58	11.1	4	3.3	0.34
M67	10.2	3	18.8	0.05
M68	12	3	5.3	0.23
M75	23	3	337.8	0.01
M76	10	5	18.5	0.05
M77	33	2	8.31	0.40
M81	14	3	4.92	0.28

Table A.8. *Summary of standard data run on the Element II. A standard is run for every six samples but this is used to correct for the drift throughout the run and the relative percentage difference between the accepted values for these USGS standards (Weis et al., 2005) is used for this correction. The standards presented here are the standard that is run after the first six samples where the drift is assumed to be minimal. 1-10 refers to a dilution factor of 10 (from the official standard), 1-100 is a dilution factor of 100 and 1-1000 is a dilution factor of 1000.*

Date	22/05/2007		16/10/2007		04/12/2007		21/02/2008		25/03/2008	
Number in run	24		27		22		22		21	
Batch numbers analysed	M30		M33, M35, M41, M42		M44, M46, M48, M49		M52, M53, M54		M56	
Standard Used	W2 1-100	%Diff	W2 1-100	%Diff	W2 1-100	%Diff	BHVO-1 1-100	%Diff	W2 1-1000	%Diff
Rb	0.360	11.5	0.418	2.8	0.436	7.0	0.194	1.0	0.031	23.4
Sr	3.550	8.2	4.307	11.4	4.524	17.0	8.648	7.3	0.348	9.9
Y	0.397	7.1	0.490	14.7	0.487	14.0	0.581	5.3	0.036	14.6
Zr	1.511	18.6	1.923	3.5	1.934	4.1	3.911	9.2	0.142	23.6
Nb	0.135	13.0	0.160	3.2	0.165	6.5	0.394	1.1	0.012	20.0
Ba	3.077	7.9	3.726	11.5	3.934	17.7	2.927	5.3	0.367	9.9
La	0.187	11.7	0.226	6.4	0.242	13.9	0.319	1.0	0.017	18.4
Ce	0.399	13.4	0.486	5.5	0.529	14.9	0.777	0.4	0.038	18.2
Pr	0.058	1.3	0.072	23.1	0.077	31.4	0.124	8.8	0.005	6.5
Nd	0.253	4.2	0.306	15.9	0.324	22.6	0.573	13.6	0.024	10.8
Sm	0.060	10.8	0.075	11.1	0.083	23.5	0.140	13.2	0.005	19.9
Eu	0.021	5.7	0.026	15.8	0.026	16.3	0.048	17.5	0.002	18.0
Gd	0.068	5.8	0.089	22.1	0.094	29.5	0.151	17.9	0.007	7.6
Dy	0.070	5.3	0.088	18.5	0.093	25.0	0.116	11.5	0.007	6.4
Er	0.038	14.4	0.049	9.3	0.051	14.8	0.054	11.6	0.004	16.4
Yb	0.037	9.5	0.048	19.3	0.050	23.6	0.044	9.7	0.004	11.4
Lu	0.006	3.2	0.008	17.0	0.008	18.9	0.007	15.3	0.001	14.0
Hf	0.045	10.0	0.057	13.6	0.058	16.2	0.097	11.2	0.004	19.6
Pb	0.155	0.6	0.181	15.6	0.233	49.3	0.075	43.5	0.050	222.5
Th	0.040	2.2	0.050	23.2	0.055	34.0	0.028	22.5	0.004	6.5
U	0.009	5.0	0.012	18.9	0.013	27.4	0.010	18.9	0.001	8.4
Tb	0.012	1.6	0.015	22.6	NA		0.022	12.4	0.001	6.8

Table A.8.continued

Date	15/04/2008		01/08/2008		13/10/2008		01/12/2008		08/12/2008	
Number in run	27		22		22		40		21	
Batch numbers analysed	M56, M57, M58		106, M56		M66, M67, 109, 110		111, M68		M67, M75, M76	
Standard Used	W2 1-1000	%Diff	BHVO-1 1-1000	%Diff	W2 1-100	%Diff	W2 1-100	%Diff	W2 1-1000	%Diff
Rb	0.034	17.4	0.014	26.8	0.335	17.7	0.413	1.5	0.042	2.2
Sr	0.359	7.2	0.567	29.6	3.308	14.5	4.256	10.1	0.406	5.1
Y	0.038	12.1	0.041	24.8	0.380	11.0	0.457	6.9	0.045	5.0
Zr	0.147	21.0	0.261	27.0	1.491	19.7	1.792	3.5	0.159	14.6
Nb	0.013	14.4	0.028	28.3	0.132	14.7	0.153	1.6	0.015	0.4
Ba	0.393	17.6	0.209	24.7	2.823	15.5	3.378	1.1	0.451	35.1
La	0.018	16.6	0.023	27.9	0.175	17.8	0.216	2.0	0.021	0.6
Ce	0.039	15.7	0.054	30.3	0.374	18.8	0.461	0.2	0.044	3.9
Pr	0.005	7.8	0.008	25.5	0.052	11.5	0.065	10.1	0.006	5.0
Nd	0.025	6.1	0.039	22.3	0.228	13.9	0.286	8.3	0.028	4.1
Sm	0.006	14.6	0.009	26.1	0.057	15.0	0.070	4.1	0.007	2.8
Eu	0.002	14.2	0.003	25.8	0.019	16.8	0.025	11.1	0.002	8.5
Gd	0.007	1.1	0.011	17.2	0.061	15.4	0.079	9.2	0.008	12.8
Dy	0.007	7.6	0.008	24.6	0.068	8.1	0.079	6.4	0.007	2.8
Er	0.003	22.3	0.004	24.4	0.037	17.7	0.044	1.8	0.004	9.0
Yb	0.004	12.7	0.003	34.3	0.036	11.6	0.059	45.9	0.004	1.6
Lu	0.001	13.0	0.000	25.9	0.006	11.6	0.013	89.7	0.001	8.3
Hf	0.004	21.5	0.007	23.9	0.041	17.6	0.049	1.3	0.004	12.3
Pb	0.049	210.7	0.009	79.8	0.137	12.6	0.176	12.4	0.058	268.5
Th	0.004	5.7	0.002	15.2	0.037	10.0	0.045	9.9	0.004	9.5
U	0.001	8.0	0.001	23.5	0.008	19.1	0.010	0.7	0.001	15.0
Tb	0.001	11.5	0.002	21.2	0.011	13.2	0.013	7.9	0.001	1.3

Table A.8.continued

Date	16/01/2009		12/03/2009		01/05/2009	
Number in run	17		21		19	
Batch numbers analysed	M75, M76, M77		M68, M75, M76, M81, 118		116	
Standard Used	BHVO-1 1-1000	%Diff	W2 1-1000	%Diff	W2 1-10	%Diff
Rb	0.016	15.8	0.039	4.3	3.4680	14.8
Sr	0.663	17.7	0.386	0.2	34.0931	11.8
Y	0.047	15.3	0.045	4.5	3.9145	8.4
Zr	0.276	22.9	0.174	6.2	15.5915	16.1
Nb	0.032	18.3	0.015	0.6	1.3499	13.0
Ba	0.249	10.4	0.340	1.9	29.8891	10.6
La	0.026	16.5	0.020	7.5	1.7920	15.6
Ce	0.063	19.5	0.047	1.9	3.8573	16.3
Pr	0.010	15.7	0.006	9.7	0.5338	9.2
Nd	0.045	9.8	0.027	2.4	2.3556	10.9
Sm	0.011	14.0	0.006	5.9	0.5790	13.8
Eu	0.004	13.3	0.002	12.7	0.1958	12.6
Gd	0.010	24.0	0.008	11.9	0.6715	7.5
Dy	0.009	15.4	0.007	2.2	0.6524	12.1
Er	0.004	12.8	0.004	1.3	0.3638	18.4
Yb	0.005	7.4	0.004	0.6	0.3573	12.0
Lu	0.001	104.8	0.001	0.9	0.0571	13.4
Hf	0.007	18.0	0.005	4.8	0.4160	16.5
Pb	0.016	208.5	0.036	130.7	1.3403	14.2
Th	0.002	1.7	0.005	18.9	0.3879	4.9
U	0.001	5.2	0.001	2.8	0.0885	11.5
Tb	0.001	31.4	0.001	4.7	0.1102	11.2

Table A.9(a) *Summary of the reproducibility of the official standards, the percent recovery of each element and the drift over Day 1 of analysis (at the University of Cambridge). %RSD refers to one standard deviation and %Rec refers to the percentage of analyte recovered from an analysis of the standard compared to the accepted value; a measure of accuracy.*

Element	BCR-2			BIR-1			BHVO-2			Daily Drift
	Average	%RSD	%Rec	Average	%RSD	%Rec	Average	%RSD	%Rec	
Rb	45.35	4	97	0.19	33	78	9.34	2	103	1.06
Sr	355.99	5	105	109.43	3	99	415.24	2	105	1.05
Y	34.13	3	92	15.31	3	93	24.97	1	96	0.99
Zr	216.98	5	115	15.94	16	110	190.66	3	111	0.88
Nb	13.540	5	123	0.485	21	88	18.190	2	101	1.15
Ba	654.95	5	97	6.43	21	101	131.76	2	101	
La	25.717	4	103	0.688	5	119	16.323	1	107	1.23
Ce	50.153	3	95	1.840	2	99	36.613	2	98	1.09
Pr	6.660	4	101	0.369	11	100	5.463	3	103	1.08
Nd	29.470	3	103	2.853	6	121	25.917	2	106	1.03
Sm	6.563	3	100	1.210	15	110	6.097	6	100	1.00
Eu	1.960	10	100	0.553	11	106	2.123	4	103	1.12
Gd	7.080	7	105	1.970	16	100	6.273	3	101	0.98
Tb	1.032	11	96	0.359	7	94	0.937	3	100	1.09
Dy	6.490	3	101	2.627	5	105	5.533	5	104	1.04
Ho	1.295	9	100	0.584	10	102	1.032	3	106	0.86
Er	3.773	7	103	1.720	4	106	2.460	3	97	1.01
Tm	0.548	17	102	0.249	13	99	0.321	2	97	1.12
Yb	3.560	7	105	1.823	4	114	2.163	2	108	0.89
Lu	0.556	15	109	0.263	3	105	0.280	10	102	1.15
Hf	5.223	7	109	0.501	7	89	4.357	6	106	0.82
Ta	0.943	17	115	0.040	26	66	1.265	2	90	0.78
Pb	12.260	4	111	4.080	14	136	6.773	20	423	0.93
Th	6.363	5	103	0.023	12	76	1.331	3	111	1.43
U	1.493	6	88	0.031	50	310	0.386	6	99	0.97

Table A.9(b) *Summary of the reproducibility of the official standards, the percent recovery of each element and the drift over Day 2 of analysis (at the University of Cambridge). %RSD refers to one standard deviation and %Rec refers to the percentage of analyte recovered from an analysis of the standard compared to the accepted value; a measure of accuracy.*

Element	BCR-2			BIR-1			BHVO-2			Daily Drift
	Average	%RSD	%Rec	Average	%RSD	%Rec	Average	%RSD	%Rec	
Rb	34.29	7	73	0.14	12	57	7.44	2	82	1.70
Sr	317.23	2	93	103.04	2	94	388.80	1	98	1.11
Y	36.69	7	99	14.75	2	89	23.54	2	91	1.05
Zr	202.60	9	108	14.20	2	98	164.83	2	96	0.98
Nb	13.050	7	119	0.459	9	83	16.753	2	93	0.94
Ba	616.54	4	91	5.85	6	91	124.23	2	95	
La	27.113	5	109	0.635	13	110	15.690	0	103	0.90
Ce	46.543	4	88	1.637	4	89	31.957	1	85	0.97
Pr	6.817	5	104	0.381	2	103	5.197	1	98	0.87
Nd	31.197	5	109	2.347	6	100	25.513	1	104	1.03
Sm	7.213	5	110	1.153	12	105	6.290	4	104	0.95
Eu	1.883	1	96	0.537	4	103	2.037	1	98	0.91
Gd	7.410	5	110	1.907	8	97	6.087	2	98	1.03
Tb	0.974	15	91	0.369	6	97	0.912	3	97	1.00
Dy	6.947	6	108	2.730	3	109	5.160	2	97	1.02
Ho	1.275	7	98	0.559	5	98	0.940	1	97	0.99
Er	3.707	7	101	1.743	8	107	2.400	5	94	1.03
Tm	0.481	20	89	0.255	9	102	0.328	7	99	1.10
Yb	3.870	7	114	1.817	8	114	2.070	2	104	1.02
Lu	0.457	30	90	0.270	5	108	0.282	1	103	1.06
Hf	5.370	11	112	0.558	3	100	4.337	4	106	0.99
Ta	0.913	13	111	0.044	17	73	1.274	5	91	1.06
Pb	9.800	6	89	3.087	9	103	4.540	4	284	0.50
Th	6.610	8	107	0.035		118	1.280	0	107	2.04
U	1.161	8	69	0.027		266	0.306	11	78	1.21

Table A.10. *Details of the electron microprobe set up and detection limits used to analyse the mantle xenoliths on the electron microprobe at the University of Cambridge.*

OLIVINE										
Element	**Xray Peak**	**Crystal**	**Peak Time (s)**	**Background time (s)**	**Background offset1**	**Background offset 2**	**Slope/ background**	**Calibration**	**Detection Limit (max) ppm**	**Detection Limit (max) wt%oxide**
Major:										
Na	Na Kα1	LATP	20	10	-600	400		Jadite	215	0.06
Mg	Mg Kα1	TAP	20	10	-550	350		Periclase	705	0.12
Si	Si Kα1	TAP	20	10	-500	300		Diopside	510	0.11
Fe	Fe Kα1	LIF	20	10	-250	300		Fe	1234	0.16
Trace:										
Al	Al Kα1	TAP	50	25	-500	300		Corrundum	46	0.02
Ca	Ca Kα1	LPET	40	20	-300	250		Diopside	46	0.01
Ti	Ti Kα1	LPET	40	20	-350	250		Ti	58	0.01
Cr	Cr Kα1	LIF	40	20	-200	300		Cr	219	0.06
Mn	Mn Kα1	LIF	40	20		300	1.0221	Mn	287	0.04
Ni	Ni Kα1	LIF	40	20	-250	300		Ni	322	0.04

DIOPSIDE										
Element	**Xray Peak**	**Crystal**	**Peak Time (s)**	**Background time (s)**	**Background offset1**	**Background offset 2**	**Slope/backgr ound**	**Calibration**	**Detection Limit (max) ppm**	**Detection Limit (max)**
Major:										
Na	Na Kα1	LATP	20	10	-600	400		Jadite	289	0.08
Mg	Mg Kα1	TAP	20	10	-550	350		Periclase	458	0.08
Si	Si Kα1	TAP	20	10	-500	300		Diopside	432	0.09
Ca	Ca Kα1	LPET	20	10	-300	250		Diopside	512	0.07
Trace:										
Al	Al Kα1	TAP	50	25	-500	300		Corrundum	48	0.02
K	K Kα1	LPET	20	10	-300	250		Diopside	325	0.08
Ti	Ti Kα1	LPET	40	20	-350	250		Ti	61	0.01
Fe	Fe Kα1	LIF	30	15	-250	300		Fe	263	0.03
Cr	Cr Kα1	LIF	30	15	-200	300		Cr	250	0.07
Mn	Mn Kα1	LIF	30	15		300	1.0221	Mn	288	0.04
Ni	Ni Kα1	LIF	30	15	-250	300		Ni	328	0.04

ORTHOPYROXENE										
Element	**Xray Peak**	**Crystal**	**Peak Time (s)**	**Background time (s)**	**Background offset1**	**Background offset 2**	**Slope/ background**	**Calibration**	**Detection Limit (max) ppm**	**Detection Limit (max)**
Major:										
Na	Na Kα1	LATP	20	10	-600	400		Jadite	214	0.06
Mg	Mg Kα1	TAP	20	10	-550	350		Periclase	602	0.10
Si	Si Kα1	TAP	20	10	-500	300		Diopside	446	0.10
Fe	Fe Kα1	LIF	20	10	-250	300		Fe	1216	0.16
Trace:										
Al	Al Kα1	TAP	50	25	-500	300		Corrundum	45	0.02
Ca	Ca Kα1	LPET	40	20	-300	250		Diopside	317	0.04
Ti	Ti Kα1	LPET	40	20	-350	250		Ti	58	0.01
Cr	Cr Kα1	LIF	30	15	-200	300		Cr	222	0.06
Mn	Mn Kα1	LIF	30	15		300	1.0221	Mn	280	0.04
Ni	Ni Kα1	LIF	30	15	-250	300		Ni	319	0.04

PYROPE										
Element	**Xray Peak**	**Crystal**	**Peak Time (s)**	**Background time (s)**	**Background offset1**	**Background offset 2**	**Slope/ background**	**Calibration**	**Detection Limit (max) ppm**	**Detection Limit (max)**
Major:										
Na	Na Kα1	LATP	20	10	-600	400		Jadite	220	0.06
Mg	Mg Kα1	TAP	20	10	-550	350		Periclase	507	0.08
Si	Si Kα1	TAP	20	10	-500	300		Diopside	414	0.09
Al	Al Kα1	TAP	20	10	-500	300		Corrundrum	388	0.15
Trace:										
P	Al Kα1	LPET	30	15	-250	600		Apatite	68	0.03
Ca	K Kα1	LPET	30	15	-300	250		Diopside	88	0.01
Ti	Ti Kα1	LPET	30	15	-350	250		Ti	69	0.01
Fe	Fe Kα1	LIF	30	15	-250	300		Fe	302	0.04
Cr	Cr Kα1	LIF	30	15	-200	300		Cr	314	0.09
Mn	Mn Kα1	LIF	30	15		300	1.0221	Mn	305	0.04

Table A.11. *Details of the electron microprobe set up and detection limits used to analyse minerals from SPK and Jos by GSC at Carleton University, Ottawa, Canada.*

Carbonates: 15kV accelerating voltage, 10 nA beam current, defocused beam (large raster, 8k to 16k magnification). Counting times 10 to 20 seconds per element.

Element	Line	Standard	Element	Line	Standard
Ca	Kα	$CaMg(CO_3)_2$	Sr	Lα	$SrSO_4$
Mg	Kα	$CaMg(CO_3)_2$	Ba	Lα	$BaSO_4$
Mn	Kα	$MnCO_3$	Zn	Kα	$ZnAl_2O_4$
Fe	Kα	$FeCO_3$			

Oxides and Olivine
20kV accelerating voltage, 25 nA beam current, focused beam (~ 3 microns in diameter). Counting times 10 to 20 seconds per element, Ni in olivine 50 secs.

Element	Line	Standard	Element	Line	Standard
Si	Kα	$CaSiO_3$	Mn	Kα	synth. $MnTiO_3$
Ti	Kα	synth. $MnTiO_3$	Ni	Kα	NiO
Al	Kα	synth. $MgAl_2O_4$	Co	Kα	Co
Cr	Kα	Cr_2O_2	Zn	Kα	$ZnAl_2O_4$
V	Kα	V	Mg	Kα	$MgAl_2O_4$
Fe	Kα	$FeTiO_3$	Ca	Kα	$CaSiO_3$,

Phlogopite (MICA routine)
15kV accelerating voltage, 18 nA beam current, focused electron beam (~2 micron diameter). Counting times were 15-20 seconds or 40,000 accumulated counts.

Element	Line	Standard	Element	Line	Standard
Si	Kα	wollastonite	Mg	Kα	olivine (Fo92)
Ti	Kα	synthetic $MnTiO_3$	Ca	Kα	wollastonite
Al	Kα	synthetic $MgAl_2O_4$	Na	Kα	albite
Cr	Kα	synthetic Cr_2O_3	K	Kα	orthoclase
V	Kα	pure element V	Ba	Kα	barite
Fe	Kα	synthetic Fe_2SiO_4	F	Kα	LiF
Mn	Kα	synthetic $MnTiO_3$	Cl	Kα	tugtupite ($Na_4AlBeSi_4O_{12}Cl$)

Apatite
15kV accelerating voltage, 18 nA beam current, focused electron beam (~2 micron diameter). Counting times were 15-20 seconds or 40,000 accumulated counts.

Element	Line	Standard	Element	Line	Standard
P	Kα	BRGM apatite	Ce	Lα	synth. CeO_2
Si	Kα	$Na_4AlBeSi_4O_{12}Cl$	Pr	Lβ	synth. PrF_3
Fe	Kα	synth. Y-Fe-grt	Nd	Lα	synth. $NdAlO_3$
Mn	Kα	synth. $MnTiO_3$	Sm	Lβ	synth. $SmAlO_3$
Ca	Kα	BRGM apatite	Y	Lα	synth. Y-Fe-grt
Sr	Lα	celestite $SrSO_4$	F	Kα	BRGM apatite
Ba	Lα	barite $BaSO_4$	Cl	Kα	$Na_4AlBeSi_4O_{12}Cl$
Na	Kα	$Na_4AlBeSi_4O_{12}Cl$	S	Kα	celestite $SrSO_4$
La	Lα	synth. $LaAlO_3$			

Perovskite

20kV accelerating voltage, 25 nA beam current, focused electron beam (~2 micron diameter). Counting times were 15-20 seconds or 40,000 accumulated counts.

Element	Line	Standard	Element	Line	Standard
Nb	Lα	synth. Nb_2O_5	Mn	Kα	synth. $MnTiO_3$
Ta	Lα	synth. Ta_2O_5	Mg	Kα	synth. $MgAl_2O_4$
Zr	Lα	synth. $ZrSiO_4$	Ca	Kα	synth. $CaSiO_3$
Si	Kα	synth. $CaSiO_3$	Sr	Lα	celestite $SrSO_4$
Ti	Kα	synthetic $MnTiO_3$	Ba	Lα	barite $BaSO_4$
Al	Kα	synthetic $MgAl_2O_4$	Na	Kα	albite
Cr	Kα	synth. Cr_2O_3	La	Lα	synth. REE glass
Fe	Kα	synth. Fe_2SiO_4	Ce	Lα	synth. REE glass

References:

Weis, D., Kieffer, B., Maerschalk, C., Pretorius, W. and Barling, J., 2005. High-precision Pb-Sr-Nd-Hf isotopic characterization of USGS BHVO-1 and BHVO-2 reference materials. Geochemistry Geophysics Geosystems, 6: 10.

Appendix B:

MIDDLE ATLAS XENOLITH DATA

Table B.1(a). *Major element data (in wt% oxide) for the main minerals from the Middle Atlas xenoliths. (n.d. refers to not detected and * refers to data taken from Wittig (2006)).*

	SiO_2	TiO_2	Al_2O_3	Cr_2O_3	FeO	MgO	MnO	CaO	BaO	NiO	Na_2O	K_2O	F	Cl	Total
3V CPX															
3V-B	52.29	0.25	6.51	0.84	3.48	15.16	0.11	19.05		0.05	1.73				99.45
3V-C	52.57	0.25	6.52	0.88	3.46	15.39	0.11	19.07		0.06	1.77				100.08
3V-D	52.16	0.26	6.46	0.85	3.52	15.58	0.08	18.88		0.05	1.74				99.58
3V-E	52.14	0.27	6.80	0.88	3.63	15.39	0.10	18.78		0.04	1.82				99.84
3V-F	52.46	0.26	6.61	0.89	3.57	15.56	0.10	18.75		0.03	1.84				100.08
3V-G	52.14	0.26	6.56	0.80	3.53	15.56	0.12	18.92		0.03	1.75				99.68
3V-H	52.64	0.26	6.32	0.80	3.55	15.78	0.11	18.70		0.03	1.70				99.88
3V-I	52.11	0.26	6.54	0.84	3.52	15.69	0.11	18.79		0.06	1.78				99.70
3V-J	52.41	0.27	6.48	0.84	3.53	15.51	0.11	18.89		0.06	1.73				99.83
3V-K	52.69	0.28	6.73	0.89	3.50	15.38	0.09	18.88		0.05	1.81				100.30
3V-M	52.71	0.26	6.44	0.85	3.58	15.40	0.10	18.75		0.03	1.77				99.88
3V-O	52.26	0.27	6.68	0.85	3.57	15.36	0.10	18.81		0.04	1.84				99.77
3V-P	52.22	0.25	6.38	0.87	3.43	15.38	0.10	19.10		0.06	1.70				99.48
3V-Q	52.58	0.28	6.84	0.86	3.52	15.47	0.10	18.77		0.06	1.81				100.29
3V-R	52.00	0.26	6.48	0.81	3.52	15.59	0.11	18.91		0.05	1.82				99.55
3V-S	52.26	0.27	6.78	0.87	3.59	15.47	0.12	18.73		0.05	1.80				99.92
3V-T	52.07	0.26	6.48	0.82	3.55	15.27	0.11	18.94		0.05	1.73				99.28
3V-U	52.33	0.26	6.48	0.83	3.52	15.61	0.11	18.76		0.06	1.75				99.70
3V-V	52.74	0.26	6.46	0.83	3.53	15.24	0.11	18.82		0.05	1.76				99.80
3V-W	52.45	0.26	6.46	0.84	3.51	15.23	0.10	18.96		0.05	1.72				99.58
3V OLIVINE															
3VOL1	41.11	0.01	0.03	0.02	10.23	48.58	0.14	0.07		0.37	n.d.				100.55
3VOL2	41.24	0.00	0.03	0.02	10.25	48.74	0.15	0.08		0.39	n.d.				100.89
3V OPX															
3VOPX1	54.35	0.06	4.83	0.44	6.69	32.28	0.15	0.82		0.09	0.14				99.84
3VOPX2	55.04	0.07	4.54	0.40	6.68	32.49	0.19	0.80		0.10	0.15				100.45
3V AMPHIBOLE*															
43 (inclusion)	42.34	1.15	15.75	1.13	4.77	17.67	0.11	10.03	3.66	0.33	0.2	0.1	0.07	0.38	97.69
44 (inclusion)	43.28	1.24	15.55	1.27	5.08	18.15	0.00	10.23	3.79	0.37	0.14	0.19	0.06	0.45	99.80
3U CPX															
3U-A	52.92	0.18	5.24	0.83	3.28	15.67	0.11	20.66		0.03	1.33				100.27
3U-B	51.69	0.19	5.25	0.82	3.33	15.86	0.10	20.65		0.05	1.28				99.22
3U-D	52.51	0.20	5.29	0.82	3.36	15.72	0.09	20.27		0.04	1.29				99.59
3U-E	52.66	0.20	5.36	0.78	3.29	15.49	0.09	20.57		0.05	1.35				99.84
3U-F	52.37	0.20	5.27	0.81	3.37	15.73	0.10	20.37		0.05	1.33				99.61
3U-G	52.72	0.20	5.28	0.80	3.30	15.85	0.11	20.39		0.05	1.27				99.98
3U OLIVINE															
3UOL1	40.92	n.d.	0.03	0.01	10.15	48.66	0.15	0.06		0.39	n.d.				100.38
3UOL2	41.01	0.00	0.02	0.03	10.12	48.44	0.16	0.06		0.42	n.d.				100.27
3U OPX															
3UOPX1	55.75	0.05	3.95	0.40	6.60	32.65	0.15	0.65		0.10	0.06				100.38
3UOPX2	55.37	0.05	4.11	0.38	6.64	32.91	0.14	0.77		0.11	0.08				100.57
3UOPX3	55.91	0.05	4.02	0.41	6.58	33.02	0.16	0.70		0.11	0.09				101.06
3U AMPHIBOLE*															
22 (inclusion)	43.98	0.98	15.36	1.34	4.69	18.29	0.11	10.60	0.04	3.22	0.16	0.44	0.12	0.12	99.57
44 (inclusion core)	44.25	0.94	15.06	1.21	4.25	18.27	0.14	10.70	0.29	3.63	0.23	0.47	0.00	0.11	99.62
45 (inclusion rim)	44.27	1.89	13.96	0.49	4.49	19.57	0.05	10.70	0.16	3.23	0.07	0.43	0.60	0.02	100.1
46 (inclusion rim)	44.65	1.79	13.48	0.63	4.17	19.32	0.06	10.64	0.00	3.37	0.17	0.44	0.38	0.01	99.29
55 (relic core)	43.92	0.88	14.92	1.29	4.96	18.12	0.21	10.69	0.00	3.40	0.09	0.45	0.20	0.09	99.48
63 (relic rim)	41.08	5.28	13.81	0.23	5.03	16.33	0.08	12.40	0.00	2.95	0.06	0.52	1.10	0.08	98.95
68 (relic rim)	43.74	0.88	15.28	1.19	4.81	18.16	0.12	10.71	0.08	3.44	0.15	0.42	0.16	0.1	99.36
69 (relic core)	43.13	0.85	14.94	1.19	4.57	18.13	0.11	10.66	0	3.4	0.13	0.39	0.45	0.09	98.09
3U MELT*															
14	62.92	1.01	25.77		2.82	0.02	1.05	2.85	0		0.41	0.63	0.3	1.32	99.1
15	63.2	0.91	25.47		2.74	0.08	0.74	2.35	0		0.47	0.69	0.36	1.21	98.22
18	62.47	1.02	25.74		2.64	0.81	2.79	0.4	0.22		0.53	0	0.24	1.3	98.16
29	64.85	1.13	23.33		2	0.09	1.44	2.39	0.21		0.3	0.77	0.95	1.05	98.51
30	65.24	1.04	23.61		2.1	0.06	1.45	2.42	0		0.34	0.54	0.53	1.14	98.76
51	66.14	0.72	22.59		1.78	0.16	0.88	1.63	0.09		0.27	0.68	0	1.24	96.55
61	60.67	0.81	26.42		2.24	0.07	0.85	2.25	0		0.48	0.61	0.54	1.19	96.65
73	60.87	0.7	27.74		2.18	0.01	0.52	2.44	0.02		0.46	0.43	0.49	1.01	97.31

Table B.1(b). *Cation proportions calculates for the main minerals from the Middle Atlas xenoliths. (n.d. refers to not detected and * refers to data taken from Wittig (2006)).*

	Si	Ti	Al	Cr	Fe	Mg	Mn	Ca	Ba	Ni	Na	K	F	Cl	Total
3V CPX															
3V-B	1.90	0.01	0.28	0.02	0.11	0.82	0.00	0.74			0.12				4.00
3V-C	1.90	0.01	0.28	0.03	0.10	0.83	0.00	0.74			0.12				4.01
3V-D	1.89	0.01	0.28	0.02	0.11	0.84	0.00	0.73			0.12				4.01
3V-E	1.89	0.01	0.29	0.03	0.11	0.83	0.00	0.73			0.13				4.01
3V-F	1.89	0.01	0.28	0.03	0.11	0.84	0.00	0.73			0.13				4.01
3V-G	1.89	0.01	0.28	0.02	0.11	0.84	0.00	0.74			0.12				4.01
3V-H	1.90	0.01	0.27	0.02	0.11	0.85	0.00	0.72			0.12				4.00
3V-I	1.89	0.01	0.28	0.02	0.11	0.85	0.00	0.73			0.13				4.01
3V-J	1.90	0.01	0.28	0.02	0.11	0.84	0.00	0.73			0.12				4.01
3V-K	1.90	0.01	0.29	0.03	0.11	0.83	0.00	0.73			0.13				4.00
3V-M	1.90	0.01	0.27	0.02	0.11	0.83	0.00	0.73			0.12				4.00
3V-O	1.89	0.01	0.28	0.02	0.11	0.83	0.00	0.73			0.13				4.01
3V-P	1.90	0.01	0.27	0.02	0.10	0.83	0.00	0.74			0.12				4.01
3V-Q	1.89	0.01	0.29	0.02	0.11	0.83	0.00	0.72			0.13				4.01
3V-R	1.89	0.01	0.28	0.02	0.11	0.84	0.00	0.74			0.13				4.02
3V-S	1.89	0.01	0.29	0.02	0.11	0.83	0.00	0.73			0.13				4.01
3V-T	1.90	0.01	0.28	0.02	0.11	0.83	0.00	0.74			0.12				4.01
3V-U	1.90	0.01	0.28	0.02	0.11	0.84	0.00	0.73			0.12				4.01
3V-V	1.91	0.01	0.28	0.02	0.11	0.82	0.00	0.73			0.12				4.00
3V-W	1.90	0.01	0.28	0.02	0.11	0.82	0.00	0.74			0.12				4.00
3V OLIVINE															
3VOL1	1.00	0.00	0.00	0.00	0.21	1.77	0.00	0.00		0.01					3.00
3VOL2	1.00	0.00	0.00	0.00	0.21	1.77	0.00	0.00		0.01					3.00
3V OPX															
3VOPX1	1.89	0.00	0.20	0.01	0.19	1.67	0.00	0.03		0.00	0.01	0.00			4.01
3VOPX2	1.90	0.00	0.18	0.01	0.19	1.67	0.01	0.03		0.00	0.01	0.00			4.01
3V AMPHIBOLE*															
43 (inclusion)	6.06	0.12	2.66	0.13	0.57	3.77	0.01	1.54	1.02	0.06	0.02	0.01	0.02	0.05	16.02
44 (inclusion)	6.08	0.13	2.57	0.14	0.60	3.80	0.00	1.54	1.03	0.07	0.02	0.01	0.01	0.05	16.05
3U CPX															
3U-A	1.91	0.00	0.22	0.02	0.10	0.84	0.00	0.80		0.00	0.09	0.00			4.01
3U-B	1.89	0.01	0.23	0.02	0.10	0.87	0.00	0.81		0.00	0.09	0.00			4.02
3U-D	1.91	0.01	0.23	0.02	0.10	0.85	0.00	0.79		0.00	0.09	0.00			4.00
3U-E	1.91	0.01	0.23	0.02	0.10	0.84	0.00	0.80		0.00	0.10	0.00			4.01
3U-F	1.91	0.01	0.23	0.02	0.10	0.85	0.00	0.79		0.00	0.09	0.00			4.01
3U-G	1.91	0.01	0.23	0.02	0.10	0.86	0.00	0.79		0.00	0.09	0.00			4.01
3U OLIVINE															
3UOL1	1.00	0.00	0.00	0.00	0.21	1.78	0.00	0.00		0.01		0.00			2.9981
3UOL2	1.00	0.00	0.00	0.00	0.21	1.77	0.00	0.00		0.01		0.00			2.9948
3U OPX															
3UOPX1	1.92	0.00	0.16	0.01	0.19	1.68	0.00	0.02		0.00	0.00	0.00			4.00
3UOPX2	1.91	0.00	0.17	0.01	0.19	1.69	0.00	0.03		0.00	0.01	0.00			4.01
3UOPX3	1.91	0.00	0.16	0.01	0.19	1.68	0.00	0.03		0.00	0.01	0.00			4.00
3U AMPHIBOLE*															
22 (inclusion)	6.15	0.10	2.53	0.15	0.55	3.81	0.01	1.59	0.00	0.02	0.87	0.08	0.03	0.01	15.91
44 (inclusion core)	6.19	0.10	2.48	0.13	0.50	3.81	0.02	1.60	0.02	0.03	0.98	0.08	0	0.01	15.947
45 (inclusion rim)	6.18	0.20	2.30	0.05	0.52	4.07	0.01	1.60	0.01	0.01	0.87	0.08	0.13	0	16.038
46 (inclusion rim)	6.26	0.19	2.23	0.07	0.49	4.04	0.01	1.60	0.00	0.02	0.92	0.08	0.08	0	15.97
55 (relic core)	6.17	0.093	2.4705	0.1433	0.583	3.795	0.025	1.609	0	0.01	0.9261	0.081	0.04	0.01	15.961
63 (relic rim)	4.055	0.392	1.6068	0.018	0.415	2.403	0.007	1.312	0	0	0.5646	0.065	0.17	0.01	18.234
68 (relic rim)	6.14	0.09	2.53	0.13	0.56	3.80	0.01	1.61	0.00	0.02	0.94	0.08	0.04	0.01	15.973
69 (relic core)	6.146	0.091	2.509	0.1341	0.545	3.851	0.013	1.628	0	0.01	0.9393	0.071	0.1	0.01	16.054

Table B.2. *Trace element concentration data (ppm) for the cpx, amphibole and melt analysed from the Middle Atlas xenoliths (n.d. refers to not detected).*

Sample Name	Batch Number	Sample Weight (mg)	Trace Element Concentration (ppm)																				
			Rb	Sr	Y	Zr	Nb	Ba	La	Ce	Pr	Nd	Sm	Eu	Gd	Tb	Dy	Er	Yb	Lu	Hf	Th	U
3V Drilled Clinopyroxene																							
3V-B	M30-3	0.089	0.70	233	13.0	12.7	0.20	2.17	9.10	32.7	4.72	20.2	3.84	1.10	3.13	0.43	2.39	1.30	1.18	0.19	0.35	0.27	0.08
3V-C	M30-4	0.218	n.d.	171	12.9	16.2	0.13	1.31	9.36	33.0	4.76	20.1	3.90	1.15	3.11	0.44	2.43	1.33	1.12	0.17	0.40	0.27	0.05
3V-D	M30-6	0.095	n.d.	245	18.3	20.5	0.85	2.14	12.11	41.8	6.44	27.8	5.43	1.61	4.44	0.61	3.42	1.81	1.57	0.23	0.47	0.38	0.08
3V-E	M30-9	0.113	n.d.	134	9.0	5.8	0.25	3.07	6.63	22.7	3.46	14.0	2.81	0.82	2.08	0.32	1.75	0.91	0.80	0.13	0.15	0.19	0.05
3V-F	M30-10	0.054	n.d.	244	16.6	17.3	0.83	5.01	11.21	38.1	6.01	24.6	5.13	1.54	3.86	0.57	3.26	1.70	1.58	0.30	0.44	0.39	0.09
3V-G	M33-2	0.097	0.32	199	13.2	13.0	0.69	0.78	8.54	29.6	5.31	23.6	4.16	1.19	2.82	0.45	2.62	1.30	1.22	0.18	0.45	0.31	0.08
3V-G2 (repeat)	M52-7	0.005	n.d.	224	12.7	25.2	1.49	0.03	8.70	30.6	5.00	20.1	3.70	1.07	2.99	0.18	2.31	1.11	1.06	0.29	n.d.	0.24	0.07
3V-H	M33-3	0.084	0.48	246	19.3	25.4	0.44	2.40	12.13	42.1	7.72	34.2	6.04	1.73	4.19	0.67	3.82	1.94	1.81	0.26	0.76	0.50	0.10
3V-I	M33-4	0.076	0.38	230	18.4	24.2	0.58	5.18	11.31	39.5	7.10	32.5	5.59	1.71	4.02	0.63	3.55	1.84	1.66	0.25	0.69	0.46	0.09
3V-J	M33-5	0.064	0.15	238	18.0	24.2	0.51	1.61	11.38	39.2	7.15	32.5	5.56	1.68	3.92	0.62	3.57	1.80	1.60	0.25	0.73	0.47	0.08
3V-K	M33-7	0.074	0.16	232	16.2	24.7	0.32	5.17	10.05	35.9	6.44	28.9	5.02	1.49	3.51	0.57	3.17	1.58	1.42	0.23	0.74	0.41	0.08
3V-M	M33-9	0.104	0.40	304	24.0	30.5	0.93	3.92	15.02	53.2	9.42	43.0	7.68	2.17	5.32	0.84	4.78	2.36	2.16	0.32	0.85	0.61	0.11
3V-M2 (repeat)	M33-19	0.047	n.d.	300	22.9	34.8	0.04	n.d.	13.49	50.5	9.94	37.5	6.64	2.40	7.29	0.96	4.60	1.99	2.23	0.26	1.13	0.60	0.13
3V-O	M33-11	0.076	0.32	247	19.6	20.7	0.89	6.31	12.55	42.7	7.75	35.4	6.20	1.70	4.78	0.70	3.90	1.95	1.81	0.27	0.60	0.50	0.09
3V-P	M33-14	0.034	n.d.	297	18.1	13.6	n.d.	17.82	13.03	46.3	9.03	33.4	6.16	2.18	6.33	0.84	3.86	1.53	1.89	0.18	0.65	0.40	0.19
3V-Q	M33-15	0.044	0.16	320	11.6	32.0	n.d.	33.22	10.24	46.7	6.97	26.2	4.53	1.52	4.47	0.57	2.56	0.94	1.25	0.08	1.15	0.63	0.21
3V-R	M33-16	0.057	n.d.	254	17.6	21.2	n.d.	8.85	10.99	37.5	7.82	31.5	5.72	1.86	5.58	0.74	3.68	1.60	1.86	0.20	0.71	0.57	0.10
3V-S	M33-17	0.035	n.d.	280	20.1	19.1	n.d.	10.42	11.64	37.7	8.38	32.6	6.06	2.02	6.09	0.85	4.03	1.72	2.11	0.20	0.73	0.55	0.12
3V-T	M33-20	0.036	n.d.	307	20.9	28.8	n.d.	13.06	15.15	57.3	10.90	41.2	7.24	2.37	6.94	0.98	4.60	1.87	2.26	0.23	0.95	0.61	0.12
3V-U	M33-21	0.042	n.d.	286	20.6	32.5	n.d.	8.58	12.80	48.1	9.32	36.2	6.35	2.21	7.26	0.92	4.24	1.89	2.21	0.22	1.13	0.62	0.12
3V-V	M33-22	0.050	n.d.	293	24.9	31.2	0.14	9.23	14.97	52.7	10.99	43.7	8.02	2.64	8.44	1.06	5.18	2.37	2.72	0.34	1.07	0.70	0.13
3V-W	M33-23	0.034	n.d.	277	13.8	27.3	n.d.	12.01	13.52	50.9	9.39	34.8	6.05	1.92	5.99	0.77	3.35	1.30	1.58	0.12	0.97	0.51	0.19
3V-MC*	M33-10	0.101	0.26	231	16.5	20.7	1.21	5.17	10.20	35.3	6.45	29.3	5.30	1.41	3.82	0.59	3.25	1.67	1.49	0.22	0.60	0.42	0.09
* on an altered crack																							
3V Picked Clinopyroxene																							
M44-2	M44-2	0.047	0.03	172	14.7	14.5	1.65	0.20	8.98	33.5	4.71	24.7	4.60	1.31	4.20	n.d.	3.09	1.36	1.31	0.21	2.11	0.41	0.07
M44-3	M44-3	0.028	0.08	183	17.2	26.0	2.25	0.48	9.34	37.7	5.14	27.4	5.22	1.49	4.87	n.d.	3.57	1.55	1.48	0.23	2.74	0.38	0.06
M44-4	M44-4	0.060	0.06	149	14.4	19.5	1.59	0.43	9.49	31.9	4.51	24.1	4.57	1.28	4.32	n.d.	3.09	1.33	1.28	0.20	2.16	4.71	0.06
M44-5	M44-5	0.054	0.08	143	13.1	27.9	1.74	0.50	7.02	26.6	3.74	20.0	3.61	1.05	3.49	n.d.	2.51	1.11	1.08	0.17	2.19	0.32	0.05
M44-7	M44-7	0.048	0.03	152	14.4	29.5	2.14	0.15	7.55	29.0	4.18	22.6	4.19	1.22	4.02	n.d.	2.94	1.28	1.22	0.19	2.50	0.33	0.05
M44-8	M44-8	0.047	0.06	173	14.4	30.5	1.57	0.05	8.31	31.2	4.39	23.5	4.28	1.25	4.11	n.d.	2.97	1.31	1.26	0.20	2.55	0.36	0.05
M44-9	M44-9	0.060	0.01	144	11.3	13.6	1.27	0.00	7.23	25.6	3.51	18.2	3.22	0.94	3.01	n.d.	2.17	0.98	0.95	0.15	1.48	0.28	0.04
M44-10	M44-10	0.070	0.05	189	14.3	30.9	2.28	1.02	9.69	32.2	4.45	23.2	4.14	1.19	3.89	n.d.	2.83	1.26	1.22	0.19	2.49	0.48	0.07

Table B.2. (continued)

Sample Name	Batch Number	Sample Weight (mg)	Trace Element Concentration (ppm)																				
			Rb	Sr	Y	Zr	Nb	Ba	La	Ce	Pr	Nd	Sm	Eu	Gd	Tb	Dy	Er	Yb	Lu	Hf	Th	U
3V Drilled Melt																							
3V-AB	M68-5	0.016	21.24	439	12.7	37.4	96.32	434.67	10.92	41.9	4.81	20.2	4.14	1.06	3.51	0.45	2.50	1.30	1.00	0.15	0.72	0.43	0.39
3V-AC	M68-8	0.040	14.54	369	15.0	28.2	63.41	221.56	9.00	34.8	4.65	21.2	4.12	1.22	3.54	0.48	2.58	1.47	1.25	0.19	0.59	0.22	0.08
3U Drilled Clinopyroxene																							
3U-A	M41-2	0.034	0.48	225	8.3	19.3	n.d.	15.55	13.20	34.6	4.76	18.2	4.08	1.08	3.58	0.46	1.82	1.10	1.03	0.15	0.55	2.43	0.82
3U-B	M41-3	0.073	4.65	261	13.9	29.2	0.39	42.26	19.08	35.3	6.55	23.8	4.92	1.55	4.89	0.61	3.06	1.55	1.51	0.25	0.94	3.61	1.01
3U-D	M41-5	0.035	2.46	398	22.3	35.8	0.01	21.29	29.95	55.9	10.33	38.9	8.65	2.46	7.85	0.99	4.79	2.64	2.55	0.43	1.02	7.04	1.57
3U-E	M41-7	0.044	0.70	294	6.1	23.0	0.43	18.56	10.12	24.8	3.99	16.1	3.93	0.90	2.85	0.35	1.37	0.88	0.80	0.12	0.59	1.85	1.49
3U-F	M41-8	0.030	0.75	370	12.5	50.4	0.40	28.17	22.14	57.3	7.58	29.1	6.43	1.65	5.67	0.64	2.59	1.59	1.42	0.25	1.32	3.86	1.43
3U-G	M41-9	0.039	0.05	335	14.5	40.5	0.51	15.37	22.85	55.8	7.96	29.7	6.52	1.54	5.51	0.67	3.15	1.79	1.65	0.28	1.12	4.03	1.24
3U Drilled Amphibole																							
3U-AA	M68-3	0.053	4.32	425	14.0	33.4	54.22	235.34	18.70	42.4	4.70	20.2	3.71	1.22	3.39	0.46	2.74	1.38	1.23	0.19	0.63	2.11	0.55
3U Drilled Melt																							
3U-AB	M68-4	0.030	15.53	363	14.3	40.5	57.12	322.26	19.86	52.7	4.87	19.9	3.91	1.31	3.67	0.48	2.86	1.42	1.22	0.20	0.80	2.05	0.69
3U- AC	M68-7	0.026	11.95	373	13.1	50.0	59.74	334.26	18.10	42.5	4.32	18.8	3.48	1.15	3.15	0.47	2.35	1.25	1.20	0.19	0.93	2.01	0.63
3U-AD	M68-9	0.044	15.99	302	15.0	32.8	35.96	284.36	19.01	45.1	4.65	20.7	3.87	1.24	3.46	0.54	2.90	1.53	1.14	0.19	0.69	1.73	0.54

Table B.3. *Sr isotope dataset for the Middle Atlas xenoliths (3U and 3V). n.d. refers to not detected; m refers to measured ratio; n refers to normalised ratio (see Appendix A for normalisation data); i refers to the initial ratio corrected to 2Ma.*

Sample	Batch	Sr ppm	Rb ppm	$^{87}Rb/^{86}Sr$	$^{87}Sr/^{86}Sr_m$	$^{87}Sr/^{86}Sr_n$	2sd	$^{87}Sr/^{86}Sr_i$
3V Drilled Clinopyroxene								
3V-B	M30-3	232.7	0.7	0.003	0.703499	0.703504	0.000027	0.703499
3V-C	M30-4	171.0	n.d.	0.000	0.703439	0.703444	0.000022	0.703444
3V-D	M30-6	245.1	n.d.	0.000	0.703468	0.703473	0.000038	0.703473
3V-E	M30-9	134.5	n.d.	0.000	0.703438	0.703443	0.000020	0.703443
3V-F	M30-10	244.2	n.d.	0.000	0.703457	0.703462	0.000019	0.703462
3V-G	M33-2	198.9	0.3	0.002	0.703424	0.703429	0.000026	0.703424
3V-G2 (repeat)	M52-7	223.9	n.d.	0.000	0.703445	0.703449	0.000008	0.703449
3V-H	M33-3	246.3	0.5	0.003	0.703434	0.703439	0.000022	0.703434
3V-I	M33-4	230.4	0.4	0.003	0.703456	0.703461	0.000020	0.703456
3V-J	M33-5	237.7	0.2	0.001	0.703461	0.703466	0.000028	0.703461
3V-K	M33-7	232.2	0.2	0.004	0.703450	0.703455	0.000015	0.703450
3V-M	M33-9	303.6	0.4	0.004	0.703449	0.703453	0.000006	0.703449
3V-M2 (repeat)	M33-19	299.7	n.d.	0.000	0.703416	0.703421	0.000011	0.703421
3V-O	M33-11	247.5	0.3	0.006	0.703440	0.703445	0.000019	0.703440
3V-P	M33-14	296.5	n.d.	0.000	0.703495	0.703500	0.000019	0.703500
3V-Q	M33-15	320.0	0.2	0.005	0.703680	0.703685	0.000012	0.703680
3V-R	M33-16	254.0	n.d.	0.000	0.703510	0.703515	0.000010	0.703515
3V-S	M33-17	279.7	n.d.	0.000	0.703505	0.703510	0.000008	0.703510
3V-T	M33-20	307.2	n.d.	0.000	0.703454	0.703459	0.000012	0.703459
3V-U	M33-21	285.7	n.d.	0.000	0.703590	0.703595	0.000023	0.703595
3V-V	M33-22	292.8	n.d.	0.000	0.703463	0.703468	0.000010	0.703468
3V-W	M33-23	276.6	n.d.	0.000	0.703464	0.703469	0.000016	0.703469
3V-MC*	M33-10	231.5	0.3	0.001	0.705644	0.705649	0.000019	0.705644
* on an altered crack								
3V Picked Clinopyroxene								
3V-AB	M68-5	438.5	21.2	0.140	0.703358	0.703352	0.000017	0.703348
3V-AC	M68-8	368.8	14.5	0.114	0.703419	0.703413	0.000016	0.703410
3V Drilled Melt								
	M44-2	171.9	0.0	0.001	0.703452	0.703455	0.000011	0.703452
	M44-3	183.2	0.1	0.001	0.703410	0.703413	0.000010	0.703410
	M44-4	148.7	0.1	0.001	0.703430	0.703433	0.000112	0.703430
	M44-5	143.0	0.1	0.002	0.703405	0.703408	0.000010	0.703405
	M44-7	151.5	0.0	0.001	0.703408	0.703411	0.000008	0.703408
	M44-8	172.8	0.1	0.001	0.703431	0.703434	0.000007	0.703431
	M44-9	143.7	0.0	0.000	0.703407	0.703410	0.000009	0.703407
	M44-10	189.3	0.1	0.001	0.703412	0.703415	0.000008	0.703412
3U Drilled Clinopyroxene								
3U-A	M41-2	224.9	0.5	0.006	0.703446	0.703451	0.000013	0.703446
3U-B	M41-3	261.5	4.6	0.051	0.703777	0.703782	0.000013	0.703776
3U-D	M41-5	398.3	2.5	0.018	0.703430	0.703435	0.000023	0.703429
3U-E	M41-7	293.9	0.7	0.007	0.703426	0.703431	0.000014	0.703426
3U-F	M41-8	370.2	0.8	0.006	0.703402	0.703407	0.000019	0.703402
3U-G	M41-9	334.8	0.0	0.000	0.703551	0.703556	0.000011	0.703551
3U Drilled Amphibole								
3U-AA	M68-3	425.1	4.3	0.029	0.703420	0.703414	0.000016	0.703413
3U Drilled Melt								
3U-AB	M68-4	363.1	15.5	0.124	0.703385	0.703379	0.000025	0.703376
3U- AC	M68-7	372.5	11.9	0.093	0.703440	0.703434	0.000036	0.703431
3U-AD	M68-9	301.7	16.0	0.153	0.703376	0.703370	0.000023	0.703366

Figure B.1(a). *Scanned image of the thin section of sample 3V used for drilling. The green crystals are the cpx; beige crystals are opx; colourless crystals are olivine; dark brown crystals the melt and the black crystals the spinel.*

Figure B.1(b). *Scanned image of the thin section of sample 3U used for drilling. The green crystals are the cpx; beige crystals are opx; colourless crystals are olivine; dark brown crystals the melt and the black crystals the spinel.*

References:

Wittig, N. (2006). Application of novel U-Th-Pb and Lu-Hf techniques to tracing the melting and metsomatic history of mantle rocks. Danish Lithosphere Centre. Copenhagen, University of Copenhagen. PhD: 351.

Appendix C:

BULTFONTEIN XENOLITH DATA

Table C.1(a). *Major element data (in wt% oxide) for clinopyroxene, orthopyroxene, olivine and garnet from sample JMK (Bultfontein garnet lherzolite).*

Sample Number	SiO_2	Al_2O_3	TiO_2	FeO	MgO	MnO	CaO	Cr_2O_3	NiO	Na_2O	K_2O	Total
Clinopyroxene												
K2-K (core)	55.22	2.97	0.26	2.62	15.86	0.11	17.75	2.07	0.04	2.76	0.01	99.66
K2-K (rim)	55.35	3.35	0.26	2.67	15.61	0.09	17.26	2.21	0.04	2.96	0.01	99.81
K2-Z (core)	55.25	3.37	0.26	2.67	15.61	0.08	17.50	2.16	0.04	3.02	0.01	99.97
K2-G (core)	55.62	3.31	0.26	2.65	15.53	0.09	17.38	2.10	0.05	2.96	0.01	99.95
K2-G (rim)	55.08	3.48	0.26	2.67	15.57	0.08	17.25	2.19	0.05	3.04	0.02	99.69
K2-E (core)	55.40	3.17	0.26	2.69	15.88	0.08	17.48	2.08	0.05	2.92	0.01	100.01
K2-E (rim)	55.48	3.41	0.27	2.74	15.81	0.09	17.12	2.15	0.07	2.98	0.01	100.13
K3-A (rim)	55.38	3.43	0.26	2.71	15.52	0.08	17.05	2.23	0.02	2.97	0.01	99.66
K3-A (core)	55.34	3.15	0.25	2.66	15.96	0.09	17.63	2.11	0.04	2.86	0.02	100.12
K3-Y (rim)	55.59	3.40	0.27	2.66	15.58	0.08	17.13	2.19	0.03	3.00	0.01	99.94
K3-C (core)	55.32	2.99	0.26	2.62	15.88	0.09	17.73	2.00	0.04	2.79	0.01	99.72
K3-C (rim)	55.58	3.24	0.25	2.68	15.71	0.10	17.68	2.06	0.03	2.93	0.01	100.27
K4-X (rim)	55.61	3.22	0.26	2.64	15.55	0.09	17.48	2.09	0.03	2.93	0.02	99.92
K4-J (rim)	54.90	3.44	0.26	2.74	15.87	0.10	17.30	2.21	0.06	3.07	0.01	99.95
K4-H (core)	54.88	2.99	0.26	2.65	15.93	0.08	17.93	2.10	0.04	2.84	0.01	99.71
K4-H (rim)	54.88	3.44	0.27	2.65	15.78	0.05	17.31	2.17	0.04	3.12	0.01	99.73
K4-N (core)	54.97	3.38	0.27	2.65	15.42	0.09	17.20	2.20	0.06	2.99	0.01	99.25
K5-W (core)	55.25	3.18	0.25	2.66	15.84	0.09	17.54	2.11	0.05	2.85	0.01	99.85
K5-W (rim)	55.41	3.46	0.27	2.65	15.43	0.10	17.21	2.14	0.05	3.03	0.01	99.76
K5-V (core)	55.40	3.01	0.26	2.64	15.87	0.09	18.04	2.05	0.03	2.79	0.01	100.20
K5-V (rim)	55.31	3.39	0.26	2.76	15.80	0.08	17.36	2.14	0.04	3.00	0.01	100.16
K5-U (core)	55.52	3.44	0.26	2.65	15.53	0.08	17.34	2.17	0.03	3.11	0.02	100.15
K5-U (core)	55.35	3.45	0.26	2.67	15.66	0.09	17.21	2.19	0.03	2.98	0.01	99.90
K5-M (core)	55.45	3.07	0.26	2.61	15.77	0.06	17.77	2.07	0.04	2.89	0.01	100.00
K5-M (rim)	55.13	3.40	0.26	2.66	15.66	0.08	17.43	2.13	0.03	2.93	0.02	99.74
K5-T (core)	55.28	3.38	0.27	2.66	15.69	0.10	17.32	2.14	0.05	3.03	0.01	99.94
K5-T (rim)	55.34	3.40	0.26	2.74	15.70	0.08	17.44	2.17	0.05	3.02	0.01	100.21
K6-B (core)	55.45	2.90	0.27	2.62	15.94	0.09	17.90	2.05	0.05	2.73	0.01	100.00
K6-B (core)	55.17	3.18	0.26	2.67	15.78	0.08	17.43	2.07	0.06	2.95	0.01	99.66
K6-S (core)	55.42	3.45	0.26	2.63	15.75	0.08	17.26	2.12	0.05	3.01	0.01	100.03
K6-F (core)	55.20	3.29	0.26	2.68	15.68	0.10	17.23	2.08	0.03	2.92	0.01	99.48

Table C.1(a) continued.

Sample Number	SiO_2	Al_2O_3	TiO_2	FeO	MgO	MnO	CaO	Cr_2O_3	NiO	Na_2O	K_2O	Total
Orthopyroxene												
K1	58.27	0.86	0.10	5.00	35.47	0.11	0.49	0.32	0.10	0.17		100.90
K2	58.81	0.84	0.10	4.97	35.11	0.12	0.48	0.28	0.10	0.18		100.98
K3-opx8	58.39	0.84	0.09	4.94	34.80	0.11	0.48	0.32	0.10	0.19		100.25
K3-opx12	58.32	0.84	0.09	5.07	35.29	0.12	0.48	0.31	0.09	0.21		100.81
K4	58.52	0.80	0.10	5.06	35.28	0.11	0.47	0.30	0.11	0.17		100.92
K5	58.29	0.83	0.09	5.01	34.94	0.11	0.48	0.31	0.10	0.20		100.38
K6	57.94	0.87	0.10	5.02	34.97	0.12	0.50	0.32	0.11	0.19		100.14
Garnet												
K2-R (rim)	42.65	20.63	0.33	7.37	21.08	0.37	4.41	3.76	0.01	0.07		100.68
K2-R (core)	42.01	20.61	0.34	7.35	20.92	0.37	4.46	3.82	0.01	0.07		99.96
K2-P (core)	42.41	20.75	0.34	7.43	20.82	0.35	4.46	3.80	0.00	0.06		100.42
K2-P (rim)	42.26	20.75	0.33	7.53	20.87	0.36	4.41	3.79	0.00	0.07		100.37
K2-Q (core)	42.66	20.65	0.30	7.45	21.12	0.35	4.34	3.63	0.02	0.06		100.58
K2-Q (rim)	42.34	20.59	0.30	7.41	21.44	0.39	4.35	3.83	0.02	0.08		100.76
K2-T (core)	42.08	20.70	0.34	7.39	20.95	0.36	4.45	3.77	b.d.l.	0.08		100.13
K2-T (rim)	42.61	20.82	0.32	7.33	20.91	0.37	4.34	3.74	b.d.l.	0.07		100.53
K2-S (rim)	42.04	20.77	0.34	7.42	20.98	0.35	4.46	3.75	b.d.l.	0.07		100.17
K2-S (core)	42.22	20.63	0.36	7.36	21.03	0.37	4.53	3.78	b.d.l.	0.08		100.36
K3-L (core)	42.39	20.61	0.36	7.46	20.74	0.36	4.59	3.97	0.01	0.06		100.56
K3-L (rim)	42.38	20.62	0.33	7.48	21.18	0.34	4.38	3.80	b.d.l.	0.06		100.57
K3-M (core)	42.53	20.57	0.34	7.35	20.84	0.36	4.48	3.88	0.02	0.07		100.43
K3-M (rim)	42.53	20.40	0.33	7.50	20.81	0.37	4.41	3.85	b.d.l.	0.04		100.27
K3-N (core)	42.58	20.55	0.33	7.43	20.97	0.38	4.46	3.88	0.01	0.09		100.68
K3-N (rim)	42.73	20.65	0.32	7.42	21.17	0.37	4.35	3.79	0.02	0.07		100.89
K3-O (rim)	42.52	20.72	0.29	7.38	21.20	0.35	4.22	3.48	0.00	0.08		100.25
K3-O (core)	42.37	20.45	0.34	7.39	20.68	0.37	4.54	4.05	0.01	0.09		100.29
K4-J (rim)	42.47	20.65	0.35	7.45	20.88	0.37	4.48	3.74	0.00	0.08		100.47
K4-J (core)	42.57	20.84	0.31	7.44	21.13	0.33	4.36	3.78	0.01	0.05		100.84
K4-K (core)	42.31	20.81	0.33	7.44	21.08	0.36	4.48	3.76	b.d.l.	0.08		100.65
K4-K (rim)	42.55	21.04	0.30	7.37	21.07	0.36	4.23	3.41	0.00	0.08		100.42

Table C.1(a) continued.

Sample Number	SiO_2	Al_2O_3	TiO_2	FeO	MgO	MnO	CaO	Cr_2O_3	NiO	Na_2O	K_2O	Total
Garnet												
K5-F (core)	42.65	20.53	0.33	7.54	21.13	0.37	4.44	3.95	0.01	0.07		101.02
K5-F (rim)	42.44	20.64	0.31	7.44	21.16	0.36	4.36	3.82	b.d.l.	0.07		100.60
K5-G (core)	42.30	20.63	0.32	7.46	21.16	0.38	4.39	3.88	0.04	0.08		100.62
K5-I (core)	42.41	20.55	0.33	7.46	21.20	0.37	4.39	3.85	0.03	0.06		100.65
K5-H (core)	42.20	20.81	0.32	7.50	21.05	0.37	4.41	3.81	0.01	0.07		100.53
K5-H (rim)	42.56	20.83	0.31	7.47	21.39	0.38	4.30	3.67	0.02	0.06		101.00
K6-B (core)	42.58	20.65	0.33	7.38	20.95	0.38	4.38	3.82	0.01	0.07		100.54
K6-A (rim)	42.32	20.59	0.32	7.35	21.05	0.39	4.53	3.78	b.d.l.	0.07		100.40
K6-C (core)	42.43	20.68	0.33	7.46	20.93	0.36	4.46	3.83	0.00	0.07		100.54
K6-C (rim)	42.40	20.70	0.31	7.35	21.10	0.36	4.27	3.76	b.d.l.	0.07		100.31
K6-D (core)	42.61	20.60	0.33	7.43	20.69	0.36	4.43	3.88	b.d.l.	0.06		100.40
K6-D (core)	42.26	20.68	0.30	7.33	21.00	0.34	4.29	3.74	0.01	0.06		100.01
Olivine												
K1	41.64	0.01	0.02	8.26	50.08	0.11	0.03	0.03	0.36			100.53
K2	41.43	0.01	0.02	8.29	49.99	0.10	0.03	0.01	0.36			100.23
K3	41.52	0.00	0.02	8.13	50.05	0.10	0.02	0.04	0.36			100.24
K4	41.39	0.01	0.02	8.21	49.73	0.09	0.02	0.03	0.36			99.86
K5	41.68	0.02	0.02	8.24	50.34	0.10	0.03	0.03	0.35			100.81
K6	41.45	0.02	0.02	8.22	49.87	0.08	0.03	0.02	0.37			100.08

Table C.1(b). *Major element cation proportions calculated for clinopyroxene, orthopyroxene, olivine and garnet from sample JMK (Bultfontein garnet lherzolite).*

Sample Number	Si	Al	Ti	Fe	Mg	Mn	Ca	Cr	Ni	Na	K	Total	Mg#	Cr#
Clinopyroxene														
K2-K (core)	1.99	0.13	0.01	0.08	0.85	0.00	0.69	0.06	0.00	0.19	0.00	4.00	0.92	0.32
K2-K (rim)	1.99	0.14	0.01	0.08	0.84	0.00	0.67	0.06	0.00	0.21	0.00	4.00	0.91	0.31
K2-Z (core)	1.99	0.14	0.01	0.08	0.84	0.00	0.67	0.06	0.00	0.21	0.00	4.01	0.91	0.30
K2-G (core)	1.98	0.14	0.01	0.08	0.86	0.00	0.68	0.06	0.00	0.20	0.00	4.01	0.91	0.30
K2-G (rim)	1.99	0.15	0.01	0.08	0.84	0.00	0.67	0.06	0.00	0.21	0.00	4.01	0.91	0.30
K2-E (core)	1.99	0.13	0.01	0.08	0.85	0.00	0.67	0.06	0.00	0.20	0.00	4.01	0.91	0.31
K2-E (rim)	1.99	0.14	0.01	0.08	0.85	0.00	0.66	0.06	0.00	0.21	0.00	4.00	0.91	0.30
K3-A (rim)	2.00	0.15	0.01	0.08	0.83	0.00	0.66	0.06	0.00	0.21	0.00	4.00	0.91	0.30
K3-A (core)	1.99	0.13	0.01	0.08	0.85	0.00	0.68	0.06	0.00	0.20	0.00	4.01	0.91	0.31
K3-Y (rim)	2.00	0.14	0.01	0.08	0.83	0.00	0.66	0.06	0.00	0.21	0.00	4.00	0.91	0.30
K3-C (core)	2.00	0.13	0.01	0.08	0.85	0.00	0.69	0.06	0.00	0.20	0.00	4.00	0.92	0.31
K3-C (rim)	1.99	0.14	0.01	0.08	0.84	0.00	0.68	0.06	0.00	0.20	0.00	4.00	0.91	0.30
K4-X (rim)	2.00	0.14	0.01	0.08	0.83	0.00	0.67	0.06	0.00	0.20	0.00	4.00	0.91	0.30
K4-J (rim)	1.98	0.15	0.01	0.08	0.85	0.00	0.67	0.06	0.00	0.21	0.00	4.02	0.91	0.30
K4-H (core)	1.98	0.13	0.01	0.08	0.86	0.00	0.69	0.06	0.00	0.20	0.00	4.01	0.91	0.32
K4-H (rim)	1.98	0.15	0.01	0.08	0.85	0.00	0.67	0.06	0.00	0.22	0.00	4.02	0.91	0.30
K4-N (core)	1.99	0.14	0.01	0.08	0.83	0.00	0.67	0.06	0.00	0.21	0.00	4.00	0.91	0.30
K5-W (core)	1.99	0.14	0.01	0.08	0.85	0.00	0.68	0.06	0.00	0.20	0.00	4.00	0.91	0.31
K5-W (rim)	2.00	0.15	0.01	0.08	0.83	0.00	0.66	0.06	0.00	0.21	0.00	4.00	0.91	0.29
K5-V (core)	1.99	0.13	0.01	0.08	0.85	0.00	0.69	0.06	0.00	0.19	0.00	4.01	0.91	0.31
K5-V (rim)	1.99	0.14	0.01	0.08	0.85	0.00	0.67	0.06	0.00	0.21	0.00	4.01	0.91	0.30
K5-U (core)	1.99	0.15	0.01	0.08	0.83	0.00	0.67	0.06	0.00	0.22	0.00	4.00	0.91	0.30
K5-U (core)	1.99	0.15	0.01	0.08	0.84	0.00	0.66	0.06	0.00	0.21	0.00	4.00	0.91	0.30
K5-M (core)	1.99	0.13	0.01	0.08	0.85	0.00	0.68	0.06	0.00	0.20	0.00	4.00	0.91	0.31
K5-M (rim)	1.99	0.14	0.01	0.08	0.84	0.00	0.67	0.06	0.00	0.20	0.00	4.01	0.91	0.30
K5-T (core)	1.99	0.14	0.01	0.08	0.84	0.00	0.67	0.06	0.00	0.21	0.00	4.01	0.91	0.30
K5-T (rim)	1.99	0.14	0.01	0.08	0.84	0.00	0.67	0.06	0.00	0.21	0.00	4.01	0.91	0.30
K6-B (core)	2.00	0.12	0.01	0.08	0.85	0.00	0.69	0.06	0.00	0.19	0.00	4.00	0.92	0.32
K6-B (core)	1.99	0.14	0.01	0.08	0.85	0.00	0.67	0.06	0.00	0.21	0.00	4.01	0.91	0.30
K6-S (core)	1.99	0.15	0.01	0.08	0.84	0.00	0.66	0.06	0.00	0.21	0.00	4.00	0.91	0.29
K6-F (core)	1.99	0.14	0.01	0.08	0.84	0.00	0.67	0.06	0.00	0.20	0.00	4.00	0.91	0.30

Table C.1(b) continued.

Sample Number	Si	Al	Ti	Fe	Mg	Mn	Ca	Cr	Ni	Na	K	Total	Mg#	Cr#
Orthopyroxene														
K1	1.98	0.03	0.00	0.14	1.80	0.00	0.02	0.01	0.00	0.01		4.00	0.93	
K2	1.99	0.03	0.00	0.14	1.78	0.00	0.02	0.01	0.00	0.01		3.99	0.93	
K3-opx8	1.99	0.03	0.00	0.14	1.77	0.00	0.02	0.01	0.01	0.01		3.99	0.93	
K3-opx12	1.98	0.03	0.00	0.14	1.79	0.00	0.02	0.01	0.01	0.01		4.00	0.93	
K4	1.99	0.03	0.00	0.14	1.79	0.00	0.02	0.01	0.00	0.01		3.99	0.93	
K5	1.99	0.03	0.00	0.14	1.78	0.00	0.02	0.01	0.01	0.01		3.99	0.93	
K6	1.98	0.04	0.00	0.14	1.79	0.00	0.02	0.01	0.01	0.01		3.99	0.93	
Garnet														
K2-R (rim)	3.02	1.72	0.02	0.44	2.23	0.02	0.33	0.21	0.00	0.00		8.00	0.84	0.11
K2-R (core)	3.00	1.73	0.02	0.44	2.23	0.02	0.34	0.22	0.00	0.00		8.01	0.84	0.11
K2-P (core)	3.01	1.74	0.02	0.44	2.21	0.02	0.34	0.21	0.00	0.00		7.99	0.83	0.11
K2-P (rim)	3.01	1.74	0.02	0.45	2.21	0.02	0.34	0.21	0.00	0.00		8.00	0.83	0.11
K2-Q (core)	3.02	1.72	0.02	0.44	2.23	0.02	0.33	0.20	0.00	0.00		8.00	0.83	0.11
K2-Q (rim)	3.00	1.72	0.02	0.44	2.26	0.02	0.33	0.21	0.00	0.00		8.02	0.84	0.11
K2-T (core)	3.00	1.74	0.02	0.44	2.23	0.02	0.34	0.21	0.00	b.d.l.		8.00	0.83	0.11
K2-T (rim)	3.02	1.74	0.02	0.43	2.21	0.02	0.33	0.21	0.00	b.d.l.		7.99	0.84	0.11
K2-S (rim)	3.00	1.74	0.02	0.44	2.23	0.02	0.34	0.21	0.00	b.d.l.		8.01	0.83	0.11
K2-S (core)	3.00	1.73	0.02	0.44	2.23	0.02	0.35	0.21	0.00	b.d.l.		8.01	0.84	0.11
K3-L (core)	3.01	1.73	0.02	0.44	2.20	0.02	0.35	0.22	0.00	0.00		8.00	0.83	0.11
K3-L (rim)	3.01	1.72	0.02	0.44	2.24	0.02	0.33	0.21	0.00	b.d.l.		8.00	0.83	0.11
K3-M (core)	3.02	1.72	0.02	0.44	2.21	0.02	0.34	0.22	0.00	0.00		7.99	0.83	0.11
K3-M (rim)	3.03	1.71	0.02	0.45	2.21	0.02	0.34	0.22	0.00	b.d.l.		7.99	0.83	0.11
K3-N (core)	3.02	1.72	0.02	0.44	2.22	0.02	0.34	0.22	0.01	0.00		8.00	0.83	0.11
K3-N (rim)	3.02	1.72	0.02	0.44	2.23	0.02	0.33	0.21	0.00	0.00		8.00	0.84	0.11
K3-O (rim)	3.02	1.73	0.02	0.44	2.25	0.02	0.32	0.20	0.00	0.00		8.00	0.84	0.10
K3-O (core)	3.02	1.72	0.02	0.44	2.20	0.02	0.35	0.23	0.00	0.00		7.99	0.83	0.12
K4-J (rim)	3.02	1.73	0.02	0.44	2.21	0.02	0.34	0.21	0.00	0.00		8.00	0.83	0.11
K4-J (core)	3.01	1.74	0.02	0.44	2.23	0.02	0.33	0.21	0.00	0.00		8.00	0.84	0.11
K4-K (core)	3.00	1.74	0.02	0.44	2.23	0.02	0.34	0.21	0.00	b.d.l.		8.00	0.83	0.11
K4-K (rim)	3.02	1.76	0.02	0.44	2.23	0.02	0.32	0.19	0.00	0.00		7.99	0.84	0.10

Table C.1(b) continued.

Sample Number	Si	Al	Ti	Fe	Mg	Mn	Ca	Cr	Ni	Na	K	Total	Mg#	Cr#
Garnet														
K5-F (core)	3.02	1.71	0.02	0.45	2.23	0.02	0.34	0.22	0.00	0.00		8.00	0.83	0.11
K5-F (rim)	3.01	1.73	0.02	0.44	2.24	0.02	0.33	0.21	0.00	b.d.l.		8.00	0.84	0.11
K5-G (core)	3.00	1.73	0.02	0.44	2.24	0.02	0.33	0.22	0.00	0.00		8.01	0.83	0.11
K5-I (core)	3.01	1.72	0.02	0.44	2.24	0.02	0.33	0.22	0.00	0.00		8.01	0.84	0.11
K5-H (core)	3.00	1.74	0.02	0.45	2.23	0.02	0.34	0.21	0.00	0.00		8.01	0.83	0.11
K5-H (rim)	3.01	1.73	0.02	0.44	2.25	0.02	0.33	0.21	0.00	0.00		8.01	0.84	0.11
K6-B (core)	3.02	1.73	0.02	0.44	2.22	0.02	0.33	0.21	0.00	0.00		7.99	0.84	0.11
K6-A (rim)	3.01	1.73	0.02	0.44	2.23	0.02	0.35	0.21	0.00	b.d.l.		8.00	0.84	0.11
K6-C (core)	3.01	1.73	0.02	0.44	2.21	0.02	0.34	0.21	0.00	0.00		8.00	0.83	0.11
K6-C (rim)	3.01	1.73	0.02	0.44	2.24	0.02	0.33	0.21	0.00	b.d.l.		8.00	0.84	0.11
K6-D (core)	3.03	1.73	0.02	0.44	2.19	0.02	0.34	0.22	0.00	b.d.l.		7.98	0.83	0.11
K6-D (core)	3.01	1.74	0.02	0.44	2.23	0.02	0.33	0.21	0.00	0.00		8.00	0.84	0.11
Olivine	***Olivine***													
K1	1.01	0.00	0.00	0.17	1.81	0.00	0.00	0.00	0.01			2.99	0.92	
K2	1.01	0.00	0.00	0.17	1.81	0.00	0.00	0.00	0.01			2.99	0.91	
K3	1.01	0.00	0.00	0.16	1.81	0.00	0.00	0.00	0.02			3.00	0.92	
K4	1.01	0.00	0.00	0.17	1.81	0.00	0.00	0.00	0.01			2.99	0.92	
K5	1.01	0.00	0.00	0.17	1.81	0.00	0.00	0.00	0.01			2.99	0.92	
K6	1.01	0.00	0.00	0.17	1.81	0.00	0.00	0.00	0.02			3.00	0.92	

Table C.2. *Pressure (p, kbar) and temperature (T, ºC) estimates for closely associated mineral pairs from each of the six thin sections cut from sample JMK (Bultfontein). [BKN] refers to Brey and Kholer (Brey and Kohler 1990) which uses Ca exchange between opx and cpx to calculate T and a barometer based on the Al (and others) exchange between garnet and opx.*
[O'Neil] refers to O'Neil and Wood (1979) which is a thermometer based on Fe-Mg exchange between olivine and garnet.
[Al,ol-gt} refers to Kholer and Brey (1990) which uses Al exhnage between olivine and garnet to calculate pressure.
[Harley] refers to Harley et al. (1984), a thermometer based on Fe-Mg exchange between opx and graner.
[cpx] refers to the work by Nimis and Taylor (2000); a thermobarometer combination based on single cpx crystals.]
[MC] refers to McGregor et al (1974) which is a barometer based on Al exchange between opx and garnet.
Therefore T[O'Neil/BKN] refers to a temperature calculated using the thermometer from O'Neil and Wood (1979) solved iteratively with a pressure calculated using Brey and Kholer (1990) and P[BKN/O'Neil] refers to the corresponding pressure. All combinations have been solved iteratively starting with a preset T of 900ºC and a preset pressure of 30kbar.

Sample	JMK 1	JMK 2	JMK 3	JMK 4	JMK 5	JMK 6
T [BKN/BKN]	1004	966	1018	1064	1046	1046
p [BKN/BKN]	37.4	34.9	38.8	43.6	41.4	41.4
T [O'Neill/BKN]	1215	900	947	961	879	879
p [BKN/O'Neill]	52.0	30.6	34.5	37.0	31.2	31.2
T [BKN/Al,ol-gt]	990	945	1001	1090	1011	1011
p [Al,ol-gt/BKN]	29.5	23.9	29.4	57.1	23.2	23.2
T [Harley/BKN]	1018	917	958	949	949	949
p [BKN/Harley]	38.2	31.7	35.1	36.3	35.4	35.4
T [cpx]	944	906	940	978	950	950
p [cpx]	37.9	38.9	38.8	38.3	37.2	37.2
T(O'Neill/MC)	1181	941	968	971	912	912
P(MC/O'Neill)	51.7	38.9	39.3	41.4	36.6	36.6
T(BKN/MC)	1011	977	1026	1072	1054	1054
P(MC/BKN)	41.2	41.2	42.8	47.9	45.6	45.6

Table C.3. *Trace element concentration data (ppm) for clinopyroxene and garnet from sample JMK (Bultfontein garnet lherzolite) and M9 (garnet lherzolite from Lesotho).*
** refers to data from Simon et al., (2008); b.d.l refers to below detection limits;*
< refers to below the detection limit which is defined by the value.

Sample Number	Batch Number	Weight (mg)	Trace Element Concentration (ppm)																										
			Rb	Sr	Y	Zr	Nb	Ba	La	Ce	Pr	Nd	Sm	Eu	Gd	Tb	Dy	Ho	Er	Tm	Yb	Lu	Hf	Ta	Pb	Th	U
JMK (garnet lherzolite)																													
Clinopyroxene (LA-ICP-MS)																													
K2-K (rim)	JMK2_cpx_1		<0.066	225.4	5.88	89.26	0.29	0.18	2.52	10.16	2.12	12.87	3.57	1.10	3.18	0.43	1.93	0.29	0.52	0.04	0.24	0.05	3.32	0.01	0.27	0.03	0.02
K2-K (rim)	JMK2_cpx_2		0.04	229.0	6.96	99.17	0.24	0.46	2.51	10.17	2.23	13.52	3.95	1.13	2.75	0.39	1.75	0.27	0.47	0.06	0.26	0.02	3.42	<0.0221	0.20	0.01	0.01
K2-K (rim)	JMK2_cpx_3		<0.071	252.3	5.42	79.69	0.19	0.08	2.54	10.65	2.18	15.00	3.68	1.10	3.43	0.35	1.86	0.25	0.53	0.06	0.27	0.03	3.15	<0.0193	0.33	0.02	0.01
K2-Z (rim)	JMK2_cpx_10		<0.069	168.1	6.82	95.35	0.30	0.12	2.30	8.79	1.85	11.82	3.21	1.04	3.13	0.38	1.89	0.32	0.56	0.05	0.35	0.03	3.45	0.02	0.14	0.03	<0.00
K2-Z (rim)	JMK2_cpx_11		<0.136	172.2	7.01	92.80	0.30	0.32	2.07	9.15	1.95	11.80	3.29	1.15	3.51	0.38	1.89	0.27	0.53	0.06	0.30	0.04	4.11	0.02	0.18	0.02	<0.00
K2-G (rim)	JMK2_cpx_24		<0.080	156.0	7.20	100.18	0.82	1.26	2.47	9.63	1.88	12.23	3.42	1.23	3.05	0.43	2.11	0.31	0.64	0.05	0.23	0.03	4.36	0.03	0.20	0.09	0.03
K2-G (rim)	JMK2_cpx_25		<0.11	162.5	7.15	105.49	0.32	0.12	2.11	8.87	1.76	11.39	3.43	1.19	3.31	0.40	2.13	0.29	0.56	0.08	0.46	0.04	4.17	0.02	0.28	<0.0222	<0.04
K2-E (core)	JMK2_cpx_32		<0.103	168.7	7.50	93.91	0.27	<0.00	2.35	9.49	2.01	12.26	3.33	1.17	3.69	0.35	1.99	0.32	0.68	0.04	0.32	0.03	3.81	0.02	0.24	0.02	<0.00
K2-E (core)	JMK2_cpx_33		<0.066	171.6	6.74	91.80	0.30	0.11	2.30	9.33	1.96	11.67	3.65	1.05	3.55	0.41	2.04	0.28	0.52	0.07	0.38	0.03	3.82	0.01	0.22	0.02	0.01
K2-E (rim)	JMK2_cpx_34		<0.092	165.4	7.43	94.44	0.37	<0.00	2.08	9.29	1.93	11.38	3.50	1.08	3.00	0.39	1.82	0.27	0.65	0.05	0.37	0.03	3.97	0.02	0.20	0.03	0.01
K2-E (rim)	JMK2_cpx_35		0.01	173.1	6.98	89.61	0.51	1.48	2.51	9.31	2.01	11.57	3.11	1.19	3.49	0.36	2.25	0.28	0.57	0.06	0.42	0.04	3.99	0.04	0.24	0.05	0.02
K3-A (rim)	JMK3_cpx_6		0.04	177.9	8.02	88.93	0.43	0.85	2.37	8.49	1.92	12.19	3.65	1.19	3.30	0.41	2.14	0.31	0.66	0.07	0.35	0.05	4.63	0.02	0.17	0.04	0.00
K3-A (core)	JMK3_cpx_7		0.01	153.1	7.42	100.23	0.25	0.17	2.17	7.78	1.87	11.45	3.34	1.09	3.39	0.41	2.09	0.30	0.74	0.07	0.39	0.05	4.64	0.02	0.19	0.03	0.01
K3-Y (rim)	JMK3_cpx_23		<0.031	161.6	8.23	97.60	0.33	0.28	2.17	7.54	1.83	11.32	3.46	1.07	3.35	0.47	2.36	0.33	0.74	0.07	0.39	0.05	4.68	0.03	0.16	0.03	0.01
K3-C (core)	JMK3_cpx_33		0.02	217.0	7.06	97.12	0.32	0.23	2.62	9.18	2.24	13.80	4.07	1.19	3.68	0.45	2.07	0.34	0.68	0.06	0.33	0.04	4.50	0.02	0.22	0.03	0.01
K3-C (core)	JMK3_cpx_34		<0.0230	220.2	7.46	99.36	0.26	0.10	2.57	9.09	2.20	13.91	4.19	1.19	3.38	0.43	2.07	0.29	0.69	0.08	0.35	0.04	4.47	0.02	0.22	0.03	<0.0150
K3-C (core)	JMK3_cpx_35		0.01	185.1	7.66	90.39	0.24	0.16	2.44	8.38	1.98	13.63	4.03	1.35	3.65	0.42	2.20	0.33	0.65	0.08	0.39	0.04	4.43	0.01	0.14	0.02	0.01
K3-C (core)	JMK3_cpx_36		<0.0216	226.8	7.38	96.25	0.21	<0.139	2.85	9.73	2.31	14.39	4.25	1.25	3.71	0.46	2.25	0.31	0.70	0.06	0.45	0.04	4.08	0.03	0.23	0.02	0.00
K3-C (rim)	JMK3_cpx_37		0.04	165.8	8.05	106.93	0.45	0.52	2.62	8.46	1.91	12.25	3.97	1.12	3.81	0.48	2.29	0.32	0.66	0.08	0.41	0.04	4.71	0.03	0.35	0.06	0.02
K4-X (rim)	JMK4_cpx_7		<0.020	186.2	7.60	92.06	0.24	0.13	2.34	8.45	2.06	12.55	3.81	1.16	3.48	0.42	2.12	0.31	0.65	0.08	0.34	0.05	4.31	0.02	0.20	0.02	0.01
K4-X (rim)	JMK4_cpx_8		<0.0188	186.6	8.17	87.85	0.21	0.17	2.40	8.61	1.95	12.18	3.64	1.12	3.23	0.42	2.16	0.31	0.63	0.06	0.45	0.05	4.38	0.01	0.13	0.03	0.00
K4-J (rim)	JMK4_cpx_9		0.01	159.0	7.31	96.27	0.26	0.02	2.15	8.27	1.89	11.86	3.51	1.08	3.31	0.41	2.05	0.30	0.62	0.07	0.37	0.04	4.42	0.02	0.18	0.03	0.01
K4-H (core)	JMK4_cpx_10		0.01	229.7	6.97	88.72	0.24	0.12	2.68	9.99	2.45	15.37	3.91	1.23	3.25	0.42	1.94	0.27	0.52	0.05	0.37	0.05	3.94	0.02	0.14	0.02	0.00
K4-H (core)	JMK4_cpx_11		<0.034	204.6	6.98	87.98	0.25	0.07	2.49	9.87	2.39	14.16	4.12	1.26	3.44	0.42	1.95	0.25	0.51	0.06	0.33	0.03	4.10	0.02	0.20	0.03	0.01
K4-H (core)	JMK4_cpx_12		<0.02	195.2	6.64	88.65	0.24	0.13	2.39	9.88	2.22	13.79	4.09	1.22	3.34	0.39	1.98	0.32	0.61	0.06	0.29	0.05	3.90	0.02	0.17	0.03	0.00
K4-H (rim)	JMK4_cpx_13		<0.032	204.5	6.56	91.09	0.25	0.02	2.48	9.24	2.27	13.48	3.89	1.23	3.58	0.41	1.95	0.31	0.55	0.04	0.37	0.04	3.82	0.03	0.21	0.02	0.01
K4-H (rim)	JMK4_cpx_14		<0.0244	196.8	6.70	89.48	0.22	<0.157	2.38	9.00	2.24	13.44	3.95	1.18	3.02	0.39	1.99	0.30	0.56	0.07	0.31	0.04	3.86	0.01	0.25	0.02	0.00
K4-N (rim)	JMK4_cpx_15		0.04	156.6	7.33	95.26	0.41	1.75	2.42	8.65	1.95	12.44	3.71	1.10	3.45	0.42	2.19	0.34	0.67	0.08	0.38	0.05	4.69	0.02	0.16	0.04	<0.0115
K4-N (rim)	JMK4_cpx_16		<0.0226	143.6	7.30	92.23	0.22	0.08	2.09	7.98	2.00	11.69	3.84	1.12	3.55	0.40	2.25	0.36	0.63	0.07	0.37	0.05	4.61	0.02	0.12	0.03	0.01
K4-N (core)	JMK4_cpx_17		0.10	184.4	7.55	105.25	0.57	4.24	2.86	9.05	2.13	13.01	3.95	1.19	3.49	0.37	2.19	0.32	0.67	0.06	0.49	0.05	4.56	0.03	0.17	0.08	0.01
K5-W (rim)	JMK5_cpx_1		0.02	158.5	6.92	89.16	0.27	0.11	2.19	8.16	1.90	11.53	3.62	0.99	3.00	0.36	2.04	0.32	0.63	0.08	0.35	0.04	4.51	0.02	0.16	0.03	0.01
K5-W (rim)	JMK5_cpx_2		<0.0199	163.9	7.57	94.69	0.25	0.05	2.37	8.56	2.06	12.81	3.81	1.16	3.47	0.43	2.10	0.32	0.58	0.07	0.36	0.06	4.60	0.03	0.14	0.03	<0.0092
K5-V (core)	JMK5_cpx_8		0.00	222.3	6.91	85.66	0.27	0.07	2.46	9.22	2.23	14.01	4.02	1.22	3.42	0.38	1.89	0.27	0.54	0.05	0.29	0.03	3.69	0.02	0.18	0.03	0.01
K5-V (core)	JMK5_cpx_9		0.00	201.0	6.94	94.73	0.24	0.02	2.42	8.69	2.13	13.32	3.90	1.13	3.25	0.41	1.97	0.27	0.56	0.07	0.31	0.04	3.79	0.02	0.15	0.03	0.01
K5-U (rim)	JMK5_cpx_13		0.00	158.9	7.29	96.02	0.23	0.07	2.07	7.76	1.84	12.06	3.36	1.13	3.26	0.39	2.16	0.29	0.65	0.07	0.42	0.04	4.57	0.02	0.14	0.02	0.01
K5-U (core)	JMK5_cpx_14		0.00	156.9	7.47	94.07	0.29	0.16	2.18	8.10	1.84	12.21	3.72	1.06	3.37	0.42	2.13	0.32	0.68	0.07	0.35	0.05	4.41	0.02	0.20	0.04	0.01
K5-M (core)	JMK5_cpx_15		<0.0208	213.5	6.92	87.05	0.30	0.23	2.61	9.46	2.33	14.10	3.89	1.20	3.66	0.41	2.03	0.29	0.57	0.06	0.31	0.05	4.03	0.01	0.21	0.03	0.01
K5-M (core)	JMK5_cpx_16		<0.0228	220.0	7.01	95.71	0.28	0.91	2.68	9.52	2.27	14.41	4.33	1.30	3.53	0.42	2.02	0.28	0.65	0.07	0.29	0.03	4.10	0.03	0.17	0.04	0.01
K5-T (core)	JMK5_cpx_20		<0.039	184.9	7.20	90.99	0.21	0.21	2.27	8.30	1.93	12.15	3.51	1.08	3.42	0.44	2.07	0.29	0.56	0.07	0.38	0.05	4.16	0.03	0.14	0.02	0.00
K5-T (rim)	JMK5_cpx_21		0.01	198.3	7.23	91.61	0.23	0.04	2.29	8.55	1.95	11.67	3.44	1.07	3.15	0.41	2.11	0.28	0.59	0.08	0.39	0.04	4.24	0.02	0.17	0.03	<0.00
K6-B (core)	JMK6_cpx_1		<0.0246	233.3	5.99	80.30	0.26	0.07	2.75	9.95	2.49	16.53	4.51	1.27	3.68	0.40	1.84	0.24	0.47	0.04	0.30	0.03	3.75	0.01	0.15	0.03	<0.0113
K6-B (core)	JMK6_cpx_2		0.01	253.0	5.54	78.11	0.19	0.20	3.68	13.16	3.14	18.39	4.65	1.30	3.80	0.39	1.69	0.24	0.47	0.04	0.27	0.03	3.39	0.02	0.19	0.03	0.01
K6-S (core)	JMK6_cpx_3		<0.040	143.8	7.50	100.82	0.28	0.15	2.12	7.36	1.72	11.19	3.20	1.07	3.10	0.41	2.10	0.27	0.66	0.07	0.40	0.04	4.59	0.01	0.10	0.02	<0.00
K6-F (core)	JMK6_cpx_7		0.01	161.7	7.68	95.87	0.30	0.17	2.18	7.85	1.87	11.84	3.45	1.06	3.68	0.41	2.30	0.33	0.66	0.06	0.42	0.04	4.37	0.02	0.20	0.03	0.00

Table C.3.continued.

Sample Number	Batch Number	Weight (mg)	Trace Element Concentration (ppm) Rb	Sr	Y	Zr	Nb	Ba	La	Ce	Pr	Nd	Sm	Eu	Gd	Tb	Dy	Ho	Er	Tm	Yb	Lu	Hf	Ta	Pb	Th	U
JMK (garnet lherzolite)																											
Clinopyroxene (drilled)																											
K1-Q	M46-27	*0.055*	0.043	168.4	5.85	56.95	0.247		1.537	7.165	1.059	9.898	2.913	0.893	2.937		1.693		0.486		0.303	0.046				0.033	0.013
K2-E	M46-9	*0.057*	0.126	149.9	4.28	64.26	0.351		1.089	4.944	0.971	7.011	2.060	0.610	2.154		1.222		0.371		0.227	0.038				0.031	0.020
K2-G	M46-11	*0.053*	0.253	155.9	3.59	48.95	0.041		1.131	5.235	0.978	6.867	1.896	0.607	1.912		1.117		0.294		0.227	0.039				0.037	0.019
K2-K	M46-17	*0.052*	0.413	232.6	5.30	65.44	0.251		1.600	6.611	1.388	9.765	2.810	0.881	2.789		1.515		0.442		0.278	0.042				0.036	0.021
K3-A1	M46-2	*0.049*	0.334	191.3	5.02	51.89	0.468		1.515	6.565	1.292	9.281	2.716	0.821	2.628		1.448		0.415		0.343	0.076				0.042	0.019
K3-A2	M46-7	*0.079*	0.249	187.4	5.20	57.01	0.137		1.559	6.220	1.258	8.864	2.541	0.777	2.681		1.519		0.416		0.280	0.045				0.080	0.032
K3-C	M46-4	*0.067*	0.983	243.5	5.58	85.02	0.191		1.550	5.972	1.128	7.886	2.337	0.700	2.561		1.473		0.420		0.321	0.055				0.147	0.095
K4-H	M46-14	*0.042*	0.101	205.1	4.45	53.68	0.190		1.464	7.509	1.411	9.940	2.755	0.853	2.753		1.351		0.377		0.242	0.048				0.046	0.011
K4-N	M46-21	*0.057*	0.153	152.5	3.73	44.55	0.195		1.163	6.065	1.055	7.114	2.034	0.623	2.096		1.153		0.305		0.216	0.031				0.040	0.015
K4-L	M46-19	*0.053*	0.105	237.4	6.47	62.47	0.205		2.171	8.640	1.963	13.433	3.579	1.119	3.577		1.923		0.526		0.333	0.052				0.034	0.017
K4-P	M46-23	*0.124*	0.285	172.4	4.47	48.40	0.262		1.340	4.405	1.140	8.026	2.273	0.698	2.323		1.316		0.371		0.243	0.034				0.042	0.027
K5-M	M46-20	*0.050*	0.542	222.9	3.37	40.24	0.734		1.389	5.563	1.170	8.182	2.084	0.604	1.995		0.985		0.252		0.165	0.027				0.065	0.036
K5-O	M46-22	*0.087*	0.573	167.2	5.19	43.29	0.202		1.405	5.549	1.210	8.581	2.419	0.769	2.512		1.516		0.433		0.275	0.043				0.022	0.020
K6-B1	M46-3	*0.124*	0.180	163.9	4.60	43.30	0.090		1.388	6.046	1.246	9.126	2.541	0.761	2.522		1.360		0.367		0.259	0.041				0.025	0.013
K6-B2	M46-5	*0.143*	0.049	167.7	3.63	32.66	0.082		1.295	5.578	1.138	8.096	2.188	0.642	2.091		1.070		0.275		0.185	0.028				0.032	0.011
K6-D	M46-8	*0.060*	0.337	200.9	6.02	54.98	0.158		1.692	7.049	1.433	10.116	2.929	0.907	3.101		1.777		0.507		0.319	0.045				0.046	0.029
K6-F	M46-10	*0.059*	0.269	128.0	4.04	39.54	0.080		1.071	4.458	0.946	6.485	1.905	0.612	1.988		1.139		0.329		0.266	0.058				0.058	0.017
Clinopyroxene (picked)																											
Associated with:																											
K-GT1	M56-2	*0.039*	b.d.l.	219.8	3.81	63.29	0.381		2.179	9.123	1.561	12.536	3.248	0.974	2.715	0.295	1.160		0.228		0.107	0.017	2.979			0.022	0.007
K-GT1	M56-3	*0.035*	0.087	192.8	7.00	72.54	0.461		2.069	8.595	1.447	11.429	3.119	1.022	3.159	0.368	1.782		0.440		0.287	0.037	3.373			0.021	0.018
K-GT1	M56-4	*0.056*	0.066	169.8	7.73	82.86	0.542		2.069	8.492	1.413	10.871	3.104	1.032	3.087	0.418	1.911		0.524		0.332	0.042	3.922			0.037	0.011
K-GT2	M56-5	*0.079*	0.151	173.6	7.63	78.04	0.734		2.130	8.809	1.453	11.448	3.155	1.041	3.136	0.413	1.948		0.492		0.339	0.042	3.799			0.050	0.012
K-GT2	M56-6	*0.068*	0.043	226.6	6.79	75.05	0.395		2.390	10.088	1.725	13.563	3.695	1.181	3.314	0.419	1.788		0.448		0.271	0.038	3.418			0.032	0.010
K-GT2	M56-7	*0.113*	0.019	219.6	6.67	75.19	0.306		2.251	9.714	1.646	13.082	3.573	1.119	3.352	0.406	1.814		0.452		0.290	0.038	3.440			0.025	0.009
K-GT3	M56-9	*0.098*	0.352	164.6	5.30	62.71	1.045		2.145	8.124	1.293	9.957	2.634	0.788	2.392	0.291	1.332		0.337		0.213	0.028	2.521			0.063	0.015
K-GT3	M56-10	*0.145*	0.236	226.9	5.98	72.41	0.929		2.495	10.213	1.749	14.000	3.603	1.059	3.085	0.369	1.556		0.375		0.221	0.030	2.925			0.065	0.016
K-GT3	M56-11	*0.096*	0.238	206.5	5.66	69.21	0.709		2.246	9.208	1.608	13.030	3.293	0.993	2.898	0.351	1.473		0.355		0.212	0.028	2.788			0.056	0.018
K-GT5	M56-13	*0.080*	0.264	154.6	6.28	68.27	1.159		2.566	9.214	1.437	11.004	2.926	0.929	2.822	0.372	1.681		0.425		0.272	0.035	3.406			0.111	0.025
K-GT5	M56-14	*0.054*	b.d.l.	159.0	6.24	67.59	0.257		1.730	7.399	1.253	9.935	2.829	0.898	2.808	0.366	1.655		0.432		0.264	0.036	3.399			0.021	0.007
K-GT5	M56-15	*0.339*	0.134	179.3	6.67	74.22	0.666		2.193	8.773	1.447	11.382	3.178	0.969	2.999	0.385	1.749		0.454		0.283	0.040	3.404			0.057	0.015
K-GT9	M56-22	*0.050*	0.055	150.2	6.88	80.75	0.599		1.983	8.089	1.343	10.416	2.911	0.961	2.916	0.387	1.818		0.467		0.310	0.044	3.954			0.044	0.017
K-GT9	M56-25	*0.099*	0.088	169.8	7.44	78.92	0.591		2.105	8.617	1.438	11.307	3.230	1.047	3.143	0.415	1.895		0.516		0.318	0.046	3.938			0.034	0.015
K-GT10	M56-26	*0.081*	0.224	171.0	7.51	80.71	1.151		2.603	9.854	1.558	11.931	3.299	1.050	3.197	0.421	1.944		0.527		0.335	0.043	3.953			0.077	0.017
K-GT10	M56-27	*0.029*	0.125	178.8	8.41	92.17	0.820		2.376	9.824	1.597	12.632	3.448	1.104	3.433	0.453	1.969		0.541		0.313	0.043	4.431			0.047	0.010
K-GT10	M56-29	*0.057*	b.d.l.	160.0	7.00	73.43	0.294		1.841	7.965	1.306	10.418	3.032	0.985	2.879	0.384	1.768		0.478		0.306	0.040	3.455			0.024	0.006
K-GT11	M56-30	*0.070*	0.061	142.8	6.62	72.59	0.455		1.749	7.448	1.248	9.812	2.847	0.899	2.792	0.363	1.749		0.454		0.293	0.040	3.479			0.030	0.009
K-GT12	M56-31	*0.193*	0.123	159.1	7.12	80.16	0.584		1.867	8.000	1.322	10.532	3.029	0.960	2.894	0.386	1.767		0.483		0.312	0.043	3.676			0.025	0.009

Table C.3.contintued.

Sample Number	Batch Number	Weight (mg)	Trace Element Concentration (ppm) Rb	Sr	Y	Zr	Nb	Ba	La	Ce	Pr	Nd	Sm	Eu	Gd	Tb	Dy	Ho	Er	Tm	Yb	Lu	Hf	Ta	Pb	Th	U
JMK (garnet lherzolite)																												
Orthopyroxene (LA-ICP-MS)																												
	JMK3_opx_8		0.01	<0.37	0.10	<0.77	0.03	0.05	<0.0116	0.03	0.01	0.04	<0.045	0.01	<0.035	0.00	0.03	0.00	0.01	0.00	<0.022	0.00	<0.029	0.00	0.02	0.00	<0.00
	JMK3_opx_9		<0.0249	<0.29	0.09	<0.85	0.04	<0.00	<0.0105	0.01	0.01	0.04	<0.035	<0.0082	<0.039	0.00	0.03	0.01	0.02	0.00	0.02	0.00	0.04	<0.0100	0.03	<0.0056	<0.0115
	JMK3_opx_10		<0.0217	0.48	0.17	0.26	0.04	0.05	0.02	0.05	0.01	0.05	0.01	<0.0101	<0.034	0.00	<0.033	0.01	0.01	<0.0047	<0.037	0.00	0.04	0.00	<0.023	0.00	0.00
	JMK3_opx_11		<0.030	0.13	0.17	1.01	0.04	0.12	0.01	0.02	<0.0042	0.03	0.02	<0.0069	0.03	0.01	0.02	0.01	0.01	0.00	<0.0210	0.00	<0.0155	<0.0060	<0.031	0.00	<0.00
	JMK3_opx_12		<0.00	0.24	0.11	1.12	0.06	0.03	<0.0095	0.01	0.00	0.03	0.01	0.01	0.03	0.01	<0.020	0.01	0.01	0.00	0.01	0.00	0.03	0.00	<0.047	<0.0072	<0.00
	JMK3_opx_13		0.02	0.76	0.19	0.47	0.06	0.09	0.00	0.02	<0.0042	<0.054	0.01	<0.0070	0.03	0.01	<0.0188	<0.0047	0.01	<0.0046	0.03	0.00	0.03	0.01	<0.0221	0.01	<0.00
	JMK3_opx_14		0.01	0.53	0.19	1.04	0.09	0.03	<0.0065	0.01	0.00	0.04	<0.031	0.01	<0.034	0.01	0.02	0.01	<0.0200	<0.0067	0.00	<0.0049	0.04	0.00	0.03	<0.0049	<0.00
Garnet (LA-ICP-MS)																												
K2-R (rim)	JMK2_gt_4		<0.137	0.86	29.35	121.65	0.13	<0.52	0.02	0.23	0.12	1.31	1.54	0.90	3.83	0.75	5.41	1.08	3.23	0.50	3.24	0.49	1.27	<0.0186	<0.113	0.00	<0.049
K2-R (rim)	JMK2_gt_5		<0.089	0.41	30.53	118.00	0.10	<0.00	0.01	0.17	0.07	1.22	1.46	0.75	3.97	0.74	5.22	1.06	3.17	0.47	2.93	0.47	1.36	0.01	<0.103	0.01	0.01
K2-R (rim)	JMK2_gt_6		<0.120	<0.00	30.69	114.68	0.10	<0.00	0.01	0.12	0.09	1.09	1.30	0.82	3.17	0.76	5.29	1.18	3.20	0.50	3.42	0.48	1.59	<0.0162	<0.170	0.00	0.01
K2-R (core)	JMK2_gt_7		<0.137	0.56	25.33	117.08	0.09	<0.00	<0.0212	0.21	0.11	1.19	1.56	0.72	3.41	0.70	5.24	0.99	2.58	0.37	2.73	0.36	1.58	0.02	0.05	<0.00	0.01
K2-R (core)	JMK2_gt_8		<0.102	0.17	26.15	122.00	0.10	0.10	0.01	0.12	0.11	1.24	1.26	0.70	3.95	0.82	4.80	1.02	2.77	0.41	2.47	0.44	1.47	<0.019	<0.204	0.01	<0.00
K2-R (core)	JMK2_gt_9		0.06	<0.00	25.81	115.62	0.10	0.08	<0.0215	0.18	0.12	1.52	1.80	0.85	3.50	0.73	5.13	0.98	2.89	0.39	2.71	0.42	1.41	<0.0187	<0.114	0.01	0.02
K2-P (rim)	JMK2_gt_12		<0.113	<1.09	29.62	113.65	0.11	<0.00	0.03	0.21	0.10	1.52	1.61	0.81	3.51	0.79	5.30	1.10	3.11	0.47	3.43	0.45	1.49	0.01	<0.131	0.01	0.02
K2-P (rim)	JMK2_gt_14		<0.090	0.33	44.98	143.28	0.07	<0.00	0.02	0.13	0.07	0.73	1.25	0.66	4.28	0.83	7.36	1.84	5.46	0.96	6.40	0.97	1.86	<0.0243	0.11	0.00	<0.00
K2-P (rim)	JMK2_gt_15		<0.089	0.15	43.37	137.90	0.08	<0.00	0.01	0.13	0.07	1.27	1.40	0.93	4.24	0.91	7.35	1.64	5.08	0.91	6.11	0.92	1.67	0.01	<0.103	0.01	0.03
K2-P (core)	JMK2_gt_16		<0.00	0.44	19.56	111.41	0.12	0.16	<0.0194	0.16	0.07	1.22	1.54	0.68	2.93	0.54	3.80	0.77	2.16	0.30	2.20	0.31	1.30	<0.0170	<0.103	<0.00	0.01
K2-P (core)	JMK2_gt_17		<0.091	0.32	19.24	111.16	0.14	0.36	0.04	0.25	0.11	1.27	1.93	0.79	3.43	0.54	3.98	0.77	2.21	0.33	2.62	0.33	1.34	0.03	<0.150	0.03	0.04
K2-Q (rim)	JMK2_gt_18		<0.100	<0.00	41.87	134.37	0.13	<0.00	0.03	0.10	0.07	1.10	1.19	0.76	3.67	0.85	8.00	1.58	5.03	0.62	5.45	0.78	1.63	<0.033	<0.163	<0.00	<0.050
K2-Q (rim)	JMK2_gt_19		<0.144	0.52	38.77	144.46	0.11	<0.55	0.02	0.16	0.06	1.32	1.48	0.96	3.97	0.82	6.57	1.39	4.20	0.61	4.58	0.69	1.96	<0.0194	<0.167	0.01	0.01
K2-T (rim)	JMK2_gt_22		<0.093	<1.27	28.20	122.96	0.09	<0.00	<0.029	0.14	0.11	1.27	1.67	0.94	3.31	0.69	4.97	1.04	2.90	0.45	3.48	0.46	1.36	<0.0178	<0.153	0.02	0.02
K2-T (rim)	JMK2_gt_23		<0.152	<0.85	26.14	107.04	0.04	0.08	<0.0192	0.21	0.10	1.69	1.49	0.81	2.82	0.60	4.75	0.91	2.78	0.36	2.54	0.43	1.27	0.01	<0.204	<0.0151	0.03
K2-S (rim)	JMK2_gt_30		0.01	<1.09	20.39	98.29	0.22	0.06	0.03	0.37	0.19	1.71	1.43	0.78	2.92	0.51	3.85	0.81	2.17	0.34	2.41	0.38	1.31	0.03	<0.131	<0.0138	0.03
K2-S (rim)	JMK2_gt_31		<0.112	<0.00	30.32	127.87	0.11	<0.00	0.02	0.24	0.10	1.41	1.24	0.84	3.33	0.69	5.67	1.07	3.37	0.45	3.55	0.53	1.27	0.01	0.02	0.01	0.02
K3-L (core)	JMK3_gt_1		0.01	0.18	22.49	96.65	0.11	<0.00	<0.0085	0.15	0.12	1.75	1.59	0.71	3.02	0.62	4.27	0.90	2.44	0.39	2.48	0.44	1.38	0.03	0.04	0.00	0.02
K3-L (core)	JMK3_gt_2		0.00	0.09	23.39	93.27	0.08	<0.00	<0.0084	0.18	0.09	1.84	1.55	0.67	2.97	0.56	4.24	0.90	2.67	0.37	2.53	0.38	1.53	0.02	<0.042	0.00	0.01
K3-L (rim)	JMK3_gt_5		0.01	0.26	32.24	105.57	0.06	<0.00	<0.0165	0.15	0.09	1.50	1.62	0.76	3.43	0.71	5.54	1.32	3.59	0.52	3.75	0.59	1.48	0.00	<0.058	<0.0125	0.02
K3-M (rim)	JMK3_gt_15		0.01	0.37	36.27	120.44	0.13	0.04	<0.0098	0.12	0.08	1.51	1.35	0.79	3.78	0.80	5.86	1.30	3.89	0.56	4.03	0.58	1.55	0.01	<0.069	0.00	0.00
K3-M (rim)	JMK3_gt_16		<0.031	0.07	35.87	117.98	0.10	<0.00	0.01	0.16	0.08	1.50	1.42	0.83	3.45	0.77	6.44	1.42	4.32	0.67	4.98	0.73	1.51	0.01	0.04	0.00	0.00
K3-M (core)	JMK3_gt_18		0.01	0.73	24.62	106.08	0.13	0.04	0.03	0.22	0.12	1.45	1.56	0.82	3.80	0.65	4.95	0.90	2.48	0.37	2.59	0.42	1.53	0.01	0.04	0.01	0.02
K3-N (rim)	JMK3_gt_19		0.01	0.40	36.90	120.26	0.07	<0.00	0.02	0.14	0.08	1.33	1.43	0.76	3.98	0.84	6.36	1.41	4.16	0.63	4.54	0.67	1.71	0.00	0.02	<0.0087	0.01
K3-N (rim)	JMK3_gt_20		<0.038	0.26	34.42	127.64	0.08	<0.00	0.01	0.12	0.07	1.45	1.23	0.85	3.99	0.77	6.43	1.31	3.88	0.60	4.36	0.55	1.74	<0.0107	0.02	<0.0085	0.01
K3-N (core)	JMK3_gt_21		0.01	0.73	22.37	100.01	0.11	<0.00	0.04	0.21	0.13	1.44	1.63	0.83	3.26	0.66	4.44	0.83	2.47	0.33	2.42	0.40	1.39	0.02	<0.071	<0.0077	0.01
K3-O (rim)	JMK3_gt_25		0.04	<1.05	33.33	134.01	0.13	0.10	<0.0210	0.15	0.10	1.57	1.42	0.93	3.90	0.80	6.23	1.30	3.38	0.49	3.53	0.54	1.82	0.01	<0.074	0.01	0.01
K3-O (core)	JMK3_gt_26		0.02	2.02	39.41	127.05	0.18	<0.00	0.05	0.37	0.10	1.21	1.51	0.80	3.61	0.85	6.57	1.51	4.11	0.66	4.06	0.69	1.78	<0.0117	<0.043	0.00	0.00
K3-O (core)	JMK3_gt_27		<0.039	0.43	26.92	123.89	0.06	<0.00	0.01	0.18	0.10	1.36	1.60	0.83	3.77	0.76	5.36	0.99	2.90	0.35	2.96	0.50	1.76	0.02	<0.041	<0.0089	0.01
K3-O (core)	JMK3_gt_28		<0.047	0.18	27.95	112.40	0.10	0.10	0.02	0.17	0.08	1.76	1.58	0.80	3.84	0.81	5.20	1.09	2.77	0.41	2.92	0.47	1.55	0.01	<0.110	0.01	0.01
K4-J (rim)	JMK4_gt_1		0.00	<0.37	38.01	120.78	0.10	0.03	0.02	0.16	0.08	1.12	1.41	0.75	4.02	0.83	6.67	1.40	4.22	0.60	4.37	0.70	1.86	0.00	0.03	0.00	0.00
K4-J (rim)	JMK4_gt_2		<0.032	0.48	33.98	119.13	0.11	0.05	0.01	0.11	0.07	1.39	1.51	0.83	4.17	0.82	5.93	1.27	3.50	0.51	3.83	0.57	1.77	<0.0090	0.00	0.01	0.00
K4-J (core)	JMK4_gt_3		<0.025	0.25	24.32	118.43	0.09	<0.00	<0.0073	0.15	0.08	1.55	1.70	0.77	3.70	0.65	4.76	0.92	2.54	0.37	2.45	0.39	1.64	0.01	<0.036	<0.0056	0.01
K4-J (core)	JMK4_gt_4		<0.0210	0.18	25.48	123.39	0.10	<0.00	0.01	0.14	0.11	1.47	1.74	0.81	3.99	0.70	4.87	0.95	2.67	0.38	2.62	0.41	1.80	0.02	<0.031	<0.0067	0.01
K4-K (core)	JMK4_gt_19		0.06	0.75	19.28	71.58	0.15	<0.00	0.06	0.27	0.12	1.35	1.46	0.63	2.59	0.51	3.79	0.74	2.06	0.31	2.14	0.33	1.07	0.02	<0.028	0.01	0.01
K4-K (core)	JMK4_gt_20		<0.022	0.20	18.64	66.82	0.17	<0.00	0.03	0.27	0.12	1.40	1.15	0.66	2.39	0.52	3.37	0.70	1.95	0.30	2.10	0.31	1.01	0.02	0.02	<0.0049	0.01

Table C.3.continued.

Sample Number	Batch Number	Weight (mg)	Trace Element Concentration (ppm) Rb	Sr	Y	Zr	Nb	Ba	La	Ce	Pr	Nd	Sm	Eu	Gd	Tb	Dy	Ho	Er	Tm	Yb	Lu	Hf	Ta	Pb	Th	U
JMK (garnet lherzolite)																											
Garnet (LA-ICP-MS)																											
K5-F (rim)	JMK5_gt_3		<0.0255	<1.28	38.00	126.93	0.10	0.05	<0.0241	0.13	0.07	1.13	1.42	0.72	3.45	0.82	6.46	1.45	4.16	0.69	4.61	0.68	1.70	<0.0072	<0.046	<0.0058	0.00
K5-F (rim)	JMK5_gt_4		0.01	<0.50	34.72	116.68	0.11	<0.00	0.01	0.15	0.07	1.07	1.52	0.82	3.64	0.77	6.21	1.34	3.92	0.59	4.12	0.68	1.78	<0.0071	0.04	<0.0057	0.01
K5-F (core)	JMK5_gt_5		<0.00	0.31	32.73	115.53	0.09	0.05	0.02	0.14	0.08	1.02	1.46	0.76	3.62	0.80	6.32	1.28	3.60	0.48	3.60	0.54	1.69	<0.0067	<0.025	0.00	0.01
K5-F (core)	JMK5_gt_6		0.01	0.54	27.16	113.21	0.09	<0.00	<0.0073	0.18	0.10	1.70	1.61	0.81	3.74	0.77	5.54	1.09	3.05	0.41	2.79	0.39	1.60	0.01	0.01	0.01	0.01
K5-F (core)	JMK5_gt_7		<0.0233	0.14	26.64	115.42	0.10	0.06	0.02	0.21	0.11	1.67	1.65	0.84	3.77	0.72	5.20	1.08	2.74	0.41	2.65	0.39	1.84	0.00	<0.035	<0.0053	0.00
K5-G (core)	JMK5_gt_10		0.01	<1.25	39.71	127.42	0.11	0.03	<0.0222	0.13	0.07	1.24	1.63	0.84	3.88	0.87	6.56	1.48	4.34	0.67	4.77	0.71	1.69	<0.0075	<0.028	<0.0060	0.01
K5-G (rim)	JMK5_gt_11		<0.036	<0.51	41.91	121.24	0.11	0.05	0.01	0.14	0.06	0.94	1.18	0.67	3.36	0.80	6.88	1.58	4.96	0.77	5.45	0.85	1.70	<0.0102	<0.046	0.00	<0.0117
K5-G (core)	JMK5_gt_11a		<0.00	0.35	39.86	126.82	0.15	0.03	0.02	0.13	0.07	1.05	1.24	0.73	3.73	0.82	6.50	1.47	4.54	0.72	5.41	0.82	1.83	0.01	<0.047	0.01	<0.00
K5-I (rim)	JMK5_gt_17		<0.0269	<0.88	31.77	98.44	0.09	<0.00	0.02	0.11	0.10	1.26	1.27	0.73	3.31	0.73	5.13	1.09	3.13	0.51	3.61	0.51	1.40	<0.0076	0.03	0.00	0.01
K5-I (rim)	JMK5_gt_18		0.01	0.33	34.06	107.16	0.10	<0.00	<0.0079	0.14	0.09	1.10	1.28	0.83	3.55	0.69	5.63	1.25	3.66	0.58	4.03	0.66	1.44	0.01	<0.039	0.01	0.00
K5-I (rim)	JMK5_gt_19		0.00	0.19	30.72	92.33	0.13	<0.00	0.05	0.15	0.09	1.22	1.27	0.72	3.31	0.65	5.05	1.08	3.23	0.50	3.76	0.53	1.37	0.01	<0.027	<0.0059	0.01
K5-H (core)	JMK5_gt_22		0.02	<0.76	41.29	150.15	0.09	<0.00	<0.0167	0.12	0.07	1.12	1.59	0.88	4.16	0.86	7.07	1.54	4.66	0.67	4.54	0.72	1.94	0.01	<0.026	0.00	0.01
K5-H (core)	JMK5_gt_23		0.00	0.41	39.74	129.61	0.09	<0.00	<0.0073	0.14	0.07	1.24	1.51	0.84	4.18	0.98	7.49	1.66	4.30	0.68	4.67	0.67	2.08	0.01	0.04	0.00	0.00
K5-H (core)	JMK5_gt_24		<0.0247	0.34	41.54	137.43	0.08	<0.00	0.01	0.12	0.07	1.17	1.49	0.77	4.07	0.82	7.11	1.55	4.49	0.66	4.44	0.70	1.94	<0.0070	<0.037	0.00	0.01
K5-H (rim)	JMK5_gt_25		0.01	<0.25	40.58	130.19	0.07	0.03	0.01	0.14	0.07	1.27	1.57	0.86	4.24	0.87	6.87	1.49	4.49	0.66	4.52	0.70	1.98	<0.0086	<0.023	0.01	0.01
K5-H (rim)	JMK5_gt_26		0.01	0.39	48.38	125.71	0.11	0.02	<0.0101	0.13	0.06	1.02	1.22	0.76	3.71	0.91	7.67	1.86	6.03	0.97	6.85	1.13	2.00	0.01	0.06	0.00	0.01
K6-B (rim)	JMK6_gt_4		0.01	0.47	32.72	109.86	0.07	<0.00	<0.0209	0.12	0.08	1.00	1.26	0.71	3.52	0.74	5.84	1.25	3.66	0.58	3.60	0.50	1.57	0.01	<0.064	<0.0079	0.01
K6-B (rim)	JMK6_gt_5		<0.048	<0.39	37.39	119.34	0.09	<0.00	0.01	0.10	0.06	1.10	1.15	0.71	3.37	0.80	6.30	1.47	4.09	0.63	4.45	0.55	1.55	0.01	<0.036	<0.0078	0.01
K6-B (rim)	JMK6_gt_6		<0.036	0.07	30.78	107.57	0.11	<0.00	0.01	0.12	0.10	1.08	1.75	0.77	3.27	0.77	5.56	1.16	3.45	0.53	3.45	0.56	1.72	0.01	0.04	<0.0082	0.01
K6-A (rim)	JMK6_gt_9		0.01	<1.29	32.73	120.81	0.11	<0.00	<0.033	0.14	0.10	1.50	2.04	0.78	3.95	0.76	5.82	1.21	3.37	0.48	3.48	0.54	1.64	<0.0120	<0.077	0.01	<0.00
K6-A (rim)	JMK6_gt_10		<0.038	0.23	25.30	111.90	0.11	<0.00	0.01	0.16	0.10	1.35	1.40	0.81	3.57	0.73	4.87	0.90	2.71	0.39	2.84	0.43	1.61	0.02	0.03	0.00	0.01
K6-C (core)	JMK6_gt_11		0.02	0.53	34.19	128.24	0.07	<0.213	0.01	0.14	0.08	1.36	1.38	0.87	3.76	0.84	6.27	1.39	3.60	0.56	3.35	0.51	1.86	0.01	0.06	0.00	0.00
K6-C (core)	JMK6_gt_12		<0.044	0.32	30.74	116.79	0.09	0.03	<0.0092	0.16	0.10	1.29	1.68	0.81	3.76	0.73	5.61	1.16	3.28	0.44	2.94	0.47	1.84	0.01	<0.046	0.01	0.00
K6-D (core)	JMK6_gt_15		<0.0286	0.24	28.45	124.61	0.10	<0.00	0.02	0.15	0.11	1.51	1.58	0.82	3.81	0.73	5.42	1.10	3.03	0.42	2.94	0.45	1.82	0.01	<0.060	0.01	0.01
K6-D (rim)	JMK6_gt_16		0.01	0.24	41.10	136.19	0.13	<0.00	0.01	0.13	0.08	1.14	1.57	0.76	4.16	0.91	7.52	1.65	4.67	0.76	4.88	0.78	2.13	0.01	0.03	0.01	0.00
Garnet (picked)																											
K-GT2	M57-3	*11.720*	0.03	0.722	27.48	117.86	0.246	0.834	0.031	0.250	0.109	1.426	1.391	0.814	2.908	0.663	4.560		2.683		2.621	0.467	1.554		0.076	0.015	0.014
K-GT3	M57-4	*3.412*	0.06	0.540	26.98	116.50	0.160	0.121	0.032	0.238	0.129	1.597	1.489	0.839	3.119	0.691	4.690		2.690		2.598	0.471	1.652		0.010	0.004	0.012
K-GT5	M57-5	*6.012*	0.02	1.019	33.33	152.59	0.315	0.242	0.039	0.343	0.159	2.115	2.001	1.114	3.928	0.863	5.776		3.415		3.375	0.611	2.129		0.067	0.012	0.019
K-GT7	M57-7	*3.610*	0.10	0.842	28.63	122.08	0.329	1.915	0.033	0.292	0.134	1.732	1.600	0.893	3.251	0.731	4.970		2.902		2.832	0.516	1.735		0.177	0.007	0.015
K-GT9	M57-9	*36.640*	0.03	0.812	19.45	82.52	0.217	0.637	0.028	0.261	0.120	1.593	1.403	0.667	2.471	0.479	3.093		2.010		1.991	0.338	1.165		b.d.l.	0.004	0.011
K-GT1	M57-2	*52.790*	0.02	0.950	27.66	130.00	0.365	0.694	0.042	0.453	0.214	2.827	2.268	1.055	3.858	0.726	4.445		2.733		2.705	0.453	1.727		0.122	0.007	0.018
Whole Rock																											
JMK	110-3	*13.620*	1.41	34.95	2.80	19.63	2.61	20.05	2.11	4.30	0.53	2.31	0.53	0.18	0.59	0.09	0.51		0.29		0.27	0.04	0.49		0.22	0.21	0.09
Kimberlite*	k8/10		8.90	2261	37.00	596	302	1428	335.53	700.93	80.18	299.31	41.96	10.65	25.01	2.67	10.84	1.560	3.01	0.33	1.63	0.19	11.61	11.90	12.06	39.01	8.62
Kimberlite*	k8/17		32.00	1443	38.00	609	273	2520	253.65	522.90	60.37	228.50	34.17	8.99	21.35	2.45	10.45	1.572	3.10	0.34	1.69	0.20	13.27	14.77	14.17	33.89	6.88
Kimberlite*	k8/115		14.10	1387	15.70	163	117	930	112.98	217.28	23.98	86.96	12.35	3.26	7.81	0.86	3.85	0.581	1.20	0.13	0.68	0.09	2.93	3.27	8.46	10.44	3.54

Table C.3.continued.

Sample Number	Batch Number	Weight (mg)	Trace Element Concentration (ppm)																								
			Rb	Sr	Y	Zr	Nb	Ba	La	Ce	Pr	Nd	Sm	Eu	Gd	Tb	Dy	Ho	Er	Tm	Yb	Lu	Hf	Ta	Pb	Th	U
M9 - Garnet lherzolite from Lestho																											
Clinopyroxene (drilled)																											
M9-2-A	M49-2	*0.062*	0.438	192.5	2.577	31.19	1.822		2.767	10.56	2.058	12.96	2.999	0.811	2.462		0.928	0.184			0.081	0.009	10.34		b.d.l.	0.093	0.016
M9-5-B	M49-3	*0.037*	0.527	216.7	1.995	55.25	0.262		2.203	10.10	1.675	10.70	2.460	0.668	2.038		0.702	0.146			0.071	0.007	15.63		b.d.l.	0.060	0.054
M9-1-C	M49-8	*0.047*	0.362	214.6	2.377	31.47	0.180		2.601	7.65	1.978	12.45	2.941	0.797	2.343		0.874	0.177			0.079	0.012	11.53		0.731	0.062	0.028
M9-5-D	M49-5	*0.070*	0.360	183.6	2.170	24.09	0.233		2.166	7.32	1.707	10.72	2.494	0.690	2.059		0.800	0.166			0.075	0.009	7.57		b.d.l.	0.091	0.023
M9-6-E	M49-7	*0.093*	0.061	207.5	2.226	49.15	0.291		2.594	11.58	2.080	13.33	3.248	0.878	2.385		0.873	0.170			0.084	0.014	15.74		b.d.l.	0.078	0.017
M9-4-F	M49-9	*0.070*	0.329	165.1	1.731	35.03	0.352		1.958	6.95	1.504	9.60	2.361	0.650	1.780		0.672	0.131			0.054	0.007	10.19		b.d.l.	0.098	0.017

Table C.4. *Summary of the Sr isotope data for the drilled and picked clinopyroxene and garnet from sample JMK (Bultfontein). (m) refers to the measured ratio; (n) to the normalised ratio (see Appendix A for the standard values used for normalisation); (i) refers to the initial ratio corrected to 90Ma.*

Sample Name	Batch Number	Age (Ma)	$^{87}Rb/^{86}Sr$	$^{87}Sr/^{86}Sr_m$	2sd	$^{87}Sr/^{86}Sr_n$	$^{87}Sr/^{86}Sr_i$
JMK - Garnet lherzolite from Bultfontein, South Africa							
Clinopyroxene (drilled)							
K1-Q	M46-27	90	0.001	0.703387	0.000019	0.703387	0.703389
K2-E	M46-9	90	0.002	0.704115	0.000023	0.704115	0.704115
K2-G	M46-11	90	0.005	0.704407	0.000024	0.704407	0.704404
K2-K	M46-17	90	0.005	0.704415	0.000086	0.704415	0.704411
K3-A1	M46-2	90	0.005	0.704977	0.000016	0.704977	0.704974
K3-A2	M46-7	90	0.004	0.704912	0.000022	0.704912	0.704907
K3-C	M46-4	90	0.012	0.705415	0.000017	0.705415	0.705403
K4-H	M46-14	90	0.001	0.704628	0.000050	0.704628	0.704629
K4-N	M46-21	90	0.003	0.705857	0.000026	0.705857	0.705856
K4-L	M46-19	90	0.001	0.704129	0.000015	0.704129	0.704130
K4-P	M46-23	90	0.005	0.704904	0.000026	0.704904	0.704901
K5-M	M46-20	90	0.007	0.704738	0.000021	0.704738	0.704732
K5-O	M46-22	90	0.010	0.704473	0.000017	0.704473	0.704463
K6-B1	M46-3	90	0.003	0.704382	0.000014	0.704382	0.704381
K6-B2	M46-5	90	0.001	0.704737	0.000016	0.704737	0.704739
K6-D	M46-8	90	0.005	0.705212	0.000015	0.705212	0.705209
K6-F	M46-10	90	0.006	0.704147	0.000020	0.704147	0.704142
Clinopyroxene (picked)							
Associated with:							
K-GT1	M56-2	90	0.000	0.704867	0.000015	0.704867	0.704867
K-GT1	M56-3	90	0.001	0.704283	0.000017	0.704283	0.704282
K-GT1	M56-4	90	0.001	0.704070	0.000014	0.704070	0.704070
K-GT2	M56-5	90	0.003	0.704080	0.000019	0.704080	0.704078
K-GT2	M56-6	90	0.001	0.704640	0.000014	0.704640	0.704640
K-GT2	M56-7	90	0.000	0.704594	0.000010	0.704594	0.704594
K-GT3	M56-9	90	0.006	0.704526	0.000011	0.704526	0.704519
K-GT3	M56-10	90	0.003	0.704788	0.000017	0.704788	0.704785
K-GT3	M56-11	90	0.003	0.704879	0.000010	0.704879	0.704876
K-GT5	M56-13	90	0.005	0.704236	0.000015	0.704236	0.704231
K-GT5	M56-15	90	0.002	0.704251	0.000021	0.704251	0.704249
K-GT9	M56-25	90	0.003	0.704094	0.000012	0.704094	0.704092
K-GT9	M56-26	90	0.004	0.704115	0.000014	0.704115	0.704110
K-GT9	M56-27	90	0.002	0.704073	0.000020	0.704073	0.704070
K-GT10	M56-29	90	0.000	0.704103	0.000011	0.704103	0.704103
K-GT10	M56-30	90	0.001	0.704054	0.000014	0.704054	0.704052
Garnet (picked)							
K-GT2	M57-3	90	0.108	0.707623	0.000866	0.707623	0.707485
K-GT3	M57-4	90	0.299	0.707775	0.000054	0.707775	0.707393
K-GT5	M57-5	90	0.051	0.707501	0.000102	0.707501	0.707435
K-GT7	M57-7	90	0.329	0.706414	0.000046	0.706414	0.705993
K-GT9	M57-9	90	0.106	0.705117	0.000028	0.705117	0.704981
K-GT1	M57-2	90	0.060	0.705825	0.000016	0.705825	0.705748
Whole Rock							
JMK	110-3	90	0.252	0.706312	0.000014	0.706294	0.705707

Table C.4.continued.

Sample Name	Batch Number	Age (Ma)	$^{87}Rb/^{86}Sr$	$^{87}Sr/^{86}Sr_m$	2sd	$^{87}Sr/^{86}Sr_n$	$^{87}Sr/^{86}Sr_i$
M9 - Garnet lherzolite from Lestho							
Clinopyroxene (drilled)							
M9-2-A	M49-2	90	0.007	0.703465	0.000022	0.703468	0.703457
M9-5-B	M49-3	90	0.007	0.703443	0.000022	0.703446	0.703434
M9-1-C	M49-8	90	0.001	0.703446	0.000015	0.703449	0.703445
M9-5-D	M49-5	90	0.005	0.703519	0.000020	0.703522	0.703513
M9-6-E	M49-7	90	0.006	0.704216	0.000025	0.704219	0.704209
M9-4-F	M49-9	90	0.006	0.703573	0.000020	0.703576	0.703566

Table C.5. *Summary of the Nd isotope data for the drilled and picked clinopyroxene and garnet from sample JMK (Bultfontein). (m) refers to the measured ratio; (n) to the normalised ratio (see Appendix A for the standard values used for normalisation); (i) refers to the initial ratio corrected to 90Ma.*

Sample Name	Batch Number	Age (Ma)	$^{147}Sm/^{144}Nd$	$^{143}Nd/^{144}Nd_m$	2sd	$^{143}Nd/^{144}Nd_n$	$^{143}Nd/^{144}Nd_i$	εNd_i	2se
JMK - Garnet lherzolite from Bultfontein, South Africa									
Clinopyroxene (picked)									
Associated with:									
K-GT1	M56-2	90							
K-GT1	M56-3	90							
K-GT1	M56-4	90							
K-GT2	M56-5	90	All cpx from K-GT2 (M56-5, 6, 7 combined)						
K-GT2	M56-6	90	0.166	0.512519	0.000101	0.512523	0.512425	-1.9	2.0
K-GT2	M56-7	90							
K-GT3	M56-9	90							
K-GT3	M56-10	90							
K-GT3	M56-11	90							
K-GT5	M56-13	90	All cpx from K-GT5 (M56-13, 15 combined)						
K-GT5	M56-15	90	0.162	0.512656	0.000103	0.512660	0.512565	0.8	2.0
K-GT9	M56-25	90	All cpx from K-GT9 (M56-25, 26, 27 combined)						
K-GT9	M56-26	90	0.085	0.511864	0.000485	0.511868	0.511818	-13.7	9.5
K-GT9	M56-27	90							
K-GT10	M56-29	90							
K-GT10	M56-30	90							
Garnet (picked)									
K-GT2	M57-3	90	0.593	0.512908	0.000048	0.512912	0.512563	0.8	0.9
K-GT3	M57-4	90	0.567	0.512540	0.000164	0.512544	0.512210	-6.1	3.2
K-GT5	M57-5	90	0.575	0.512825	0.000085	0.512829	0.512491	-0.6	1.7
K-GT7	M57-7	90	0.561	0.512699	0.000113	0.512703	0.512373	-2.9	2.2
K-GT9	M57-9	90	0.535	0.512887	0.000026	0.512891	0.512576	1.0	0.5
K-GT1	M57-2	90	0.487	0.512862	0.000015	0.512866	0.512579	1.1	0.3
Whole Rock									
JMK	110-3	90	0.100	0.512786	0.000017	0.512790	0.512658	2.65	0.3

Table C.6(a). *Sr isotope results from the sequential leaching experiment carried out on JMK (Bultfontein xenolith). The amount of Sr and Rb refers to the weight of each analyte in the 10% aliquot analysed for trace elements and is not a concentration.*

Sample	Acid Leach	Batch Number	Rb (ng)	Sr (ng)	$^{87}Rb/^{86}Sr$	$^{87}Sr/^{86}Sr_m$	$^{87}Sr/^{86}Sr_n$	2SE
JMK								
Whole rock	N/A	110.3	1.58	38.90	0.252	0.706312	0.705707	0.000014
Leached whole rock D	1N HCl	111.6	0.84	18.34	0.133	0.705403	0.705395	0.000012
Leached whole rock E	3N HCl	111.7	0.59	17.31	0.098	0.705207	0.705199	0.000008
Leached whole rock F	6N HCl	111.8	0.66	15.41	0.123	0.705069	0.705061	0.000015
Leachate D	1N HCl	111L.6	4.88	116.33	0.121	0.707881	0.707873	0.000010
Leachate E	3N HCl	111L.7	7.98	152.70	0.151	0.707855	0.707847	0.000010
Leachate F	6N HCl	111L.8	6.77	148.75	0.132	0.707792	0.707784	0.000010

Table C.6(b). *Nd isotope results from the sequential leaching experiment carried out on JMK (Bultfontein xenolith). The amount of Sm and Nd refers to the weight of each analyte in the 10% aliquot analysed for trace elements and is not a concentration.*

Sample	Acid Leach	Batch Number	Sm (ng)	Nd (ng)	$^{147}Sm/^{143}Nd$	$^{144}Nd/^{143}Nd_m$	$^{144}Nd/^{143}Nd_n$	2SE
JMK								
Whole rock	N/A	110.3	0.57	2.63	0.100	0.512786	0.512790	0.000017
Leached whole rock D	1N HCl	111.6	0.42	1.73	0.149	0.512751	0.512745	0.000027
Leached whole rock E	3N HCl	111.7	0.46	1.63	0.172	0.512764	0.512758	0.000026
Leached whole rock F	6N HCl	111.8	0.39	1.39	0.170	0.512766	0.512760	0.000020
Leachate D	1N HCl	111L.6	0.78	4.84	0.097	0.512709	0.512703	0.000029
Leachate E	3N HCl	111L.7	1.16	7.32	0.097	0.512733	0.512727	0.000022
Leachate F	6N HCl	111L.8	1.17	7.26	0.098	0.512737	0.512731	0.000021

Figure C.1(a). *Scanned image of thin section JMK 1 from sample JMK (Bultfontein xenolith) used for drilling.*

Figure C.1(b). *Scanned image of thin section JMK 2 from sample JMK (Bultfontein xenolith) used for drilling.*

Figure C.1(c). *Scanned image of thin section JMK 3 from sample JMK (Bultfontein xenolith) used for drilling.*

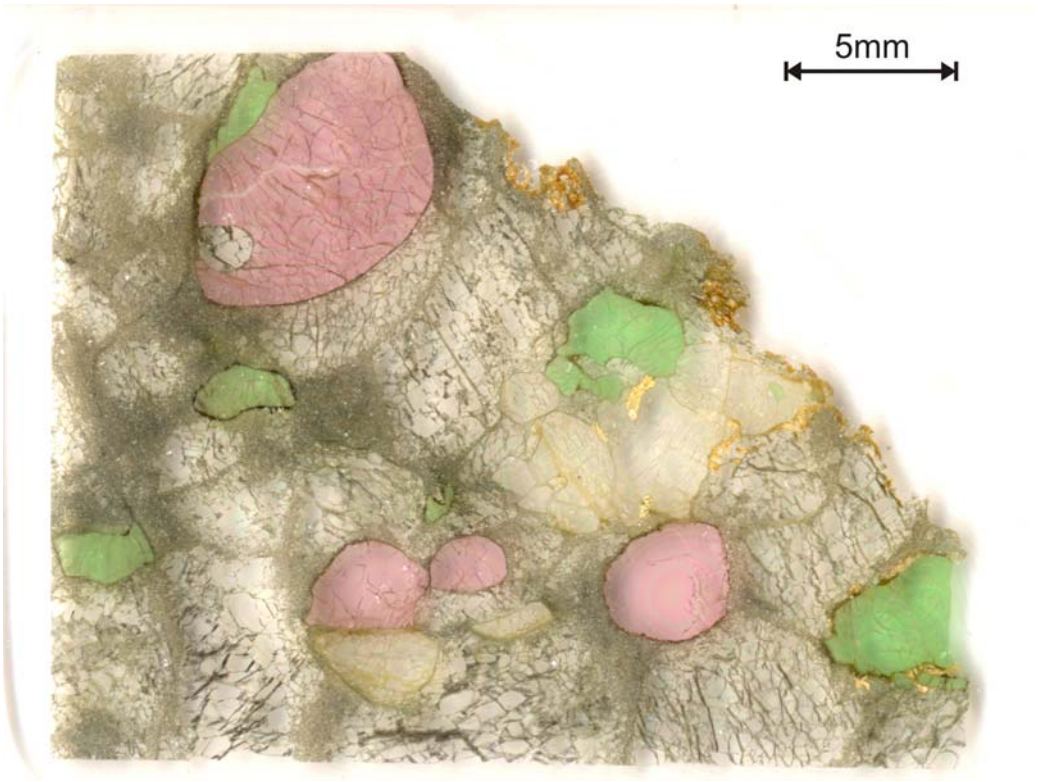

Figure C.1(d). *Scanned image of thin section JMK 4 from sample JMK (Bultfontein xenolith) used for drilling.*

Figure C.1(e). *Scanned image of thin section JMK 5 from sample JMK (Bultfontein xenolith) used for drilling.*

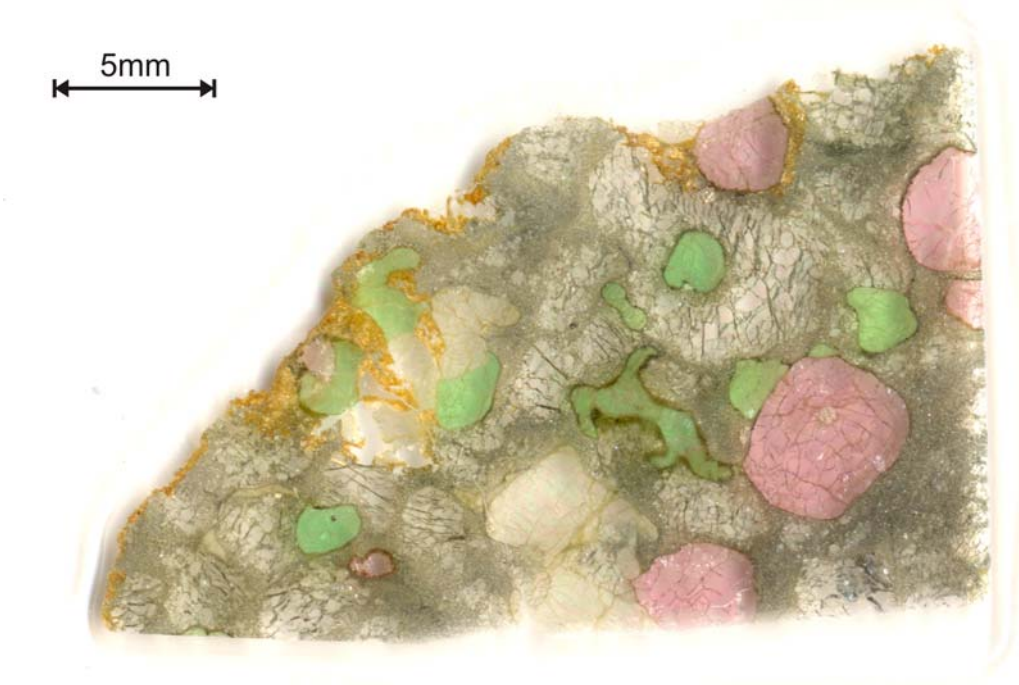

Figure C.1(f). *Scanned image of thin section JMK 6 from sample JMK (Bultfontein xenolith) used for drilling.*

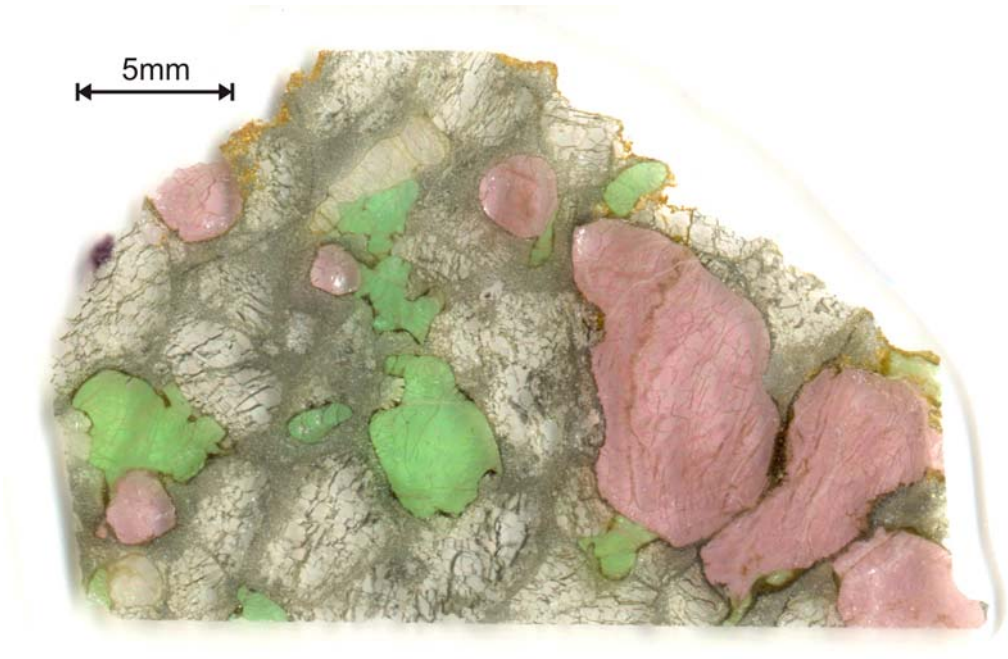

Figure C.2(a). *Scanned image of a polished slab (~5mm thick) of JMK (Bultfontein xenolith) outlining the areas where the garnet was cut out in order to pick garnet and cpx that were spatially related for Sr and Nd isotopes. These labels correspond to those used in Table C.2., Table C.3. and Table C.4.*

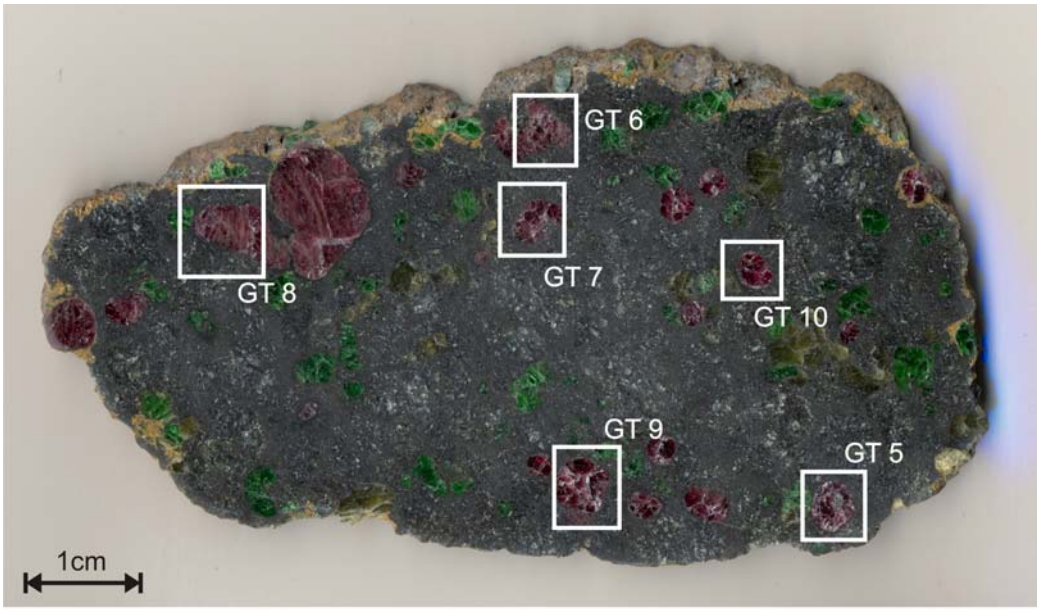

Figure C.2(a). *Scanned image of a polished slab (~5mm thick, opposite side to Figure C.2(a))) of JMK (Bultfontein xenolith) outlining the areas where the garnet was cut out in order to pick garnet and cpx that were spatially related for Sr and Nd isotopes. . These labels correspond to those used in Table C.2., Table C.3. and Table C.4.*

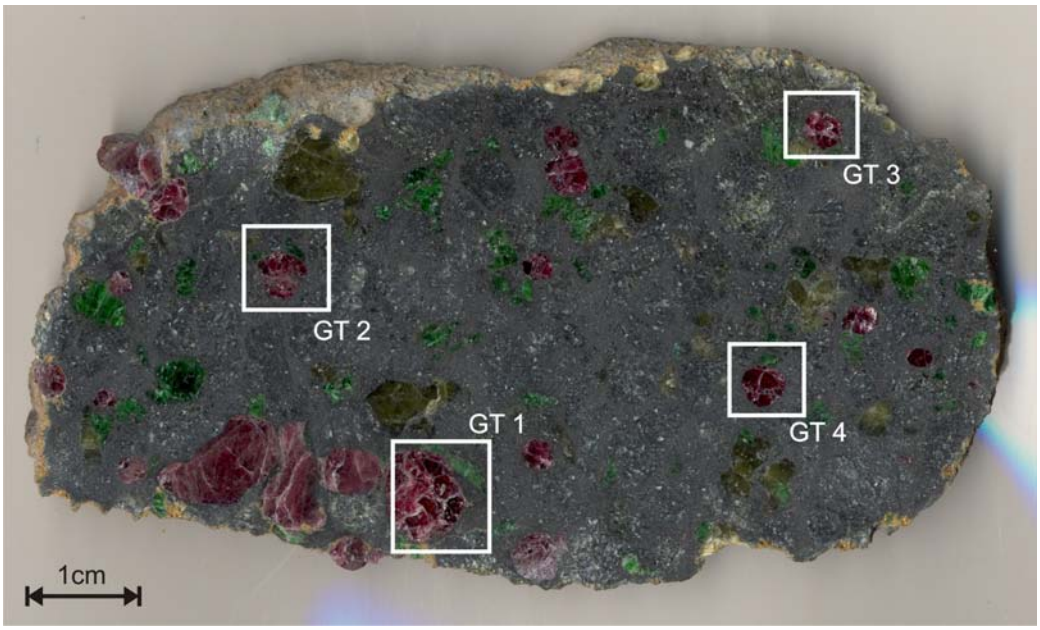

References:

Brey, G. P. and T. Kohler (1990). "Geothermobarometry in 4-Phase Lherzolites .2. New Thermobarometers, and Practical Assessment of Existing Thermobarometers." Journal of Petrology 31(6): 1353-1378.

Harley, S. L. (1984). "An experimental study of the partitioning of Fe and Mg between garnet and orthopyroxene." Contributions to Mineralogy and Petrology 86: 359-373.

Kohler, T. and G. P. Brey (1990). "Ca-exchange between olivine and clinopyroxene as a geothermobarometer calibrated

from 2 to 60 kbar in primitive natural lherzolites." Geochimica et Cosmochimica Acta 54(9): 2375-2388.

MacGregor, I. D. (1974). "The system MgO-Al2O3-SiO2-olubility of Al2O3 in enstatite for spinel and garnet peridotite compositions." American Mineralogist 59: 110-119.

Nimis, P. and W. R. Taylor (2000). "Single clinopyroxene thermobarometry for garnet peridotites. Part I. Calibration and testing of a Cr-in-Cpx barometer and an enstatite-in-Cpx thermometer " Contributions to Mineralogy and Petrology 139(5): 541-554.

O'Neil, H. S. C. and B. J. Wood (1979). "An experimental study of Fe-Mg partitioning between garnet and olivine and its calibration as a geothermometer." Contributions to Mineralogy and Petrology 70: 59-70.

Simon, N. S. C., R. W. Carlson, et al. (2008). "The origin and evolution of the Kaapvaal cratonic lithospheric mantle." Journal of Petrology.

Appendix D:

GREENLAND XENOLITH DATA

Table D.1(a). *Major element data (in wt% oxide) for clinopyroxene, orthopyroxene, olivine and garnet from samples G-06-07Z (Greenland garnet lherzolite) and G-06-07Y (Greenland spinel lherzolite).*

SAMPLE	WT% OXIDES											
NUMBER	SiO_2	Al_2O_3	TiO_2	FeO	MgO	MnO	CaO	Cr_2O_3	NiO	Na_2O	K_2O	Total
G-06-07Z (garnet lherzolite)												
Clinopyroxene												
Z1 D (core)	54.61	2.75	0.30	2.55	15.68	0.08	19.63	1.36	2.08	0.04	0.00	99.08
Z1 B (core)	53.74	1.72	0.38	3.18	16.73	0.08	21.06	1.48	0.89	0.04	0.00	99.30
Z2 A (core)	54.68	2.81	0.29	2.81	15.80	0.08	19.60	1.29	2.09	0.06	0.01	99.52
Z2 A (rim)	54.81	2.83	0.29	2.78	15.78	0.07	19.56	1.30	2.04	0.04	0.00	99.50
Z2 W (core)	54.61	2.72	0.29	2.80	15.90	0.08	19.76	1.30	2.06	0.04	0.01	99.56
Z2 D (core)	54.62	2.79	0.29	2.66	15.70	0.08	19.68	1.33	2.09	0.04	0.01	99.28
Z2 W (core)	54.91	2.76	0.29	2.69	15.88	0.06	19.64	1.37	2.08	0.03	0.01	99.72
Z2 W (rim)	54.62	2.77	0.29	2.78	16.01	0.05	19.66	1.22	2.01	0.06	0.01	99.48
Z2 V (core)	54.61	2.79	0.30	2.74	15.81	0.06	19.52	1.36	2.07	0.03	0.01	99.29
Z2 V (rim)	54.76	2.81	0.30	2.84	15.80	0.08	19.51	1.29	2.12	0.04	0.01	99.56
Garnet												
Z2 GT A (core)	42.10	21.23	0.24	8.73	19.52	0.44	4.70	2.40	b.d.l.	0.06		99.41
Z2 GT A (rim)	42.55	21.63	0.18	8.33	19.99	0.41	4.56	2.08	b.d.l.	0.05		99.80
Z2 GT A (rim)	42.83	21.69	0.21	8.56	19.94	0.42	4.59	2.11	0.02	0.07		100.45
Z2 GT E (core)	42.38	21.71	0.20	8.80	20.03	0.42	4.65	1.97	b.d.l.	0.06		100.23
Z2 GT E (rim)	42.67	21.72	0.19	8.77	20.17	0.40	4.66	1.98	0.00	0.06		100.64
Z2 GT B (core)	42.10	21.76	0.19	8.55	19.97	0.39	4.57	2.10	0.01	0.05		99.69
Z2 GT B (core)	42.03	21.52	0.19	8.61	19.92	0.43	4.65	2.09	0.00	0.08		99.52
Z1 GT A (rim)	42.51	21.56	0.19	8.68	19.91	0.36	4.65	2.10	0.01	0.04		100.02
Z1 GT B (core)	42.69	21.54	0.20	8.88	20.15	0.40	4.57	2.10	0.01	0.06		100.60
Z1 GT B (rim)	42.33	21.68	0.19	8.61	20.14	0.41	4.62	2.16	0.00	0.03		100.18
Orthopyroxene												
OPX 1	58.08	1.01	0.12	5.78	34.58	0.14	0.39	0.22	0.08	0.13	0.01	100.54
OPX 2	58.07	0.98	0.12	5.90	34.75	0.11	0.40	0.20	0.10	0.11	0.01	100.76
OPX 3	57.99	0.90	0.12	5.71	34.30	0.11	0.41	0.21	0.12	0.12	0.01	99.99
OPX 4	57.75	0.98	0.13	5.81	34.66	0.13	0.40	0.24	0.10	0.13	0.01	100.34
OPX 5	58.04	1.00	0.12	5.66	34.33	0.11	0.40	0.22	0.08	0.09	0.01	100.07
OPX 6	57.84	0.99	0.13	5.81	34.39	0.13	0.42	0.22	0.10	0.11	0.01	100.15

Table D.1(a).continued.

SAMPLE NUMBER	WT% OXIDES SiO_2	Al_2O_3	TiO_2	FeO	MgO	MnO	CaO	Cr_2O_3	NiO	Na_2O	K_2O	Total
G-06-07Z (garnet lherzolite)												
Olivine												
OL 1	41.24	0.01	0.03	9.26	49.01	0.12	0.02	0.02	0.40	0.03		100.13
OL 2	41.06	0.01	0.03	9.29	48.94	0.09	0.03	0.02	0.37	0.03		99.86
OL 3	41.41	0.01	0.02	9.45	48.87	0.12	0.02	0.01	0.38	0.03		100.32
OL 4	41.28	0.01	0.02	9.36	48.99	0.08	0.03	0.01	0.39	0.06		100.23
OL 5	41.40	0.01	0.03	9.53	48.77	0.11	0.02	0.01	0.36	0.03		100.27
G-06-07 Y (spinel lherzolite)												
Clinopyroxene												
CPX 1	55.12	0.16	0.07	2.68	16.35	0.12	21.51	1.78	1.24	0.03	0.01	99.06
CPX 2	55.45	0.16	0.08	3.05	16.29	0.14	21.33	1.93	1.32	0.04	b.d.l.	99.79
CPX 3	55.03	0.18	0.08	3.14	16.11	0.11	21.12	1.96	1.34	0.02	0.01	99.08
CPX 4	54.92	0.16	0.08	2.76	15.83	0.09	22.06	1.78	1.29	0.02	0.00	98.99
Olivine												
OL 1	41.27	0.00	0.01	10.14	47.73	0.17	0.02	0.01	0.39	0.03	99.77	99.77
OL 2	41.42	0.00	0.01	9.72	47.79	0.21	0.02	0.03	0.38	0.02	99.60	99.60
OL 3	41.17	b.d.l.	0.01	9.83	47.95	0.16	0.02	0.01	0.35	0.05	99.55	99.55

Table D.1(b). *Major element cation proportions calculated for clinopyroxene, orthopyroxene, olivine and garnet from samples G-06-07Z (Greenland garnet lherzolite) and G-06-07Y (Greenland spinel lherzolite).*

SAMPLE	CATION PROPORTIONS													
NUMBER	Si	Al	Ti	Fe	Mg	Mn	Ca	Cr	Ni	Na	K	Total	Mg#	Cr#
G-06-07Z (garnet lherzolite)														
Clinopyroxene														
Z1 D (core)	1.99	0.12	0.01	0.08	0.85	0.00	0.77	0.04	0.00	0.15	0.00	4.00	92	25
Z1 B (core)	1.97	0.07	0.01	0.10	0.91	0.00	0.83	0.04	0.00	0.06	0.00	4.00	90	37
Z2 A (core)	1.98	0.12	0.01	0.09	0.85	0.00	0.76	0.04	0.00	0.15	0.00	4.00	91	24
Z2 A (rim)	1.99	0.12	0.01	0.08	0.85	0.00	0.76	0.04	0.00	0.14	0.00	4.00	91	24
Z2 W (core)	1.98	0.12	0.01	0.08	0.86	0.00	0.77	0.04	0.00	0.14	0.00	4.01	91	24
Z2 D (core)	1.99	0.12	0.01	0.08	0.85	0.00	0.77	0.04	0.00	0.15	0.00	4.00	91	24
Z2 W (core)	1.99	0.12	0.01	0.08	0.86	0.00	0.76	0.04	0.00	0.15	0.00	4.00	91	25
Z2 W (rim)	1.98	0.12	0.01	0.08	0.87	0.00	0.76	0.03	0.00	0.14	0.00	4.00	91	23
Z2 V (core)	1.99	0.12	0.01	0.08	0.86	0.00	0.76	0.04	0.00	0.15	0.00	4.00	91	25
Z2 V (rim)	1.99	0.12	0.01	0.09	0.85	0.00	0.76	0.04	0.00	0.15	0.00	4.00	91	24
Garnet														
Z2 GT A (core)	3.03	1.80	0.01	0.53	2.09	0.03	0.36	0.14	0.00	b.d.l.		7.99		
Z2 GT A (rim)	3.04	1.82	0.01	0.50	2.13	0.03	0.35	0.12	0.00	b.d.l.		7.98		
Z2 GT A (rim)	3.04	1.81	0.01	0.51	2.11	0.03	0.35	0.12	0.00	0.00		7.98		
Z2 GT E (core)	3.02	1.82	0.01	0.52	2.13	0.03	0.36	0.11	0.00	b.d.l.		8.00		
Z2 GT E (rim)	3.03	1.82	0.01	0.52	2.13	0.02	0.35	0.11	0.00	0.00		8.00		
Z2 GT B (core)	3.01	1.84	0.01	0.51	2.13	0.02	0.35	0.12	0.00	0.00		8.00		
Z2 GT B (core)	3.02	1.82	0.01	0.52	2.13	0.03	0.36	0.12	0.00	0.00		8.00		
Z1 GT A (rim)	3.03	1.81	0.01	0.52	2.12	0.02	0.36	0.12	0.00	0.00		7.99		
Z1 GT B (core)	3.03	1.80	0.01	0.53	2.13	0.02	0.35	0.12	0.00	0.00		8.00		
Z1 GT B (rim)	3.02	1.82	0.01	0.51	2.14	0.02	0.35	0.12	0.00	0.00		8.00		
Orthopyroxene														
OPX 1	1.99	0.04	0.00	0.17	1.76	0.00	0.01	0.01	0.00	0.01	0.00	3.99	92	
OPX 2	1.98	0.04	0.00	0.17	1.77	0.00	0.01	0.01	0.00	0.01	0.00	4.00	92	
OPX 3	1.99	0.04	0.00	0.16	1.76	0.00	0.01	0.01	0.00	0.01	0.00	3.99	92	
OPX 4	1.98	0.04	0.00	0.17	1.77	0.00	0.01	0.01	0.00	0.01	0.00	4.00	92	
OPX 5	1.99	0.04	0.00	0.16	1.76	0.00	0.01	0.01	0.00	0.01	0.00	3.99	92	
OPX 6	1.99	0.04	0.00	0.17	1.76	0.00	0.02	0.01	0.00	0.01	0.00	3.99	92	

Table D.1(b)continued.

SAMPLE	CATION PROPORTIONS													
NUMBER	Si	Al	Ti	Fe	Mg	Mn	Ca	Cr	Ni	Na	K	Total	Mg#	Cr#
G-06-07Z (garnet lherzolite)														
Olivine														
OL 1	1.01	0.00	0.00	0.19	1.78	0.00	0.00	0.00	0.00	0.02		3.00	90	
OL 2	1.01	0.00	0.00	0.19	1.79	0.00	0.00	0.00	0.00	0.02		3.00	90	
OL 3	1.01	0.00	0.00	0.19	1.78	0.00	0.00	0.00	0.00	0.02		3.00	90	
OL 4	1.01	0.00	0.00	0.19	1.78	0.00	0.00	0.00	0.00	0.02		3.00	90	
OL 5	1.01	0.00	0.00	0.19	1.77	0.00	0.00	0.00	0.00	0.02		3.00	90	
G-06-07 Y (spinel lherzolite)														
Clinopyroxene														
CPX 1	2.02	0.01	0.00	0.08	0.89	0.00	0.84	0.05	0.00	0.09	0.00	3.99	92	88
CPX 2	2.02	0.01	0.00	0.09	0.88	0.00	0.83	0.06	0.00	0.09	b.d.l.	3.99	91	89
CPX 3	2.02	0.01	0.00	0.10	0.88	0.00	0.83	0.06	0.00	0.10	0.00	3.99	90	88
CPX 4	2.02	0.01	0.00	0.08	0.87	0.00	0.87	0.05	0.00	0.09	0.00	4.00	91	88
Olivine														
OL 1	1.01	0.00	0.00	0.21	1.75	0.00	0.00	0.00	0.01	0.00		2.99	89	
OL 2	1.02	0.00	0.00	0.20	1.75	0.00	0.00	0.00	0.01	0.00		2.98	90	
OL 3	1.01	b.d.l.	0.00	0.20	1.76	0.00	0.00	0.00	0.01	0.00		2.99	90	

Table D.2. *Trace element concentration data (ppm) for clinopyroxene and garnet from samples G-06-07Z, G-06-07Y and the host UMLs. B.d.l. refers to below detection limit.*

Sample Number	Batch Number	Weight (mg)	Trace element concentration (ppm)																										
			Rb	Sr	Y	Zr	Nb	Ba	La	Ce	Pr	Nd	Sm	Eu	Gd	Tb	Dy	Ho	Er	Tm	Yb	Lu	Hf	Ta	Pb	Th	U
G-06-07-Z (garnet lherzolite)																													
Clinopyroxene (LA-ICP-MS)																													
Z1 D (rim)	G0607Z1_cpx_7		0.54	187.3	2.14	45.42	0.385	1.540	3.75	12.58	2.13	9.89	1.73	0.656	1.87	0.163	0.825	0.092	0.191	0.020	<0.073	0.012	1.35	0.062	0.178	0.038	0.005
Z1 D (rim)	G0607Z1_cpx_8		0.11	162.4	2.43	46.70	0.267	<0.35	3.44	11.78	1.86	9.08	2.15	0.562	1.44	0.195	0.781	0.114	0.182	0.025	0.116	0.018	1.53	0.045	0.172	0.038	0.011
Z1 U (core)	G060721_cpx_12		<0.098	194.7	3.05	41.08	0.336	0.320	3.33	13.50	2.15	11.38	2.55	0.773	2.00	0.216	0.890	0.108	0.226	0.028	0.071	0.011	1.63	0.036	0.253	0.018	<0.00
Z1 B (core)	G060721_cpx_16		<0.00	185.9	2.47	39.11	0.275	<0.39	4.45	14.36	2.27	11.05	2.22	0.622	1.82	0.192	0.687	0.106	0.153	<0.0152	0.123	0.013	1.22	0.057	0.262	0.024	<0.00
Z1 K (rim)	G060721_cpx_17		0.06	200.0	2.63	44.80	0.342	0.073	4.61	15.42	2.34	10.58	2.38	0.745	2.19	0.210	0.950	0.107	0.192	0.022	0.076	<0.0133	1.19	0.055	0.231	0.031	<0.032
Z1 K (core)	G060721_cpx_18		0.02	186.2	2.77	50.45	0.298	<0.37	3.94	15.46	2.43	12.15	2.75	0.795	1.86	0.204	0.913	0.117	0.192	0.020	0.061	<0.0102	1.38	0.046	0.201	0.040	<0.00
Z2 A (core)	G060722_cpx_7		0.01	182.9	2.16	44.04	0.348	0.140	5.32	16.22	2.31	11.44	2.34	0.732	1.81	0.192	0.635	0.092	0.123	0.012	0.114	<0.0108	1.08	0.041	<0.169	0.041	<0.00
Z2 A (core)	G060722_cpx_8		<0.07	184.9	2.44	41.56	0.280	<0.00	5.33	15.51	2.28	11.28	2.28	0.780	1.92	0.204	0.755	0.116	0.150	0.013	<0.051	0.007	1.17	0.050	0.158	0.045	<0.00
Z2 A (core)	G060722_cpx_9		0.05	175.6	2.28	38.21	0.342	0.067	5.35	14.76	2.17	10.25	2.23	0.711	1.53	0.193	0.791	0.127	0.176	0.013	0.112	0.016	1.32	0.032	0.224	0.036	0.031
Z2 W (core)	G060722_cpx_11		<0.081	177.9	2.84	39.69	0.328	0.065	5.96	15.55	2.31	11.47	2.51	0.727	2.32	0.228	1.070	0.107	0.207	0.020	0.117	<0.0208	1.36	0.044	0.280	0.029	0.006
Z2 C (rim)	G060722_cpx_15		<0.128	180.8	3.12	51.51	0.377	0.065	4.26	14.37	2.35	12.26	2.51	0.727	1.89	0.194	0.890	0.099	0.198	0.030	0.135	<0.0109	1.61	0.067	0.253	0.042	0.012
Z2 C (rim)	G060722_cpx_16		<0.126	189.6	3.00	55.34	0.538	0.800	4.13	14.60	2.35	11.03	2.73	0.688	2.08	0.213	0.856	0.123	0.202	0.021	0.138	<0.0108	1.70	0.050	0.230	0.075	0.013
Z2 C (rim)	G060722_cpx_17		<0.073	187.1	3.20	52.70	0.345	0.118	4.35	14.27	2.29	12.06	2.49	0.747	2.53	0.229	1.090	0.094	0.232	0.026	<0.072	0.016	1.67	0.054	0.152	0.023	0.022
Z2 D (core)	G060722_cpx_18		0.03	191.8	2.78	48.73	0.305	<0.00	6.46	16.54	2.50	11.52	2.40	0.707	2.05	0.203	0.978	0.132	0.196	0.020	0.093	0.010	1.25	0.059	0.257	0.046	0.017
Clinopyroxene (drilled)																													
Z1 X	M48-4	*0.038*		195.5	2.486				2.851	12.206	1.757	9.871	2.094	0.585	1.796		0.836		0.186		0.092	0.015			b.d.l.	0.044	
Z1 U	M48-8	*0.047*		207.2	2.285				2.752	10.980	1.474	8.123	1.708	0.529	1.721		0.717		0.169		0.069	0.007			b.d.l.	0.033	
Z2 Y	M48-3	*0.092*	0.68	156.6	1.526				2.163	7.807	1.154	6.609	1.362	0.396	1.263		0.538		0.115		0.062	0.008			b.d.l.	0.031	
Z2 W	M48-5	*0.036*	0.71	169.6	1.916				2.523	9.354	1.259	7.310	1.484	0.443	1.491		0.641		0.139		0.062	0.006			b.d.l.	0.023	
Z2 V	M48-7	*0.043*	1.01	197.5	1.975				2.850	10.882	1.412	7.767	1.703	0.493	1.581		0.650		0.135		0.067	0.005			b.d.l.	0.038	
Z2 T	M48-9	*0.035*	1.83	218.5	2.628				2.654	9.347	1.643	9.257	2.022	0.606	1.905		0.841		0.184		0.083	0.012			b.d.l.	0.058	
Clinopyroxene (picked)																													
	M67 4	*0.405*	1.19	181.4	2.958	46.25	0.89		4.559	14.325	2.100	9.924	2.144	0.655	1.782	0.197	0.820		0.210		0.160	0.007	1.371		5.747	0.069	0.029
	M67 5	*0.227*	1.09	180.2	2.653	44.12	0.56		5.076	15.156	2.160	10.180	2.345	0.684	1.905	0.201	0.800		0.210		0.107	0.018	1.351		3.802	0.078	0.036
	M67 7	*0.072*	1.52	154.4	2.520	44.99	1.39		3.258	11.635	1.820	8.866	1.951	0.592	1.734	0.187	0.663		0.191		0.079	0.020	1.465		98.094	0.062	0.049
	M67 8	*0.103*	0.91	200.3	3.256	54.44	0.77		4.099	14.729	2.255	10.940	2.467	0.740	2.044	0.227	0.888		0.234		0.120	0.006	1.736		10.206	0.050	0.018
	M67 9	*0.110*	1.36	151.5	2.569	41.90	0.62		3.626	12.008	1.844	8.987	2.095	0.593	1.724	0.189	0.744		0.208		0.068	0.006	1.373		0.593	0.051	0.034
	M67 10	*0.039*	1.47	174.2	2.862	45.68	0.79		4.378	13.996	2.065	9.896	2.197	0.629	1.692	0.200	0.780		0.214		0.100	0.010	1.500		31.783	0.086	0.075
	M67 11	*0.064*	0.28	143.6	2.348	86.00	0.39		2.924	10.836	1.712	8.653	1.893	0.576	1.556	0.181	0.657		0.172		0.130	0.095	2.369		10.009	0.032	0.021

Table D.2.continued.

Sample Number	Batch Number	Weight (mg)	Trace element concentration (ppm)																									
			Rb	Sr	Y	Zr	Nb	Ba	La	Ce	Pr	Nd	Sm	Eu	Gd	Tb	Dy	Ho	Er	Tm	Yb	Lu	Hf	Ta	Pb	Th	U
G-06-07-Z (garnet lherzolite)																												
Garnet (LA-ICP-MS)																												
Z1 C (core)	G060721_gt_1		0.321	2.050	21.03	30.55	0.151	0.930	<0.031	0.160	0.037	0.68	0.577	0.366	1.71	0.355	3.32	0.772	2.45	0.427	2.94	0.437	0.350	<0.0155	<0.133	<0.0140	0.020
Z1 C (rim)	G060721_gt_2		0.016	<0.83	21.47	21.24	0.138	0.088	0.004	0.179	0.053	0.70	0.590	0.391	1.93	0.398	3.90	0.771	2.36	0.434	2.59	0.411	0.303	<0.0164	<0.00	0.003	0.016
Z1 C (rim)	G060721_gt_3		<0.088	<0.00	20.36	23.05	0.062	<0.00	0.029	0.122	0.043	0.49	0.506	0.383	2.06	0.431	3.73	0.793	2.35	0.364	2.57	0.434	0.318	<0.00	<0.102	<0.0151	<0.00
Z1 C (rim)	G060721_gt_4		1.040	7.030	19.95	23.22	0.096	0.150	0.006	0.093	0.031	0.34	0.545	0.327	1.51	0.373	3.35	0.692	2.31	0.375	2.69	0.381	0.322	0.011	<0.138	0.005	0.007
Z1 B (rim)	G060721_gt_5		<0.179	0.160	17.91	15.79	0.075	<0.00	0.007	0.065	0.031	0.27	0.370	0.235	1.48	0.295	2.98	0.648	2.04	0.354	2.18	0.321	0.183	<0.0171	<0.147	0.003	<0.00
Z1 B (rim)	G060721_gt_6		<0.092	0.170	19.39	26.54	0.092	<0.00	<0.029	0.110	<0.0201	0.40	0.660	0.341	1.75	0.375	3.32	0.691	2.10	0.362	2.69	0.394	0.514	0.003	<0.00	<0.0224	<0.00
Z1 B (rim)	G060721_gt_10		0.035	0.340	22.43	24.38	0.086	0.560	<0.031	0.103	0.054	0.38	0.502	0.349	1.54	0.464	3.15	0.735	2.34	0.357	2.56	0.438	0.130	0.007	0.162	0.006	<0.050
Z1 A (rim)	G060721_gt_13		<0.119	<0.81	20.17	24.23	0.057	<0.00	<0.037	0.140	0.055	0.52	0.730	0.410	1.89	0.425	3.24	0.687	2.36	0.371	2.67	0.362	0.310	0.009	<0.169	<0.0144	0.007
Z1 A (rim)	G060721_gt_14		0.327	12.020	21.55	23.80	0.598	2.570	0.020	0.139	0.037	0.60	0.640	0.443	1.68	0.439	3.25	0.837	2.55	0.329	2.65	0.399	0.398	0.029	<0.102	0.003	0.023
Z2 A (rim)	G060722_gt_1		0.033	0.480	20.38	30.70	0.078	<0.00	0.004	0.112	0.077	0.63	0.680	0.386	2.19	0.400	3.37	0.739	2.43	0.387	2.69	0.441	0.239	<0.0167	<0.202	0.006	0.008
Z2 A (rim)	G060722_gt_2		<0.135	0.160	20.85	21.60	0.065	<0.00	0.014	0.118	0.023	0.38	0.560	0.339	1.53	0.411	3.28	0.821	2.32	0.347	2.64	0.423	0.397	0.006	0.075	0.006	0.008
Z2 A (core)	G060722_gt_3		<0.089	0.840	18.25	23.99	0.144	<0.00	0.006	0.138	0.072	1.14	0.480	0.383	1.72	0.350	3.07	0.867	2.54	0.348	2.93	0.414	0.247	<0.017	<0.00	<0.0153	<0.00
Z2 A (core)	G060722_gt_4		0.049	<0.00	21.48	21.08	0.054	<0.00	0.022	0.146	0.077	0.38	0.560	0.384	1.58	0.437	3.42	0.792	2.57	0.412	3.18	0.465	0.316	<0.00	<0.154	<0.0161	0.008
Z2 A (core)	G060722_gt_5		0.088	<0.00	19.72	20.57	0.089	<0.00	0.006	0.127	0.048	0.50	0.454	0.340	1.66	0.356	3.04	0.832	2.32	0.353	2.78	0.482	0.384	0.008	<0.107	0.008	0.015
Z2 A (rim)	G060722_gt_6		0.041	0.400	20.50	40.63	0.082	<0.00	0.014	0.145	0.048	0.69	0.700	0.443	2.06	0.408	3.46	0.767	2.67	0.354	2.74	0.385	0.240	0.004	0.048	<0.00	0.010
Z2 A (rim)	G060722_gt_10		0.121	0.170	22.34	25.40	0.122	<0.75	0.015	0.128	0.051	0.42	0.570	0.332	1.78	0.455	3.32	0.834	2.61	0.407	3.02	0.443	0.373	0.010	<0.254	<0.0169	0.009
Z2 B (rim)	G060722_gt_12		<0.131	<0.89	20.70	23.15	<0.065	<0.00	<0.029	0.142	0.061	0.38	0.580	0.424	1.32	0.436	3.28	0.766	2.40	0.370	2.44	0.493	0.232	<0.0177	0.020	0.006	0.026
Z2 B (rim)	G060722_gt_13		0.069	0.130	19.25	18.65	0.078	<0.00	0.018	0.108	0.038	0.45	0.368	0.262	1.52	0.380	2.90	0.742	2.16	0.297	2.45	0.371	0.284	0.008	<0.108	0.002	0.021
Garnet (picked)																												
	M67 2	*0.74*	0.392	11.16	17.74	19.93	1.76		0.033	0.147	0.043	0.421	0.480	0.289	1.450	0.343	2.578		2.007		2.098	0.372	0.294		0.771	0.004	0.010
	M67 3	*0.36*	0.873	4.32	18.72	20.21	0.47		0.024	0.129	0.041	0.445	0.474	0.288	1.496	0.354	2.709		2.087		2.223	0.394	0.294		1.409	0.003	0.010
Whole Rock																												
G-06-07-Z	110-5	*14.080*	10.07	115.7	1.937	17.03	8.265	67.91	4.822	9.602	1.072	4.126	0.681	0.188	0.569	0.071	0.355		0.170		0.136	0.022	0.415		0.611	0.532	0.195

Table D.2.continued.

Sample Number	Batch Number	Weight (mg)	Trace element concentration (ppm)																						
			Rb	Sr	Y	Zr	Nb	Ba	La	Ce	Pr	Nd	Sm	Eu	Gd	Tb	Dy	Ho	Er	Tm	Yb	Lu	Hf	Ta	Pb	Th	U
G-06-07Y (spinel lherzolite)																											
Clinopyroxene (picked)																											
	M35-2	*0.075*	2.150	239.4	8.334	69.61	b.d.l.		4.390	19.36	4.427	22.31	5.372	1.933	4.734	0.664	2.525		0.646		0.502	b.d.l.			8.494	0.045	0.014
	M35-3	*0.048*	2.309	175.2	5.899	89.02	b.d.l.		2.361	10.87	2.582	13.35	3.686	1.534	3.538	0.522	1.695		0.432		0.524	b.d.l.			5.482	0.043	0.013
	M35-4	*0.033*	3.198	211.5	7.979	74.10	0.297		4.320	17.78	4.088	19.12	4.923	2.036	4.515	0.705	2.168		0.572		0.734	b.d.l.			3.152	0.100	0.033
	M35-5	*0.048*	2.745	241.6	8.903	82.72	0.074		3.923	16.17	4.388	20.43	5.199	1.978	5.158	0.759	2.666		0.636		0.676	b.d.l.			0.069	0.265	0.112
	M35-7	*0.045*	4.237	218.8	6.622	65.61	b.d.l.		2.664	10.78	3.002	14.16	3.649	1.582	3.980	0.601	2.039		0.459		0.589	b.d.l.			17.475	0.081	0.144
	M35-8	*0.089*	1.268	244.7	9.014	66.81	0.080		4.184	18.51	4.993	23.69	5.775	2.221	5.808	0.781	2.932		0.690		0.537	b.d.l.			3.580	0.050	0.014
	M35-9	*0.036*	3.240	214.5	6.951	80.78	b.d.l.		3.022	12.38	3.386	16.16	3.959	1.816	4.649	0.671	2.028		0.500		0.713	b.d.l.			13.429	0.179	0.057
	M35-10	*0.079*	1.262	207.1	7.889	91.45	0.115		2.917	12.99	3.610	17.98	4.488	1.736	4.631	0.668	2.494		0.588		0.508	b.d.l.			1.381	0.062	0.015
	M35-11	*0.077*	1.611	213.1	8.669	87.94	0.366		3.980	16.28	4.309	19.92	4.848	1.870	5.058	0.716	2.752		0.676		0.576	b.d.l.			3.358	0.095	0.024
HOST UML (Whole rock)																											
Whole Rock																											
G-06-03/04	109-2	*12.31*	44.13	604.4	10.37	180.05	77.67	348.6	63.11	133.5	15.18	58.79	8.76	2.346	6.201	0.648	2.645		0.921		0.503	0.077	3.995		1.302	6.820	1.752
G-06-01	109-3	*11.40*	58.64	921.2	13.18	201.48	106.67	532.4	79.84	165.0	18.56	70.64	10.95	2.952	7.984	0.854	3.518		1.135		0.617	0.088	4.970		4.998	8.402	2.349
G-06-07	109-4	*11.07*	63.23	839.8	12.15	202.88	96.16	493.8	70.72	144.9	16.34	62.44	9.54	2.591	6.955	0.749	3.139		1.051		0.589	0.085	4.948		2.710	7.013	1.957
G-06-14	109-5	*9.29*	40.82	682.3	9.85	140.57	90.14	323.2	66.73	141.5	16.08	62.23	9.23	2.483	6.607	0.667	2.847		0.862		0.414	0.059	3.535		2.002	6.991	1.619
G-06-05	109-6	*9.09*	32.50	565.3	9.39	122.02	89.40	256.5	68.77	149.1	17.12	66.51	9.60	2.571	6.922	0.695	2.730		0.837		0.432	0.058	3.102		1.583	7.609	1.813
G-06-04	109-7	*10.05*	41.55	714.9	11.07	144.70	106.21	297.1	79.99	171.7	19.76	75.72	10.96	2.985	7.743	0.780	3.304		0.989		0.517	0.066	3.598		2.150	8.825	1.874

Table D.3. *Summary of the Sr isotope data for the drilled and picked clinopyroxene and garnet from samples G-06-07 Z and G-06-07 Y (both Greenland). (m) refers to the measured ratio; (n) to the normalised ratio (see Appendix A for the standard values used for normalisation); (i) refers to the initial ratio corrected to 164Ma.*

Sample Name	Batch Number	Age (Ma)	$^{87}Rb/^{86}Sr$	$^{87}Sr/^{86}Sr_m$	2sd	$^{87}Sr/^{86}Sr_n$	$^{87}Sr/^{86}Sr_i$
G-06-07-Z (garnet lherzolite)							
Clinopyroxene (drilled)							
Z1 X	M48-4	164	0.007	0.703322	0.000019	0.703322	0.703305
Z1 U	M48-8	164	0.007	0.703477	0.000016	0.703477	0.703461
Z2 Y	M48-3	164	0.009	0.703156	0.000018	0.703156	0.703134
Z2 W	M48-5	164	0.009	0.703261	0.000040	0.703261	0.703241
Z2 V	M48-7	164	0.015	0.703330	0.000016	0.703330	0.703313
Z2 T	M48-9	164	0.007	0.703537	0.000019	0.703537	0.703522
Clinopyroxene (picked)							
	M67 4	164	0.019	0.703093	0.000010	0.703087	0.703043
	M67 5	164	0.018	0.703261	0.000012	0.703255	0.703214
	M67 7	164	0.029	0.703194	0.000022	0.703188	0.703121
	M67 8	164	0.013	0.703110	0.000009	0.703104	0.703073
	M67 9	164	0.026	0.703151	0.000014	0.703145	0.703085
	M67 10	164	0.024	0.703083	0.000016	0.703077	0.703020
	M67 11	164	0.006	0.703097	0.000013	0.703091	0.703078
Garnet (picked)							
	M67 2	164	0.102	0.708992	0.000020	0.708986	0.708749
	M67 3	164	0.585	0.709219	0.000033	0.709213	0.707849
Whole rock							
	110-5	164	0.117	0.706551	0.000007	0.706533	0.706260
G-06-07Y (spinel lherzolite)							
Clinopyroxene (picked)							
G-06-07Y-A*	M35-2	164	0.015	0.703632	0.000010	0.703627	0.703612
G-06-07Y-B*	M35-3	164	0.038	0.703654	0.000023	0.703649	0.703621
G-06-07Y-C*	M35-4	164	0.044	0.703622	0.000012	0.703617	0.703583
G-06-07Y-D*	M35-5	164	0.033	0.703980	0.000008	0.703975	0.703953
G-06-07Y-E*	M35-7	164	0.056	0.703607	0.000012	0.703602	0.703559
G-06-07Y-F*	M35-8	164	0.015	0.703650	0.000010	0.703645	0.703640
G-06-07Y-G*	M35-9	164	0.044	0.703670	0.000012	0.703665	0.703632
G-06-07Y-H*	M35-10	164	0.018	0.703657	0.000010	0.703652	0.703644
G-06-07Y-I*	M35-11	164	0.022	0.703670	0.000014	0.703665	0.703653
HOST KIMBERLITE							
Whole rock							
G-06-03/04	92-2	164	0.211	0.704507	0.000013	0.704489	0.703996
G-06-01	92-3	164	0.184	0.703901	0.000009	0.703883	0.703454
G-06-07	92-4	164	0.218	0.704428	0.000007	0.704410	0.703902
G-06-14	92-5	164	0.173	0.704135	0.000008	0.704117	0.703713
G-06-05	92-6	164	0.166	0.703969	0.000010	0.703951	0.703563
G-06-04	92-7	164	0.168	0.704095	0.000006	0.704077	0.703685

Table D.4. *Summary of the Nd isotope data for the drilled and picked clinopyroxene and garnet from samples G-06-07 Z and G-06-07 Y (both Greenland). (m) refers to the measured ratio; (n) to the normalised ratio (see Appendix A for the standard values used for normalisation); (i) refers to the initial ratio corrected to 164Ma.*

Sample Name	Batch Number	Age (Ma)	$^{147}Sm/^{144}Nd$	$^{143}Nd/^{144}Nd_m$	2sd	$^{143}Nd/^{144}Nd_n$	$^{143}Nd/^{144}Nd_i$	εNd_i	2se
G-06-07-Z (garnet lherzolite)									
Clinopyroxene (picked)									
	M67 4	164	*Combined cpx analyses from M67*						
	M67 5	164	0.136	0.512130	0.000252	0.512134	0.511995	-8.63	4.9
	M67 7	164							
	M67 8	164							
	M67 9	164							
	M67 10	164							
	M67 11	164							
Garnet (picked)									
	M67 2	164	*Not enough analyte for an isotopic analysis*						
	M67 3	164							
Whole rock									
	110-5	164	0.140	0.512737	0.000021	0.512741	0.512594	1.40	0.5
HOST KIMBERLITE									
Whole rock									
G-06-03/04	92-2	164	0.090	0.512795	0.000006	0.512799	0.512704	5.30	0.1
G-06-01	92-3	164	0.094	0.512798	0.000006	0.512802	0.512703	5.29	0.1
G-06-07	92-4	164	0.085	0.512799	0.000011	0.512803	0.512714	5.49	0.2
G-06-14	92-5	164	0.090	0.512799	0.000009	0.512803	0.512709	5.39	0.2
G-06-05	92-6	164	0.088	0.512789	0.000008	0.512793	0.512701	5.24	0.2
G-06-04	92-7	164	0.088	0.512790	0.000006	0.512794	0.512702	5.26	0.2
									0.1

Table D.6(a). *Sr isotope results from the sequential leaching experiment carried out on G-06-07 Z (Greenland xenolith). The amount of Sr and Rb refers to the mass of analyte in the 10% aliquot analysed for trace elements and is not a concentration.*

Sample	Acid Leach	Batch Number	Rb (ng)	Sr (ng)	$^{87}Rb/^{86}Sr$	$^{87}Sr/^{86}Sr_m$	$^{87}Sr/^{86}Sr_n$	2SE
G-06-07-Z								
Whole rock	N/A	110-5	13.30	158.30	0.117	0.706551	0.706533	0.000007
Leached whole rock A	1N HCl	111.2	6.69	44.36	0.436	0.706286	0.706278	0.000007
Leached whole rock B	3N HCl	111.3	4.27	37.48	0.329	0.705910	0.705902	0.000008
Leached whole rock B	6N HCl	111.4	3.14	29.94	0.304	0.705930	0.705922	0.000009
Leachate A	1N HCl	111L.2	32.14	718.20	0.129	0.706331	0.706323	0.000009
Leachate B	3N HCl	111L.3	77.37	1026.55	0.218	0.706447	0.706439	0.000008
Leachate C	6N HCl	111L.4	51.64	655.41	0.228	0.706450	0.706442	0.000009

Table D.6(b). *Nd isotope results from the sequential leaching experiment carried out on G-06-07 Z (Greenland xenolith). The amount of Nd and Sm refers to the mass of analyte in the 10% aliquot analysed for trace elements and is not a concentration.*

Sample	Acid Leach	Batch Number	Sm (ng)	Nd (ng)	$^{147}Sm/^{143}Nd$	$^{144}Nd/^{143}Nd_m$	$^{144}Nd/^{143}Nd_n$	2SE
G-06-07-Z								
Whole rock	N/A	110-5	0.94	5.53	0.140	0.512737	0.512741	0.000021
Leached whole rock A	1N HCl	111.2	0.60	3.62	0.100	0.512770	0.512764	0.000010
Leached whole rock B	3N HCl	111.3	0.67	4.10	0.099	0.512773	0.512767	0.000008
Leached whole rock B	6N HCl	111.4	0.51	3.05	0.102	0.512761	0.512755	0.000010
Leachate A	1N HCl	111L.2	0.98	5.33	0.112	0.512801	0.512795	0.000026
Leachate B	3N HCl	111L.3	1.92	10.57	0.110	0.512797	0.512791	0.000018
Leachate C	6N HCl	111L.4	1.27	7.11	0.109	0.512788	0.512782	0.000018

Figure D.1(a). *Scanned image of thin section G-06-07 Z1 from sample G-06-07 Z (Greenland xenolith) used for drilling.*

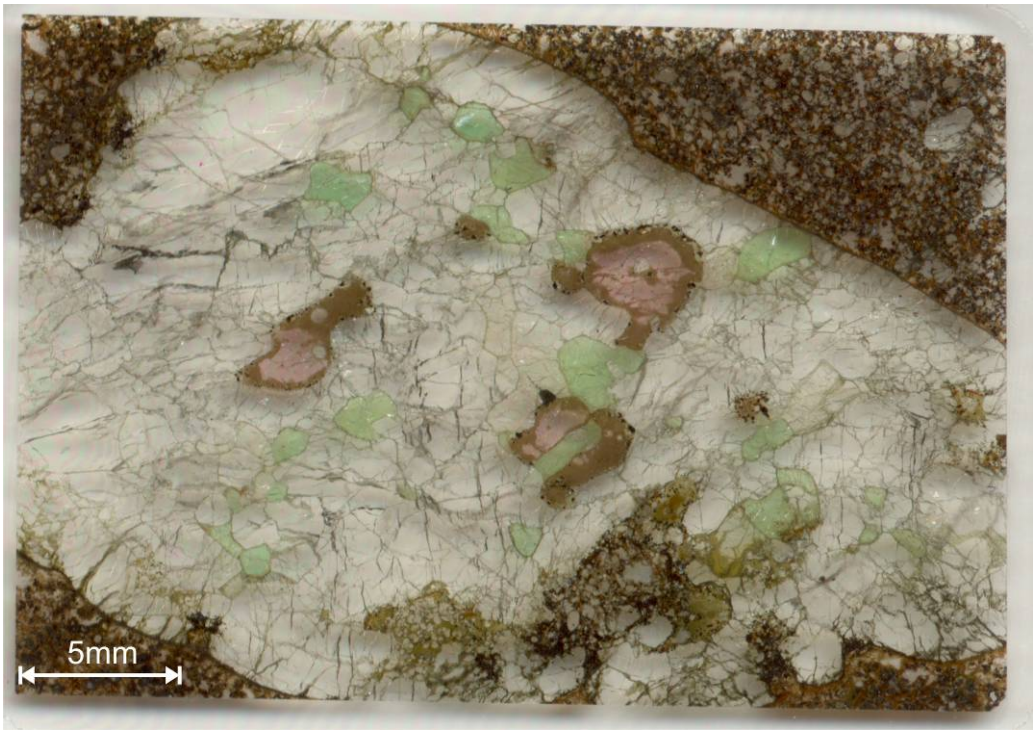

Figure D.1(b). *Scanned image of thin section G-06-07 Z2 from sample G-06-07 Z (Greenland xenolith) used for drilling.*

Figure D.1(c). *Scanned image of thin section G-06-07Y. Cpx was picked from a coarse crush of this sample for isotope and trace element analysis.*

Appendix E:

SALTPETRE KOP OLIVINE MELILITITE DATA

Table E.1(a). *Representative major element data (wt%) for the minerals from the Saltpetre Kop (SPK) olivine melilitite taken from Boctor and Yoder (1986).*

Mineral	SiO_2	Al_2O_3	Fe_2O_3	FeO	MgO	CaO	Na_2O	K_2O	MnO	TiO_2	P_2O_5	Total	Notes
Olivine	41.16	0.1		10.2	48.94	0.04	n.d.		0.2	<0.03		100.76	Core of olivine
Spinel	0.2	13.64	38.44	24.07	11.63	0.07			0.92	10.38		99.59	Groundmass spinel
Perovskite	0.16	0.44		1.68	0.09	37.55	0.36	<0.03	<0.03	56.23		96.55	
Phlogopite	29.74	16.05		5.81	20.71	n.d.	0.32	4.6	0.12	3.43		95.89	Core of phenocryst
Melilite	43.41	6.82		2.38	8.41	35.51	3.36	0.12	0.02	0.07		100.08	
Whole Rock	36.2	7.2	3.2	8	19.5	18.2	2.4	1		2.4	1.6	99.7	

Table E.1(b). *New microprobe major element data (wt%) for melilite, monticellite and wollastonite from the SPK olivine melilitite, analysed by GSC at Carleton University, Ottawa, Canada.*

Mineral	SiO_2	TiO_2	Al_2O_3	FeO	MnO	MgO	CaO	SrO	BaO	Na_2O	K_2O	Total	Notes
Melilite													
	42.46	0.09	6.60	2.00	0.05	8.90	35.94	0.33	0.07	2.84	0.16	99.45	Euhedral, core
	42.43	0.06	6.48	2.65	0.08	8.42	35.46	0.46	0.08	3.14	0.13	99.40	Euhedral, rim
	42.96	0.08	6.15	3.09	0.04	8.47	35.30	0.53	0.26	3.17	0.13	100.18	Small euhedral, in nepheline
	42.32	0.04	6.00	2.42	0.07	9.18	36.51	0.34	0.01	2.68	0.15	99.72	Euhedral, core
	42.82	0.10	6.55	2.25	0.03	8.79	35.35	0.35	0.07	3.14	0.09	99.54	Euhedral, rim
	42.58	0.10	6.01	2.36	0.00	8.89	36.00	0.36	0.08	2.73	0.14	99.26	Coarse euhedral, core
	42.87	0.08	6.46	2.76	0.06	8.42	35.50	0.45	0.14	3.17	0.18	100.09	Small euhedral, core
Monticellite													
	36.73	0.05	0.01	13.06	0.53	17.60	32.01	n.d.	0.02	0.10	n.d.	100.12	Anhedral, rimming olivine
	35.93	0.00	0.01	13.45	0.47	15.95	32.30	n.d.	0.03	0.03	0.04	98.22	Anhedral, in matrix
	36.13	0.05	0.02	13.42	0.53	17.17	32.37	0.10	0.05	0.08	0.01	99.90	Around olivine
	36.13	0.04	0.03	13.84	0.56	16.35	32.98	0.01	n.d.	0.04	n.d.	99.97	Euhedral, in matrix
	35.42	0.04	0.02	13.72	0.46	16.11	32.87	n.d.	n.d.	0.09	n.d.	98.74	Euhedral, in matrix
	36.03	0.02	0.02	11.29	0.30	17.46	33.65	0.02	0.01	0.07	n.d.	98.86	Euhedral rim on olivine
Wollastonite													
	39.78	0.15	1.06	0.78	0.09	0.10	50.57	0.18	n.d.	0.15	0.14	92.99	Altered, in matrix
	40.06	0.21	0.83	0.33	0.07	0.07	50.55	0.18	n.d.	0.12	0.14	92.56	Altered, in matrix

Table E.2(a). *Trace element concentration data (ppm) for the olivine, melilite, perovskite, apatite and phlogopite from the SPK olivine melilite. The whole rock data (*) is taken from Janney et al. (2002).*

Mineral	Olivine	Phlogopite	Perovskite	Apatite	Melilite	Whole Rock*	Whole Rock*
Batch #	M77-4	M77-7	M77-10	M77-8	M81-5	SPK-1	SPK-2
Rb	1.166	515.4	19.22	1.675	4.651	66	43
Sr	8.190	180.5	2275	5877	2599	1396	1421
Y	0.998	23.92	407.0	364.488	7.751	26	29
Zr	23.09	563.2	1222	176.58	24.00	139	312
Nb	3.809	126.0	2981	65.45	22.765	143	155
Ba	75.70	109351	175.4	1206	403.9	1663	2608
La	5.161	240.7	5307	1548	76.79	191	182
Ce	8.580	414.0	9306	2175	125.6	308	301
Pr	0.879	41.90	972.8	233.4	11.700	31.5	31.3
Nd	2.848	134.2	3170	815.5	48.71	106	105
Sm	0.423	19.92	444.9	138.5	7.033	15.8	15.4
Eu	0.089	5.587	90.14	34.93	1.854	4.29	4.13
Gd	0.246	10.88	219.5	101.8	4.702	10.5	10.1
Dy	0.192	6.746	124.5	66.35	2.048	6.12	6.14
Er	0.095	2.038	34.76	22.97	0.464	1.98	2.16
Yb	0.105	0.989	18.22	13.84	0.266	1.17	1.31
Lu	0.021	0.125	3.562	2.021	0.031	0.15	0.17
Hf	0.460	11.015	39.80	3.950	0.612	3.06	6.05
Pb	0.235	0.710	28.64	30.52	3.022	15.4	49.3
Th	0.770	37.34	947.5	52.90	7.723	27.1	29.2
U	0.261	11.71	188.1	9.344	0.729	5.54	7.04
Tb	0.039	1.557	31.91	15.49	0.436	1.32	1.29

Table E.2(b). *Trace element data (in ng of analyte in the leachate) for the leachates of the picked mineral separates.*

Mineral Leached	Olivine	Perovskite	Phlogopite
Batch #	M75-7	M75-8	M75-9
Rb	0.364	0.015	0.751
Sr	67.31	2.581	52.38
Y	0.734	0.013	0.522
Zr	4.171	0.204	3.352
Nb	0.008	0.002	0.011
Ba	23.33	1.413	167.1
La	1.666	0.051	0.809
Ca	2.371	0.075	0.948
Pr	0.250	0.008	0.095
Nd	0.898	0.028	0.342
Sm	0.157	0.004	0.064
Eu	0.066	0.002	0.031
Gd	0.269	0.003	0.129
Dy	0.103	0.002	0.062
Er	0.049	0.001	0.035
Yb	0.050	0.002	0.037
Lu	0.009	0.001	0.006
Hf	0.060	0.005	0.059
Pb	0.567	0.009	0.125
Th	0.018	0.001	0.007
U	0.010	0.000	0.005
Tb	0.019	0.000	0.010

Table E.3(a). *Sr isotope data for olivine, melilite, phlogopite, perovskite and apatite. (m) refers to measured ratio; (n) to the normalised ratio (see Appendix A for standard data); (i) refers to the initial ratio which is age corrected to 74.7Ma. The whole rock data (*) is taken from Janney et al. (2002). The mass of Rb and Sr refers to the mass in the analyte (in ng).*

Mineral	Sample #	Age (Ma)	Rb (ng)	Sr (ng)	$^{87}Rb/^{86}Sr$	$^{87}Sr/^{86}Sr_n$	2SE	$^{87}Sr/^{86}Sr_i$
Olivine								
	M77-2	74.7	0.15	0.79	0.538	0.704904	0.000055	0.704334
	M77-3	74.7	0.08	0.64	0.373	0.704649	0.000042	0.704253
	M77-4	74.7	0.45	3.18	0.412	0.704718	0.000028	0.704281
Perovskite								
	M77-10	74.7	0.00	0.35	0.024	0.704381	0.000022	0.704355
	M77-11	74.7	0.00	0.40	0.036	0.704361	0.000019	0.704323
Apatite								
	M77-8	74.7	0.00	1.08	0.001	0.704221	0.000014	0.704220
	M77-13	74.7	0.00	0.10	0.009	0.704491	0.000054	0.704481
	M77-14	74.7	0.00	0.18	0.015	0.704403	0.000036	0.704388
	M77-15	74.7	0.00	0.79	0.003	0.704334	0.000026	0.704331
Phlogopite								
	M77-5	74.7	3.17	1.10	8.351	0.713783	0.000110	0.704926
	M77-7	74.7	6.56	2.30	8.264	0.713086	0.000054	0.704321
Melilite								
	M81-2	74.7	0.02	6.95	0.009	0.704262	0.000021	0.704252
	M81-3	74.7	0.10	7.13	0.042	0.704321	0.000012	0.704277
	M81-4	74.7	0.01	4.54	0.007	0.704263	0.000009	0.704256
	M81-5	74.7	0.01	7.69	0.005	0.704270	0.000008	0.704265
	M81-7	74.7	0.01	5.02	0.004	0.704251	0.000008	0.704247
Whole Rock*								
	SPK-1	74.7	12.30	606.00	0.059	0.704315	0.000030	0.704253
	SPK-3	74.7	16.60	524.00	0.092	0.704328	0.000030	0.704231

Table E.3(b). *Sr isotope data for the leachates from the picked minerals.*

Mineral Leached	Batch #	$^{87}Sr/^{86}Sr_n$	2SE
Olivine	M75-7	0.704321	0.000013
Perovskite	M75-8	0.704366	0.000022
Phlogopite	M75-9	0.704397	0.000026

Figure E.1. *False colour QEMSCAN images of a thin section of the SPK olivine melilitite.*
(a) *Distribution of olivine and monticellite in the Area A (outlined in (c)).*
(b) *Distribution of phlogopite, perovskite and apatite in the groundmass in Area A (outline in (c)).*
(c) *Distribution of melilite and the alteration products of melilite in the thin section. This illustrates the bands of alteration that may be the result of fluid passing through the sample.*

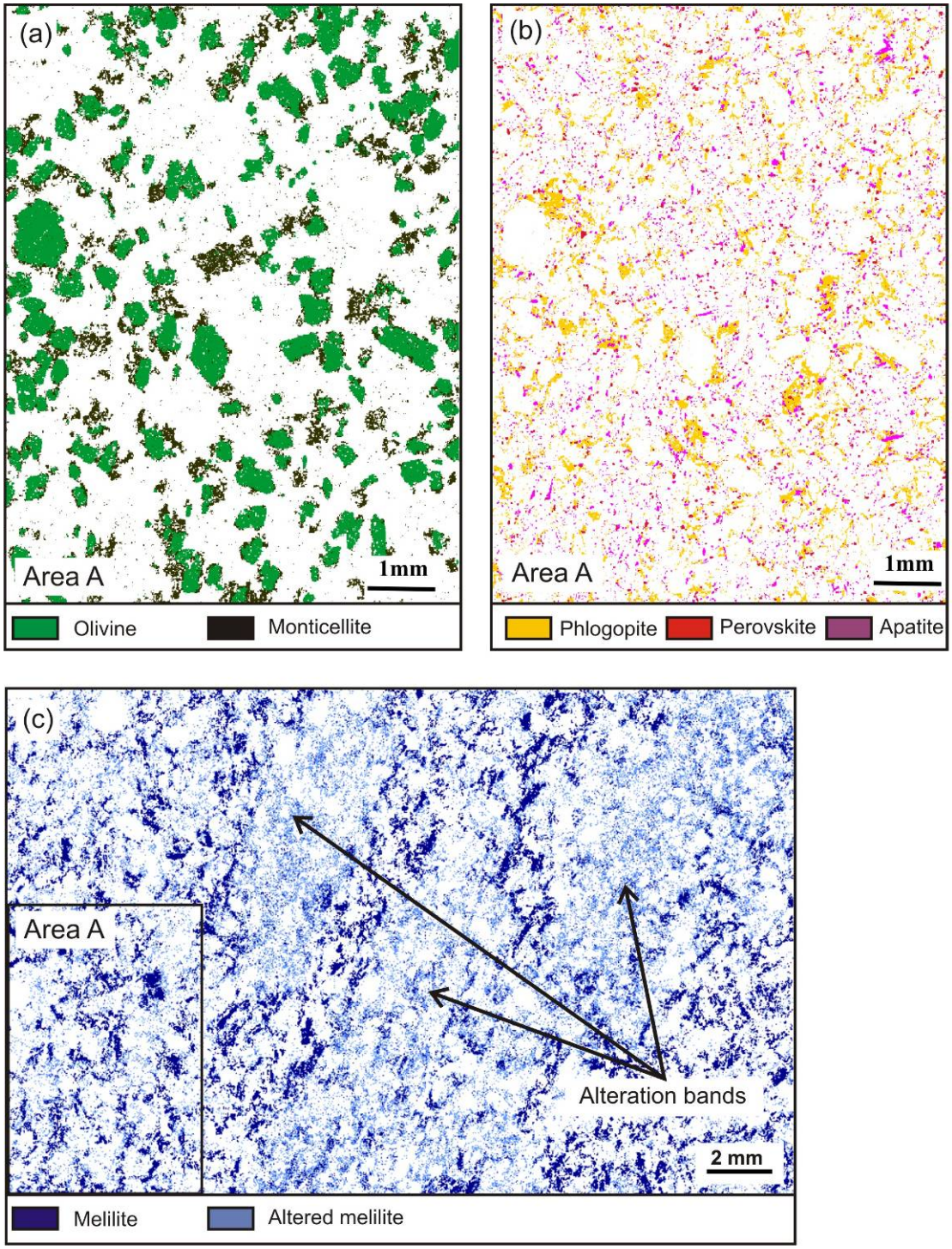

Figure E.2 (a). *Photograph of the picked olivine from SPK.*

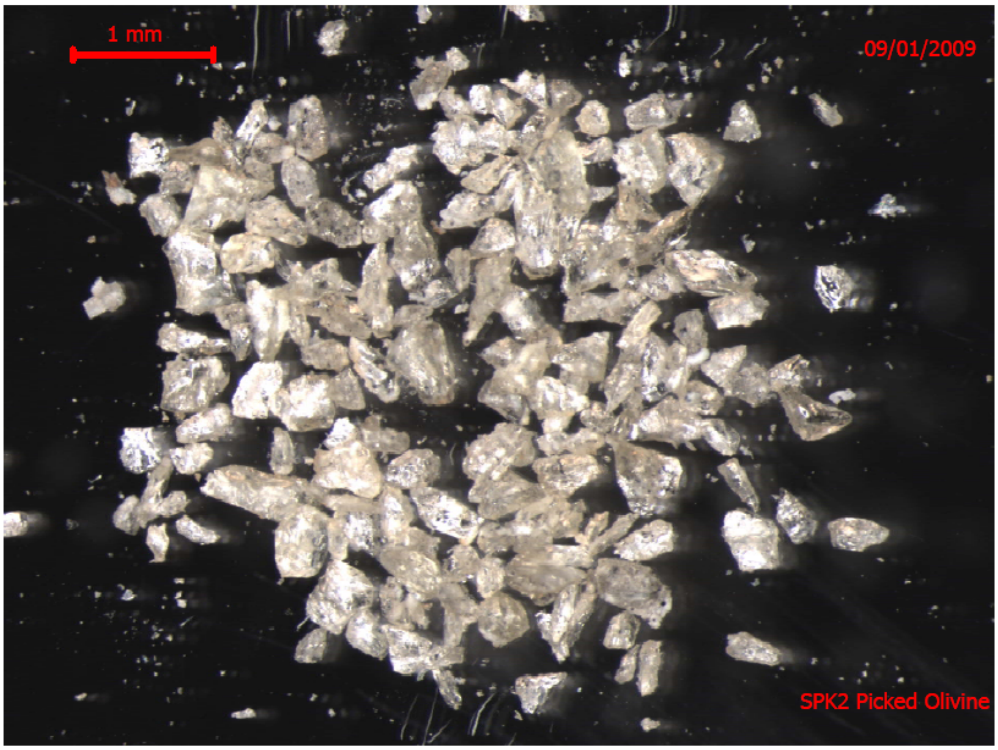

Figure E.2(b). *Photograph of some of the perovskite crystals picked.*

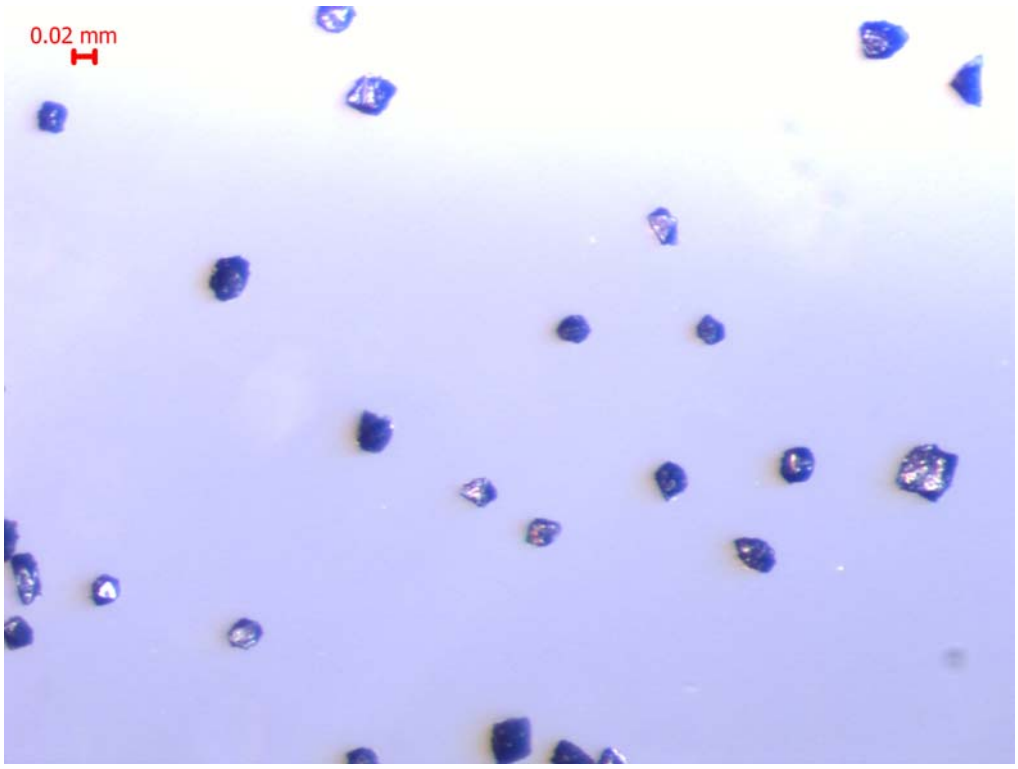

Figure E.2(c). *Photograph of an apatite crystal picked for analysis.*

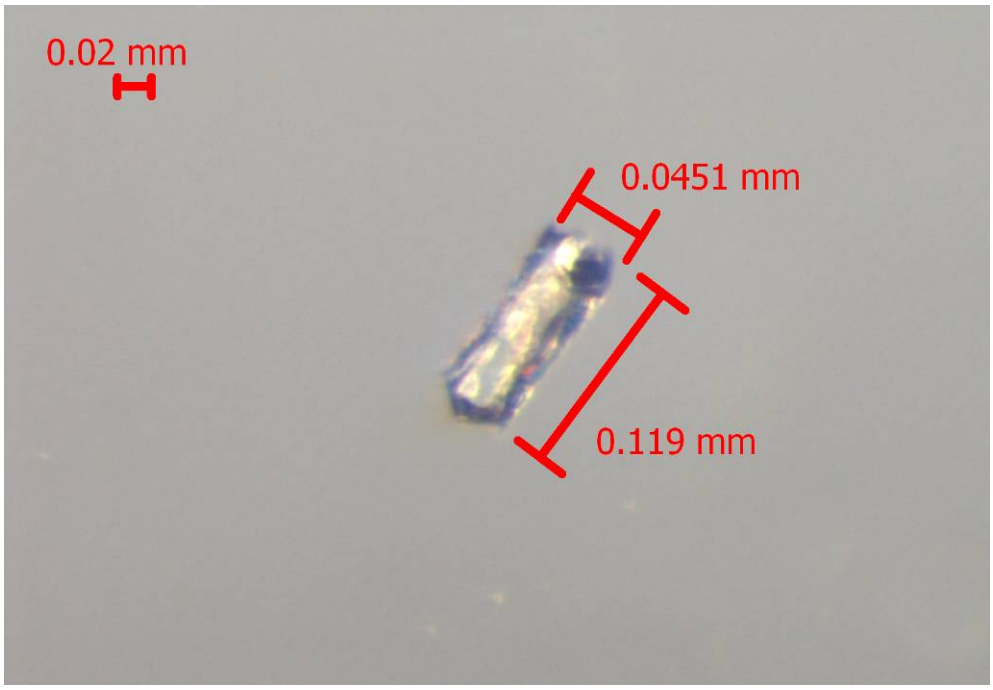

References:

Boctor, N. Z. and H. S. Yoder (1986). "Petrology of Some Melilite-Bearing Rocks from Cape-Province, Republic of South Africa - Relationship to Kimberlites." American Journal of Science 286(7): 513-539.

Janney, P. E., A. P. Le Roex, et al. (2002). "A chemical and multi-isotope study of the Western Cape olivine melilitite province, South Africa: Implications for the sources of kimberlites and the origin of the HIMU signature in Africa." Journal of Petrology 43(12): 2339-2370.

Appendix F:

JOS KIMBERLITE DATA

Table F.1(a). *Major element data (wt%) for calcite from the Jos kimberlite, analysed by GSC at Carleton University, Ottawa, Canada. n.d. refers to not detected. CO_2 is calculated from the other major element data.*

Mineral	CaO	FeO	MgO	SrO	BaO	MnO	ZnO	PbO_2	CO_2^*	Total	Notes
Calcite A (Magmatic?)											
	55.47	0.11	0.15	0.72	0.36	n.d.	0.00	0.07	44.19	101.06	Tabular
	55.08	0.12	0.17	0.77	0.23	n.d.	n.d.	0.17	43.92	100.46	Tabular
	55.45	0.00	0.18	0.76	0.19	0.03	n.d.	n.d.	44.11	100.72	Tabular
	57.50	0.12	0.20	1.01	0.52	0.01	0.01	0.08	46.02	105.46	Tabular
	54.86	0.04	0.37	1.02	0.61	n.d.	0.03	n.d.	44.10	101.03	Tabular
	55.06	0.08	0.20	0.78	0.21	n.d.	0.14	n.d.	43.95	100.42	Tabular
	55.40	n.d.	0.27	0.88	0.20	n.d.	0.01	0.01	44.21	100.97	Euhedral
	55.11	n.d.	0.16	0.78	0.18	n.d.	n.d.	0.00	43.81	100.04	Euhedral
	55.23	n.d.	0.20	0.80	0.16	n.d.	n.d.	0.02	43.96	100.38	Euhedral
	54.90	0.09	0.14	0.83	0.23	n.d.	0.07	n.d.	43.75	100.01	Subhedral/Anhedral
	54.37	n.d.	0.15	0.86	0.24	n.d.	0.07	n.d.	43.30	98.99	Subhedral/Anhedral
	55.27	n.d.	0.15	0.71	0.23	n.d.	n.d.	n.d.	43.90	100.26	Subhedral/Anhedral
	55.26	0.12	0.18	0.78	0.23	n.d.	0.16	0.19	44.16	101.09	Subhedral/Anhedral
Caclite B (Carbohydrthermal?)											
	50.70	2.43	1.50	0.25	n.d.	0.10	n.d.	n.d.	43.08	98.06	Anhedral
	48.77	1.37	3.35	0.45	n.d.	0.27	0.39	n.d.	43.34	97.93	Anhedral
	48.99	1.52	3.52	0.51	0.05	0.22	n.d.	0.13	43.62	98.56	Anhedral
	49.58	1.15	3.75	0.51	n.d.	0.36	0.03	0.02	44.17	99.57	Anhedral
	49.40	1.44	3.78	0.52	0.04	0.25	n.d.	0.09	44.18	99.70	Anhedral
	49.41	1.23	3.83	0.56	0.10	0.32	n.d.	n.d.	44.17	99.62	Anhedral

Table F.1(b). *Major element data (wt%) for apatite from the Jos kimberlite, analysed by GSC at Carleton University, Ottawa, Canada. n.d. refers to not detected.*

Mineral	P_2O_5	FeO	MnO	CaO	SrO	BaO	Na_2O	La_2O_3	Ce_2O_3	Nd_2O_3	Sm_2O_3	Y_2O_3	SiO_2	F	Cl	SO_3	Total
Apatite																	
	40.45	0.17	0.03	54.40	0.57	0.04	0.18	0.14	0.30	0.09	0.00	0.07	0.61	0.94	0.07	0.09	98.15
	38.80	0.15	n.d.	54.01	0.33	n.d.	0.19	0.07	0.06	0.02	0.03	0.02	0.98	1.69	0.03	0.16	96.56
	36.51	0.27	n.d.	54.31	0.37	0.03	0.19	0.01	n.d.	n.d.	n.d.	n.d.	2.03	1.42	0.03	0.09	95.24
	40.03	0.24	n.d.	54.14	0.48	0.01	0.18	0.19	0.52	0.24	0.23	0.09	0.53	1.08	0.06	0.09	98.11
	38.54	0.21	n.d.	55.35	0.46	0.01	0.22	0.23	0.19	0.16	0.33	0.03	0.86	1.24	0.04	0.08	97.94
	36.77	0.15	n.d.	54.39	0.44	0.00	0.10	0.04	n.d.	0.09	n.d.	0.02	2.10	1.27	0.03	0.08	95.47
	36.39	0.24	0.06	54.37	0.35	0.01	0.13	0.04	0.18	n.d.	n.d.	0.03	2.33	1.01	0.02	0.17	95.35
	38.24	0.34	n.d.	55.45	0.33	0.03	0.10	0.07	0.06	n.d.	0.30	0.03	1.89	1.10	0.02	0.06	98.01
	38.10	0.38	n.d.	54.14	0.31	0.05	0.08	0.05	0.11	n.d.	n.d.	0.05	1.85	1.22	0.02	0.35	96.73
	35.61	1.20	n.d.	51.90	0.40	n.d.	0.12	0.09	0.00	0.12	0.17	0.01	3.83	1.64	0.01	0.72	95.83
	41.12	0.11	n.d.	54.83	0.56	n.d.	0.13	0.23	0.29	0.00	0.18	0.02	0.77	0.92	0.04	0.08	99.29
	36.71	0.23	0.01	55.11	0.40	0.11	0.09	0.01	0.15	0.02	0.18	0.00	1.84	1.31	0.04	0.27	96.49
	37.92	0.13	0.02	54.65	0.54	0.01	0.17	0.01	n.d.	n.d.	0.02	0.07	1.78	1.23	0.03	0.10	96.69
	37.67	0.11	0.02	54.56	0.45	0.03	0.24	n.d.	n.d.	0.11	n.d.	0.01	1.75	1.62	0.03	0.15	96.75
	38.35	0.21	n.d.	55.27	0.35	n.d.	0.05	0.06	0.14	0.01	n.d.	n.d.	1.67	1.26	0.02	0.10	97.51
	40.54	0.19	n.d.	54.45	0.31	0.10	0.12	0.03	0.03	0.09	0.16	0.01	0.66	1.58	0.08	0.11	98.46
	36.72	0.08	n.d.	55.18	0.40	0.00	0.09	0.09	0.10	0.06	0.09	0.01	1.84	1.54	0.02	0.08	96.31
	37.84	0.05	0.02	55.07	0.31	0.05	0.10	0.08	0.04	0.00	n.d.	n.d.	1.44	1.24	0.03	0.12	96.39
	37.94	0.15	n.d.	54.13	0.39	n.d.	0.07	0.00	0.00	0.04	n.d.	n.d.	1.65	1.26	0.01	0.15	95.80
	36.94	0.18	0.02	55.37	0.38	0.11	0.09	0.05	0.13	0.00	0.01	0.01	1.89	1.10	0.04	0.14	96.48
	37.96	0.51	n.d.	54.20	0.37	n.d.	0.10	0.07	0.21	0.12	0.31	0.02	1.38	1.55	0.02	0.16	96.97
	33.47	0.52	0.01	54.74	0.43	0.03	0.50	0.09	0.12	0.00	0.01	0.03	3.12	1.20	0.02	0.16	94.45
	40.33	0.21	0.05	54.50	0.51	n.d.	0.23	0.17	0.41	0.09	n.d.	0.03	0.53	1.22	0.06	0.10	98.44
	39.11	0.19	n.d.	55.47	0.33	0.01	0.13	0.00	0.12	0.12	n.d.	0.04	0.95	1.19	0.02	0.08	97.77
	39.68	0.20	0.04	54.12	0.55	0.01	0.22	0.19	0.51	0.25	0.32	n.d.	0.67	1.07	0.06	0.11	97.99
	39.20	0.20	n.d.	53.38	0.44	0.08	0.20	0.11	0.24	0.15	n.d.	0.06	0.51	1.41	0.04	0.05	96.07
	37.33	0.19	n.d.	54.30	0.38	n.d.	0.11	n.d.	n.d.	0.06	0.24	0.06	1.31	1.40	0.04	0.08	95.51

Table F.1(c). *Major element data (wt%) for perovskite from the Jos kimberlite, analysed by GSC at Carleton University, Ottawa, Canada. n.d. refers to not detected.*

Mineral	SiO_2	TiO_2	ZrO_2	Al_2O_3	Cr_2O_3	FeO	MnO	MgO	CaO	SrO	BaO	Na_2O	Nb_2O_5	Ta_2O_5	La_2O_3	Ce_2O_3	Total	Notes
Perovskite																		
	0.02	53.55	0.10	0.11	0.18	1.12	0.02	0.06	35.18	0.19	n.d.	0.80	1.19	0.34	1.02	2.82	96.68	core
	0.06	55.36	0.12	0.08	0.03	1.01	0.06	0.07	39.87	0.20	n.d.	0.31	0.81	0.00	0.51	0.87	99.37	rim
	0.11	54.62	0.05	0.08	0.24	1.24	0.03	0.09	36.70	0.18	0.01	0.62	0.95	0.15	0.74	2.25	98.06	core
	0.10	55.68	0.04	0.07	0.09	1.11	0.03	0.06	38.60	0.23	n.d.	0.33	0.67	0.02	0.46	0.93	98.43	rim
	0.03	53.94	0.06	0.05	0.23	1.13	n.d.	0.05	36.44	0.19	0.05	0.60	0.93	0.20	0.82	2.40	97.10	core
	0.15	55.47	0.12	0.04	0.12	0.98	0.06	0.10	38.21	0.16	0.03	0.40	0.82	0.04	0.49	1.22	98.41	rim
	0.12	54.94	0.09	0.17	0.03	1.14	0.02	0.09	38.35	0.20	0.08	0.38	0.46	0.13	0.58	1.75	98.53	core
	0.13	54.13	0.07	0.28	n.d.	1.36	n.d.	0.11	39.40	0.30	0.07	0.15	0.74	0.00	0.33	0.62	97.68	rim
	0.06	54.62	0.10	0.13	0.08	0.98	n.d.	0.07	38.29	0.22	n.d.	0.37	0.46	0.04	0.63	1.75	97.80	core
	0.07	55.44	0.02	0.20	0.02	1.03	0.05	0.06	38.76	0.18	n.d.	0.24	0.58	0.08	0.51	1.17	98.41	rim
	0.04	54.06	0.06	0.05	0.33	1.02	0.02	0.05	36.58	0.20	0.05	0.70	0.70	0.29	0.78	2.38	97.32	core
	0.06	55.02	0.04	0.05	0.19	0.89	0.01	0.06	38.09	0.21	0.00	0.42	0.77	0.09	0.53	1.37	97.78	rim
	n.d.	53.10	0.11	0.05	0.24	1.16	n.d.	0.02	34.03	0.18	0.03	0.83	1.15	0.23	0.90	2.75	94.77	core
	0.07	55.29	0.08	0.08	0.05	1.16	0.05	0.06	38.00	0.17	0.08	0.35	0.89	0.01	0.51	0.97	97.83	rim
	0.04	52.43	0.06	0.31	n.d.	1.34	n.d.	0.09	34.67	0.30	n.d.	0.60	0.86	0.23	0.98	2.94	94.85	core

Table F.1(d). *Major element data (wt%) for olivine from the Jos kimberlite, analysed by GSC at Carleton University, Ottawa, Canada. n.d. refers to not detected.*

Mineral	SiO_2	TiO_2	Al_2O_3	Cr_2O_3	V_2O_3	FeO	MnO	CoO	NiO	ZnO	MgO	CaO	Total	Ni ppm	Forsterite	Notes
Olivine Phenocryst																
	40.44	0.04	0.02	0.02	0.01	13.05	0.13	n.d.	0.23	0.01	46.23	0.10	100.28	1830	86.33	Phenocryst core
	40.44	0.07	n.d.	0.04	0.02	10.55	0.11	0.01	0.22	0.03	47.88	0.11	99.46	1700	89.00	Phenocryst rim
	40.29	0.04	0.01	0.03	0.03	11.29	0.13	0.02	0.36	0.05	47.85	0.08	100.18	2820	88.31	Phenocryst core
	40.90	0.02	n.d.	0.03	n.d.	9.87	0.12	0.01	0.36	n.d.	49.19	0.08	100.58	2860	89.89	Phenocryst rim
	39.88	0.04	0.01	0.01	0.03	14.61	0.18	0.05	0.20	0.06	45.36	0.04	100.47	1550	84.69	Phenocryst core
	40.82	0.03	n.d.	0.04	0.01	10.77	0.13	0.01	0.27	n.d.	48.03	0.09	100.20	2120	88.82	Phenocryst rim
	40.97	0.01	0.05	0.02	n.d.	10.96	0.15	0.02	0.38	n.d.	47.86	0.12	100.54	3010	88.62	Phenocryst core
	41.11	0.01	0.03	0.04	n.d.	9.44	0.15	0.03	0.21	0.05	49.11	0.23	100.41	1620	90.26	Phenocryst rim
	41.09	0.01	n.d.	0.03	n.d.	7.34	0.14	0.02	0.33	0.07	49.06	0.05	98.13	2590	92.25	Phenocryst core
	41.53	n.d.	0.01	0.01	n.d.	7.58	0.09	0.01	0.32	n.d.	50.45	0.05	100.04	2530	92.23	Phenocryst core
	40.57	0.04	0.01	0.04	n.d.	10.75	0.14	0.01	0.32	n.d.	47.98	0.16	100.02	2500	88.83	Phenocryst rim
	40.34	0.02	0.01	n.d.	0.05	13.33	0.16	0.03	0.33	0.06	46.16	0.02	100.50	2580	86.06	Phenocryst core
	40.56	0.01	0.01	0.08	0.02	10.80	0.15	0.02	0.13	0.01	47.53	0.15	99.46	990	88.69	Phenocryst rim
	40.57	0.02	0.01	0.03	n.d.	10.66	0.14	0.06	0.28	n.d.	47.36	0.07	99.20	2210	88.79	Phenocryst unzoned
	40.61	0.02	0.02	0.01	0.01	13.21	0.14	0.04	0.26	0.02	45.77	0.08	100.17	2040	86.07	Phenocryst core
	40.90	0.03	0.01	0.02	n.d.	10.71	0.16	n.d.	0.28	n.d.	47.55	0.15	99.81	2220	88.78	Phenocryst rim
	41.02	0.02	0.04	0.01	0.01	9.73	0.10	0.04	0.40	n.d.	48.30	0.15	99.82	3140	89.84	Phenocryst unzoned
	41.07	0.01	n.d.	n.d.	0.07	9.75	0.14	0.03	0.33	n.d.	49.20	0.03	100.63	2610	89.99	Phenocryst unzoned
	41.04	0.04	n.d.	0.01	n.d.	11.26	0.15	0.05	0.38	n.d.	47.00	0.07	99.99	2960	88.16	Phenocryst core
	41.30	n.d.	n.d.	0.01	0.02	7.99	0.14	0.04	0.34	n.d.	50.09	0.01	99.94	2650	91.79	Phenocryst unzoned
	41.41	0.02	n.d.	0.03	0.01	7.29	0.13	n.d.	0.38	0.04	50.87	0.03	100.20	3000	92.56	Phenocryst core
	40.81	0.03	0.02	0.03	0.01	10.94	0.17	0.02	0.23	0.03	47.98	0.15	100.42	1790	88.66	Phenocryst rim
	40.90	n.d.	0.02	0.02	n.d.	11.45	0.15	n.d.	0.31	0.05	47.40	0.03	100.34	2460	88.06	Phenocryst core
	40.81	0.04	0.02	0.06	0.03	10.51	0.20	0.01	0.15	n.d.	48.45	0.17	100.44	1140	89.15	Phenocryst rim
	40.81	0.03	n.d.	0.02	n.d.	10.31	0.15	n.d.	0.38	0.08	48.29	0.04	100.10	2960	89.31	Phenocryst core
	40.64	0.02	0.02	0.04	n.d.	13.23	0.16	n.d.	0.24	n.d.	46.31	0.07	100.72	1870	86.19	Phenocryst core
	41.38	0.02	n.d.	0.06	0.02	9.32	0.17	0.04	0.23	0.02	49.34	0.21	100.80	1790	90.42	Phenocryst rim

Table F.1(d) continued. *Major element data (wt%) for olivine from the Jos kimberlite, analysed by GSC at Carleton University, Ottawa, Canada. n.d. refers to not detected.*

Mineral	SiO_2	TiO_2	Al_2O_3	Cr_2O_3	V_2O_3	FeO	MnO	CoO	NiO	ZnO	MgO	CaO	Total	Ni ppm	Forsterite	Notes
Olivine Megacryst/Xenocryst																
	41.38	n.d.	0.01	0.03	0.01	8.46	0.13	0.03	0.37	0.04	49.73	0.04	100.22	2890	91.29	Megacryst core
	40.56	0.03	0.01	0.03	n.d.	10.65	0.13	0.02	0.14	0.05	48.13	0.15	99.90	1080	88.96	Megacryst rim
	41.51	n.d.	0.01	0.02	n.d.	7.56	0.09	0.02	0.33	0.05	50.58	0.02	100.20	2610	92.26	Megacryst core
	40.49	0.03	0.01	0.03	n.d.	10.46	0.14	0.05	0.20	n.d.	48.12	0.10	99.63	1590	89.13	Megacryst rim
	41.52	0.03	n.d.	0.01	0.03	7.60	0.12	0.02	0.34	0.02	50.85	0.04	100.56	2690	92.27	Megacryst core
	40.77	0.02	0.01	0.04	n.d.	10.46	0.14	0.01	0.24	0.07	48.13	0.07	99.96	1850	89.14	Megacryst rim
	41.29	0.01	0.03	0.03	0.01	7.70	0.12	n.d.	0.36	n.d.	50.24	0.06	99.84	2810	92.08	Megacryst core
	41.06	0.04	n.d.	0.07	n.d.	10.78	0.16	n.d.	0.16	n.d.	48.71	0.12	101.11	1230	88.95	Megacryst rim
	41.16	n.d.	n.d.	0.01	n.d.	8.38	0.11	n.d.	0.36	0.02	50.28	0.02	100.36	2820	91.45	Megacryst core
	40.80	n.d.	n.d.	0.03	0.01	10.23	0.22	0.05	0.17	n.d.	48.08	0.25	99.85	1350	89.33	Megacryst rim
	41.56	0.01	n.d.	0.01	0.03	7.14	0.14	n.d.	0.39	0.02	51.36	0.02	100.69	3070	92.76	Megacryst core
	40.94	0.02	n.d.	0.04	0.04	10.22	0.15	0.02	0.18	n.d.	48.67	0.10	100.38	1390	89.46	Megacryst rim
	41.30	0.02	0.02	0.04	n.d.	7.59	0.11	0.02	0.39	0.04	50.18	0.04	99.74	3070	92.18	Megacryst core
	40.35	0.06	n.d.	0.08	n.d.	10.65	0.14	0.01	0.23	n.d.	47.73	0.11	99.37	1800	88.88	Megacryst rim
	41.20	0.01	n.d.	0.02	n.d.	7.83	0.10	0.01	0.38	n.d.	50.78	0.01	100.35	2990	92.04	Megacryst core
	40.91	0.05	0.01	0.06	n.d.	10.90	0.18	0.04	0.17	0.01	48.10	0.14	100.57	1330	88.72	Megacryst rim
	41.49	n.d.	0.02	0.06	0.01	7.54	0.13	0.02	0.37	0.09	50.86	0.06	100.67	2940	92.32	Megacryst core
	40.22	0.04	0.01	0.02	0.02	10.52	0.14	0.04	0.31	n.d.	47.87	0.09	99.29	2450	89.02	Megacryst rim
	41.23	0.02	n.d.	0.01	n.d.	7.58	0.11	0.01	0.37	n.d.	50.43	0.02	99.78	2930	92.22	Megacryst core
	40.44	0.02	n.d.	0.04	0.02	10.53	0.15	0.01	0.16	0.08	47.74	0.15	99.33	1230	88.99	Megacryst rim
	41.61	0.03	0.03	0.02	n.d.	7.65	0.10	0.02	0.38	n.d.	50.12	0.07	100.05	3020	92.11	Megacryst core
	40.77	0.02	n.d.	0.02	0.01	10.68	0.15	0.04	0.18	n.d.	47.96	0.17	100.00	1450	88.90	Megacryst rim

Table F.2(a). *Trace element concentration data (ppm) for the phenocrystal olivine, xenocrystal olivine, calcite, perovskite, apatite and phlogopite from the Jos kimberlite. b.d.l refers to below detection limits. .*

Mineral	Xenocrystal Olivine	Phenocrystal Olivine	Perovskite	Apatite	Phlog	Calcite A	Calcite B	Whole Rock	Whole Rock
Batch #	M76-14	M76-20	M76-17	JOS-AP6	M76-23	M81-8	M81-10	116-5	116-10
Rb	0.138	0.833	41.63	3.216	315.7	b.d.l.	b.d.l.	18.78	21.77
Sr	1.225	4.163	2323	4870	41.34	4352	1153	1877	2166
Y	0.048	0.353	215.9	148.8	0.613	b.d.l.	0.057	2.154	2.865
Zr	1.897	7.907	2460	32.86	117.9	0.416	0.319	41.16	54.48
Nb	0.610	15.27	3275	5.399	49.72	0.051	0.185	116.6	142.6
Ba	5.666	47.19	534.2	556.3	8502	103.8	156.3	1630	1876
La	0.595	6.032	5187	1465	7.593	b.d.l.	0.211	73.69	85.42
Ce	1.168	12.30	10821	2886	12.92	b.d.l.	0.702	61.62	81.84
Pr	0.121	1.250	1106	292.8	1.361	b.d.l.	0.009	12.51	14.72
Nd	0.427	4.196	4209	1008	4.411	b.d.l.	0.148	43.93	51.24
Sm	0.053	0.564	520.6	123.3	0.587	0.007	0.005	5.513	6.410
Eu	0.014	0.115	98.58	29.57	0.391	0.043	0.005	1.386	1.614
Gd	0.030	0.404	213.1	110.2	0.604	0.034	0.007	3.137	3.628
Dy	0.013	0.133	82.84	40.31	0.156	b.d.l.	0.001	1.248	1.494
Er	0.005	0.033	19.22	14.27	0.048	b.d.l.	b.d.l.	0.378	0.470
Yb	0.006	0.017	6.236	4.713	0.157	b.d.l.	b.d.l.	0.176	0.224
Lu	0.001	0.002	0.602	0.613	0.051	b.d.l.	0.000	0.025	0.034
Hf	0.040	0.203	80.59	0.490	1.754	0.070	0.007	0.926	1.218
Pb	0.008	0.022	4.735	10.05	0.181	b.d.l.	b.d.l.	9.350	10.521
Th	0.080	0.546	957.7	87.64	0.733	b.d.l.	0.002	0.039	0.054
U	0.013	0.148	127.1	3.047	0.198	b.d.l.	b.d.l.	1.959	2.262
Tb	0.003	0.031	23.93	10.04	0.035	b.d.l.	0.000	0.309	0.372

Table F.2(b). *Trace element data (ng of analyte) for the leachates of the picked mineral separates.*

Mineral Leached	Xenocrystal olivine	Phenocrystal olivine	Phlogopite	Perovskite
Batch #	M75-3	M75-2	M75-5	M75-4
Rb	0.128	0.203	7.075	0.012
Sr	27.256	26.830	31.465	1.145
Y	0.139	0.108	0.220	0.005
Zr	0.249	0.412	0.621	0.032
Nb	0.020	0.023	0.040	0.004
Ba	7.768	3.845	23.224	0.566
La	1.122	0.877	1.007	0.039
Ca	1.330	1.143	1.197	0.061
Pr	0.114	0.100	0.108	0.006
Nd	0.402	0.326	0.380	0.021
Sm	0.051	0.043	0.056	0.003
Eu	0.016	0.014	0.019	0.001
Gd	0.035	0.030	0.044	0.002
Dy	0.022	0.020	0.030	0.001
Er	0.010	0.009	0.014	0.000
Yb	0.009	0.010	0.013	0.000
Lu	0.002	0.002	0.002	0.000
Hf	0.003	0.006	0.011	0.001
Pb	0.021	0.096	0.576	0.001
Th	0.008	0.008	0.016	0.007
U	0.007	0.007	0.025	0.002
Tb	0.005	0.004	0.006	0.000

Table F.3(a). *Sr isotope data for phenocrystal olivine, xenocrystal olivine, calcite, phlogopite, perovskite and apatite. (m) refers to measured ratio; (n) to the normalised ratio (see Appendix A for standard data); (i) refers to the initial ratio which is age corrected to 98Ma.*

Mineral	Sample #	Age (Ma)	Rb (ng)	Sr (ng)	$^{87}Rb/^{86}Sr$	$^{87}Sr/^{86}Sr_n$	2SE	$^{87}Sr/^{86}Sr_i$
Xenocrystal olivine								
	M76-14	98	0.13	1.17	0.326	0.705229	0.000062	0.704789
Phenocrystal olivine								
	M76-20	98	0.16	0.78	0.579	0.705660	0.000032	0.704879
Perovskite								
	M76-2	98	0.00	0.32	0.006	0.705147	0.000039	0.705139
	M76-3	98	0.00	0.12	0.003	0.705151	0.000030	0.705147
	M76-4	98	0.00	0.10	0.005	0.705165	0.000018	0.705158
	M76-5	98	0.00	0.26	0.009	0.704867	0.000015	0.704855
	M76-7	98	0.00	0.04	0.015	0.705290	0.000030	0.705269
	M76-8	98	0.00	0.19	0.004	0.705084	0.000011	0.705078
	M76-9	98	0.00	0.31	0.007	0.704966	0.000042	0.704957
	M76-15	98	0.05	15.64	0.009	0.704931	0.000009	0.704919
	M76-17	98	0.09	5.23	0.010	0.704933	0.000017	0.704920
Phlogopite								
	M76-16	98	105.25	13.58	22.491	0.735380	0.000020	0.705018
	M76-23	98	20.21	2.65	22.259	0.782753	0.000022	0.752705
Calcite A								
	M81-8	98	b.d.l.	0.84	0.000	0.708591	0.000016	0.708591
	M81-11	98	b.d.l.	4.94	0.000	0.708725	0.000008	0.708725
	JOS-CC-3	98	0.01	5.79	0.004	0.708563	0.000016	0.708442
Calcite B								
	M81-9	98	b.d.l.	3.83	0.000	0.706381	0.000008	0.706381
	M81-10	98	b.d.l.	3.51	0.000	0.706493	0.000016	0.706493
	JOS-CC-1	98	0.01	6.20	0.005	0.705447	0.000016	0.705299
	JOS-CC-2	98	0.01	4.38	0.006	0.707173	0.000016	0.706997
	JOS-CC-4	98	0.01	23.75	0.002	0.706758	0.000014	0.706712
	JOS-CC-5	98	0.02	25.62	0.002	0.707166	0.000017	0.707109
Apatite								
	JOS-AP-1	98	0.01	0.62	0.049	0.704817	0.000023	0.703409
	JOS-AP-2	98	0.01	0.15	0.168	0.705215	0.000074	0.700379
	JOS-AP-3	98	0.01	0.47	0.064	0.705726	0.000026	0.703878
	JOS-AP-4	98	0.00	0.33	0.037	0.705195	0.000029	0.704133
	JOS-AP-5	98	0.01	1.30	0.015	0.704787	0.000024	0.704353
Whole Rock								
	116-5	98	180.10	18001.42	0.029	0.706358	0.000008	0.706319
	116-10	98	217.30	21612.87	0.029	0.706364	0.000010	0.706325
	JOS-1*	98			0.033	0.706272	0.000015	0.706226

Table F.3(b). *Sr isotope data for the leachates from the picked minerals.*

Mineral Leached	Batch #	$^{87}Sr/^{86}Sr_n$	2SE
Xenocrystal olivine	M75-3	0.706556	0.000011
Phenocrystal olivine	M75-2	0.707999	0.000011
Phlogopite	M75-5	0.707356	0.000074
Perovskite	M75-4	0.705926	0.000013

Table F.4. *Nd isotope data for phlogopite and perovskite. (m) refers to measured ratio; (n) to the normalised ratio (see Appendix A for standard data); (i) refers to the initial ratio which is age corrected to 98Ma. The whole rock analysis is taken from Dowall et al.(2004).*

Mineral	Sample #	Nd (ng)	Sm (ng)	$^{147}Sm/^{144}Nd$	$^{143}Nd/^{144}Nd_n$	2SE	$^{143}Nd/^{144}Nd$
Perovskite							
	M76-2	0.74	0.09	0.073	0.512681	0.000076	0.512636
	M76-3	0.22	0.03	0.073	0.512611	0.000108	0.512566
	M76-5	0.46	0.06	0.074	0.512689	0.000104	0.512643
	M76-8	0.39	0.05	0.075	0.512886	0.000114	0.512839
	M76-9	0.54	0.07	0.076	0.512623	0.000086	0.512576
	M76-15	2.65	0.32	0.074	0.512639	0.000022	0.512593
	M76-17	1.05	0.13	0.075	0.512647	0.000070	0.512600
Whole Rock							
	JOS-1*			0.075	0.512618	0.00001	0.51257

***Figure F.1**. False colour QEMSCAN images of a thin section of the Jos kimberlite illustrating the mineral relationships.*

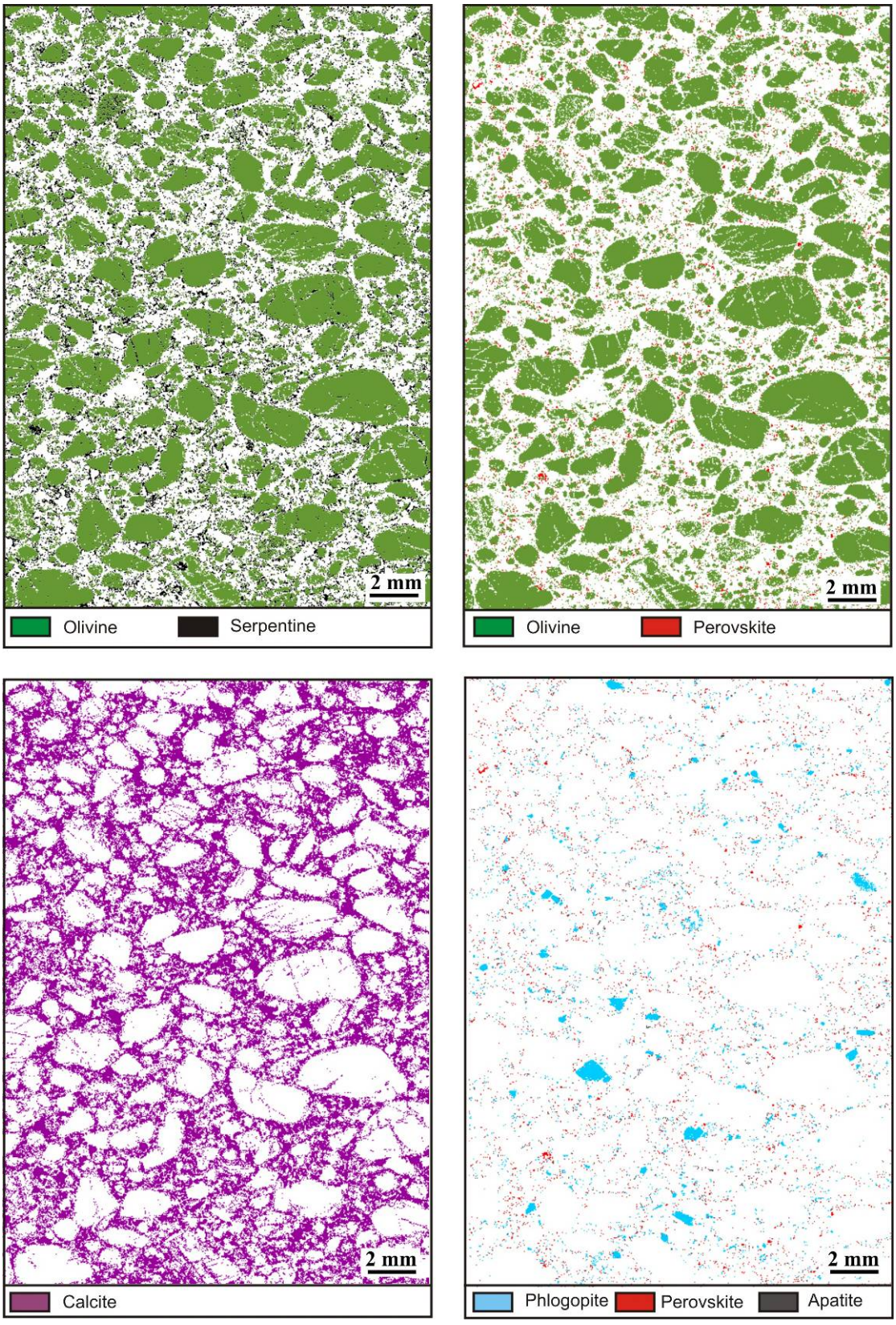

***Figure F.2**. Chondrite normalised (McDonough and Sun, 1995) multi-element plots for the leachate and the corresponding leached mineral. The patterns do not represent normalised concentrations but the mass of analyte (ng) normalised to chondrite.*

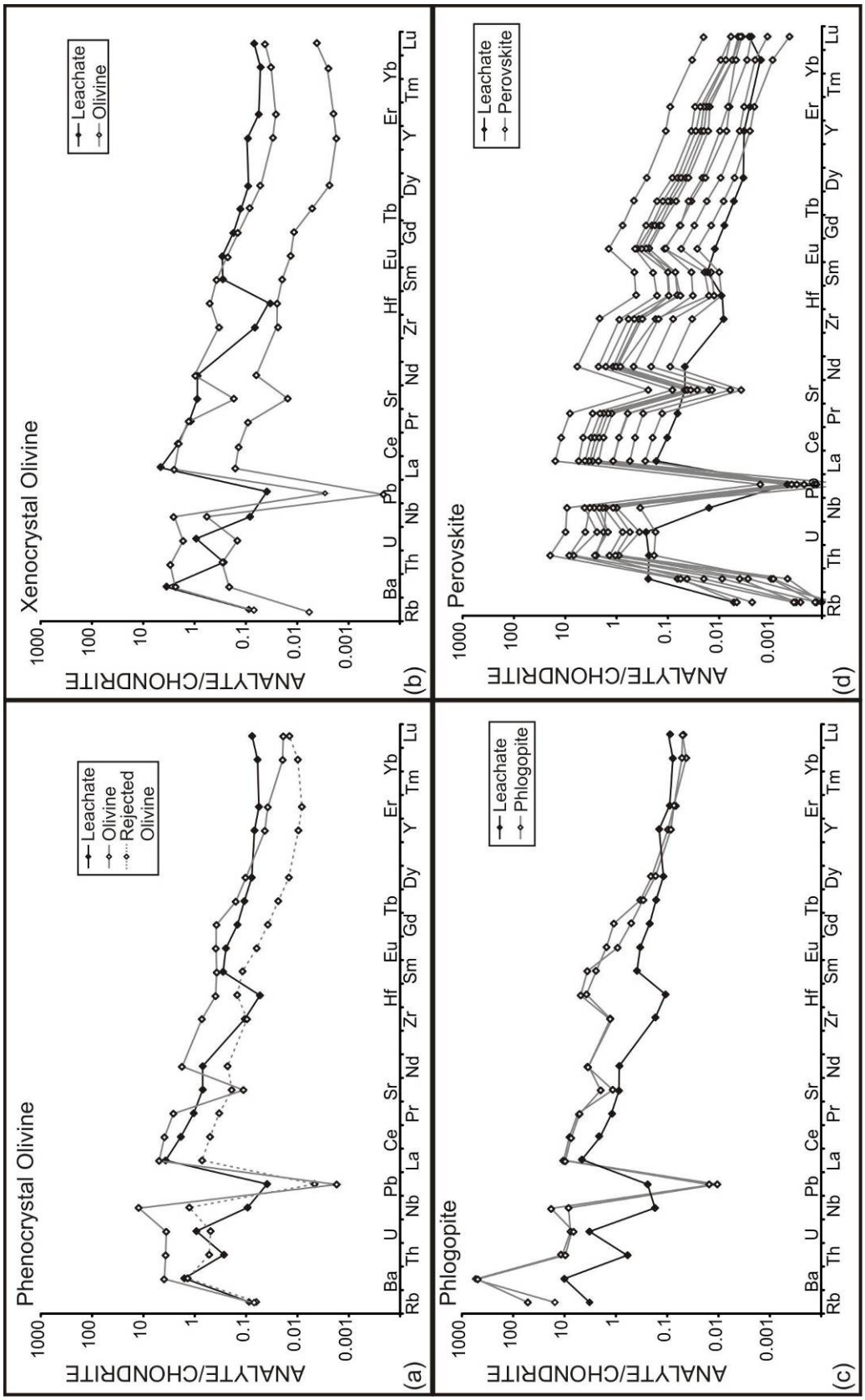

***Figure F.3**. Normalised Sr isotope ratios for leached minerals and the corresponding leachates from the Jos kimberlite. The whole rock value is shown for reference. Calcite and apatite were not leached as they are so readily dissolved in weak acids.*

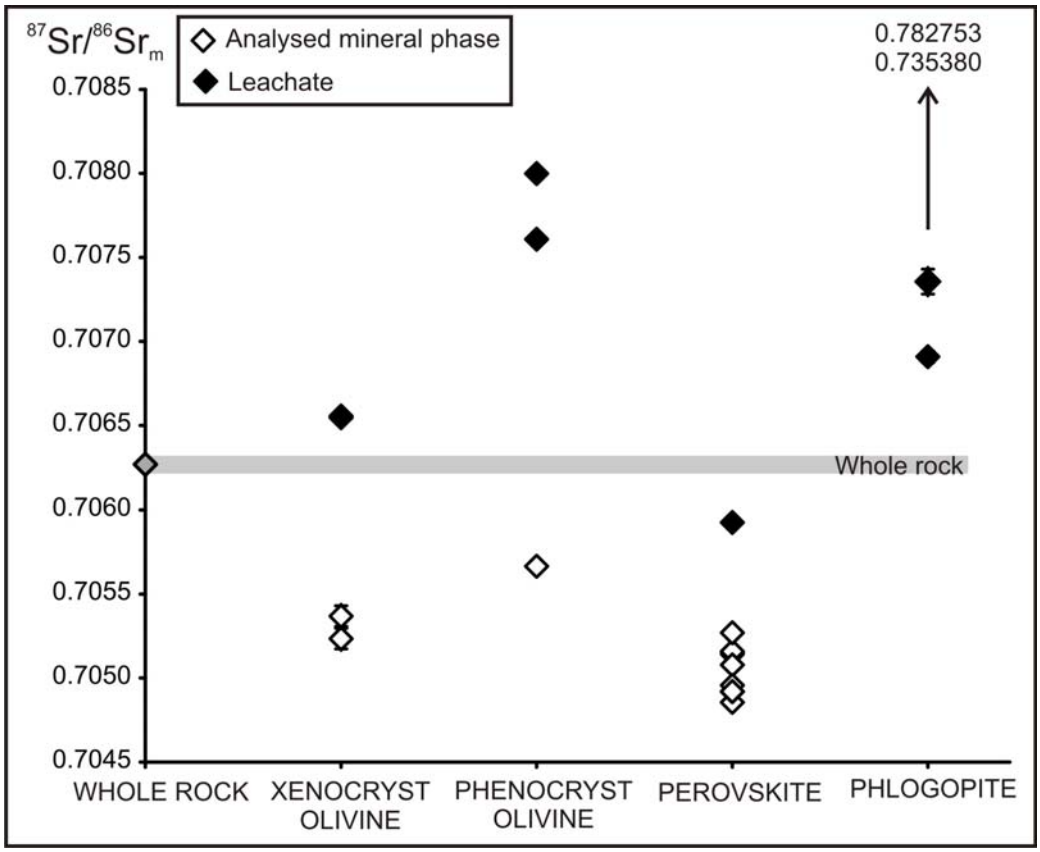

Figure F.4(a). *Photograph of the picked and leached xenocrystal olivine.*

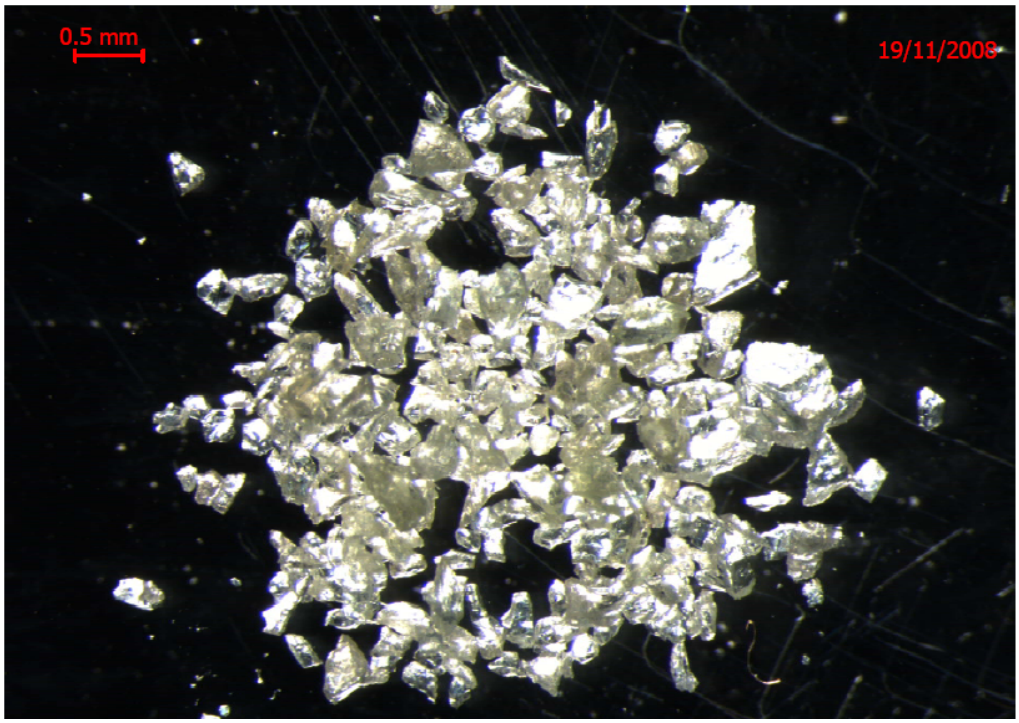

Figure F.4(b). *Photograph of the picked and leached phenocrystal olivine, note the distinctive euhedral crystal shape.*

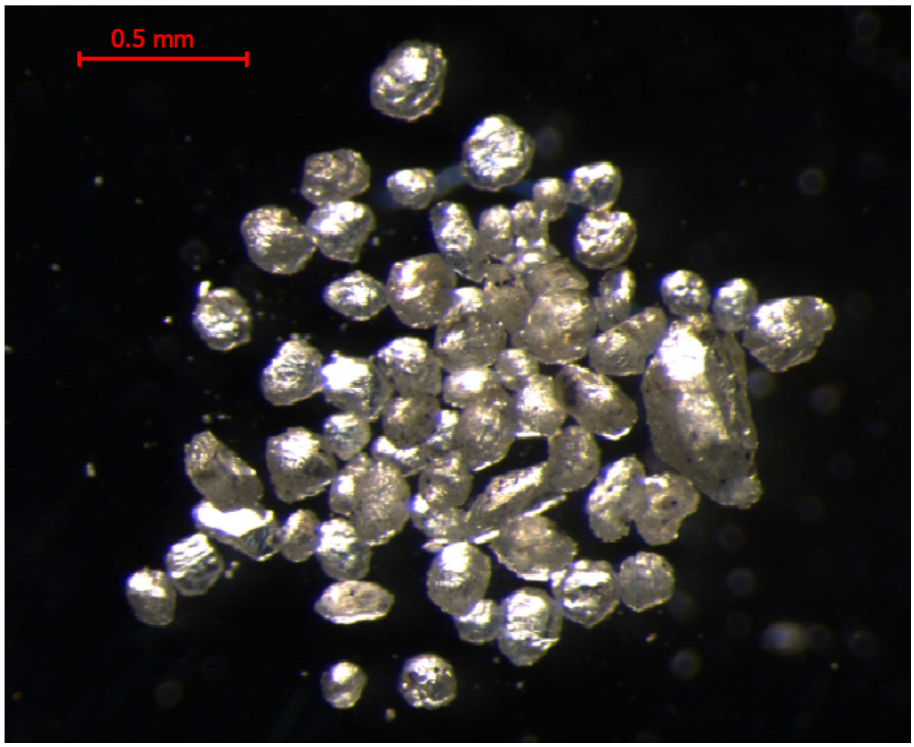

Figure F.4(c). *Photograph of the picked and leached phlogopite.*

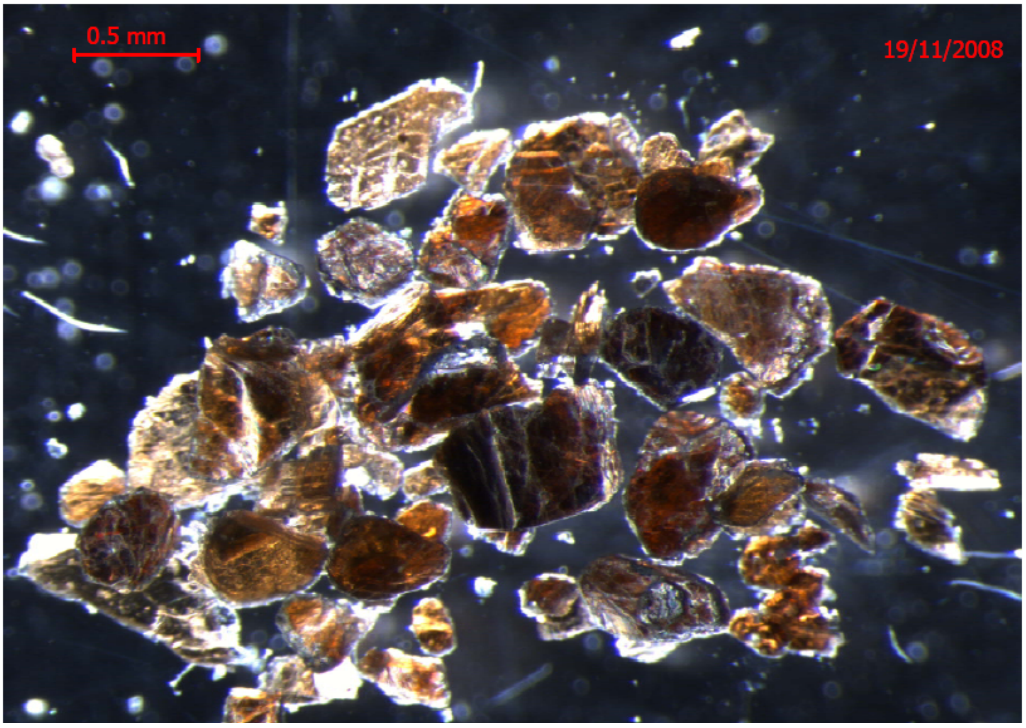

Figure F.4(d). *Photograph of picked and leached perovskite.*

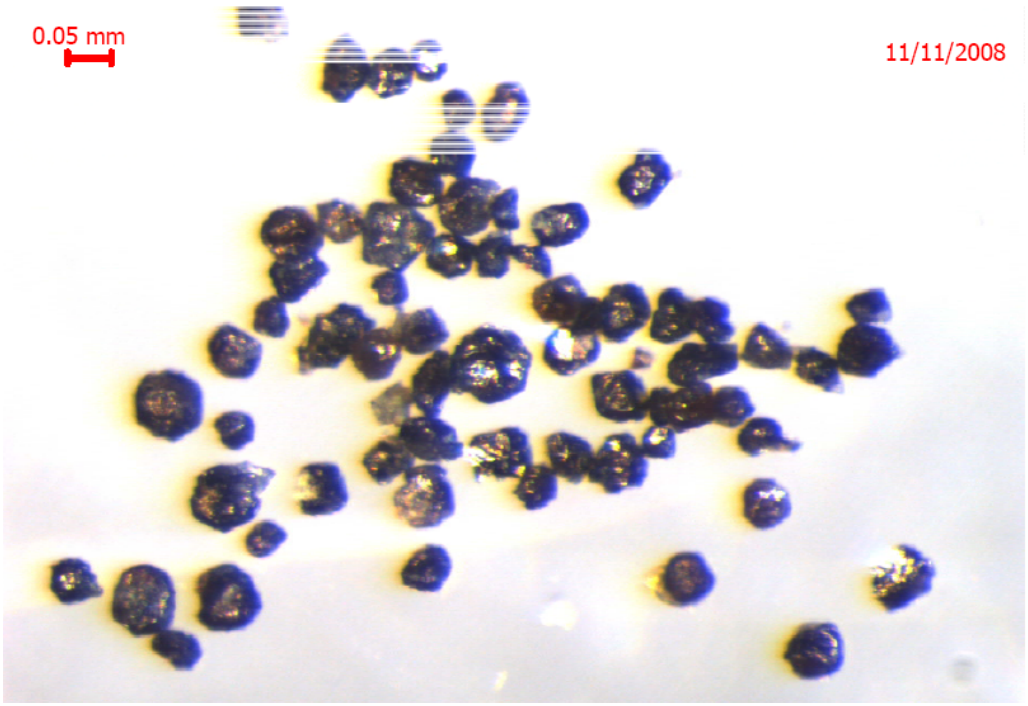

Figure F.4(e) *Photograph of five examples of apatite crystals picked for analysis.*

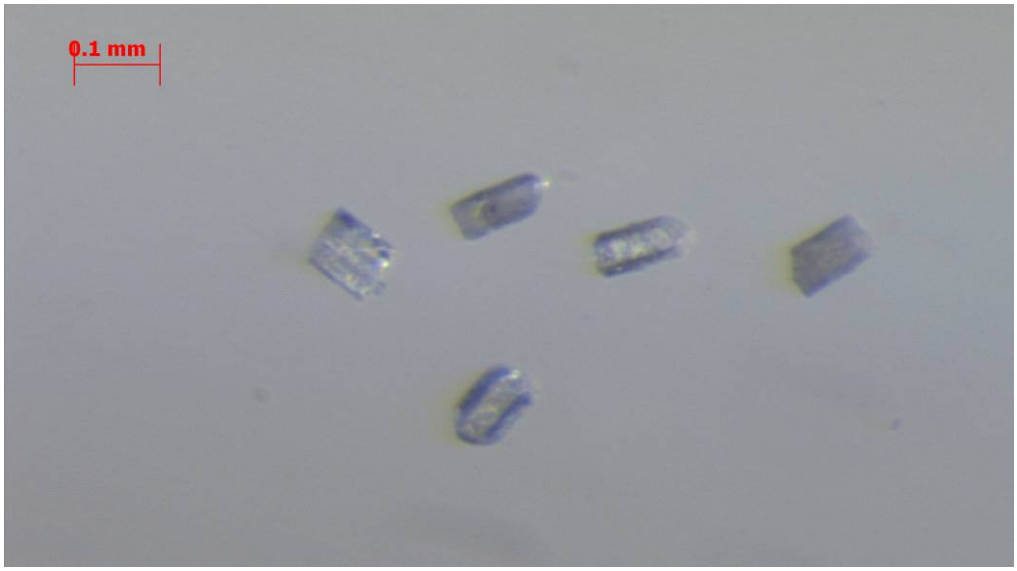

References:

Dowall, D., 2004. Elemental and isotopic geochemistry of kimberlites from the Lac de Gras field, Northwest Territories, Canada, Durham University, Durham.

McDonough, W.F. and Sun, S.S., 1995. The Composition of the Earth. Chemical Geology, 120(3-4): 223-253.